



THE UNIVERSITY OF QUEENSLAND
A U S T R A L I A

**Trajectory Optimisation of a Partially-Reusable
Rocket-Scramjet-Rocket Small Satellite Launch System**

Sholto O. Forbes-Spyratos

B.Eng. (Mechanical and Aerospace) (Hons. I) & B.Sc. (Physics)

A thesis submitted for the degree of Doctor of Philosophy at
The University of Queensland in 2018

School of Mechanical Engineering

Centre for Hypersonics

Abstract

The small satellite industry is expanding rapidly, driving a need for dedicated, cost effective, small satellite launchers. The small satellite launchers currently under development are mostly designed to be disposable, contrary to the design trends of larger launch systems, which are moving towards reusability. These contradictory design philosophies are due to the unfavourable scaling of the systems necessary for reusability, which are not cost effective for small sized launch systems. A possible way to introduce effective reusability to small scale launch systems is to incorporate airbreathing engines within the launch system design. Scramjets are particularly suitable for launch system integration, due to their high Mach number operation and wide operational regime. Because of these advantages, work is ongoing at The University of Queensland to develop a small satellite launch system incorporating a scramjet accelerator. This launcher is a rocket-scramjet-rocket, three stage system, designed to be partially reusable. The trajectory simulations of this launch system have previously been designed assuming that flying the scramjet-powered stage at its maximum dynamic pressure will maximise the efficiency of the scramjet engines, and that this will benefit the performance of the launch system. However, there are complex trade-offs between the rocket and airbreathing stages, which must be accounted for within a partially-airbreathing launch system. The rocket stages perform significantly better at high altitudes, where the efficiency loss due to the drag and atmospheric pressure are diminished. Conversely, the airbreathing stage requires high density air to operate effectively, and will generally perform better at low altitudes. This work develops an optimal trajectory profile for a rocket-scramjet-rocket, three stage launch system, determining the flight path which maximises the payload-to-orbit capabilities of the launch system.

Significant work has previously been carried out on the design and shape optimisation of the scramjet-powered stage of the launch system, designated the SPARTAN. However, the first stage has not been designed, and the third stage previously used an Aerojet Rocketdyne RL-10-3A motor, which is a costly, pump-fed motor. A first stage rocket is developed, based on a Falcon-1e scaled down lengthwise to 8.5m, an appropriate size to accelerate the SPARTAN to the minimum operable conditions of the scramjet engines. The third stage rocket is redesigned, to be powered by a cost effective SpaceX Kestrel upper stage motor. The aerodynamics of the first stage and the SPARTAN are simulated using inviscid CFD, along with a viscous correction, to produce accurate aerodynamic databases. The aerodynamics of the third stage are modelled using Missile Datcom.

A package is created to calculate the maximum payload-to-orbit trajectory of the rocket-scramjet-rocket launch system in six degrees of freedom, designated LODESTAR. In order to determine the maximum payload-to-orbit trajectory shape, optimal control theory is used. For this, LODESTAR utilises GPOPS-2 a pseudospectral method optimal control software. The launch trajectory is initially simulated without the fly-back of the SPARTAN, assuming that the SPARTAN lands at some position downrange. A launch trajectory is first simulated in which the SPARTAN flies at maximum

dynamic pressure, for comparison with previous reference cases. In order for the SPARTAN to fly at its maximum dynamic pressure for the duration of its trajectory, the first stage pitches rapidly, flying at negative angle of attack. The SPARTAN then flies at close to horizontal flight, releasing the third stage at a low trajectory angle.

The maximum payload-to-orbit trajectory of the launch system is calculated, and is found to differ significantly from the trajectory in which the SPARTAN flies at maximum dynamic pressure. The SPARTAN is found to deviate from its maximum dynamic pressure at both stage separation points, and for a segment in the middle of its trajectory. Higher first stage-SPARTAN and SPARTAN-third stage separation points result in the efficiency of the SPARTAN reducing, but increase the efficiency of the rocket stages, improving the overall efficiency of the system. Additionally, an altitude raising manoeuvre is performed in a region where the specific impulse of the scramjet engines is relatively homogeneous with varied flight conditions, resulting in a very small performance increase. Overall, flying an optimal trajectory increases the payload-to-orbit of the system launching to sun synchronous orbit to 189.2kg, an increase of 16.3% compared to a trajectory in which the SPARTAN flies at maximum dynamic pressure.

The fly-back of the SPARTAN is included within the trajectory optimisation, and a maximum payload-to-orbit flight path is simulated. It is found that the SPARTAN must ignite its scramjet engines during its return flight, causing the fly-back to become an important consideration in the optimal trajectory shape. When fly-back is included, the first stage pitches towards the east, though the final orbital inclination is a polar sun synchronous orbit, and the SPARTAN banks heavily throughout its acceleration. This manoeuvre decreases the performance of the SPARTAN, but also reduces the amount of fuel used during fly-back, for a net performance gain. The fly-back is found to exhibit multiple ‘skipping’ manoeuvres. These skipping manoeuvres serve to increase the glide range of the SPARTAN, minimising the fuel necessary during the return flight. Additionally, the scramjet engines are powered on at the trough of the first three skips, which allows the scramjet engines to ignite at the points of highest possible specific impulse. In total, 17.2% of the SPARTAN’s fuel mass is used during the return flight, and the launch system is able to deliver 170.2kg of payload to sun synchronous orbit while returning the SPARTAN successfully to its initial launch site.

The design of the launch system is undergoing significant modifications and improvements. For this reason, a study is conducted to quantify the sensitivity of the launch system to variations in key design parameters. The behaviour of the maximum payload-to-orbit trajectory, both with and without SPARTAN fly-back, is investigated as the physical characteristics of the launch system are modified. It is found that in all cases, as the ‘useful’ energy available to the SPARTAN is increased, the trade-off between the efficiency of the SPARTAN and the third stage rocket shifts to favour the SPARTAN, and vice-versa. The sensitivities of coupled design parameters are compared, to quantify their relative impact on the performance of the launch system. The magnitudes of these relative impacts are assessed, to indicate the design trade-offs which will produce an increase in the launch

system performance. Importantly, it is found that if a reduction in the maximum dynamic pressure of the SPARTAN by -1kPa reduces the structural and thermal protection mass of the SPARTAN by greater than -26.5kg (or -28.4kg with SPARTAN fly-back), then the performance of the launch system will improve.

Declaration by author

This thesis is composed of my original work, and contains no material previously published or written by another person except where due reference has been made in the text. I have clearly stated the contribution by others to jointly-authored works that I have included in my thesis.

I have clearly stated the contribution of others to my thesis as a whole, including statistical assistance, survey design, data analysis, significant technical procedures, professional editorial advice, and any other original research work used or reported in my thesis. The content of my thesis is the result of work I have carried out since the commencement of my research higher degree candidature and does not include a substantial part of work that has been submitted to qualify for the award of any other degree or diploma in any university or other tertiary institution. I have clearly stated which parts of my thesis, if any, have been submitted to qualify for another award.

I acknowledge that an electronic copy of my thesis must be lodged with the University Library and, subject to the policy and procedures of The University of Queensland, the thesis be made available for research and study in accordance with the Copyright Act 1968 unless a period of embargo has been approved by the Dean of the Graduate School.

I acknowledge that copyright of all material contained in my thesis resides with the copyright holder(s) of that material. Where appropriate I have obtained copyright permission from the copyright holder to reproduce material in this thesis.

Publications During Candidature

Journal papers

S. O. Forbes-Spyratos, M. P. Kearney, M. K. Smart, and I. H. Jahn. “Trajectory Design of a Rocket-Scramjet-Rocket Multi-Stage Launch System”. In: *Journal of Spacecraft and Rockets* (2018). DOI: [10.2514/1.A34107](https://doi.org/10.2514/1.A34107)

Conference papers

S. Forbes-Spyratos, M. Kearney, M. Smart, and I. Jahn. “Trajectory design of a rocket-scramjet-rocket multi-stage launch system”. In: *21st AIAA International Space Planes and Hypersonics Technologies Conference, Hypersonics 2017*. Xiamen, China, 2017. ISBN: 9781624104633

S. O. Forbes-Spyratos, M. P. Kearney, M. K. Smart, and I. H. Jahn. “Fly-back of a scramjet-powered accelerator”. In: *AIAA Scitech, 2018*. Orlando, FL, 2018. ISBN: 9781624105241. DOI: [10.2514/6.2018-2177](https://doi.org/10.2514/6.2018-2177)

J. Chai, M. Smart, S. Forbes-Spyratos, and M. Kearney. “Fly Back Booster Design for Mach 5 Scramjet Launch”. In: *68th International Astronautical Congress*. Aelaide, Australia, 2017

Publications Included in This Thesis

This thesis comprises partly of publications, as allowed by University of Queensland Policy PPL 4.60.07. The papers that have been included have all been published in peer reviewed journals at the time of submission.

S. O. Forbes-Spyratos, M. P. Kearney, M. K. Smart, and I. H. Jahn. “Trajectory Design of a Rocket-Scramjet-Rocket Multi-Stage Launch System”. In: *Journal of Spacecraft and Rockets* (2018). DOI: [10.2514/1.A34107](https://doi.org/10.2514/1.A34107)

Contributor	Contribution
Sholto O. Forbes-Spyratos	Conception and Design (85%) Performed simulations (100%) Analysis of results (90%) Wrote and edited paper (85%)
Ingo H. Jahn	Conception and Design (5%) Analysis of results (5%) Wrote and edited paper (7.5%)
Michael P. Kearney	Conception and Design (5%) Wrote and edited paper (7.5%)
Michael K. Smart	Conception and Design (5%) Analysis of results (5%) Wrote and edited paper (5%)

Contributions by Others to the Thesis

Except for the contributions by others to publications above, there are no contributions by others to this thesis.

XX talk to ingo about this, should I put dawid or alex, also above, should michael get more contribution for the c-rest?

Statement of Parts of the Thesis Submitted to Qualify for the Award of Another Degree

None.

For Kaitlin, with love to my family and friends, and utmost gratitude to my advisors.

I'm trying to find a way off this planet.
Rocket Raccoon

Keywords

airbreathing propulsion, scramjets, hypersonics, access-to-space, small satellite launchers, airbreathing launch systems

Australian and New Zealand Standard Research Classification (ANZSRC)

ANZSRC code: 090107 Hypersonic Propulsion and Hypersonic Aerodynamics, 10%

ANZSRC code: 090106 Flight Dynamics, 10%

ANZSRC code: 090108, Satellite, Space Vehicle and Missile Design and Testing, 20%

ANZSRC code: 090104 Aircraft Performance and Flight Control Systems, 30%

ANZSRC code: 010303 Optimisation, 30%

Fields of Research (FoR) Classification

FoR code: 0901, Aerospace Engineering, 100%

CONTENTS

List of figures	xxi
List of tables	xxiv
1 Introduction	1
1.1 Research aims	3
1.2 Thesis Outline and Contributions	5
2 Literature review	7
2.1 Scramjets	7
2.2 Reusable Rocket-Powered Satellite Launch Systems	9
2.3 Small Satellite Launchers	10
2.4 Airbreathing Access-to-Space Systems	13
2.4.1 Small Airbreathing Launchers	14
2.5 Airbreathing Launch Vehicle Ascent Trajectories	15
2.5.1 Single-Stage Vehicles	17
2.5.2 Multi-Stage Vehicles	17
2.6 Hypersonic Vehicle Fly-Back Trajectories	20
2.7 The University of Queensland's Rocket-Scramjet-Rocket Launch System	21
2.7.1 Scramjet Engine Model	23
2.7.2 The Trajectory of the SPARTAN	23
2.7.3 The Third Stage Rocket	24
2.7.4 Exoatmospheric Rocket Engines	28
2.8 Optimal Control	28
2.8.1 Shooting Methods	29

CONTENTS

2.8.2	Collocation Methods	30
2.9	Available Optimal Control Solvers	33
2.10	Aerodynamic Analysis	35
2.10.1	Cart3D	36
2.10.2	Missile Datcom	37
2.11	Summary	38
3	Launch Vehicle Design and Simulation	41
3.1	Second Stage Scramjet	43
3.1.1	The SPARTAN Accelerator	43
3.1.2	Propulsion	44
3.1.3	The Aerodynamics of the SPARTAN	48
3.1.4	Trimmed Aerodynamic Database of the SPARTAN with Engine-On	59
3.1.5	Trimmed Aerodynamic Database of the SPARTAN with Engine-Off	59
3.2	First Stage Rocket	61
3.2.1	Aerodynamics Including First Stage	63
3.3	Third Stage Rocket - Baseline	65
3.3.1	Heat Shield Sizing	66
3.3.2	Fuel Tank Sizing	67
3.3.3	The Aerodynamics of the Third Stage Rocket	68
3.4	Summary	70
4	LODESTAR	71
4.1	Vehicle Simulation	73
4.1.1	6DOF Equations of Motion	73
4.2	Mission Definition	74
4.3	Optimal Control Problem Structure	76
4.3.1	Trajectory Connection Points	78
4.3.2	I. First Stage Vertical Ascent	79
4.3.3	II. First Stage Pitching Ascent	80
4.3.4	III. Second Stage Ascent Trajectory	81
4.3.5	IV. Second Stage Return Trajectory	82
4.3.6	V. Third Stage Powered Ascent	84
4.3.7	VI. Third Stage Unpowered Ascent	84
4.3.8	VII. Hohmann Transfer	85
4.4	Optimal Solution Analysis	87
4.5	The Optimisation Process	89
4.6	Summary	89

5 Optimised Ascent Trajectory	91
5.1 Case 1: Constant Dynamic Pressure Trajectory	93
5.2 Case 2: Optimised Ascent Trajectory	99
5.3 Sensitivity Analysis	106
5.3.1 Case 3: Dynamic Pressure Sensitivity	107
5.3.2 Case 4: SPARTAN Drag Sensitivity	108
5.3.3 Case 5: C-REST Engine Specific Impulse Sensitivity	109
5.3.4 Case 6: SPARTAN Mass Sensitivity	110
5.3.5 Case 7: SPARTAN Fuel Mass Sensitivity	112
5.3.6 Case 8: Third Stage Mass Sensitivity	114
5.3.7 Case 9: Third Stage Specific Impulse Sensitivity	115
5.3.8 Case 10: Third Stage Drag Sensitivity	117
5.4 Comparison of Design Parameters	118
5.5 Summary	120
6 Optimised Trajectory Including Fly-Back	123
6.1 Case 11: Combined SPARTAN Ascent-Descent & Third Stage	123
6.2 Ascent Trajectory	124
6.3 Fly-Back Trajectory	128
6.4 Design Sensitivity Analysis	132
6.4.1 Case 12: Dynamic Pressure Variation with Fly-Back Inclusion	134
6.4.2 Case 13: SPARTAN Drag Sensitivity with Fly-Back Inclusion	135
6.4.3 Case 14: C-REST Specific Impulse Variation with Fly-Back Inclusion	137
6.4.4 Case 15: SPARTAN Mass Sensitivity	138
6.4.5 Case 16: SPARTAN Fuel Mass Sensitivity	140
6.4.6 Case 17: Third Stage Mass Sensitivity	141
6.4.7 Case 18: Third Stage I_{SP} Sensitivity	142
6.5 Comparison of Sensitivities	143
6.6 Summary	145
7 Conclusions	147
8 Recommendations for future work	151
References	153
A Modelling and Simulation	169
A.1 Propulsion Interpolation Scheme	169
A.2 SPARTAN Flow Results	170

CONTENTS

A.3	Cart3D Mesh	171
A.4	Performance of the SPARTAN During Fly-Back	172
B	Example and Verification	173
B.1	GPOPS-2 Example - Brachistochrone Problem	173
B.2	Optimised Trajectory Analysis	174
B.2.1	Mesh History	175
B.2.2	Verification	175
C	Alternate Trajectory Cases	181
C.1	Maximum Payload-To-Orbit Trajectory With Dynamic Pressure Constraint	181
C.2	Sonic Boom Ground Effects	181
C.3	Alternate Launch Locations	183
D	Trajectory Plot Comparisons	189
D.1	Optimised Ascent Trajectory Comparisons With No Fly-Back	189
D.1.1	Case 3: Maximum Dynamic Pressure Sensitivity Comparison	189
D.1.2	Case 4: SPARTAN Specific Impulse Sensitivity Comparison	192
D.1.3	Case 5: SPARTAN Drag Sensitivity Comparison	193
D.1.4	Case 6: SPARTAN Mass Sensitivity Comparison	196
D.1.5	Case 7: SPARTAN Fuel Mass Sensitivity Comparison	197
D.1.6	Case 8: Third Stage Mass Sensitivity Comparison	200
D.1.7	Case 9: Third Stage Specific Impulse Sensitivity Comparison	201
D.1.8	Case 10: Third Stage Drag Sensitivity Comparison	204
D.2	Optimised Ascent Trajectory Comparisons With Fly-Back	205
D.2.1	Case 12: Dynamic Pressure Sensitivity Comparison	205
D.2.2	Case 13: SPARTAN Drag Sensitivity Comparison	209
D.2.3	Case 14: SPARTAN Specific Impulse Sensitivity Comparison	212
D.2.4	Case 15: SPARTAN Mass Sensitivity Comparison	215
D.2.5	Case 16: SPARTAN Fuel Mass Sensitivity Comparison	218
D.2.6	Case 17: Third Stage Mass Sensitivity Comparison	221
D.2.7	Case 18: Third Stage Specific Impulse Sensitivity Comparison	224
E	Viscous Drag Variation	227

LIST OF FIGURES

1.1	The scramjet-powered second stage of the SPARTAN[16].	3
2.1	A simple schematic of a scramjet engine[24].	8
2.2	Characteristic performance for airbreathing and rocket engines with Mach number[25].	8
2.3	Comparison of Blue Origin and SpaceX partially-reusable launch systems with existing and historic launch systems[35].	10
2.4	The trajectory of the Falcon Heavy[36].	11
2.5	The trajectory of the Ariane featuring Adeline[37].	11
2.6	The airbreathing vehicle flight corridor [9].	14
2.7	An example of an airbreathing ascent trajectory of the Maglifter RBCC/Rocket launch vehicle[63]. This trajectory shows a constant dynamic pressure section during fanramjet mode[63].	16
2.8	The single stage-to-orbit vehicle of Powell et al [53] and its launch trajectory, with pull-up manoeuvre evident. V_R indicates Earth relative velocity.	17
2.9	The two stage-to-orbit launch vehicle of Wilhite [54]. The launch trajectory is shown, with pull-up indicated.	18
2.10	The two stage-to-orbit launch vehicle of Tsuchiya and Mori [56], with trajectories including pull-up and return for both airbreathing and airbreathing/rocket vehicles shown.	19
2.11	The two stage-to-orbit launch system developed by Mehta and Bowles [57], with trajectory and pull-up shown.	19
2.12	The optimised maximum range trajectory of a hypersonic vehicle[74].	22
2.13	An early design of the socket-scramjet-rocket launch system incorporating the SPARTAN [75].	22
2.14	The C-RESTM10 propulsion database, specific impulse.	24

LIST OF FIGURES

2.15	The flight trajectory of the SPARTAN. a) shows the physical trajectory and b) shows the forces on the vehicle and performance indicators.	25
2.16	The elevons of the SPARTAN[12].	25
2.17	The third stage rocket of the rocket-scramjet-rocket launch system[12].	26
2.18	A comparison of single shooting and multiple shooting[83].	30
2.19	Examples of h and p collocation methods[83].	31
2.20	Comparison of optimisation techniques[74]. A hypersonic vehicle is optimised for maximum range. The hp-adaptive method can be observed to have produced the most optimal result.	33
2.21	The Skylon spaceplane, simulated using Cart3D at Mach 12.189, $\alpha = 7.512^\circ$ [134]. Cell distribution produced by mesh adaptation is shown.	37
2.22	Comparisons of Cart3D with experimental data and the FUN3D Navier-Stokes CFD solver. P1, P2 and P3 indicate pressure tap locations. Modified from Sagerman et al.[130].	38
3.1	The launch process of the rocket-scramjet-rocket launch system, presented in simplified form.	42
3.2	The rocket-scramjet-rocket launch system, top view, showing the SPARTAN and first stage.	43
3.3	The rocket-scramjet-rocket launch system, side view, showing the SPARTAN and fuel tanks, along with the third and first stages.	43
3.4	The features of the SPARTAN.	44
3.5	The locations of conditions relevant to C-REST engine simulation.	45
3.6	Flow conditions after the conical shock generated by the vehicle nose cone as a function of flight Mach number and angle of attack. Figure a) shows the Mach number, b) shows the pressure ratio, and c) shows the temperature ratio following the conical shock, at the engine inlet.	46
3.7	Specific impulse of the CRESTM10 engines with input temperature and Mach number. Available data points are indicated.	47
3.8	Operable equivalence ratio of the CRESTM10 engines with input temperature and Mach number. Available data points are indicated.	48
3.9	The process for generating aerodynamic databases.	50
3.10	Surface triangulation of the Baseline SPARTAN, generated using Pointwise[141]. . .	51
3.11	The convergence of a Cart3D simulation.	52
3.12	View of the SPARTAN surface triangulation showing engine outlet boundaries. . .	53
3.13	The total thrust output of the SPARTAN, including the C-REST database, and Cart3D nozzle and boat tail simulations.	53

3.14	The specific impulse of the SPARTAN, including the C-rest database, and Cart3D nozzle and boat tail simulations.	54
3.15	Centre of gravity positions throughout the flight of the SPARTAN.	55
3.16	SPARTAN model showing control surfaces.	56
3.17	The forces on the SPARTAN during flight.	56
3.18	Flap deflection required for trim of the SPARTAN. Negative up.	57
3.19	Viscous drag coefficient across various Mach numbers.	58
3.20	Engine-on Cart3D simulation at Mach 6, 2° angle of attack, and 25km altitude. . . .	59
3.21	Aerodynamic coefficients with the C-REST engines powered-on. Coefficients correspond to a reference area of 62.77m^2 . note what CG	60
3.22	Cart3D flow result for the SPARTAN, at Mach 6, 2° angle of attack.	61
3.23	Aerodynamic Characteristics of the SPARTAN with C-REST engine powered-off. Coefficients correspond to a reference area of 62.77m^2	62
3.24	Unstarted scramjet engines at mach 3, 2° angle of attack.	63
3.25	Cart3D result for the SPARTAN and first stage vehicles at Mach 2, -1° angle of attack. . . .	64
3.26	Aerodynamic characteristics of the SPARTAN including the first stage rocket. . . .	64
3.27	Thrust vectoring moment balancing of the first stage.	65
3.28	The third stage rocket, showing major internal features.	65
3.29	Variation in coefficient of thrust with area ratio [146].	66
3.30	Aerodynamic characteristics of the third stage rocket, for a reference area of 0.95m^2 . .	69
3.31	Thrust vector moment balancing of the third stage.	69
4.1	The simplified optimisation process.	72
4.2	The Earth-fixed components of the geodetic rotational coordinate system.	74
4.3	The vehicle-based components of the coordinate system.	75
4.4	Sun synchronous orbit illustration, passing over the equator at the same time each day[153].	75
4.5	Approximate location of the ELA launch site. Image from Google maps.	76
4.6	Illustration of the segmented launch profile.	78
4.7	The Hohmann transfer manoeuvre.	86
4.8	The process of the rocket-scramjet-rocket trajectory optimisation. Relevant sections are indicated in square brackets at each process step.	90
5.1	Maximum payload-to-orbit trajectory path with the SPARTAN flying at constant dynamic pressure (Case 1). Initial heading angle 92.6°	94
5.2	The first stage trajectory of the launch system, with the SPARTAN constrained to flight at constant dynamic pressure (Case 1).	96
5.3	The constant dynamic pressure flight path of the SPARTAN (Case 1).	97

LIST OF FIGURES

5.4	The third stage trajectory of the launch system, with the SPARTAN constrained to flight at constant dynamic pressure (Case 1).	98
5.5	The optimised maximum payload-to-orbit trajectory of the launch system (Case 2).	99
5.6	The optimised maximum payload-to-orbit trajectory of the launch system under power of the first stage rocket (Case 2).	100
5.7	The optimised maximum payload-to-orbit trajectory of the SPARTAN (Case 2).	102
5.8	Net I_{SP} contours for the SPARTAN at Mach numbers from 5-9, showing optimised trajectory and constant dynamic pressure trajectory.	103
5.9	The specific impulse of the C-REST engines, plotted for inlet temperature (T1) and inlet Mach number (M1). Data points are shown in black.	104
5.10	The third stage trajectory of the launch system flying the maximum payload-to-orbit trajectory (Case 2).	105
5.11	The sensitivity of the key design parameters of the launch system.	118
6.1	Maximum payload-to-orbit trajectory path with the inclusion of SPARTAN fly-back (Case 11). Initial heading angle of -12.44°	125
6.2	The first stage of the optimised maximum payload-to-orbit trajectory with SPARTAN fly-back (Case 11).	126
6.3	The acceleration of the SPARTAN flying an optimised maximum payload-to-orbit trajectory with SPARTAN fly-back (Case 11).	127
6.4	Net I_{SP} contours for the SPARTAN at Mach numbers between 6 and 8, showing the optimised trajectory path.	128
6.5	The third stage trajectory of an optimised maximum payload-to-orbit trajectory with SPARTAN fly-back (Case 11).	129
6.6	The fly-back trajectory of the SPARTAN flying an optimised maximum payload-to-orbit trajectory (Case 11).	130
6.7	The sensitivity of the key design parameters of the launch system, including SPARTAN fly-back. Red and green coloured areas indicate decreases or increases in the magnitude of sensitivity respectively, compared to the sensitivity study without SPARTAN fly-back in Section 5.4.	144
A.1	The transformation to a normalised interpolation scheme.	169
A.2	CART3D flow result for the SPARTAN, at Mach 1.1, 6° angle of attack.	170
A.3	CART3D flow result for the SPARTAN, at Mach 3, 6° angle of attack.	171
A.4	Adapted mesh of the SPARTAN at Mach 6 3° angle of attack.	171
A.5	Adapted mesh around the SPARTAN and first stage vehicles, flying at Mach 2, -1° angle of attack.	172

A.6	The performance of the SPARTAN during the boost phase. Light blue indicates that the scramjet engines are turned on.	172
B.1	The solution to the Brachistochrone problem, solved in GPOPS-2[103].	174
B.2	The mesh history of each phase of the optimised, maximum payload-to-orbit trajectory with SPARTAN fly-back. the phases are shown in each subfigure as follows: a) first stage rocket, b) SPARTAN acceleration, c) SPARTAN fly-back and d) third stage.	176
B.3	The Hamiltonian time history of each phase of the optimised solution.	177
B.4	The error between the integrated dynamics of the system, and the solution states. Normalised to the range of each state.	178
B.5	The error between the forward simulated states, and the solution states. Normalised to the range of each state.	179
C.1	The optimised maximum payload-to-orbit trajectory of the launch system constrained to 50kPa between Mach numbers 6 to 8, under power of the first stage rocket.	183
C.2	The optimised maximum payload-to-orbit trajectory of the SPARTAN, constrained to 50kPa between Mach numbers 6 to 8.	185
C.3	The third stage trajectory of the launch system flying the maximum payload-to-orbit trajectory, constrained to 50kPa between Mach numbers 6 to 8.	186
C.4	The level of population annoyance with increasing overpressure.	187
C.5	187
C.6	The optimised maximum payload-to-orbit trajectory of the launch system launching onto a southerly orbit, from Streaky Bay.	188
D.1	Comparison of SPARTAN ascent trajectories with variation in the maximum dynamic pressure of the SPARTAN.	190
D.2	Comparison of third stage rocket ascent trajectories with variation in the maximum dynamic pressure of the SPARTAN.	191
D.3	Comparison of SPARTAN ascent trajectories with variation in the specific impulse of the SPARTAN.	192
D.4	Comparison of third stage rocket ascent trajectories with variation in the specific impulse of the SPARTAN.	193
D.5	Comparison of SPARTAN ascent trajectories with variation in the drag of the SPARTAN.	194
D.6	Comparison of third stage rocket ascent trajectories with variation in the drag of the SPARTAN.	195
D.7	Comparison of SPARTAN ascent trajectories with variation in the mass of the SPARTAN.	196

LIST OF FIGURES

D.8 Comparison of third stage rocket ascent trajectories with variation in the mass of the SPARTAN.	197
D.9 Comparison of SPARTAN ascent trajectories with variation in the fuel mass of the SPARTAN.	198
D.10 Comparison of third stage rocket ascent trajectories with variation in the fuel mass of the SPARTAN.	199
D.11 Comparison of SPARTAN ascent trajectories with variation in the mass of the third stage.	200
D.12 Comparison of third stage rocket ascent trajectories with variation in the mass of the third stage.	201
D.13 Comparison of SPARTAN ascent trajectories with variation in the specific impulse of the third stage.	202
D.14 Comparison of third stage rocket ascent trajectories with variation in the specific impulse of the third stage.	203
D.15 Comparison of SPARTAN ascent trajectories with variation in the drag of the third stage.	204
D.16 Comparison of third stage rocket ascent trajectories with variation in the drag of the third stage.	205
D.17 Comparison of SPARTAN ascent trajectories with variation in the maximum dynamic pressure of the SPARTAN.	206
D.18 Comparison of third stage rocket ascent trajectories with variation in the maximum dynamic pressure of the SPARTAN.	207
D.19 Comparison of SPARTAN return trajectories with variation in the maximum dynamic pressure of the SPARTAN.	208
D.20 Comparison of SPARTAN ascent trajectories with variation in the drag of the SPARTAN.	209
D.21 Comparison of third stage rocket ascent trajectories with variation in the drag of the SPARTAN.	210
D.22 Comparison of SPARTAN return trajectories with variation in the drag of the SPARTAN.	211
D.23 Comparison of SPARTAN ascent trajectories with variation in the specific impulse of the SPARTAN.	212
D.24 Comparison of third stage rocket ascent trajectories with variation in the specific impulse of the SPARTAN.	213
D.25 Comparison of SPARTAN return trajectories with variation in the specific impulse of the SPARTAN.	214
D.26 Comparison of SPARTAN ascent trajectories with variation in the mass of the SPARTAN.	215

D.27 Comparison of third stage rocket ascent trajectories with variation in the mass of the SPARTAN	216
D.28 Comparison of SPARTAN return trajectories with variation in the mass of the SPARTAN	217
D.29 Comparison of SPARTAN ascent trajectories with variation in the fuel mass of the SPARTAN	218
D.30 Comparison of third stage rocket ascent trajectories with variation in the fuel mass of the SPARTAN	219
D.31 Comparison of SPARTAN return trajectories with variation in the fuel mass of the SPARTAN	220
D.32 Comparison of SPARTAN ascent trajectories with variation in the mass of the third stage	221
D.33 Comparison of third stage rocket ascent trajectories with variation in the mass of the third stage	222
D.34 Comparison of SPARTAN return trajectories with variation in the mass of the third stage	223
D.35 Comparison of SPARTAN ascent trajectories with variation in the specific impulse of the third stage	224
D.36 Comparison of third stage rocket ascent trajectories with variation in the specific impulse of the third stage	225
D.37 Comparison of SPARTAN return trajectories with variation in the specific impulse of the third stage	226
E.1 Comparison of SPARTAN ascent trajectories with variation in the viscous drag of the SPARTAN	229
E.2 Comparison of third stage ascent trajectories with variation in the viscous drag of the SPARTAN	230
E.3 Comparison of SPARTAN return trajectories with variation in the viscous drag of the SPARTAN	231

LIST OF TABLES

2.1	A selection of the small satellite launchers which are operational or in development	12
2.2	Comparison of upper stage rocket engines, sourced from the Encyclopedia Astronautica reference website[78].	27
2.3	Summary of programs capable of pseudospectral optimisation.	34
3.1	Mass breakdown of the modified SPARTAN vehicle.	44
3.2	First Stage Engine Properties[78].	63
3.3	Third stage heat shield breakdown.	67
3.4	Third stage fuel distribution.	68
4.1	Segment coupling conditions for combined trajectory optimisation.	80
4.2	Optimisation setup of the first stage phase.	81
4.3	Optimisation setup of the second stage ascent. * This is only used in the constant dynamic pressure simulation.	82
4.4	Optimisation setup of the second stage return.	83
4.5	Optimisation setup of the third stage powered ascent.	85
5.1	Summary of the key results from a maximum payload-to-orbit trajectory with the SPARTAN constrained to 50kPa.	95
5.2	A summary of key results from the maximum payload-to-orbit trajectory (Case 2).	101
5.3	Comparison of key trajectory parameters with variation in the maximum dynamic pressure of the SPARTAN.	107
5.4	Comparison of key trajectory parameters with variation in the drag of the SPARTAN.	108
5.5	Comparison of key trajectory parameters with variations in the specific impulse of the C-REST engines.	110

LIST OF TABLES

5.6	Comparison of key trajectory parameters with variation in the structural mass of the SPARTAN.	111
5.7	Comparison of key trajectory parameters with variation in the fuel mass of the SPARTAN.	113
5.8	Comparison of key trajectory parameters with variation in the mass of the third stage.	114
5.9	Comparison of key trajectory parameters with variation in the third stage specific impulse.	116
5.10	Comparison of key trajectory parameters with variation in the drag of the third stage.	117
6.1	Selected trajectory conditions for a maximum payload-to-orbit trajectory including SPARTAN fly-back.	124
6.2	Comparison of key trajectory parameters with variation in the maximum dynamic pressure of the SPARTAN, with fly-back.	134
6.3	Comparison of key trajectory parameters with variation in the drag of the SPARTAN, with fly-back.	136
6.4	Comparison of key trajectory parameters with variation in the specific impulse of the C-REST engines, with fly-back.	137
6.5	Comparison of key trajectory parameters with variation in the structural mass of the SPARTAN, with fly-back.	139
6.6	Comparison of key trajectory parameters with variation in the fuel mass of the SPARTAN, with fly-back.	140
6.7	Comparison of key trajectory parameters with variation in the mass of the third stage, with fly-back.	142
6.8	Comparison of key trajectory parameters with variation in the specific impulse of the third stage, with fly-back.	143
B.1	Optimisation setup of the Brachistochrone problem.	174
C.1	A summary of key results from the maximum payload-to-orbit trajectory, constrained to 50kPa between Mach numbers 6 to 8.	182
C.2	A summary of key trajectory parameters of the maximum payload-to-orbit trajectory launched in a southerly direction.	184
E.1	Summary of key trajectory parameters with SPARTAN viscous drag variation.	228

CHAPTER 1

INTRODUCTION

In recent years, the space sector has seen a significant shift in the paradigm of space launch system design. The sector has moved towards privatisation, with new and innovative launch systems competing to offer the most cost-efficient and reliable launches. The sector has also seen a split between those who produce large satellite launchers and those who produce small satellite launchers. For large payload launchers, reusability is a major focus in the design of new launch systems, with the purpose of making a launch system cost efficient over multiple launches[5]. For small payload launchers, reusability is more complex than for large launchers, as the additional systems necessary for reusability add a larger fraction of system mass, and require a proportionally larger fuel mass. Consequently, the focus of small launch system design is currently on producing expendable launch systems as cheaply and efficiently as possible, using state of the art technologies such as 3D printing to expedite the process and minimise cost[6]. However, if reusability is able to be successfully integrated into small launch system design, it has the potential to increase the cost efficiency and launch flexibility, potentially opening up the small satellite market significantly.

A potential candidate for integrating reusability into small satellite launch systems is the use of airbreathing engines[7, 8]. Airbreathing engines produce higher specific impulse than rockets, and do not require oxidiser to be carried on-board a launch vehicle[9]. The higher efficiency and reduced propellant mass of airbreathing vehicles allows the additional mass of the systems necessary for reusability to be mitigated[10]. An airbreathing vehicle can be designed in a similar fashion to a conventional aircraft, with wings, stabilisers and ailerons[11, 12]. A vehicle designed in this fashion has a high lift-to-drag ratio, and good manoeuvrability, allowing for a return flight and landing on a conventional landing strip[12]. This style of return removes the need for transport, enabling a fast turn-around and cost-efficient re-use.

The primary airbreathing engines in consideration for launch vehicles are ramjet and scramjet engines[13]. These engines offer good efficiency and have operational regimes that allow them to

CHAPTER 1. INTRODUCTION

effectively accelerate a launch vehicle over a range of Mach numbers. Ramjets and scramjets rely on the high velocity of the aircraft to compress the flow of air entering the engine before combustion. Ramjets slow the air to subsonic speeds before combustion and are limited to operation at low Mach numbers, whereas scramjets keep the flow supersonic throughout, and operate within the hypersonic regime, above Mach 5. These engines have limited operational regimes, and require atmospheric flight in order to take oxidiser from the air. These operational constraints mean that a launch system cannot be solely powered by airbreathing engines. Rocket power is necessary for at least the exoatmospheric portion of the trajectory. As a result, the designs of airbreathing launch systems require rocket stages, usually separated into multiple stages to increase weight efficiency[7]. If a scramjet engine is used as the airbreathing engine of the launch system, rocket power is also desirable for accelerating scramjet accelerator to minimum operational speed, as the alternative is using turbojets and ramjets sequentially[7], which is weight and cost intensive.

Calculating a suitable trajectory for an airbreathing launch system is an integral part of the preliminary vehicle and mission design process. A trajectory must be calculated that allows the launch system to achieve its objectives of placing a payload into orbit, while recovering any reusable stages. Ideally, the calculated trajectory will achieve the maximum possible payload-to-orbit, while adhering to the structural, heating and propulsive limitations of the vehicle. The trajectory design for a partially-airbreathing launch system is complex and requires consideration of each of the individual stages in order to maximise the performance of the launch system, and consequently, its cost efficiency. The airbreathing engines of a ramjet or scramjet-powered stage require high dynamic pressure to operate effectively, and airbreathing stages are generally designed for high lift-to-drag. Conversely, rocket-powered stages operate more efficiently at higher altitude, and are generally designed for weight and cost efficiency. For these launch systems, the various stages and engines involved during launch require trade-offs in engine efficiency and thrust generation, stage mass, and vehicle aerodynamics. These factors require the launch trajectory of the system to be thoroughly simulated and optimised, to ensure that the launch vehicle is operating effectively.

Optimal control theory is a general set of techniques which find a control law to maximise a given metric of a system, subject to a set of constraints[14, 15]. Optimal control theory can be used to calculate the optimised trajectory profile for a launch vehicle in a robust and computationally efficient manner, allowing a trajectory to be calculated in which the flight path of each individual stage is considered simultaneously to produce a maximum-payload trajectory[15]. Optimal control is able to produce an optimised trajectory which satisfies the specific structural and flight constraints of the vehicle being simulated, allowing the physical limitations of the vehicle, such as heating and structural loading limits, to be imposed[15]. These constraints also allow any necessary mission conditions to be established, such as reaching orbital velocity and achieving fly-back. An optimal trajectory calculated for multiple launch vehicle stages simultaneously, without predispositions, can offer valuable insights into the performance of a launch vehicle, and drive future design decisions. This concurrent

optimisation of multiple stages is particularly important for launch systems incorporating airbreathing engines, where the performance and operational requirements of each stage are significantly different.

This study applies optimal control theory to a three stage rocket-scramjet-rocket launch system being developed by The University of Queensland. The second stage of this system is a scramjet-powered accelerator, designated the SPARTAN[12]. This launch system is designed to be partially reusable, with at least the second stage scramjet vehicle flying back to the initial launch site, as well as possibly the first stage booster[12], although this is beyond the scope of this study. In previous studies it has been assumed that by maximising the performance of the SPARTAN, that the performance of the launch system is also maximised[12]. The trajectory of the launch system has been designed around the SPARTAN flying at its maximum dynamic pressure, and all other trajectory stages have conformed to this assumption. However, these studies did not consider the interaction between stages, or the fly-back of the SPARTAN. This study will develop trajectory planning tools for partially-airbreathing launch systems, and calculate an optimised launch trajectory for the rocket-scramjet-rocket system incorporating the SPARTAN. This optimised trajectory will be calculated with the aim of producing an optimal trajectory profile which may be applied to any multi-stage rocket-airbreathing-rocket system for delivering small satellites to Earth orbit. The impact of the fly-back of the scramjet stage on the optimised trajectory will be studied, and the ability of the rocket-scramjet-rocket system to effectively deliver small payloads to orbit with fly-back will be assessed.



Figure 1.1: The scramjet-powered second stage of the SPARTAN[16].

1.1 Research aims

The aim of this work is to design the trajectory of a rocket-scramjet-rocket small satellite launch system. The purpose of this optimised trajectory is to maximise the payload-to-orbit capabilities of the launch system, thereby also maximising the cost efficiency of the system. The optimal trajectory

CHAPTER 1. INTRODUCTION

will be utilised to assess the feasibility of return flight, as well as to determine the impact of key vehicle design parameters on the performance of the launch system.

These aims will be achieved by addressing the following objectives:

1. *Development of a detailed design and aerodynamic simulation for a rocket-scramjet-rocket launch system.*

A detailed launch system design and robust dynamic simulation are required in order for optimal control to be applied to a launch system. The design must be representative of a standard rocket-scramjet-rocket launch system for the optimal trajectory results to be generally applicable. The dynamic simulation must be high fidelity and robust in order for the optimised trajectory to be meaningful.

2. *Calculation of the maximum payload-to-orbit trajectory for a rocket-scramjet-rocket launch system using optimal control, with and without fly-back.*

The optimal trajectory shape of a multi-stage rocket-scramjet-rocket system is sensitive to the design and aerodynamic characteristics of each stage, and cannot be easily assumed. The use of optimal control techniques allows a maximum-payload trajectory to be calculated with few assumptions as to the general shape of the trajectory. The inclusion of the fly-back of the scramjet stage in the trajectory optimisation allows the impact of the fly-back to be minimised.

3. *Analysis of the sensitivity of the maximum payload-to-orbit trajectory to variations in key design parameters of the launch system*

The optimal trajectory shape and maximum payload-to-orbit are dependent on the design of the launch system. Assessing the sensitivity of the optimised trajectory shape and payload-to-orbit to key aerodynamic and propulsive properties allows the relative impacts of various design parameters to be calculated and contrasted.

1.2 Thesis Outline and Contributions

Chapter 2 - Literature Review

A review of literature related to the various aspects of this study is presented. The theory behind scramjet propulsion is outlined, followed by a background of reusable and small satellite launch systems. A review of the trajectories of partially-airbreathing launch systems is presented, comparing the optimised trajectories of various conceptual vehicles. An overview of optimal control techniques is presented, with particular emphasis on the pseudospectral method of solving optimal control problems, which is employed within this study. Lastly, an overview of the optimal control and aerodynamic solvers, which are used in this study is presented.

Chapter 3 - Launch Vehicle Design and Simulation

The design, aerodynamics and engine models of all three stages are detailed. The SPARTAN scramjet-powered stage is presented first, followed by the first and third stages. The design of each stage is shown, along with sizing and mass breakdowns. The propulsion model used for each stage is detailed, along with the modelling and interpolation schemes used. The aerodynamic characteristics and simulation methodology of each stage is presented, and the process for trimming each vehicle is specified.

Chapter 4 - LODESTAR

The method used for the simulation and optimisation of the trajectory is detailed, including the creation of the trajectory analysis program, LODESTAR, which has been created for this study. The specifics of the optimal control methodology are presented. The simulation methodology is detailed, along with the construction of the optimal control simulation for the mission used in this study. The specific set-up of the optimal control program is detailed for each trajectory stage, specifying the costs and constraints which drive the optimal control solver. Finally, the methods for validating the final solutions are specified.

Chapter 5 - Optimised Ascent Trajectory

The ascent of the SPARTAN and third stage rocket are optimised using LODESTAR, for maximum payload-to-orbit. The first stage rocket is optimised to the first-second stage separation point, for minimum fuel usage. The optimal trajectory is analysed. It is found that a pull-up at the end of the scramjet stage trajectory significantly improves payload-to-orbit. The sensitivity of the optimal trajectory to variation of key vehicle design parameters is studied. Optimised trajectories are calculated, and the trends in maximised payload-to-orbit and optimal trajectory shape are analysed to study the relative impact of the design parameters of the SPARTAN.

Chapter 6 - Optimised Trajectory Including Fly-Back

The trajectory of the launch system is optimised for maximum payload-to-orbit, including the fly-back of the SPARTAN to its initial launch location. It is found to be necessary to reignite the scramjet engines during the return flight of the SPARTAN to achieve fly-back. The SPARTAN is found to bank during acceleration to lessen the fuel consumed during the return flight. In a similar fashion to Chapter 5, the effects of key vehicle parameters on the optimised trajectory are studied. The sensitivity of the optimised trajectory and payload-to-orbit are analysed, with emphasis on how the fly-back trajectory is affected by the varied vehicle parameters.

Conclusions and Recommendations

The body of this thesis concludes by summarising the most significant findings from this work. Recommendations for future work are made.

CHAPTER 2

LITERATURE REVIEW

This chapter examines the relevant literature associated with the different aspects of the work conducted as part of this thesis. A brief overview of the theory behind scramjet engines is presented, followed by surveys of the current state of small satellite and reusable launch systems. Next, various conceptual airbreathing launch systems are presented, along with the trajectories and return flights which have been simulated for these systems, with particular emphasis on whether the trajectories were optimised or not. The SPARTAN scramjet-powered accelerator is detailed, followed by a review of the design of the third stage rocket. The theory behind optimal control methods is presented, followed by a survey into currently available optimal control solvers. Lastly, an overview of various aerodynamic modelling methods with emphasis on applicability to preliminary design is detailed.

2.1 Scramjets

A Scramjet, or supersonic combustion ramjet, is an airbreathing engine design which combusts air at supersonic speeds and is capable of high Mach number operation. Across their operating range, scramjets offer much higher specific impulse than rockets, the only other propulsion system capable of operating efficiently at hypersonic speeds[17, 18]. Scramjets compress air without moving parts, using geometry changes within the engine [19], as well as on the forebody of the vehicle to create inlet shocks which provide the compression required for combustion[20]. After combustion, the combustion products are expanded through a thrust nozzle, shown in Figure 2.1. This is similar in operation to a ramjet engine, though a scramjet does not generate a normal shock, allowing supersonic air to enter the combustor. Maintaining supersonic speeds throughout the engine allows scramjets to operate efficiently at Mach numbers of 5 and greater. Scramjets were proposed in the 1940's [21] and found to be capable of positive net thrust in 1993[22], but have yet to be developed to a level which

would allow for commercial application. Though scramjets are still in-development, the potential advantages which they offer over rockets for certain applications are driving their development in a number of institutions[23].

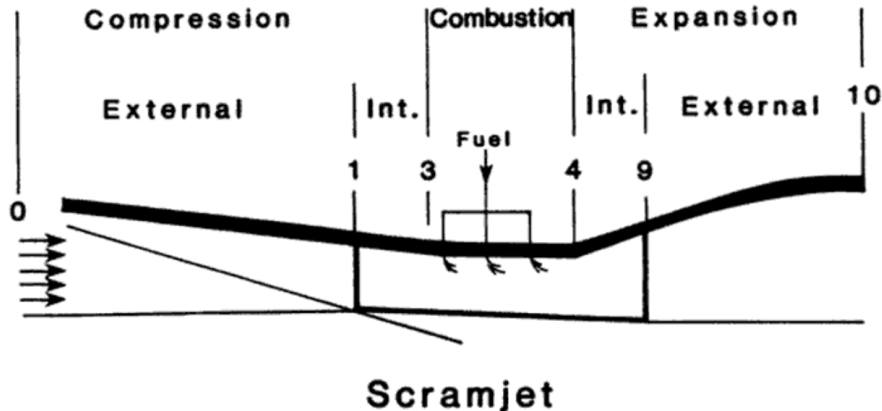


Figure 2.1: A simple schematic of a scramjet engine[24].

Scramjet engines are suitable for a number of applications where sustained flight or acceleration is desired at high Mach numbers. The high efficiency of scramjet engines means that significantly less propellant (fuel + oxidiser) is used during flight compared to rocket engines, and consequently, that a much smaller fraction of a scramjet-powered vehicle consists of fuel mass[10]. The smaller fuel mass fraction of a vehicle powered by scramjet engines mitigates the mass of the vehicle systems, allowing features such as wings, control surfaces, landing gear, and passenger transport capabilities to be included in the vehicle design[10].

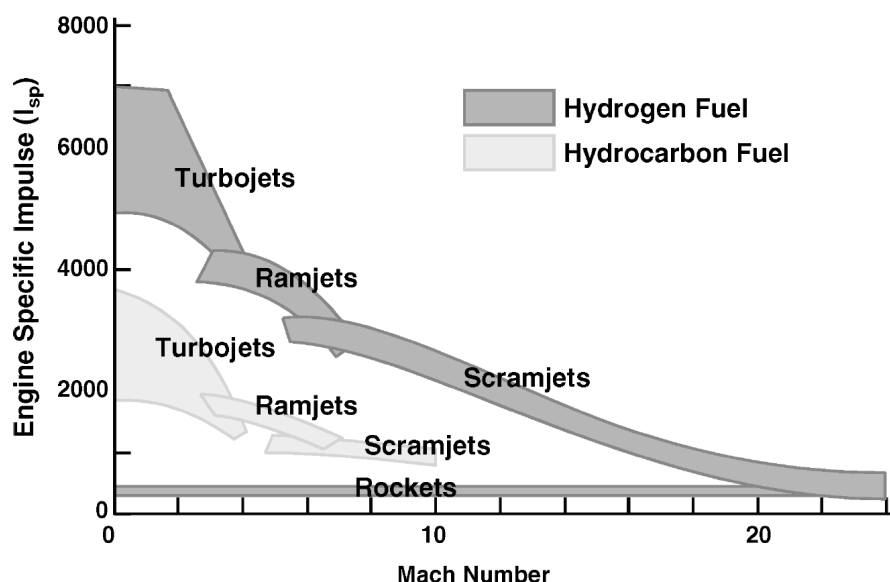


Figure 2.2: Characteristic performance for airbreathing and rocket engines with Mach number[25].

Theoretically, the operable range of scramjets is wide[26]; the specific impulse of a scramjet decreases with velocity, until it is equal to rockets around Mach 19[25], as shown in Figure 2.2. However, in practical designs, the operating range for a scramjet engine is far more limited. For a fixed geometry scramjet, the operable region is constrained by the geometries of the forebody of the vehicle, the inlet, and the combustor of the scramjet engine[9]. The Mach number range of a scramjet engine varies by design, but Mach number ranges of 5-10[12], 7-11[27] and 6-10[28] have been suggested as appropriate operable regimes for scramjet-powered launch vehicles. The operable range of scramjet engines can be improved with mechanisms to vary the geometry of the inlet during flight[29]. However, the systems necessary for variable geometry inlets add weight and complexity to the scramjet engine, and can be detrimental to overall system performance[9].

2.2 Reusable Rocket-Powered Satellite Launch Systems

Launch system technologies have progressed rapidly over the last 60 years. From the early vehicles based on intercontinental ballistic missile technology such as the Thor based launch systems, capable of launching 40-400kg to LEO in the 1960s, to the more modern Atlas V based systems of the 2000s capable of launching 9750-18500kg to LEO[30]. The materials, propulsion technology, aerodynamics and guidance algorithms have all improved significantly, enabling rockets to become more efficient, cheaper to produce, and more reliable. As the demand for satellite launches grows, and the cost of development of launchers becomes cheaper, the potential for profiting from space launches increases. This has driven a large portion of the space flight industry to move towards privatisation, with a heavy focus on reusable technology.

Reusable launch technology has been possible for many years, in the form of the space shuttle. However, the space shuttle was weighed down by large launch costs and operational complexity, and was not a commercial success[31]. Recently, reusable launchers have become the focus of many of the largest private launch companies, as reusability becomes more achievable due to technological advances[32, 33]. The SpaceX Falcon 9 and Falcon Heavy have been demonstrated on multiple occasions, landing booster stages successfully, and re-flying reused boosters multiple times[32]. In the near future the Blue Origin New Glenn is planned[32], with potentially the Airbus Adeline to follow (to be used on the Ariane 6)[34]. The Falcon and New Glenn rockets are shown in Figure 2.3, and the trajectories of the Falcon Heavy and Adeline are shown in Figures 2.4 and 2.5.

The aim of reusing launch vehicles is to reduce the cost-over-time of the reused components drastically, which subsequently allows the cost of individual launches to be reduced[38]. Reducing costs lowers the barrier of entry for space launches, potentially improving the diversity of space-based enterprises. Reusing launch system components also allows faster turnaround times for launches, as refurbishment of stages is much faster than manufacturing stages from scratch. Reduced turnaround times are key for improving mission scheduling, allowing satellites to be launched more rapidly, on a

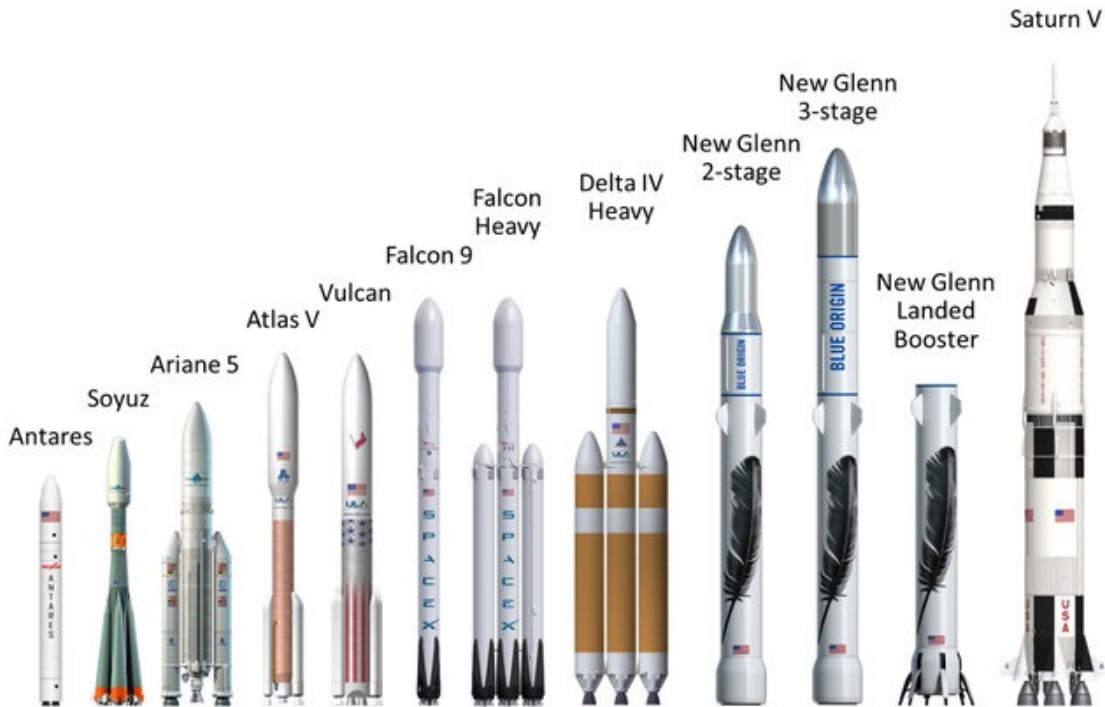


Figure 2.3: Comparison of Blue Origin and SpaceX partially-reusable launch systems with existing and historic launch systems[35].

more flexible time frame.

For a launch vehicle to be reusable, it must necessarily have the ability to come back to Earth safely, without damage to major system components. In addition, it is preferable for the vehicle to return to its initial launch site, to reduce the cost and time necessary for transport. This return flight requires the addition of system components which allow the reusable stage to fly to a specified landing point. Control surfaces[39], structural components[40], additional fuel[40], and in the case of the Adeline, additional engines[34], must be incorporated within a reusable launch vehicle design. The additional weight that these components contribute further increases the fuel and structural mass necessary to initially accelerate the reusable stage. The impact of reusability on the mass and cost of the vehicle is minimised when the velocity at the initiation of the return trajectory is decreased. Because of this mass increase on any stage which is to be designed to be reusable, most current reusable launch vehicle designs include only reusable first stages, with later stages being expendable.

2.3 Small Satellite Launchers

The vast improvements in computational technologies in recent years have allowed satellites to decrease in size and cost to a large degree. These factors have lowered the barrier of entry into small satellite manufacturing significantly, driving a surge in the demand for small satellite launches. Many

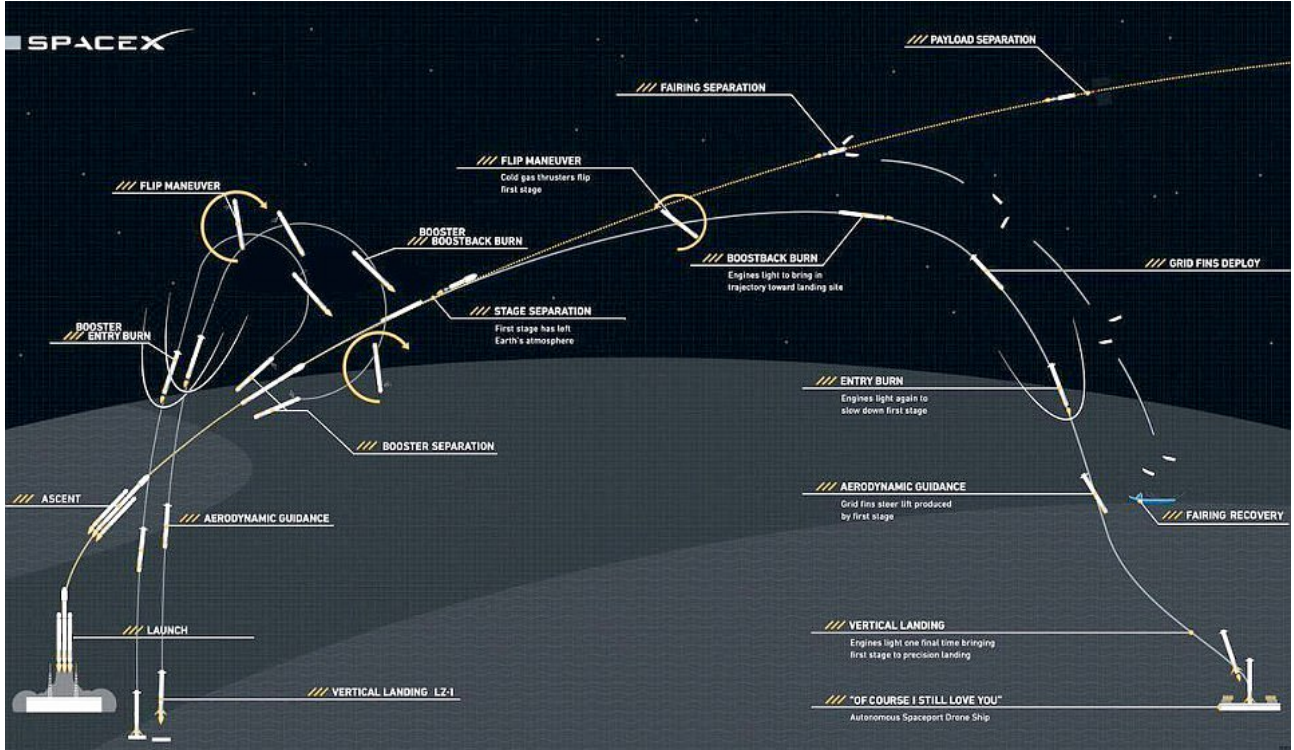


Figure 2.4: The trajectory of the Falcon Heavy[36].

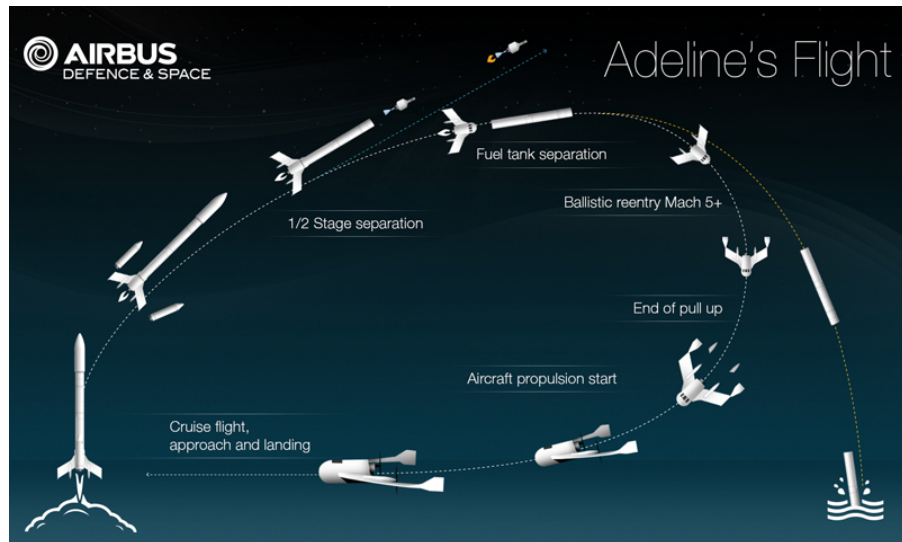


Figure 2.5: The trajectory of the Ariane featuring Adeline[37].

Launcher	Company	Country	Payload Capacity	Cost/Kg (USD)	Availability	Stages & Propulsion	Reusability
Electron [41]	RocketLab	NZ/USA	150Kg to SSO	\$32,600	Available	Rocket-rocket	No
Bloostar [42]	Zero2Infinity	Spain	100kg to SSO	\$40,000	-	Balloon-rocket-rocket-rocket	No
Eris [43]	Gilmour Space Technologies	Aus/SG	380kg to LEO	\$23,000-38,000	Q4 2020		No
Intrepid-1 [44]	Rocket Crafters	USA	376kg to SSO	\$23,936	Q1 2019	Rocket-rocket	No
KZ-1A [45]	CASIC	China	250kg to SSO	-	-	Rocket-rocket	No
Vector-H [46]	Vector Space Systems	USA	160kg to LEO	\$21,875	2018	Rocket-Rocket-(Third rocket optional)	No
SMILE [47]	NLR	EU	50kg	<\$50,000	-	-	-
Firefly α [48]	Firefly Aerospace	USA	630kg to SSO	-	2019	Rocket-Rocket	No
LauncherOne [49]	Virgin Orbit	UK	300kg to SSO	\$33,000	-	Aircraft-rocket-rocket	Aircraft
XS-1 [50]	Boeing	USA	-	-	-	-	First Stage
500R [51]	Orbital Access	UK	500kg to SSO	-	-	Aircraft-Rocket	Fully Reusable

Table 2.1: A selection of the small satellite launchers which are operational or in development.

private and public companies are currently developing small satellite launchers which will allow small satellites to be launched into bespoke orbits on schedules determined by the customer[5]. The details of a selection of the most promising or innovative of the small satellite launchers currently in active development is shown in Table 2.1. Many of these launchers are projected to be available within the next few years, and will offer cost-per-kg comparable to piggybacking on larger launches.

The majority of the small satellite launchers in development are expendable[6]. These expendable small satellite launch systems aim to reduce costs by creating a launch system which is as cost-efficient as possible to produce and launch[6]. This generally entails making use of conventional, well-tested designs, combined with state of the art manufacturing techniques, such as 3-D printing[6, 43]. This method allows for rapid development, although it has an intrinsic cost limit due to the requirement of manufacturing a new launch system for each launch.

Reusable small satellite launchers have higher initial costs-per-vehicle, but also have the potential for large advantages in the long term[12]. Reusable small satellite launchers have the potential for lower cost-per-launch than expendable systems, with increased launch flexibility[12]. One of the most promising methods of reusability for small launchers is the addition of airbreathing engines[52].

2.4 Airbreathing Access-to-Space Systems

The addition of airbreathing stages to a satellite launch system to allow for partial or full reusability of a launch system has been investigated for a number of years by multiple institutions[12, 28, 53–61]. The reduced fuel usage of airbreathing engines allows for the inclusion of systems which enable fly-back and landing of the stage in a similar manner to a conventional aircraft, potentially offering multi-launch re-use with increased launch flexibility and decreased costs[12]. However, the addition of airbreathing engines to a launch system introduces significant design challenges, and no airbreathing access to space systems have yet been deployed.

The technological challenges present for an airbreathing launch system stem from the inherent limitations of jet engines. Turbojets, ramjets and scramjets all operate across different Mach number regimes, and require atmospheric flight to operate[52]. This means that within an airbreathing access-to-space system, a combination of various airbreathing engines and/or rockets must be used during launch. Figure 2.6 shows the operating corridor for an example launch system using turbojet, scramjet, and rocket engines, indicating the point at which engine transition occurs, as well as the lower dynamic pressure limit on engine operation and the upper dynamic pressure limit on the aircraft structure. This operational corridor imposes unique constraints on the design of airbreathing launch systems and their trajectories. An airbreathing access to space system must be capable of resisting high structural and thermal loads, as well as being able to sustain atmospheric flight for long periods, necessitating a high lift-to-drag ratio.

Airbreathing access-to-space systems have been investigated in various forms including; single

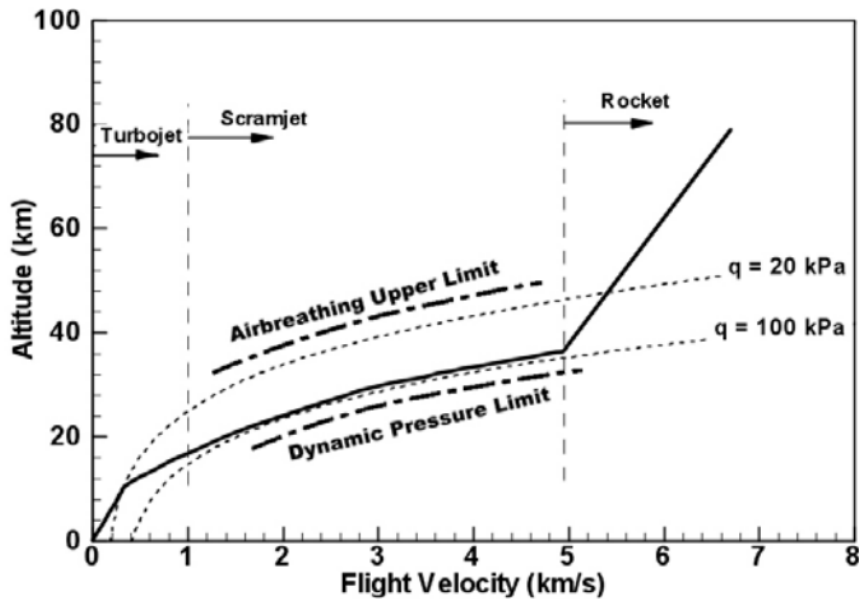


Figure 2.6: The airbreathing vehicle flight corridor [9].

stage[28, 53–55, 58–60], dual stage [56, 57, 61] and tri stage [12] designs. A single stage design has the advantage of being fully contained within one vehicle, which is convenient for reusability and return trajectories. However, it has been suggested by Smart & Tetlow [52] that these designs suffer from severe limitations as they must contain multiple engines which add mass at later stages of the trajectory and decrease the efficiency of the vehicle. Smart & Tetlow suggest that multistage systems offer significant improvements in payload mass fractions, and have the advantage of using airbreathing stages only within their operable range. Dual stage designs have been investigated in some detail using the 'spaceplane' concept by Mehta & Bowles [57] using life cycle cost analysis in order to take flexibility and reusability into account. Mehta & Bowles conclude that a two stage design is the optimal configuration for reusable hypersonic space access systems, however this study is only based on comparison with single stage to orbit systems, and it is more useful to consider their conclusions as an endorsement of multi stage airbreathing designs in general. They find that multi stage vehicles have higher potential for payload than single stage to orbit (SSTO) systems and have less propellant requirements, partly due to a greater atmospheric cruise capability.

2.4.1 Small Airbreathing Launchers

The use of airbreathing engines has particular applicability to small launch systems. As discussed in section 2.3, incorporating reusability into rocket-powered small satellite launchers is complex, due to the high mass fraction of the systems necessary for re-use at small scales. The use of airbreathing engines may allow a small launch system to incorporate reusable elements without excessive mass penalties. Smart & Tetlow[52] have found that the addition of a scramjet-powered stage may enable

the development of a partially reusable small satellite launch system in the near future. Simulations carried out for three stage systems utilising scramjet and rocket engines for small payload delivery show favourable payload mass fractions with a reusable scramjet stage [52]. Scramjet powered vehicles may also offer the ability to put small payloads into orbit with greatly increased flexibility and launch window when compared to similarly sized rocket systems. This has been assessed in a study by Flaherty[62] comparing the United States Air Force's Reusable Military Launch System all-rocket launch vehicle RMLS102 against the Alliant Techsystems rocket/scramjet launch system ATK-RBCC. These vehicles are similarly sized and comparisons were made for payloads launched to rendezvous with satellites in randomly generated orbits[62]. These vehicles were compared using the range of orbital trajectories that each vehicle was able to rendezvous with within one day, determined by launch vehicle range[62]. The vehicles were compared by their ability to reach a range of trajectories intercept locations in limited time, and the ATK-RBCC vehicle was found to be able to cover at least 1.7 times area of the rocket-powered vehicle[62], in a large part due to the airbreathing vehicle's ability to fly fuel efficiently over long distances. This means in general that a partially scramjet powered accelerator is able to fulfil the specific delivery needs of small payloads over a wider range of orbits within smaller time periods when compared to a fully rocket powered accelerator. This can be advantageous for time critical and orbit dependant payloads which have specific mission requirements to be met.

2.5 Airbreathing Launch Vehicle Ascent Trajectories

The trajectory of an airbreathing launch vehicle is more complex than that of a fully rocket-powered launch system. A airbreathing launch system trajectory must be designed around a number of factors:

- The requirement for the airbreathing stages to fly in-atmosphere
- The variable efficiency of the airbreathing engines
- The relative efficiency of the different types of engines within the system
- The aerodynamic performance of each vehicle or engine-mode of the system
- The structural limitations of the system

A simple way to design the trajectory of an airbreathing launch system is to constrain the flight of the high speed airbreathing section to a constant dynamic pressure[60, 63–66]. Constant dynamic pressure trajectories can be advantageous for an airbreathing accelerator due to the trade-off between structural loading and engine performance[63]. As dynamic pressure increases so does the structural loading on the vehicle, however the performance of a ramjet or scramjet engine is directly reliant on dynamic pressure[63]. A constant dynamic pressure trajectory is viewed as being an acceptable

compromise between these two factors. Figure 2.7 shows an example of a constant dynamic pressure trajectory flown by an airbreathing vehicle, where the airbreathing mode operates between 200-430s.

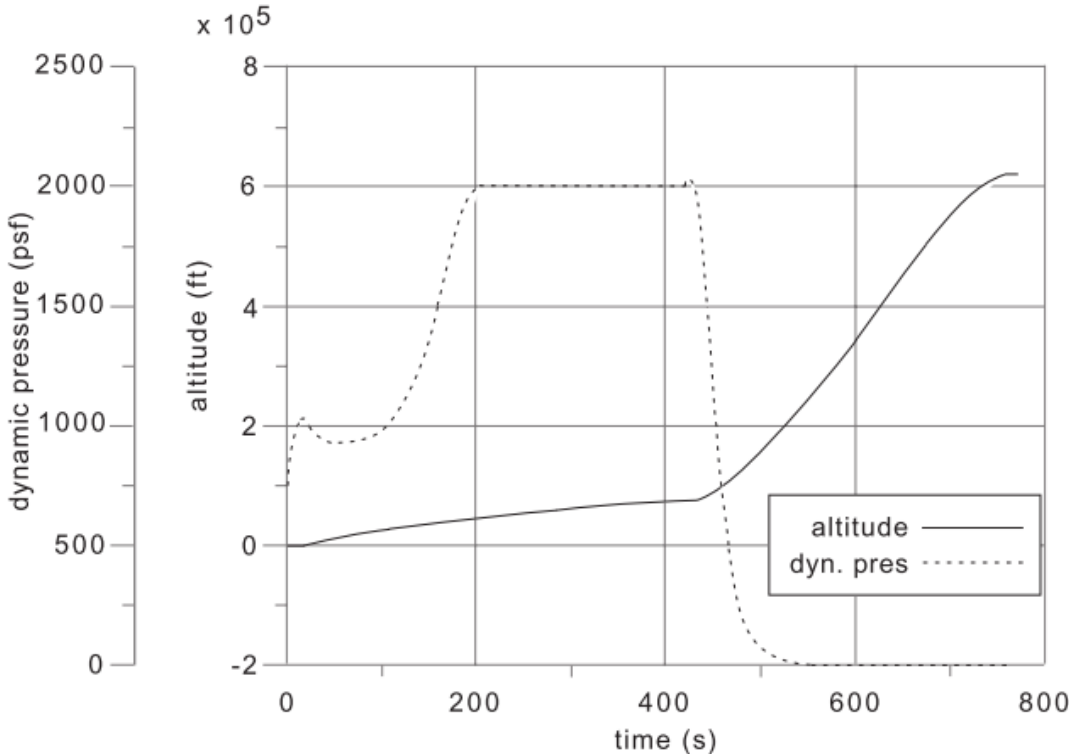


Figure 2.7: An example of an airbreathing ascent trajectory of the Maglifter RBCC/Rocket launch vehicle[63]. This trajectory shows a constant dynamic pressure section during fan-ramjet mode[63].

Although a constant dynamic pressure trajectory is likely to produce high efficiency flight for the high speed airbreathing portion of an ascent trajectory, there are a variety of factors that must be considered in designing the trajectory of a launch system. For example, a constant dynamic pressure flight may produce suboptimal conditions for the switch from airbreathing engines to rocket power for exoatmospheric flight. For a constant dynamic pressure trajectory the transition to rocket power will occur at a very low trajectory angle and altitude[12]. It may be more optimal overall for the vehicle to fly at less than maximum dynamic pressure for a time during airbreathing engine operation, allowing the trajectory angle and altitude to be raised before the rocket engines are powered-on, increasing the efficiency of the rocket engines and reducing the dynamic pressure experienced by the rocket stage[54, 56, 57]. The consideration of all stages and propulsion methods, when designing the trajectory of a launch vehicle, can produce a more optimal trajectory, which maximises the performance of the launch system, eg. increasing payload-to-orbit, or increasing the range of orbits attainable by the launch vehicle.

2.5.1 Single-Stage Vehicles

Optimal trajectories have previously been developed for launch systems integrating airbreathing and rocket propulsion within single-stage-to-orbit (SSTO) vehicles[28, 53, 58–60, 67, 68]. These optimal trajectory studies found unanimously that a pull-up manoeuvre before the end of the airbreathing engine cut-off was the optimal flight path for the SSTO airbreathing-rocket vehicles being investigated. An example of one of these vehicles, its trajectory, and associated pull-up manoeuvre is shown in Figure 2.8, developed by Powell et al [53]. A pull-up was found to be optimal for vehicles where the rocket engines are not ignited until circularization altitude [53, 67], vehicles where the rocket engine is ignited immediately after airbreathing engine cut-off [58, 59, 68] as well as for vehicles which operate in combined scramjet-rocket mode[28, 60]. For SSTO vehicles a pull-up manoeuvre is a simple trade-off between the altitude at airbreathing engine cut-off and the velocity achievable at cut-off. Due to the entire vehicle being lifted into orbit, this becomes a relatively simple problem of engine efficiency. The airbreathing engine is used for its high efficiency, until the dynamic pressure drops below the operable limit of the airbreathing engine, or until the thrust provided by the airbreathing engine is significantly counteracted by the effects of drag and gravity.

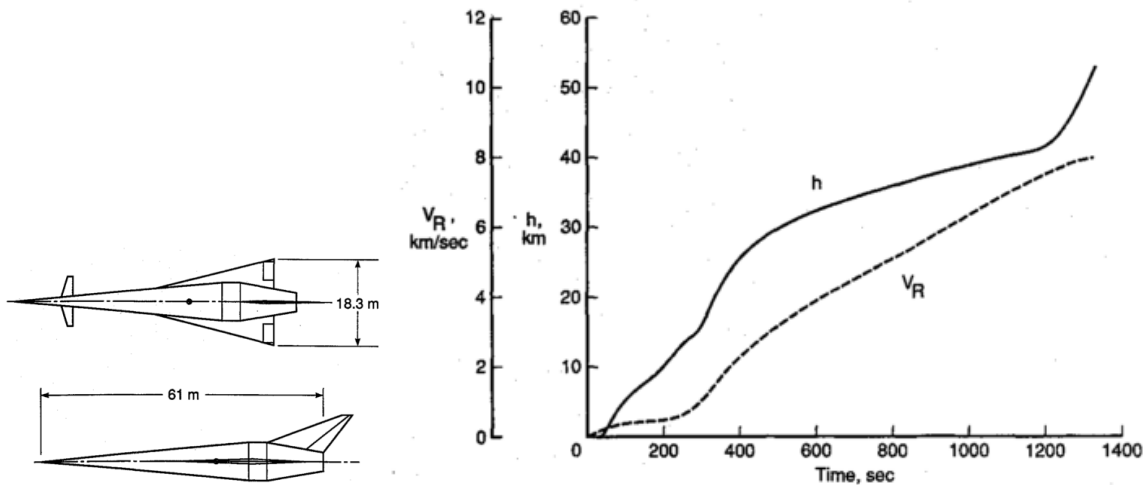


Figure 2.8: The single stage-to-orbit vehicle of Powell et al [53] and its launch trajectory, with pull-up manoeuvre evident. V_R indicates Earth relative velocity.

2.5.2 Multi-Stage Vehicles

For a multi-stage to orbit vehicle, calculating the optimal trajectory for maximum payload flight is significantly more difficult. A multi-stage vehicle has one or more stage transition points, where the vehicle separates a component which is discarded or reused later, and does not continue to orbit. At a stage transition point there is a large change in the mass and aerodynamics of the launch system. This

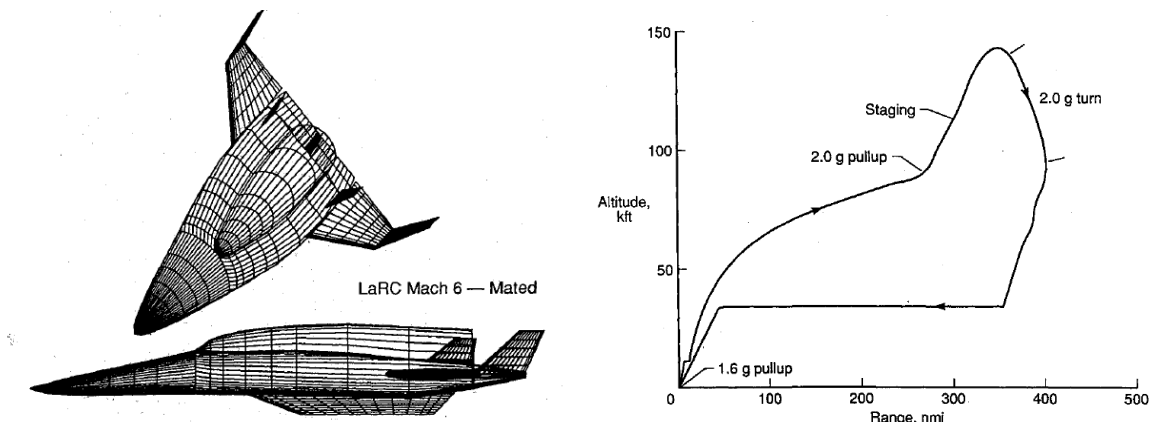


Figure 2.9: The two stage-to-orbit launch vehicle of Wilhite [54]. The launch trajectory is shown, with pull-up indicated.

change in flight dynamics makes finding the optimal stage transition point more complicated. To find the optimal separation point there is a trade-off between:

- The high efficiency of the scramjet engines
- The thrust produced by the scramjet engines
- The potential thrust of the rocket engines
- The energy necessary to increase the altitude of the scramjet stage
- The aerodynamic efficiency when performing the required direction change

All of these factors must be considered in order to generate an optimal trajectory.

There has been a number of studies which have identified a pull-up manoeuvre as being advantageous for a multi-stage system [54, 56, 57]. However, in these studies a pull-up manoeuvre has been specified in order to decrease the dynamic pressure of the vehicle at airbreathing-rocket stage separation. In the studies by Tsuchiya et al.[56] and Wilhite et al.[54], decreased dynamic pressure is necessary for the successful operation of the orbital rocket stages, of the systems under investigation. The launch vehicles and trajectories developed in these studies are shown in Figures 2.10 and 2.9 respectively. In these studies the airbreathing stages pull-up to the maximum allowable dynamic pressure for the rocket-powered orbital stages. When the orbital stages are able to operate, stage separation occurs. These pull-up manoeuvres demonstrate the advantages of a pull-up for the operation of the orbital stages, allowing the aerodynamic and thermal loading on the vehicle to be reduced. However, these pull-up manoeuvres are not performed as part of optimal trajectories, instead they are designed to ensure that the performance constraints of the systems are met. Mehta & Bowles [57] prescribe a 2g pull-up at flight conditions of Mach 10, 95000 ft for an airbreathing stage in order to “lower dynamic pressures and to achieve the optimal launching flight path angle for the orbiter

2.5. AIRBREATHING LAUNCH VEHICLE ASCENT TRAJECTORIES

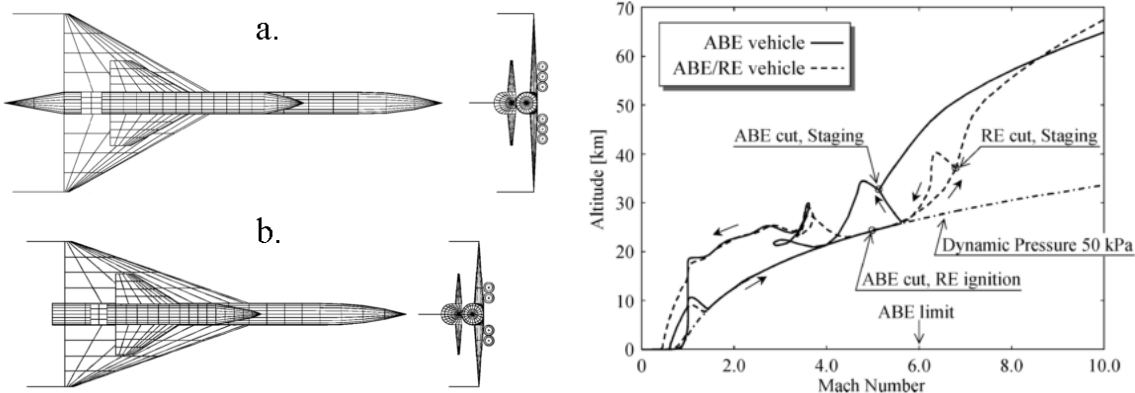


Figure 2.10: The two stage-to-orbit launch vehicle of Tsuchiya and Mori [56], with trajectories including pull-up and return for both airbreathing and airbreathing/rocket vehicles shown.

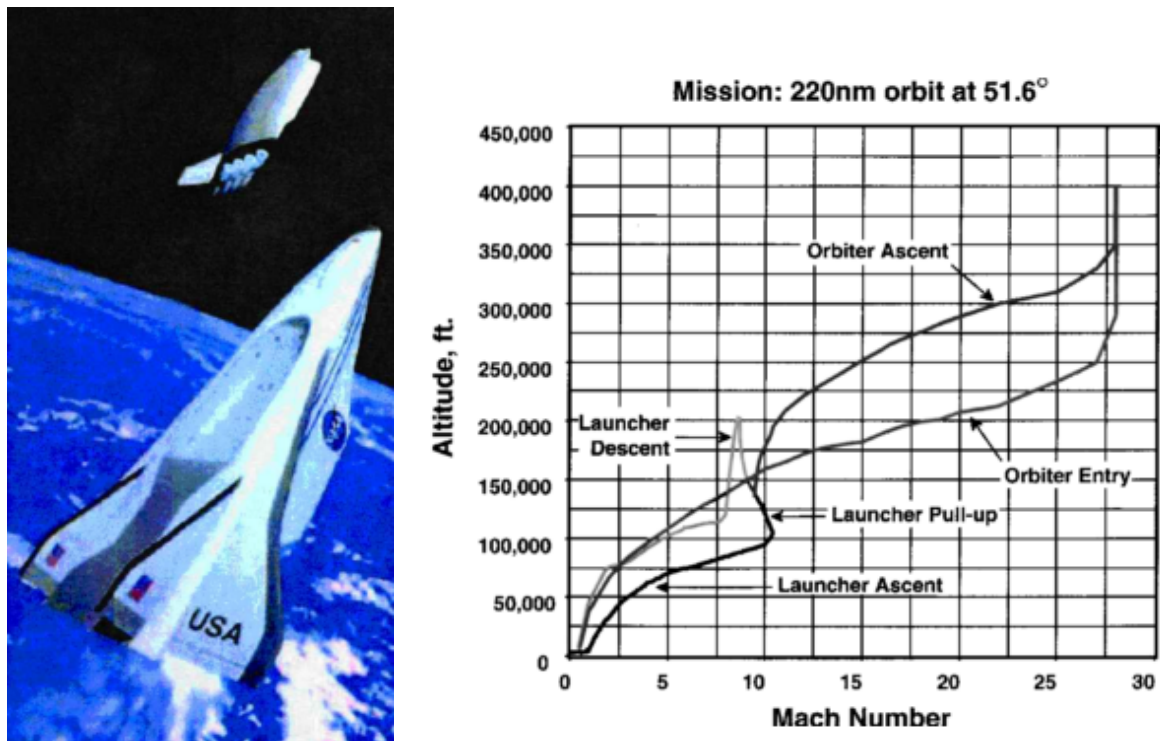


Figure 2.11: The two stage-to-orbit launch system developed by Mehta and Bowles [57], with trajectory and pull-up shown.

vehicle". The launch vehicle and trajectory developed by Mehta & Bowles is shown in Figure 2.11. This prescribed manoeuvre indicates that a pull-up before airbreathing-rocket transition is considered the optimal trajectory, however this study does not optimise the shape or magnitude of the pull-up manoeuvre, only considering the increased performance of the rocket vehicle.

2.6 Hypersonic Vehicle Fly-Back Trajectories

The fly-back of an airbreathing launch vehicle is a crucial component of the trajectory. The ability to land a reusable launch vehicle safely in the intended location is a key requirement, and if this fly-back can transport the launch vehicle back to the initial launch location, then transport costs and turnaround times can be significantly reduced.

There are three main methods that have been studied for potential hypersonic vehicle return; glide-back, cruise-back and boost-back. Glide-back involves the hypersonic vehicle returning to base and landing entirely using its aerodynamics. This requires sufficient lift to sustain the hypersonic vehicle over the entire return range, as well as the controllability to land the hypersonic vehicle in level flight. For a hypersonic trajectory a fully glide-back return flight is most likely unobtainable. This is due to the large downrange distance flown, and the large initial velocity at the beginning of the fly-back trajectory, when the vehicle is oriented away from the landing site. Multiple studies have investigated the maximum staging velocity allowable for the glide-back flight of a booster. In these studies, the maximum separation velocity for glide-back to be feasible has been found to be between Mach 3-4 at 30km-120km downrange distance, with higher initial velocities or longer downrange distances requiring fly-back under power[69, 70].

Cruise-back involves the inclusion of subsonic engines, which are used to power the fly-back of the hypersonic vehicle until landing similar to a conventional aircraft. These engines may be included solely for the fly-back[69], or used in the acceleration phase for low velocity acceleration[54, 57, 70]. The addition of subsonic engines powering a constant velocity cruise-back phase allows the accelerator to return to base with a similar trajectory to that of traditional aircraft, allowing the velocity and altitude of the accelerator to be precisely controlled. However, the addition of subsonic engines necessary for cruise-back increases the mass of the vehicle significantly, leading to decreased mass efficiency and increased design complexity[69].

A preferable mode of powered fly-back is to use the existing hypersonic airbreathing engines during the return trajectory in a boost-back trajectory. Using the existing airbreathing engines allows for range to be added to a return trajectory, without the inclusion of additional engines. The hypersonic airbreathing engines can be operated at appropriate times during the fly-back, when they will be most impactful on the return trajectory range. However, the hypersonic airbreathing engines may only be used within their operating region, and vary in thrust and efficiency dependent on flight conditions. Hypersonic airbreathing engines have maximum efficiency at low Mach numbers[12], with the thrust

2.7. THE UNIVERSITY OF QUEENSLAND’S ROCKET-SCRAMJET-ROCKET LAUNCH SYSTEM

produced depending on the dynamic pressure and inlet conditions, which vary with the trajectory path and angle of attack of the vehicle. This added complexity requires the use of trajectory optimisation methods to find the most efficient flight path for return to the launch site, and to ensure that the return of the vehicle under its own power is viable.

The possibility of an airbreathing vehicle reigniting high speed airbreathing engines for short periods has been investigated by Tsuchiya and Mori [56]. Tsuchiya and Mori investigate two conceptual launch vehicles; a vehicle powered solely by airbreathing propulsion returning after separation of an orbital stage at Mach 5.1, and an airbreathing/rocket vehicle returning after a separation at Mach 6.8[56]. Both vehicles use the high speed airbreathing engines during return flight. The optimal launch and return trajectories for these vehicles are shown in Figure 2.10. Both vehicles ignite the airbreathing engines at around Mach 3.5 for “several tens of seconds” to extend the range of the fly-back manoeuvres. After this, the vehicles descend and land at the launch site. These boosters fly to a downrange distance of 600-625km from the launch site, and less than 5% of the vehicles initial propellant was required to return the vehicles to the initial launch sites[56].

If powered fly-back is necessary, the additional fuel weight used during this phase can negatively impact on the potential performance of a launch system. Optimising the fly-back trajectory of the reusable stages of a launch vehicle can decrease the amount of fuel used, and minimise the impact of the return phase. The problem of optimising the fly-back of a launch vehicle for minimum fuel is analogous to maximising the range possible on a small amount of fuel, with manoeuvring. The maximum range trajectory of a hypersonic vehicle operating at high altitudes has been shown to be a ‘skipping’ trajectory, where the altitude of the vehicle is repeatedly raised and lowered[71–74]. A skipping trajectory has been shown to be range optimal for hypersonic vehicles able to skip out of the atmosphere [71], as well as vehicles flying entirely within the atmosphere[70–73]. A skipping trajectory has also been shown to be optimal for an airbreathing hypersonic vehicle thrusting throughout the trajectory[74]. This optimised trajectory is shown in Figure 2.12. The range optimal operation of the scramjet engine is shown to be repeated ignitions at the trough of each skip[74]. The scramjets are ignited as the vehicle climbs after the trough, as the Mach number decreases to the minimum operable conditions of the scramjet engines[74]. Minimising the Mach number during operation in this way maximises the efficiency of the scramjet engines[74].

2.7 The University of Queensland’s Rocket-Scramjet-Rocket Launch System

The three stage, partially reusable, access to space system under development at The University of Queensland utilises the SPARTAN[75] scramjet powered vehicle as the reusable second stage, shown in Figure 2.13. This system is considered in this study as a representative model for three stage, air-

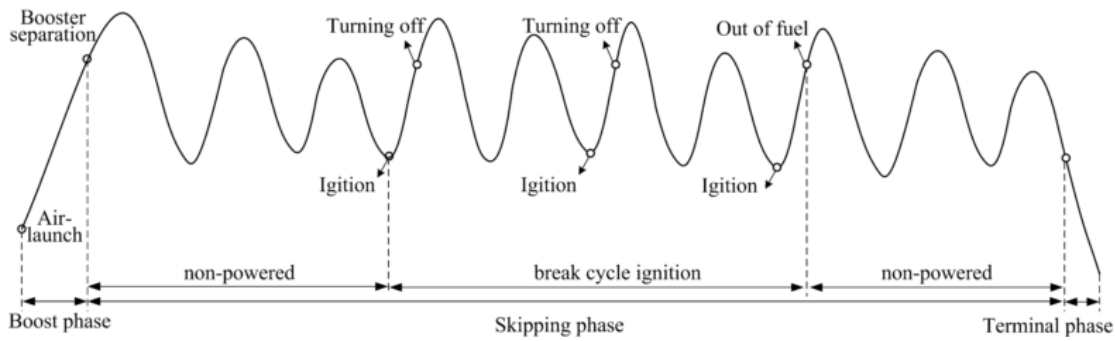


Figure 2.12: The optimised maximum range trajectory of a hypersonic vehicle[74].

breathing access to space system designs. This launch system is designed for small payload deliveries to orbit and will in the future utilise a fly-back rocket booster to accelerate the SPARTAN stage to minimum Mach number required for stable burn, at which point separation occurs and the second stage uses a scramjet engine to accelerate to between approximately Mach 5-9. The first and second stages are to be reusable, the first stage via conversion into a propeller powered drone, and the second stage through either a glide, or scramjet-powered flight to a suitable landing site. The third stage will

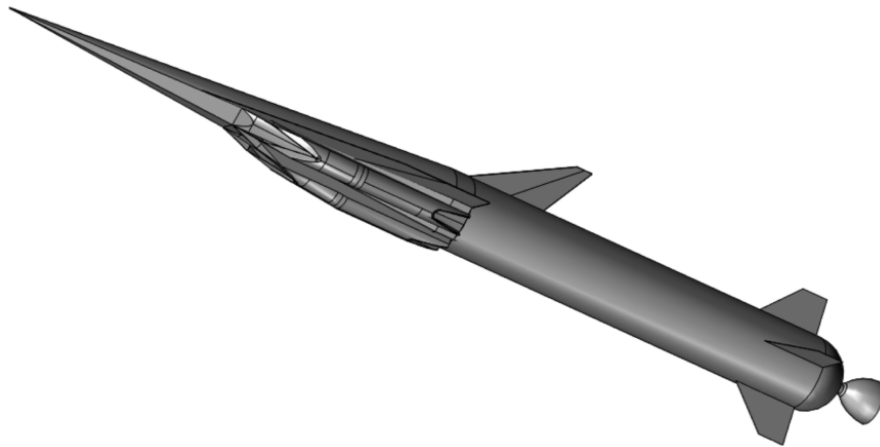


Figure 2.13: An early design of the socket-scramjet-rocket launch system incorporating the SPARTAN [75].

be a disposable rocket stage, which will then deliver the payload to orbit, exiting the atmosphere and performing a Hohmann transfer. Preliminary designs of the SPARTAN have been completed, with the shape of the SPARTAN optimised for payload delivery to heliosynchronous orbit. Studies have indicated that the expendable third stage makes up only 8.8% of the mass of the launch system, and that if the SPARTAN and first stage rockets are able to be reused, approximately 90% of the launch system mass would be reusable[12].

2.7.1 Scramjet Engine Model

To deliver a payload to orbit, the SPARTAN uses four Rectangular-to-Elliptical Shape Transition (REST) scramjet engines, with inlets configured to allow installation on a conical forebody (C-REST). The C-REST engines, which the SPARTAN uses, have been configured to fly between Mach 5 and 10. This type of engine is known as a C-RESTM10 engine[12]. The REST engine has been shown experimentally to operate successfully at off design conditions[7, 76], and has shown good agreements with numerical CFD models[7].

A C-RESTM10 propulsion database has been used in previous studies to model the scramjet engines of the SPARTAN[12]. The specific impulse profile of the C-RESTM10 engine, taken from the C-RESTM10 propulsion database, is shown in Figure 2.14. This database has been created through separate modelling of the compression within the inlet, combustion within the combustor, and expansion through the internal nozzle[77]. The inlet compression was modelled by performance curves based on a set of CFD solutions[77]. These performance curves were used to obtain the flow conditions at the end of the inlet. The combustor was modelled using quasi-one-dimentional cycle analysis, assuming a combustion efficiency of 80%[77]. Lastly, the properties at the end of the combustor were expanded assuming a nozzle efficiency of 90%[77]. The C-RESTM10 is designed for operation at $M_0 = 10$, and the contraction ratio and combustor divergence are not optimal for operation at low Mach numbers. At low Mach numbers, an equivalence ratio of 1 may cause the flow to choke and unstart. Consequently, an equivalence ratio of less than 1 was set at low Mach numbers, in order to avoid unstart[77]. At these Mach numbers, the C-REST engines are operating in dual-mode[77].

2.7.2 The Trajectory of the SPARTAN

To date, studies of the SPARTAN have assumed a constant dynamic pressure trajectory[12]. Past studies of the SPARTAN vehicle have assumed that a fly-back to launch site is possible after third stage separation[12]. However, this fly-back has not yet been simulated.

Figure 2.15 shows the trajectory of the SPARTAN, simulated in three degrees of freedom to fly close to a constant 50kPa dynamic pressure, using a pole-placement angle of attack controller[12]. The ascent trajectory of the SPARTAN begins at Mach 6, and terminates at Mach 9.34, when the hydrogen fuel is exhausted[12]. The net specific impulse of the SPARTAN varies from 1492s at the beginning of the trajectory, to 439s by the time the fuel is depleted[12]. This significant decrease in efficiency means that by the end of the trajectory, the net efficiency of the SPARTAN is approximately that of a rocket[12].

The SPARTAN is trimmed throughout the trajectory by ailerons on the wing, shown in Figure 2.16. These elevons were sized through variation of the width, b_E , to have an area equal to 15% of the area of the wing, and to have a cord length, c_E , of 15% of the cord length of the wing[12]. Over the flight of the SPARTAN, the flap deflection changes from 10.6° to 12.2°[12]. The drag contribution of

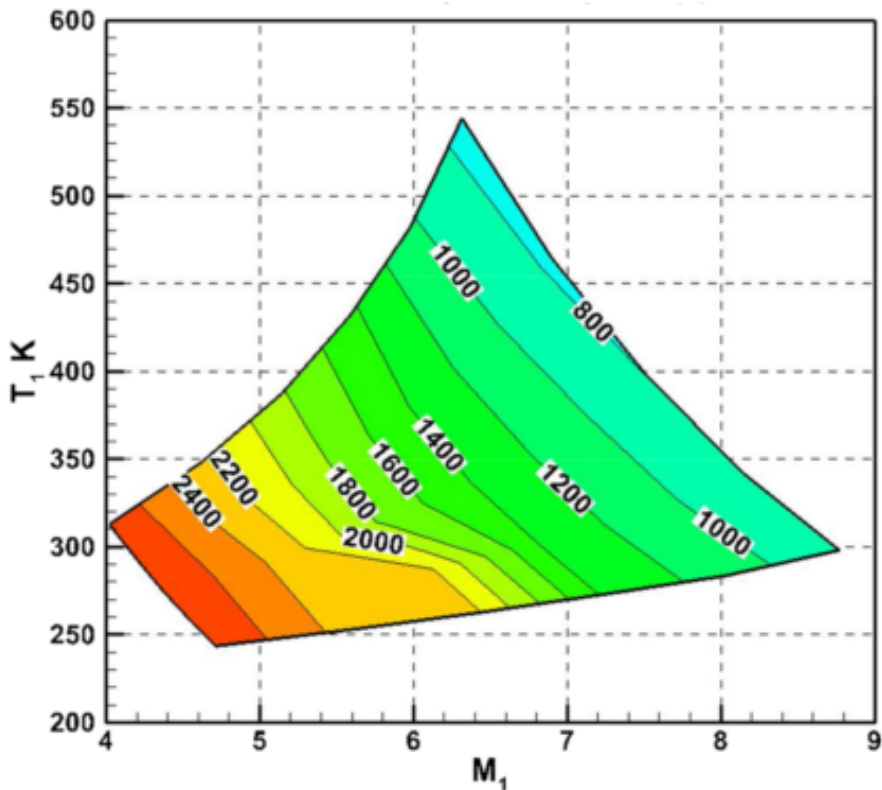


Figure 2.14: The C-RESTM10 propulsion database, specific impulse.

the flap varies from 14.3% to 14.5%, and the lift contribution from 18.8% to 21.0%[77].

This trajectory enables the delivery of 279.8kg of payload to sun synchronous orbit, when using a third stage powered by a Pratt & Whitney RL-10-3A[77]. This trajectory was designed around the SPARTAN flying a constant dynamic pressure trajectory, with the first and third stage trajectories confirming to this constraint. It has been suggested that for the design of this launch system to be improved, an optimised trajectory is necessary[12].

2.7.3 The Third Stage Rocket

The third stage rocket of the rocket-scramjet-rocket launch system consists of a rocket motor, fuel tanks, structure, payload and a thermal protection system[12], shown in Figure 2.17. The third stage rocket separates from the SPARTAN at the end of its trajectory, and performs a pull-up manoeuvre to exit the atmosphere. Once the density of the atmosphere is low enough, the thermal protection system separated from the vehicle for mass efficiency, and once exoatmospheric, the third stage performs a Hohmann transfer to reach the desired orbit. The third stage has to this point been designed to be powered by the Pratt & Whitney RL-10-3A[12], and has exhibited good performance when powered by this engine. However, the RL-10-3A is a pump-fed engine, and is likely to be prohibitively expensive for a small launch system.

2.7. THE UNIVERSITY OF QUEENSLAND'S ROCKET-SCRAMJET-ROCKET LAUNCH SYSTEM

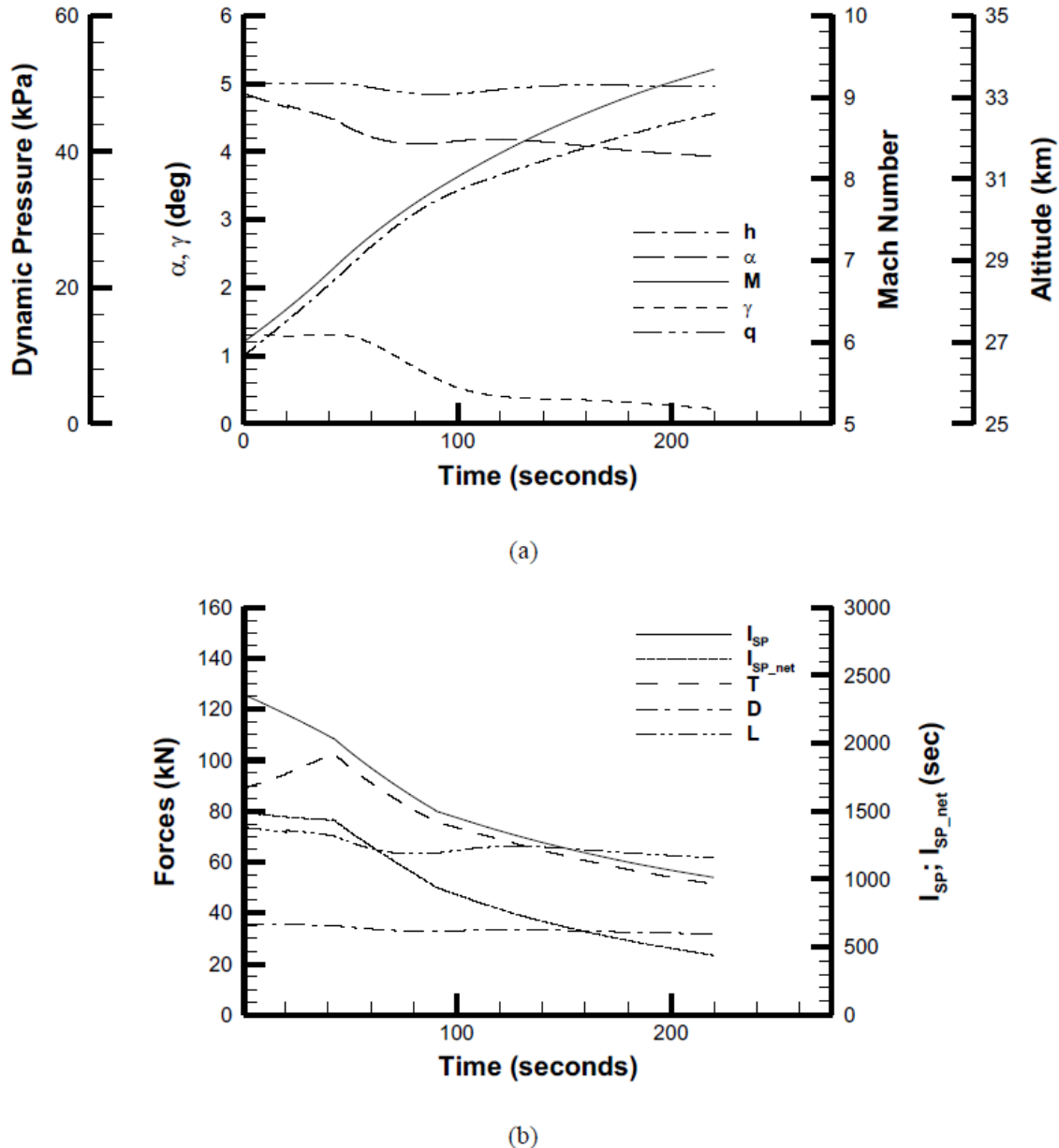


Figure 2.15: The flight trajectory of the SPARTAN. a) shows the physical trajectory and b) shows the forces on the vehicle and performance indicators.

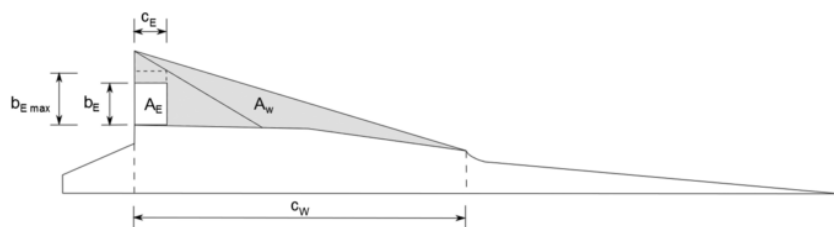


Figure 2.16: The elevons of the SPARTAN[12].

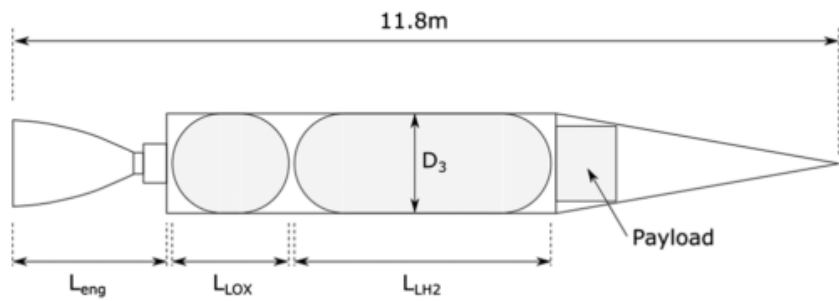


Figure 2.17: The third stage rocket of the rocket-scramjet-rocket launch system[12].

Engine	Fuel Supply	Fuel	Thrust	Isp	Mass	Diameter	Length	Thrust Vector Capability
Rl-10A-3A	Pump-Fed	LOX/LH ₂	73.4kN	444s	141kg	1.01m	1.78m	Yes, Unknown limits
Aestus II	Pump-fed	MMH/NTO	46kN	337.5s	148	-	2.2m	6°
RS-72	Pump-fed	MMH/NTO	55.4kN	338s	154kg	-	2.286	6°
ATE	Pump-fed	MMH/NTO	20kN	345s	57.9kg	0.38m	1.4m	15°
AJ10-118K	Pressure-fed	A-50/NTO	43.3kN	320.5s	124.5kg	1.53m	2.7m	Fixed
Kestrel	Pressure-fed	LOX/Kerosene	30.7kN	317s	52kg	1.1m	1.9m	Yes, Unknown limits
Aestus	Pressure-fed	MMH/NTO	27.5kN	320s	110kg	1.27m	2.2m	4° & 4° by mechanical adjustment
OMS	Pressure-fed	MMH/NTO	26.7kN	316s	118kg	1.168m	1.956m	8°

Table 2.2: Comparison of upper stage rocket engines, sourced from the Encyclopedia Astronautica reference website[78].

2.7.4 Exoatmospheric Rocket Engines

The third stage requires a rocket engine with sufficient thrust to accelerate out of the atmosphere, and a diameter small enough to allow the rocket to fit within the fuselage of the SPARTAN. The major factors when choosing a rocket engine are efficiency and thrust-to-weight ratio, as well as cost. It is desirable to use a rocket engine which has already been developed and flight tested, to reduce the costs and potential complications of engine development. Table 2.2 shows a comparison study of small sized upper stage rocket engines which are currently in use, or have been used, for commercial space flight. The pump-fed motors have significantly higher specific impulse than pressure fed motors. However, while the cost of these engines is not generally published, pressure fed engines cost significantly less than pump-fed engines, due to the cost of the turbopump and the associated complexity of a pump-fed system. As such, it is desirable to use a pressure-fed rocket engine for a small satellite launch system if possible. Of the pressure-fed engines, the Kestrel exhibits a significantly higher thrust/mass ratio than the other engines, with comparable specific impulse and size. This advantage makes the Kestrel engine a reasonable choice to power the third stage rocket.

2.8 Optimal Control

Calculating the optimal trajectory of a launch system with multiple stages and multiple modes of propulsion is a complex process. Defining the trajectory of a launch system purely from vehicle analysis is unlikely to yield a trajectory which maximises the performance of the system. A simulation method is required which is able to calculate a trajectory path which maximises the performance of the launch system, while taking into account the aerodynamic and propulsive properties of each stage and propulsion mode. Optimal control theory is used in situations where an optimal trajectory path must be found with little prior knowledge of the shape of the trajectory. Optimal control theory has been widely used in aerospace applications, including being used to optimise the launch of hypersonic launch vehicles[53, 58–60, 67, 68].

For an optimisation of a complex trajectory there are a variety of optimal control methods that are useful for specific problem types. These are separated into two categories: direct and indirect solution methods. Indirect methods are based on the calculus of variations or minimum principle model, and generally result in high accuracy solutions to optimisation problems [79]. However indirect models suffer from the drawbacks of small radii of convergence and the fact that the equations to be solved often exhibit strong nonlinearity and discontinuities. This means that indirect methods will not be solvable unless the problem is very well defined with a minimum of nonlinearity, making indirect methods unsuitable for many complex optimisation problems, such as aerospace vehicle simulations which can exhibit strong nonlinear behaviour and have a wide solution space.

Direct methods transform an optimisation problem into a nonlinear programming (NLP) problem

which can be solved computationally [80]. NLP solvers solve the optimisation problem defined as [81]:

$$\text{Minimise} \quad f(x) \quad (2.1)$$

$$\text{Subject to} \quad g_i(x) \leq 0 \quad \text{for } i = 1, \dots, m \quad (2.2)$$

$$\text{and} \quad h_j(x) = 0 \quad \text{for } j = 1, \dots, n \quad (2.3)$$

An optimisation problem that has been discretised in this form can thus be solved using any of a variety of NLP solvers. One of the most effective methods of solving twice differentiable NLP problems is sequential quadratic programming (SQP) [82] for which there is a variety of commercial solvers available such as NPSOL, SNOPT, and packages within MATLAB.

In order for these packages to be able to solve an optimisation problem it must be presented in discretised form, and as such must be transformed using approximation techniques. The task of approximating a continuous optimisation problem in discrete NLP solvable form is not simple. SQP solvers can very easily run into convergence issues when provided with an optimisation problem which has not been well defined. Also, any approximation must be carried out with care that the accuracy of the solution is not compromised. There are multiple ways to approximate a continuous optimisation problem directly as an NLP problem, the most common of which are shooting and collocation methods. The choice of discretisation method can affect the stability and accuracy of the solution as well as the solution time of the problem.

2.8.1 Shooting Methods

Shooting methods in optimal control are forward-time methods of discretisation. Shooting methods explicitly enforce the dynamics of the system, and update the free conditions and system controls to move towards an optimal solution from an initial guess. Shooting methods are generally simple to apply, and require little specialised knowledge to use once they have been implemented.

The Single Shooting Method

The oldest and simplest method of approximating continuous optimisation problems as NLP problems is the direct single shooting method. Direct single shooting discretises the control function over the solution space, and solves this directly as an NLP by integrating the vehicle dynamics, or state variables, along the trajectory at each trajectory guess[14, 15, 83, 84]. Single shooting is simple to apply and has been used since the 1970s for rocket trajectory optimisation [85]. Single shooting methods suffer from nonlinearity problems, ie. an optimisation problem solved using the single

shooting method will potentially struggle to solve if the problem exhibits even small nonlinearities, due to being unable to converge to an optimal solution. This makes the single shooting method unsuitable for complex problems such as a scramjet model, as there are many nonlinear factors inherent in atmosphere and airbreathing engine modelling.

The Multiple Shooting Method

Direct multiple shooting solves some of the instabilities of the single shooting method by splitting the trajectory into multiple shooting arcs, and collocating these at specific time points[14, 15, 83, 84]. This creates a system of discontinuities, illustrated in Figure 2.18, which are gradually minimised by the solver algorithm until the trajectory is continuous. These discontinuities allow greater flexibility for the solver than is afforded by the single shooting method.

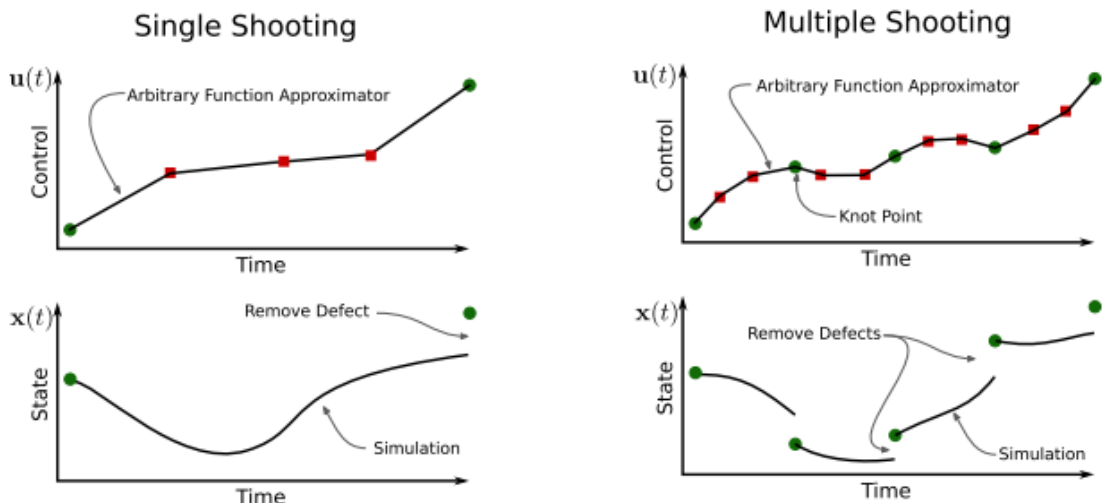


Figure 2.18: A comparison of single shooting and multiple shooting[83].

The multiple shooting method has greatly improved convergence compared to the single shooting method, removing much of the susceptibility to instabilities resulting from nonlinear effects. However, the multiple shooting approach still suffers from a relatively small radius of convergence and slow computation times. Radius of convergence is extremely important to this study as the optimal solution cannot be approximated to a great degree of accuracy, and as such multiple shooting was deemed inappropriate for this study. It was desired to find a method with a global radius of convergence to apply to the optimisation problem being considered.

2.8.2 Collocation Methods

Collocation methods are arguably the most powerful methods for solving optimal control problems[14]. Collocation methods are simultaneous methods, where both the states and controls are

approximated using a specific form of functional[14, 83]. In these methods, the dynamics of the system are not explicitly enforced, but instead are constrained at specified points along the trajectory, called collocation points, or nodes[83]. This means that the derivative of the state functions become a constraint within the NLP, being equated to the polynomial approximation functions by the solver algorithm. Collocation methods provide larger radius of convergence, greater robustness, and smaller computational times compared to multiple shooting[84]. However, the solution accuracy of collocation methods is less than that of multiple shooting methods[84], although this can be improved through the choice of basis functions used for collocation[14].

Collocation methods can be represented in two ways; h and p schemes[83]. p schemes, or global methods, represent the entire trajectory as high order polynomials, and converge by increasing the order of these polynomial[83]. This method works well if the underlying solution is smooth, however, if there are discontinuities present, a p scheme will fail[83]. h schemes separate the trajectory into a series of medium order polynomials, stitched together at set points using defect constraints, similarly to the multiple shooting method[14, 83, 86]. These joining points are called knot points[83, 86]. A comparison between h and p methods is shown in Figure 2.19.

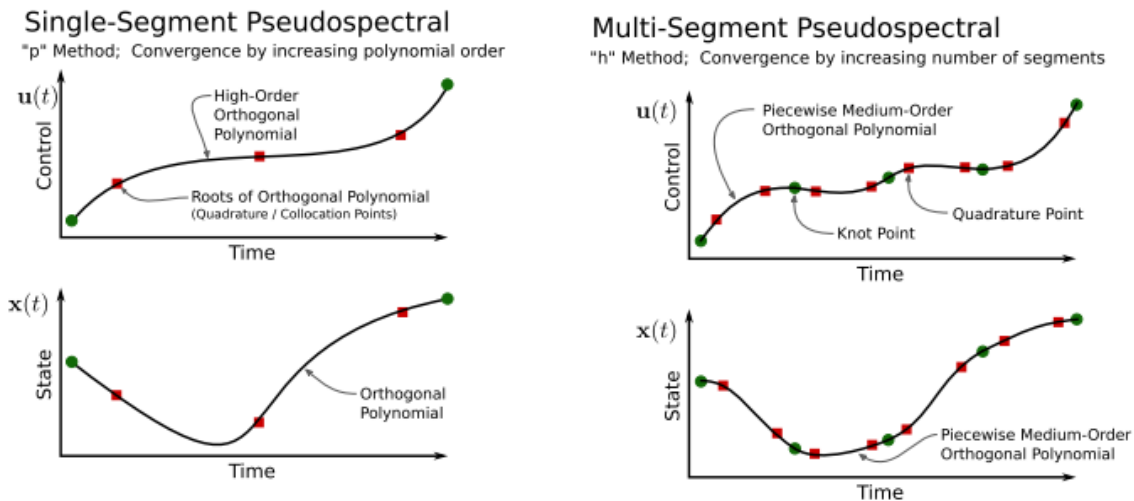


Figure 2.19: Examples of h and p collocation methods[83].

The Pseudospectral Method

The most accurate and effective type of collocation methods use orthogonal polynomials to approximate the state and control functionals[87]. In trajectory optimisation, this type of collocation is referred to as the pseudospectral method[83]. The pseudospectral method was first introduced in 1972 by Kreiss & Oliger [88] as an efficient way to compute meteorology and oceanography problems. The pseudospectral method has recently garnered a large amount of attention for its ability to rapidly and accurately solve a wide variety of optimal control problems. The pseudospectral method employs

the use of orthogonal polynomials such as Legendre or Chebychev polynomials to approximate the state and control functions at a specific set of collocation points[14, 83, 87, 89]. When a solution is well behaved and smooth, the pseudospectral method converges at an exponential rate, with a high accuracy known as spectral accuracy[86, 90].

There are multiple types of pseudospectral methods, distinguished by the polynomial and collocation points used. Usually, these polynomials are Chebyshev or Lagrange polynomials[14, 87], and the collocation points are the roots of a Legendre polynomial[91]. Chebyshev polynomials have been used since the introduction of pseudospectral methods in optimal control, but have been superseded in many cases by Lagrange polynomials, which offer simpler collocation conditions[14]. There are many possible types of collocation nodes, although there are three most commonly used sets; Legendre-Gauss (LG); Legendre-Gauss-Radau (LGR); and Legendre-Gauss-Lobatto (LGL)[14, 91]. The choice of collocation type determines how the roots of the problem are calculated, and changes the formulation of the problem slightly[91]. Practically, there is very little difference between these node sets [91].

The pseudospectral method is usually employed as a p method, where a global polynomial is used, and convergence is achieved by increasing the order of this polynomial[14]. Recently, hp-adaptive pseudospectral methods have been introduced, which segment the mesh using an h method, whilst also having a variable polynomial degree, as in the p method[90]. These hp methods converge by varying the degree of the approximating polynomial as well as the number of segments simultaneously. Utilising both h and p methods improves the accuracy and robustness of the solution, as illustrated in Figure 2.20, from a study by Chai et al.[74] comparing the single shooting method to p (Gauss) and hp-adaptive pseudospectral methods. Additionally, the hp-adaptive method decreases the computational effort and memory usage necessary during the solution process[74, 90].

A secondary usability advantage of the pseudospectral method is the ability to generate Hamiltonian and costate values easily[14, 92, 93]. The Hamiltonian and costate values allow a solution to easily and quickly be checked to determine if some of the necessary conditions for optimality are being met. This is useful to determine if the optimal solution calculated by the pseudospectral solver is valid.

The pseudospectral method has been proven to be extremely effective for simulations in aerospace applications and has been proven in flight applications such as the zero propellant manoeuvre of the International Space Station in 2007, where the ISS was rotated 180 degrees without any propellant used following a pseudospectral method solution [94]. The pseudospectral method has been used successfully in a multitude of studies for the trajectory optimisation of hypersonic vehicles[71, 72, 74, 95–101]. These results indicate that the pseudospectral method is robust for complex, nonlinear systems, and that the pseudospectral method can be used for systems with many state variables.

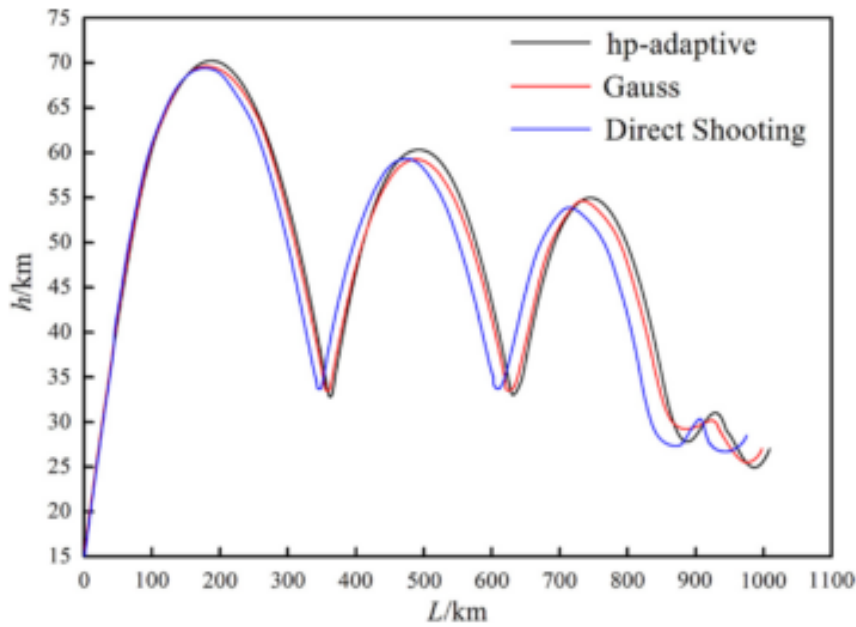


Figure 2.20: Comparison of optimisation techniques[74]. A hypersonic vehicle is optimised for maximum range. The hp-adaptive method can be observed to have produced the most optimal result.

2.9 Available Optimal Control Solvers

There are a number of optimal control solvers available, both commercially and open source. A summary of the most prominent available solvers is shown in Table 2.3. These programs are mostly general solvers, and must be configured specifically in order to solve a particular optimal control problem. The exception is ASTOS[102], which is a standalone program designed for aerospace trajectory optimisation.

Functionally, most of the available solvers are similar in operation. The states and controls of the optimal control problem are defined to the program by the user, along with any constraints; continuous or endpoint. The cost function of the problem is input, and dynamic model of the system is defined. An initial guess is provided, and once activated, the solver will move toward an optimal solution from this initial guess. The most significant practical difference between the solvers lies in the robustness of the optimal solution, ie. how easily a particular solver is able to converge to the optimal solution. For a simple and continuous optimisation problem all solvers will be able to approach the same solution (though with varying efficiency). However, for a complex and nonlinear optimisation problem, some solvers will converge much more easily and rapidly than others. Generally, this stems from the underlying transcription method used. The most common form of discretisation used by these solvers is the pseudospectral method, although other forms of collocation, as well as multiple shooting, are also used. Of the methods used, hp-adaptive pseudospectral methods exhibit the best convergence and accuracy properties[74]. The readily available packages which utilise hp adaptive

pseudospectral methods are GPOPS-2[103] and ICLOCS2[104].

ICLOCS2 is a software package in the alpha stages of development, which is based upon ICLOCS, a multiple shooting solver[104]. ICLOCS2 is able to implement a range of transcription methods, including a hp adaptive Legendre-Gauss Pseudospectral method[104]. As ICLOCS2 is relatively new at the time of writing, it has not yet been implemented in any published works and documentation is limited.

GPOPS-2 is a proprietary hp-adaptive pseudospectral method solver, which implements a variety of hp-adaptive pseudospectral methods, so that the best method may be chosen for a given problem[103]. GPOPS-2 is specifically designed to be as flexible as possible, to accommodate for a wide range of problem formulations[103]. GPOPS-2 is well proven in aerospace applications, and has been used for spacecraft orbit optimisation as well as in-atmosphere trajectory optimisation[99, 105]. GPOPS-2 is well suited to solving multi-phase optimal control problems, which is necessary for efficient multi-stage launch optimisation[103]. GPOPS-2 represents the state of the art in trajectory optimisation software, and as such is used by a number of institutions around the world.

Both ICLOCS2 and GPOPS-2 uses IPOPT[106] (Interior Point OPTimizer) as the standard nonlinear programming solver (with the option of installing others). IPOPT is a widely used open source nonlinear optimisation package which utilises an interior point line search filter method.

Software	Publisher	Platform	Optimisation Type
DIDO[107]	Elissar Global	MATLAB	Chebychev Pseudospectral
GPOPS II[103]	RP Optimization Research	MATLAB	hp Adaptive Legendre-Gauss-Radau Pseudospectral
PROPT (IPOPT) [108]	TOMLAB	MATLAB	Legendre-Gauss Pseudospectral
ICLOCS2[104]	Imperial College	MATLAB	Multiple Shooting / hp Legendre-Gauss Pseudospectral
POST2[109]	NASA	FORTRAN	Direct Shooting
OTIS[110]	NASA	Fortran	Pseudospectral + Various
TRANSWORHP[111]	ESA	Fortran/C++	Full Discretisation
ASTOS[102]	Astos Solutions	Standalone	Multiple Shooting/Collocation
ACADO[112]	Open Source	C++	Direct
JModelica[113]	Modelon AB, Open Source	Modelica/Python	Collocation/ Pseudospectral

Table 2.3: Summary of programs capable of pseudospectral optimisation.

2.10 Aerodynamic Analysis

Simulating the trajectory of access to space systems requires the aerodynamics of each stage of the launch system to be characterised at every flight condition experienced during launch. For this to be possible, it is necessary to create large aerodynamic coefficient databases, which cover the operable region of the vehicle, and include the effects of control surface deflections and propulsion.

There are a variety of tools available to calculate the aerodynamics of aerospace vehicles. These tools are primarily designed towards either accuracy or efficiency, as more accurate methods require more computational power, longer computational times and, usually, more man-hours to produce a solution. This trade off means a tool must be selected which best suits the requirements of a given problem. For a preliminary vehicle design, it is often desirable to select a tool which is as computationally efficient as possible, as the design of the vehicle is liable to change often. Whereas for more advanced stages of vehicle design, an accurate tool is desirable, to assess the design of the vehicle in detail.

The lowest fidelity, and highest efficiency methods include packages which use empirical relations derived from databases of existing vehicles, such as Missile Datcom[114], as well as panel method codes such as HYPAERO[12], cbaero[115] and HOTSOSE[116]. Low fidelity methods offer rapid solutions, with highly variable accuracy. For simple, standard vehicle shapes, low fidelity methods may offer high accuracy, as low fidelity solutions are usually calibrated to higher fidelity simulations or experiments. However, for complex vehicle geometries, for example geometries involving engine flow-paths, low fidelity models may be highly inaccurate, and are not acceptable for use[117].

Medium fidelity methods consist of inviscid Euler solvers such as Cart3D[118] and FUN3D[119], which are able to provide reasonable accuracy, with medium run times, by neglecting viscous effects within the solution. These solvers are often used in the later stages of preliminary design, or when higher fidelity is necessary due to design features, but rapid solutions are still desired. Neglecting the viscous effects in the fluid flow means that the solution obtained from an inviscid solver will only be an approximation of the real flow, and that the accuracy of the solution varies depending on the type problem being solved. For problems such as lift on a thin airfoil, inviscid Euler methods may be quite accurate, however for a problem such as boundary growth on a flat plate these methods will not accurately model the solution[120]. A particular advantage that many inviscid Euler codes provide is automatic adjoint mesh adaptation, the ability for the mesh to be automatically and rapidly generated, and updated sequentially throughout the solution process, refining areas of complex geometry or flow. This enables multiple solutions to be easily computed, without the need to regenerate meshes manually. For preliminary design purposes, inviscid-flow Euler CFD solvers are used extensively across industry and academia[121], as they are able to capture the lift and drag of an aircraft sufficiently well. However, inviscid solvers naturally do not capture the aerodynamic forces on a vehicle due to viscous effects. This deficiency can be corrected using an approximation of the viscous forces, to

improve the accuracy of the solution generated by an inviscid solver, while retaining the computation advantages of inviscid CFD[122].

High fidelity methods consist of Navier-Stokes CFD solvers such as Eilmer3/4[123], Fluent[124], CFX[125], COMSOL[126], TAU[127], and OpenFOAM[128]. These solvers will resolve the fluid flow and aerodynamic forces to a high level of accuracy, including viscous effects. However, the mesh for the problem must be generated prior to the calculation of the solution, which increases the working time significantly. Additionally, the computation times are much longer, and require more computational resources than lower fidelity methods. These factors make the generation of an aerodynamic database using high fidelity CFD an extremely time consuming process, which is suited for use on mature vehicle designs, or when accurate flow simulation is absolutely necessary. This is the case for the simulation of the internal flow paths of scramjet engines, which contain complex flow fields featuring high Reynolds-number flow, complex shock wave structures, and large thermal and composition gradients that strongly impact performance[129]. For this reason, scramjet engines must be simulated using high-fidelity methods to produce an accurate solution.

2.10.1 Cart3D

Cart3D is an inviscid Euler solver CFD package, designed for use during preliminary vehicle design and analysis[121]. Cart3D is computationally efficient and requires only a surface triangulation of the vehicle being analysed to initiate a simulation. Cart3D is utilised in this study due to its efficiency and ease of use, along with its demonstrated accuracy for hypersonic flow calculations[130–133]. Cart3D features adjoint mesh adaptation, and uses cartesian ‘cut-cells’ which intersect the surface, allowing complex geometries to be analysed automatically. The mesh automatically refines as the simulation progresses, reducing error. The absence of a requirement for a user generated mesh allows Cart3D to be easily applied to complex launch vehicle designs, as well as allowing for simple modification of control surface deflections and flight conditions. Cart3D has been used extensively for aerodynamic simulations in preliminary design, including analysis of the plumes of the Skylon spaceplane[134], HIFIRE-5[135], and in low sonic boom shape optimisations[132]. Cart3D has shown good agreement when compared to experimental results for winged boosters at hypersonic speeds[130], as well as supersonic missiles[131] and aircraft[132], and lifting bodies across wide Mach number ranges[133]. In addition, good agreement has been shown between Cart3D, experimental results, and full Navier-Stokes solutions for the HIFIRE-1 hypersonic test payload[130]. The model of the HIFIRE-1 and pressure coefficient results at each pressure tap are shown in Figure 2.22. Good agreement is shown between Cart3D and experimental results at all nearly all tested locations, with the exception at an identified area of shock-induced boundary layer separation, which an inviscid solution does not capture[130]. This indicates that Cart3D matches experimental results well in regions where the flow can be closely approximated by an inviscid analysis, however, regions of separation cause the accuracy of

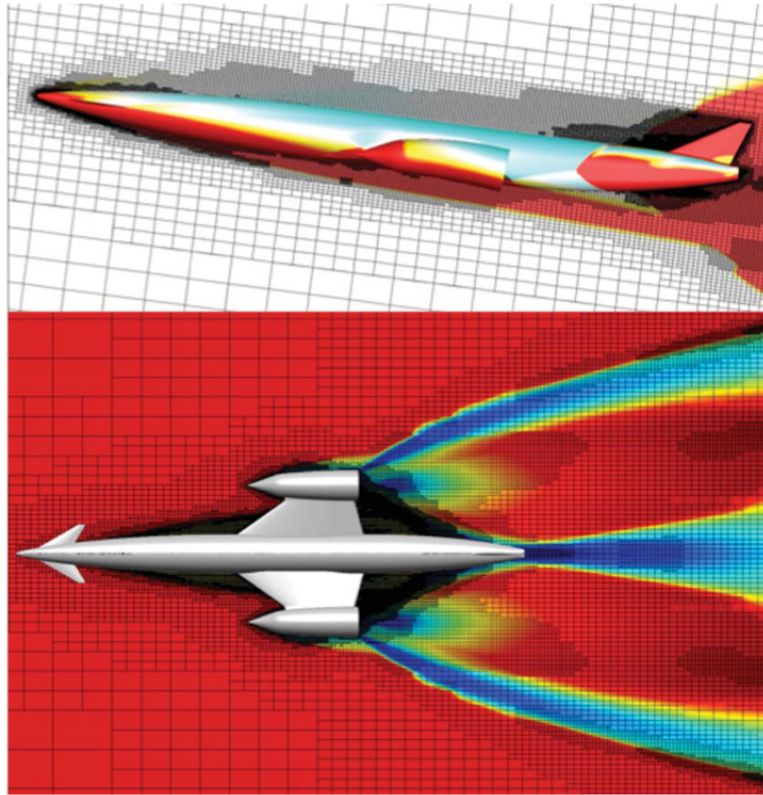


Figure 2.21: The Skylon spaceplane, simulated using Cart3D at Mach 12.189, $\alpha = 7.512^\circ$ [134]. Cell distribution produced by mesh adaptation is shown.

Cart3D to diverge significantly. Finally, in a comparison between Cart3D and the Overflow-D Navier-Stokes solver, it was shown that both codes produce similar pressure distributions for simulations of the space shuttle fuel tanks at low Mach numbers[136]. The Overflow-D simulations were stated to require at least 20 times more CPU time than Cart3D[136], an example of the efficiency afforded by Cart3D.

2.10.2 Missile Datcom

Missile Datcom is a widely used, semi-empirical, aerodynamic prediction tool for missile configurations. Missile Datcom is used in this study for its extremely high computational efficiency and ease of use, along with its proven accuracy[137]. Missile Datcom uses component-buildup methods by which the aerodynamics of each component of a missile or rocket design are estimated and then added together to determine the aerodynamics of the entire vehicle. Missile Datcom uses a combination of empirical and theoretical methods and is capable of calculating the aerodynamic forces, stability derivatives, and moments over a range of angle of attack and Mach number values. The high efficiency of Missile Datcom allows an aerodynamic database to be generated simply and rapidly. Missile Datcom has been shown to produce close agreement with experimental wind tunnel data

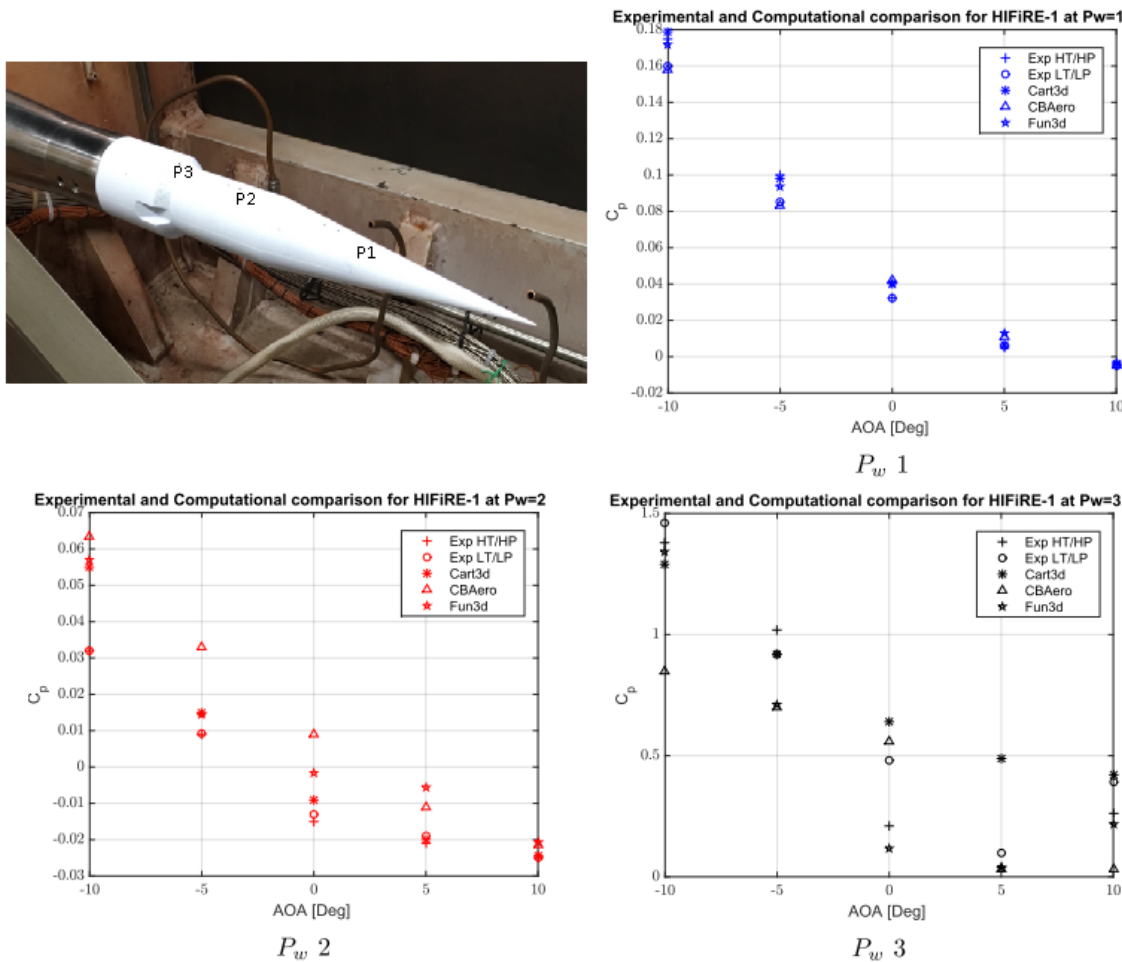


Figure 2.22: Comparisons of Cart3D with experimental data and the FUN3D Navier-Stokes CFD solver. P1, P2 and P3 indicate pressure tap locations. Modified from Sagerman et al.[130].

for normal force and pitching moment coefficients, and reasonable agreement for axial force coefficients[137].

2.11 Summary

This section provided a review of available literature, pertaining to the design and trajectory optimisation of a rocket-scramjet-rocket launch system. The background of the operation of scramjet engines was outlined, along with a brief historical view. Some detail was then provided on current reusable launchers, and the small satellite launchers which are currently operational or in development. Previous work on airbreathing launchers was detailed, and the ascent trajectories of these launchers have been assessed. Prior works suggest that the optimal trajectory for an airbreathing-rocket vehicle operating as a single stage involves a pull-up from maximum dynamic pressure, before the vehicle transitions from airbreathing to rocket power. This pull-up is also observed in some multi-stage vehicle

trajectories, performed in order to satisfy operational requirements, rather than specifically improving the performance of the launch system. The return trajectories of prior hypersonic launch systems have been investigated, and it was determined that a full glide-back of a vehicle is likely not possible without operation of the airbreathing engines. However, performing a ‘skipping’ manoeuvre may assist in maximising the glide range. The rocket-scramjet-rocket launch system being developed at The University of Queensland was detailed, along with the propulsion model used, and previous trajectory simulations. A study of exoatmospheric rocket engines was conducted, and the SpaceX Kestrel engine was found to exhibit the best performance-per-kg compared to other pressure-fed engines. The background of optimal control theory was outlined, and the specific optimal control techniques which are most applicable to trajectory optimisation were detailed, along with a survey of existing optimal control solvers. A survey into CFD solvers was conducted, and the specifics of Cart3D and Missile Datcom, which are utilised in this study, were detailed.

CHAPTER 3

LAUNCH VEHICLE DESIGN AND SIMULATION

In order to be competitive in the emerging small satellite market, a small satellite launcher must be cost-effective, reliable, and capable of launching on a flexible schedule. The inclusion of airbreathing engines within a small satellite launch system has the potential for improving cost effectiveness compared to disposable rocket-powered launchers, by allowing partial reusability of a launch system. The airbreathing engine most appropriate for small satellite launch systems is the scramjet engine, which operates efficiently within the hypersonic regime, with the capability to operate over a relatively large Mach number range compared to turbojet or ramjet engines. A launch system incorporating scramjets must necessarily include two rocket-powered flight stages: a first stage rocket to accelerate the system from launch to the minimum operational Mach number of the ramjet or scramjet engines, and a third stage rocket to accelerate the payload at exoatmospheric conditions and place it into the correct orbit. This chapter presents the design and modelling of a rocket-scramjet-rocket launch system in which the scramjet stage is reusable for multiple launches. This rocket-scramjet-rocket launch system is designed to launch satellites on the order of 200kg to a 567km altitude sun-synchronous orbit and is based on the SPARTAN scramjet accelerator developed by Preller & Smart [12]. The SPARTAN is a scramjet-powered accelerator being developed by The University of Queensland and Hypersonix, to launch small satellites as part of a rocket-scramjet-rocket launch system. The rocket-scramjet-rocket launch system described in this chapter is used as a representative model for an airbreathing, partially-reusable, multi-stage small satellite launcher.

The trajectory of a launch system involving scramjet propulsion is significantly different to that of a fully rocket-powered launch system, due to the requirement for the scramjet stage to fly within the atmosphere. Figure 3.1 shows a simplified representation of the launch trajectory for the vehicle simulated in this study. The launch system is launched vertically under rocket power, from a traditional small rocket launch facility. The SPARTAN is mounted to the front of the first stage rocket allowing

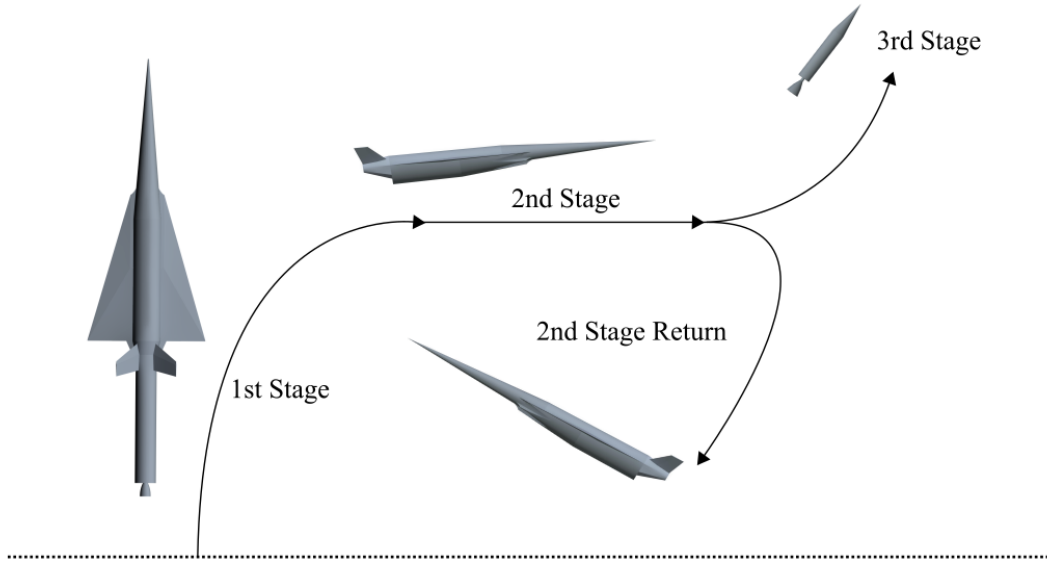


Figure 3.1: The launch process of the rocket-scramjet-rocket launch system, presented in simplified form.

the SPARTAN to take the brunt of the aerodynamic forces and heating, as well as allowing the use of the control surfaces of the SPARTAN. During first stage rocket operation, the launch system pitches rapidly, reaching close to horizontal flight to allow the SPARTAN to stay at high dynamic pressure conditions. The SPARTAN is accelerated to its minimum operating velocity of approximately Mach 5, at which point separation occurs. The SPARTAN's four scramjet engines are ignited, and The SPARTAN is accelerated through the atmosphere, reaching approximately Mach 9. At this point, the specific impulse of the scramjet engines, and thus the efficiency of the SPARTAN, have decreased, and the third stage rocket is separated. The third stage rocket accelerates and performs a pull-up, before cutting its engine and coasting out of the atmosphere. Once the rocket is exoatmospheric, the engine is reignited, performing first a circularisation burn, and then a Hohmann transfer to the intended orbit. Meanwhile, the SPARTAN banks and executes a fly-back manoeuvre to return to its initial launch site. The SPARTAN extends landing gear, and lands on a traditional runway in the style of a conventional aircraft. The SPARTAN is able to be rapidly refurbished and remounted for further launches. To fulfil the requirements of this trajectory, The SPARTAN must be able to fly and manoeuvre from velocities greater than Mach 9 to landing, as well as being able to withstand high structural and heating loads without significant deterioration.

The launch configuration of the three stage launch system incorporating the SPARTAN is shown in Figures 3.2 & 3.3. The size and external design of the SPARTAN scramjet accelerator are used exactly as defined for the Baseline SPARTAN vehicle designed by Preller & Smart[12]. Both the

first and third stage rockets are designed in this study, and are sized around the baseline SPARTAN vehicle. The first stage rocket has not previously been designed, and as such is created for this study, while the third stage is redesigned to use a SpaceX Kestrel engine. This third stage design replaces the third stage used in previous SPARTAN studies, which was powered by a Pratt & Whitney RL-10-3A engine[12]. The pump-fed RL-10-3A engine was deemed to costly, and it has been replaced by a significantly cheaper pressure-fed Kestrel engine in this study. The internal layout of the SPARTAN has been reconfigured around this redesigned third stage. The SPARTAN design is presented first, as the design of the SPARTAN drives the operational requirements and sizing of the launch system, and thus the design of the first and third stage rockets.

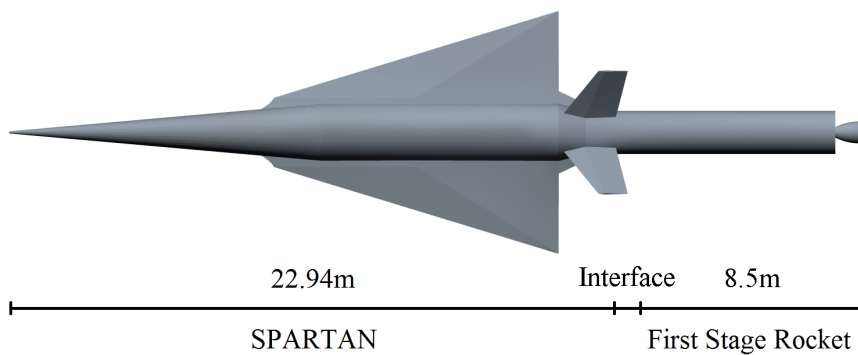


Figure 3.2: The rocket-scramjet-rocket launch system, top view, showing the SPARTAN and first stage.



Figure 3.3: The rocket-scramjet-rocket launch system, side view, showing the SPARTAN and fuel tanks, along with the third and first stages.

3.1 Second Stage Scramjet

3.1.1 The SPARTAN Accelerator

The SPARTAN vehicle, shown in Figure 3.4, is based on the work by Preller & Smart [12]. The SPARTAN is 22.94m long, with a frontal cone half angle of 5° [12]. A mass breakdown of the SPARTAN is shown in Table 3.1, adapted from[12]. The fuel tank sizes and total fuel mass are sized to accommodate the Kestrel-powered third stage, described in Section 3.3. This study assumes that the

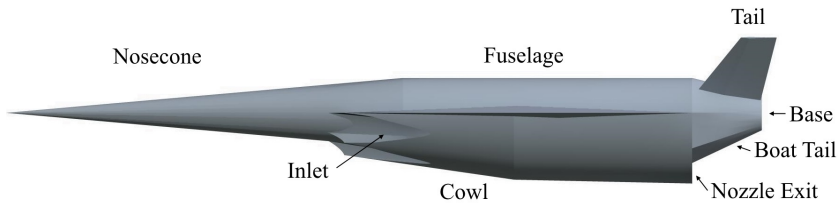


Figure 3.4: The features of the SPARTAN.

Part	Fuselage	Wings	Tanks	Systems	Landing Gear	Scramjets	Fuel
Mass (kg)	2861.6	350.7	179.4	707.5	188.9	669.0	1562.0

Table 3.1: Mass breakdown of the modified SPARTAN vehicle.

third stage is stored within the fuselage of the SPARTAN for simplicity. It is assumed that the release mechanism for the third stage is able to be situated within the available space surrounding the third stage, however the release mechanism is not considered further in this study.

The fuel tanks are sized to fit around the kestrel-powered third stage. There are three fuel tanks; two cylindrical tanks situated underneath the third stage; and a truncated conical tank in the nose. The conical fuel tank is designed to fit immediately forward of the third stage. This fuel tank is 8m long, leaving 1.47m³ of space in the nose for cooling systems, frontal landing gear, and any additional systems or sensors which are necessary in the nose cone. The cylindrical tanks are positioned underneath and slightly to either side of the third stage, leaving space underneath for vehicle systems. The cylindrical fuel tanks are designed to be 8.5m long, with diameters of 0.87m, sized to give a nominal total tank volume of 22m³. The resized fuel tanks hold a total of 1562kg of LH2 fuel. This assumes an LH2 density of 71kg/m³, slightly denser than LH2 at phase transition point at 1 atm. The mass of the fuel tanks is scaled, by area, from Dawid Preller's Baseline vehicle model of the SPARTAN[12], giving a total fuel tank mass of 179.4kg.

3.1.2 Propulsion

The SPARTAN is powered by four underslung scramjet engines, fuelled by liquid hydrogen. These engines are Rectangular To Elliptical Shape Transition (REST) engines, configured to allow for a conical forebody (C-REST). REST engines have a rectangular to elliptical shape transition inlet, and an elliptical combustor, offering simplicity in design as well as reduced thermal loading and viscous drag compared to scramjets with planar geometries [138]. REST engines are also specifically designed to operate over a wide range of Mach numbers, and at off design conditions, making them particularly applicable to use on scramjet accelerator vehicles.

Propulsion Modelling

The thrust generated by the C-REST engines determines how rapidly the SPARTAN accelerates, and the efficiency of the engines determines how rapidly fuel is consumed, and influences the separation point of the third stage rocket. The C-REST engines are simulated separately to the aerodynamic simulations of the SPARTAN, using a combination of quasi-1D and high fidelity CFD simulations[12, 77]. The engine model takes the conditions at the inlet, and calculates the exit conditions and propulsive properties of the engine. The engine exit conditions are added into the aerodynamic simulations and the propulsive properties are used in the simulated vehicle model.

Before the flow enters the engine, it is affected by the conical shock generated by the forebody of the SPARTAN. Figure 3.5 shows the locations of the flow properties, which are necessary to calculate engine performance. The ambient atmospheric conditions are calculated by interpolation using the 1976 NASA Atmospheric properties[139]. The flow properties at the inlet of the engines is calculated using the Taylor-Maccoll analysis method for conical shocks[140]. This calculation is performed in the cone_shock program provided for this study by Prof. Michael Smart. The flow conditions as a function of flight conditions following the conical shock are shown in Figure 3.6.

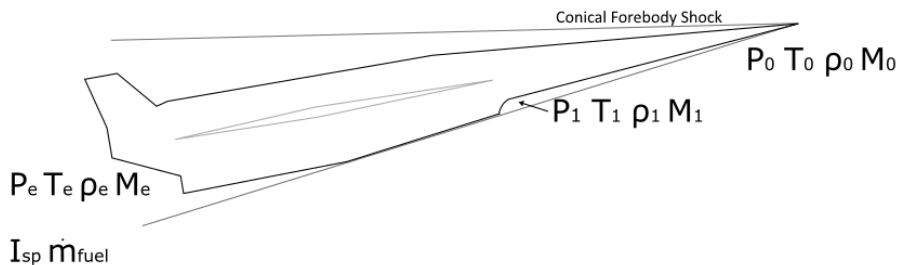


Figure 3.5: The locations of conditions relevant to C-REST engine simulation.

The engine model used is based on the C-RESTM10 database[12, 77], analysed using quasi-1D simulation and provided for this study by Prof. Michael Smart. This database has previously been used in simulations of the SPARTAN, as detailed in Section 2.7.1. This database provides data points of engine performance over inlet conditions within the operational range, at 50kPa dynamic pressure equivalent conditions. The specific impulse data set is shown in Figure 3.7. This data is interpolated for the given inlet conditions, to calculate specific impulse produced by the engine. As the data points of the C-REST database are unevenly distributed for inlet Mach and temperature, care must be taken in order to interpolate smoothly to allow the optimal control solver to converge successfully. To ensure that smooth interpolation is achieved, the C-REST database is first interpolated using linear interpolation, for each ‘set’ of four nodes which form a square. A uniform grid is created using this linear interpolation, on which a cubic spline interpolation is applied using Matlab’s grid-dedInterpolant function. This is explained in detail in Appendix A. During flight the C-REST inlet conditions generally stay within the region bounded by the available data. However, for the purposes

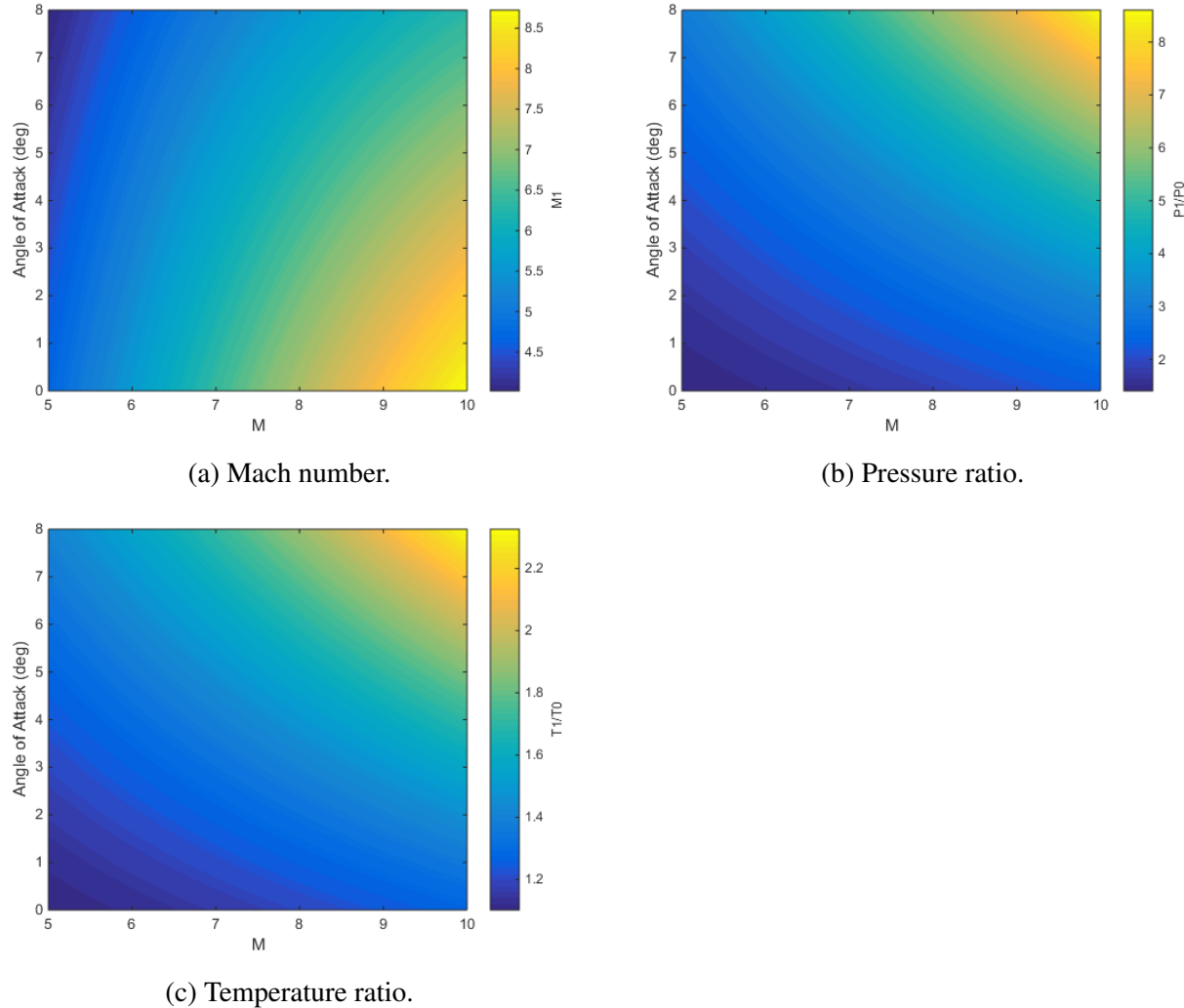


Figure 3.6: Flow conditions after the conical shock generated by the vehicle nose cone as a function of flight Mach number and angle of attack. Figure a) shows the Mach number, b) shows the pressure ratio, and c) shows the temperature ratio following the conical shock, at the engine inlet.

of the trajectory optimisation, it is necessary to provide data for a wide range of inlet conditions (T_1 , M_1). To calculate ISP and equivalence ratios outside of the modelled range of inlet conditions, the existing data is extrapolated. This extrapolation is performed in the same manner as the interpolation, a linear extrapolation, followed by a cubic spline interpolation of the extrapolated points. This allows for smooth continuity between the interpolated and extrapolated points, while ensuring that the extrapolated regions provide reasonable values.

For operation at high Mach numbers, the fuel mass flow rate is assumed to be stoichiometric, so that $\dot{m}_f = 0.0291\dot{m}$. This ensures that the scramjet engines are performing at high efficiency throughout the acceleration of the scramjet stage. However, the C-REST engine is a fixed geometry engine,

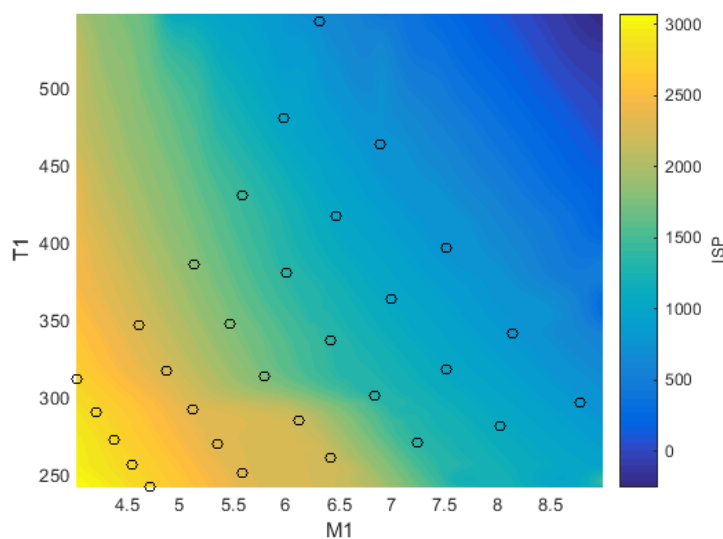


Figure 3.7: Specific impulse of the CRESTM10 engines with input temperature and Mach number. Available data points are indicated.

primarily designed for operability at high Mach numbers[12]. At lower Mach numbers, the addition of excessive fuel may cause the engine to choke and unstart, resulting in total loss of thrust[12]. To avoid unstart, an equivalence ratio (ϕ) of less than 1 is necessary at low Mach numbers. In this region the equivalence ratio is set to the maximum value which does not cause the engine to unstart. The equivalence ratio interpolation is linear, as the number of data points available for interpolation is low. The prescribed equivalence ratio over the range of SPARTAN operation is shown in Figure 3.8. For these conditions, the fuel mass flow rate is determined by approximating the flow into the inlet as an ideal gas;

$$\dot{m} = 0.9m_c A_{cap} P_0 M_0 \sqrt{\frac{\gamma_0}{R_{air} T_0}}, \quad (3.1)$$

$$\dot{m}_{fuel} = \left(\frac{m_{fuel}}{m_{ox}}\right)_{st} \phi \dot{m}. \quad (3.2)$$

The multiplier of 0.9 is an approximate term included to account for losses due to asymmetry within

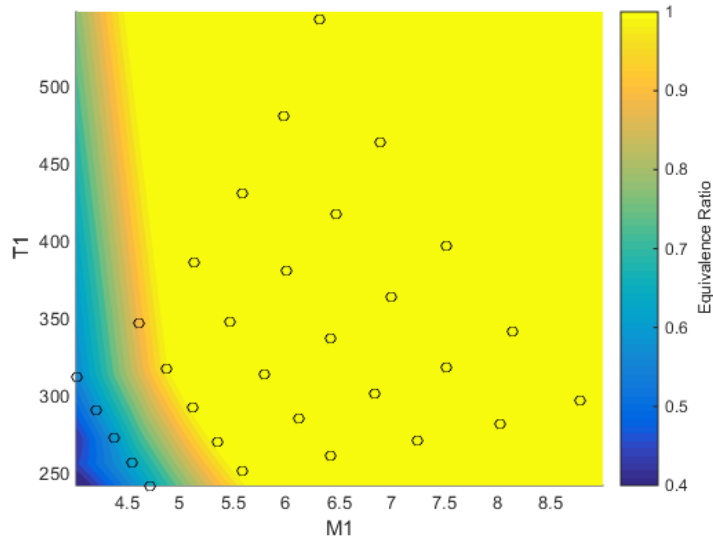


Figure 3.8: Operable equivalence ratio of the CRESTM10 engines with input temperature and Mach number. Available data points are indicated.

the engine[77]. The thrust for each engine, T , is obtained by inclusion of the interpolated specific impulse, ie.

$$T = g_0 \dot{m} I_{sp}. \quad (3.3)$$

In the available database, the C-REST engine was modelled to a nozzle exit area of 0.5586m^2 . This is smaller than the exit area modelled on the version of the SPARTAN used in this work, of 0.9719m^2 . For this reason, additional thrust is obtained from an additional nozzle segment, and the specific impulse of the C-REST engines will be higher than calculated in the database. The modelling of this additional nozzle segment and the thrust obtained are detailed in Section 3.1.3.

3.1.3 The Aerodynamics of the SPARTAN

In order for the trajectory of the SPARTAN to be successfully simulated and optimised, the aerodynamics of the SPARTAN must be calculated for the large range of flight conditions experienced during its acceleration and return flights. The aerodynamics of the SPARTAN are calculated at set flight conditions covering the breadth of necessary conditions, and the results are tabulated in databases. During trajectory simulations, the aerodynamics of the SPARTAN are determined by interpolation over the aerodynamic databases using bivariate splines, and the drag and lift produced are calculated using the standard definition of the aerodynamic coefficients:

$$F_d = \frac{1}{2} \rho c_d v^2 A, \quad (3.4)$$

$$F_L = \frac{1}{2} \rho c_L v^2 A. \quad (3.5)$$

The trimmed aerodynamic databases of the SPARTAN are generated in full prior to trajectory simulation to improve the computational efficiency of the simulation. The aerodynamic coefficients of lift, drag and moment are tabulated, and these tables are interpolated during simulation. The aerodynamics are calculated for Mach numbers between 0-10, angles of attack between 0° and 10° , and for altitudes between 0-40km. Separate aerodynamic simulations are performed for engine-on and engine-off conditions, as the operation of the scramjet engines changes the aerodynamic characteristics of the SPARTAN significantly. When the engines are powered-on, the engines are generating thrust on the internal nozzle, as well as on the boat tail and base. When the scramjet engines are not operational air flows through the engine flowpath without fuel injection, generating a large amount of drag.

The process for generating the aerodynamic databases is shown in Figure 3.9. First, a CAD model of the SPARTAN is developed, providing the centre of gravity of the SPARTAN, as well as a geometry database which is used to create triangulated surface meshes. These surface meshes are then imported into the inviscid CFD solver Cart3D[118], which calculates flow solutions to determine the aerodynamics of the SPARTAN at various flight conditions. CFD solutions are generated for the SPARTAN with the scramjet engines turned off, as well as with the scramjet engines operational, and for a range of flap deflections. The flap deflections necessary to trim the vehicle are calculated at every flight condition, by balancing the aerodynamic moment of the SPARTAN with the aerodynamic moment generated by the flaps. The additional lift and drag generated by the flaps are then added to the untrimmed aerodynamics to create a trimmed database. Finally, the viscous components of the aerodynamics of the SPARTAN are calculated, and added to the aerodynamic database. These processes are described in detail in the following sections.

Cart3D Simulations

The aerodynamics of the SPARTAN have been calculated using Cart3D, an inviscid CFD package used in the preliminary design of aerospace vehicles. Cart3D utilises adjoint mesh adaption with a Cartesian cut-cells approach to produce an iteratively refined mesh to fit a flow solution. Cart3D is used to generate the aerodynamic database of the SPARTAN vehicle due to its applicability in both the subsonic and supersonic regimes, and its robustness across multiple flow solutions[130–133, 136]. Cart3D has previously been used to analyse hypersonic vehicles, and has shown good agreement with experimental data across multiple studies[130–133], as described in Section 2.10.1.

Initially, a surface triangulation of the SPARTAN is created in Pointwise, shown in Figure 3.10. This is then imported into CART3D as a watertight surface. The Cart3D Meshes are then initiated with an outer boundary distance of 40 times the vehicle length. This boundary distance has been observed

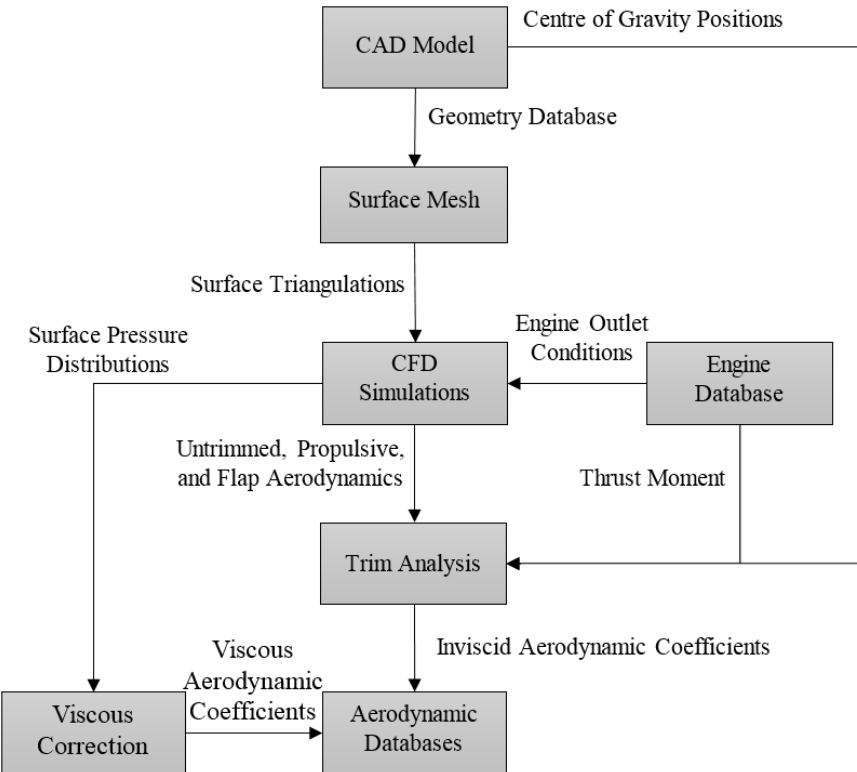


Figure 3.9: The process for generating aerodynamic databases.

to produce suitable free stream conditions and good mesh convergence. Nine mesh adaption levels are used. Nine levels have been observed to generally produce good convergence, with moderate computation times of 1-3 hours per simulation. The convergence of the residuals and forces are investigated to ascertain if a solution has converged. Figure 3.11 shows an example solution validation for Mach 6, 2° angle of attack, engine-on conditions. Good convergence can be observed in the force functionals, with a corresponding decrease in the error estimate of the functional indicating solution convergence.

Following simulation in CART3D over the required flight conditions, the aerodynamic coefficients are extracted. The simulation files are processed using Clic, a subprogram of CART3D used to calculate aerodynamic forces and moments, given surface pressure distributions. For engine-off aerodynamics, the aerodynamic coefficients of the entire SPARTAN are extracted. However, for the engine-on aerodynamics of the SPARTAN, the engine flowpath, boat tail and base of the SPARTAN are removed when the aerodynamic coefficients are extracted. The flowpath of the scramjet engines is assumed to be replaced by the conditions given by the C-RESTM10 engine database, and a separate Cart3D simulation is used to calculate the aerodynamic forces on the boat tail and base.

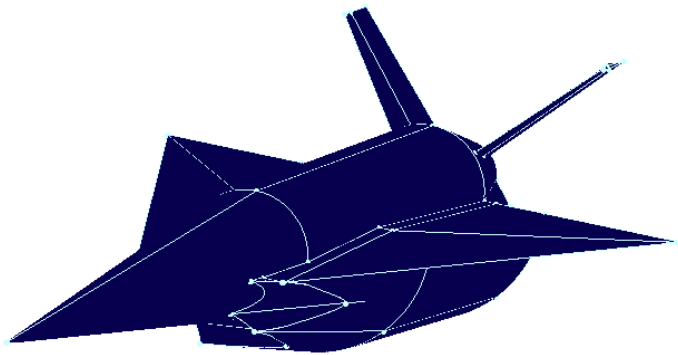


Figure 3.10: Surface triangulation of the Baseline SPARTAN, generated using Pointwise[141].

Engine-On Aerodynamic Analysis

When the scramjet engines are turned on, the exhaust exits the nozzle of the engines and expands onto the boat tail of the SPARTAN. This changes the aerodynamics of the boat tail significantly, necessitating separate Cart3D simulations to calculate the varied aerodynamic coefficients of the boat tail. In addition, the scaled engine modelled in the CRESTM10 propulsion analysis has an exit area of 0.5586m^2 , smaller than the nozzle exit area on the SPARTAN, of 0.9719m^2 . The larger nozzle exit of the SPARTAN provides additional expansion area, and additional thrust, which must be modelled using Cart3D.

The exhaust of the C-REST engines is simulated using CART3D, using SurfBC boundary conditions, which produce outflow and inflow conditions at the inlet and exit of the scramjet engines[142]. The exit conditions calculated by the C-RESTM10 database, as defined in Section 3.1.2, are set as the inflow conditions for the Cart3D surface. The inflow surfaces are positioned inside the nozzle on the SPARTAN model, scaled to match the exit area of the engines simulated for the C-RESTM10 database, 0.5586m^2 . The surface triangulation of the SPARTAN with outflow surfaces is shown in Figure 3.12. Cart3D performs simulations nondimensionally, and requires the outflow conditions of a boundary to be normalised. The outflow conditions of P_e , ρ_e and M_e given by the C-RESTM10 propulsion model are normalised to Cart3D nondimensionalised variables as follows[143, 144];

$$P_e^* = P_e / (\gamma_0 P_0), \quad (3.6)$$

$$\rho_e^* = \rho_e / \rho_0, \quad (3.7)$$

$$M_e^* = \sqrt{\gamma_e / \gamma_0 (M_e \sqrt{P_e^* / \rho_e^*})^2}. \quad (3.8)$$

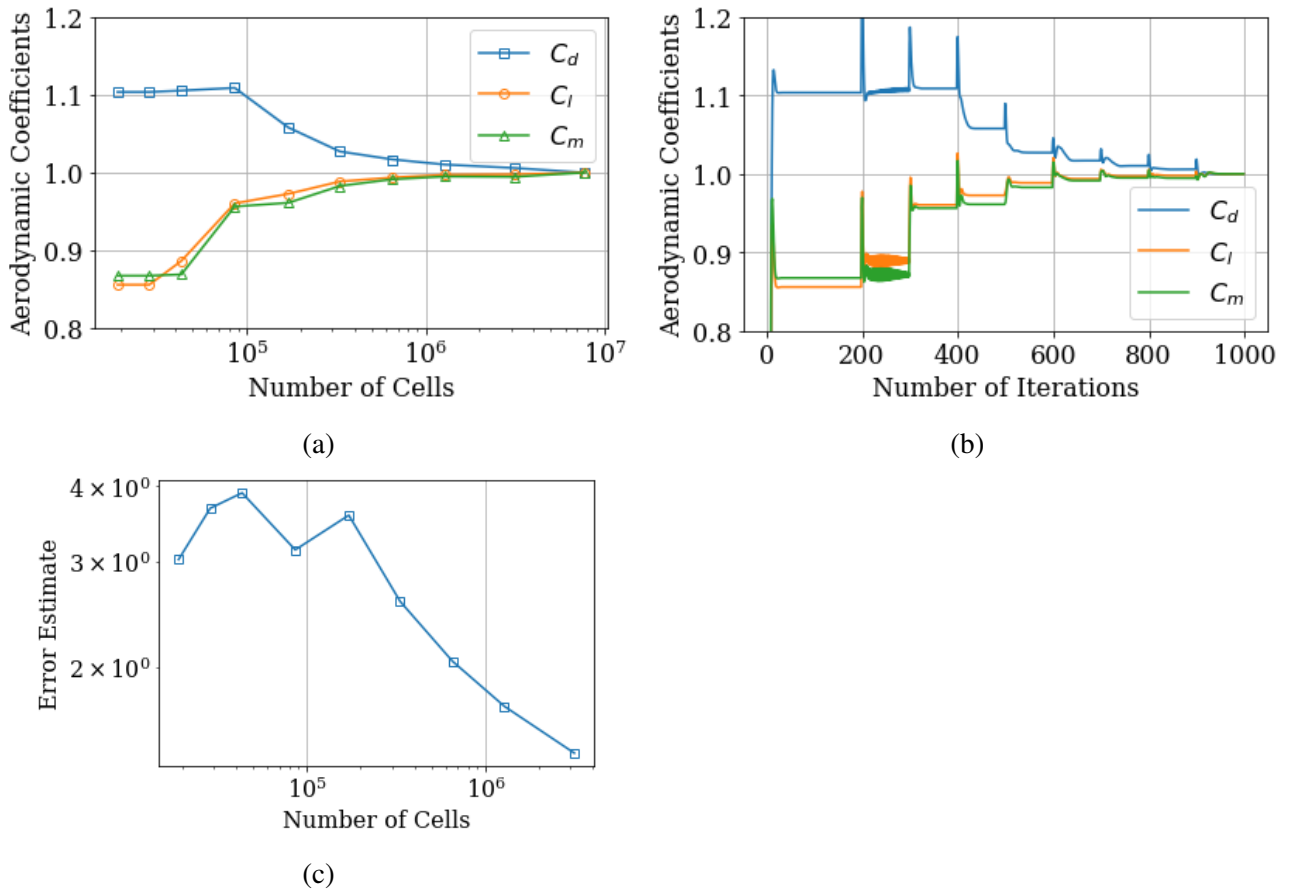


Figure 3.11: The convergence of a Cart3D simulation.

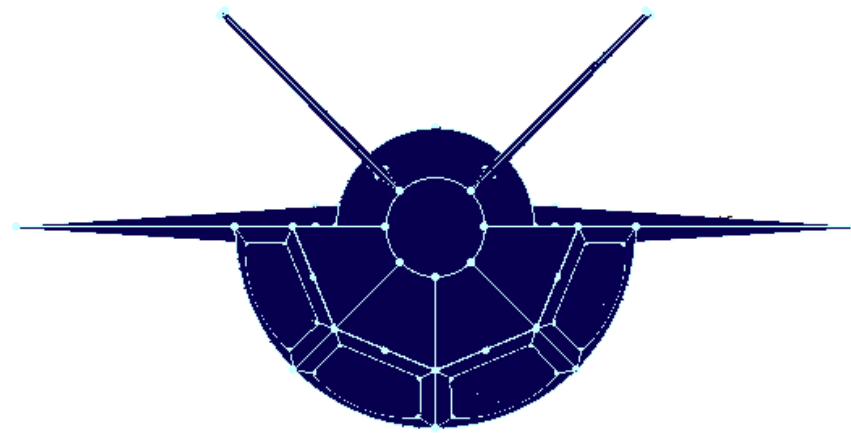


Figure 3.12: View of the SPARTAN surface triangulation showing engine outlet boundaries.

Where * indicates the nondimensionalised input to Cart3D. This nondimensionalisation includes a correction on the Mach number to account for variation in the specific heat ratio, which is not possible to include directly in Cart3D[134]. The exhaust of the scramjet engines expands through the additional area of the SPARTAN’s nozzle, and is further expanded onto the boat tail on the rear of the SPARTAN fuselage. This expansion causes significant force on the boat tail of the SPARTAN, generating additional lift, thrust, and moment forces. The total thrust generated by the SPARTAN, including the thrust generated by the additional nozzle expansion, and the forces on the boat tail, are shown in Figure 3.13, with the corresponding specific impulse shown in Figure 3.14.

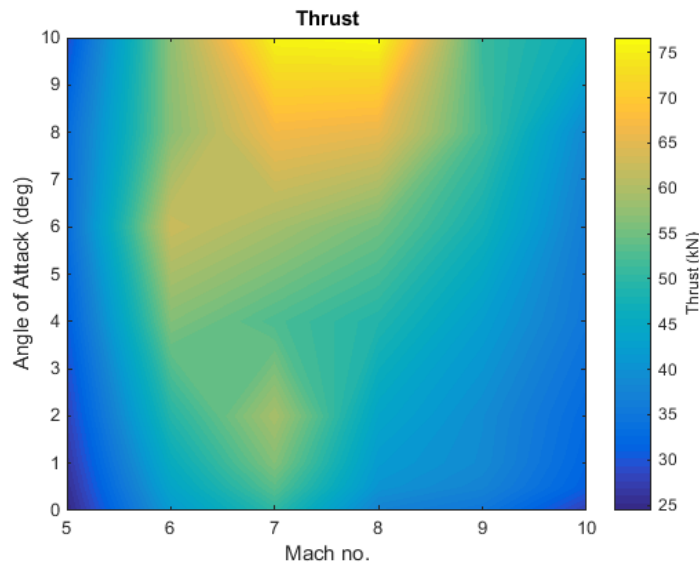


Figure 3.13: The total thrust output of the SPARTAN, including the C-REST database, and Cart3D nozzle and boat tail simulations.

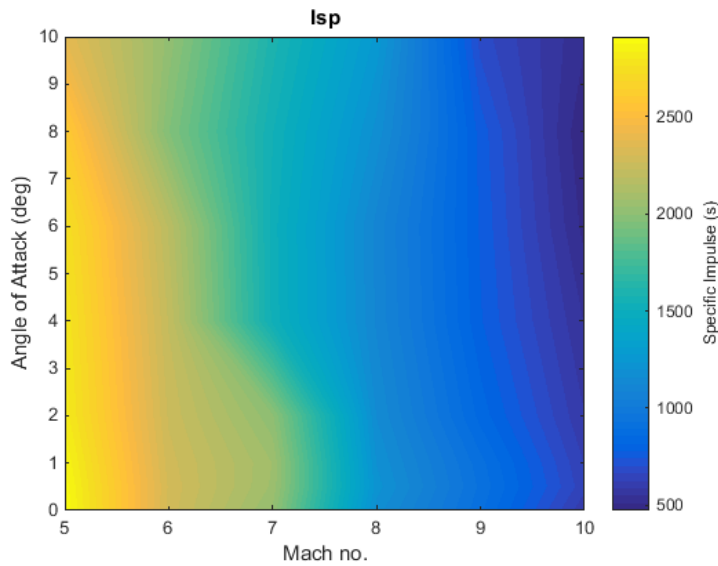


Figure 3.14: The specific impulse of the SPARTAN, including the C-rest database, and Cart3D nozzle and boat tail simulations.

Centre of Gravity Analysis

The centre of gravity locations of the SPARTAN are calculated using CREO. For simplicity, it is assumed that structural, systems and landing gear masses are homogeneously distributed throughout the centre fuselage of the SPARTAN. The calculated centre of gravity for the SPARTAN full of fuel and including the third stage rocket is 15.23m along the body length. The centre of gravity varies as fuel is depleted throughout the acceleration phase, and at third stage release, changing the flap deflections required for trim. The cylindrical fuel tanks are depleted first, in order to shift the centre of gravity forward, and improve the aerodynamic stability of the SPARTAN during the majority of flight. Depleting fuel from the cylindrical fuel tanks first would likely also serve to reduce fuel slosh during flight, although the fuel slosh is not modelled in this study, and it is assumed that the centre of gravity of each individual tank remains constant. After the cylindrical tanks have been depleted, the fuel in the conical tank within the nose is used. The third stage is released at the end of acceleration, and the centre of gravity changes significantly. When the third stage is released there is still fuel stored in the conical tank for flyback, during which centre of gravity change must also be modelled. Consequently, aerodynamic databases are created for centre of gravity conditions of;

- full of fuel including third stage,
- conical fuel tank full of fuel, including third stage,
- empty of fuel including third stage,
- conical fuel tank full of fuel after third stage release,

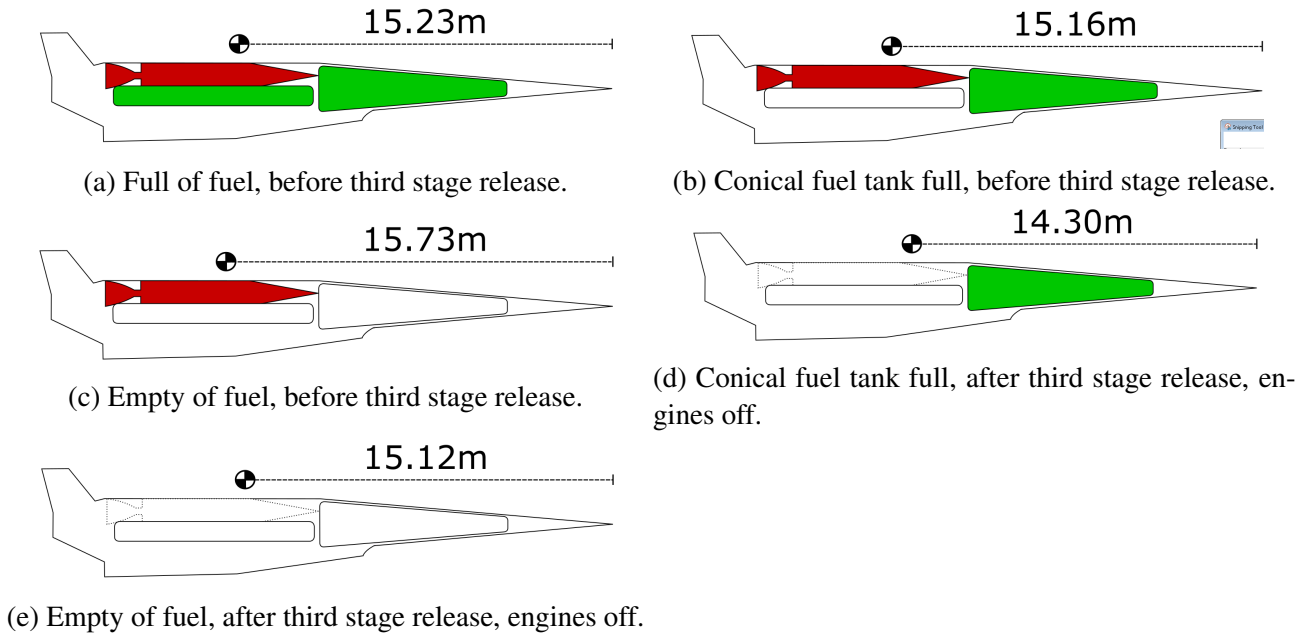


Figure 3.15: Centre of gravity positions throughout the flight of the SPARTAN.

- and empty of fuel after third stage release.

Each of these conditions, along with the corresponding centre of gravity, is shown in Figure 3.15. At each of the listed centre of gravity conditions, aerodynamic coefficients and flap deflections necessary for trim are calculated. As each fuel tank is depleted, and the centre of gravity shifts, the aerodynamics at the two closest centre of gravity conditions are interpolated to produce the aerodynamics of the SPARTAN.

Calculation of Trimmed Flap Deflections

The SPARTAN as designed by Preller[12] is trimmed using control surfaces on the wings, shown in figure 3.16. The flaps of the SPARTAN are modelled at deflected states of -20° , -10° , 10° , and 20° . Each of these deflected states are modelled in CREO and a surface mesh is created in Pointwise. Cart3D is used to simulate each of these flap deflected states, and Clic is used to extract the aerodynamic coefficients, for Mach numbers between 0.2 and 10. These aerodynamic coefficients are tabulated, and interpolation splines fitted, so that the flight Mach number and the moment generated by the flaps are used to interpolate for the flap deflection, ie. $\theta_{Flaps} = f(M, M_{Flaps})$. Trim is determined by calculating the aerodynamic moment coefficient with zero flap deflection, then calculating the flap deflection necessary to balance the aerodynamic moments to zero. The moments generated by the untrimmed SPARTAN, as well as the thrust moments on the engines and boat tail when the C-REST engines are powered-on, are balanced by the moment generated by the flaps, so that:

$$M_{Flap} = -M_{Untrimmed} \quad (3.9)$$

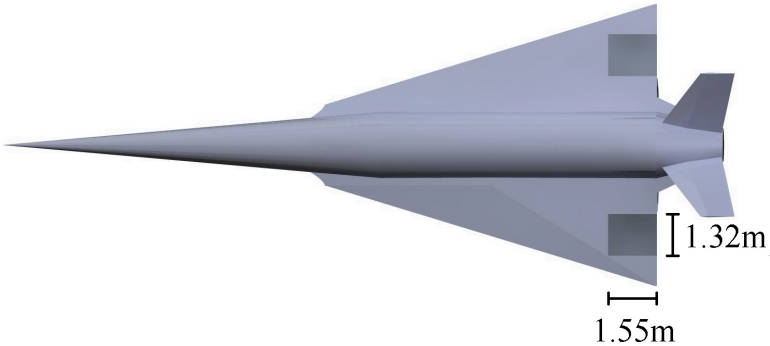


Figure 3.16: SPARTAN model showing control surfaces.

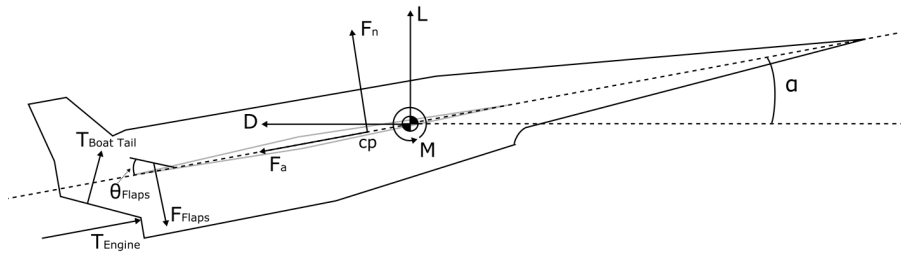


Figure 3.17: The forces on the SPARTAN during flight.

The flap deflections necessary for trim are shown in Figure 3.18, calculated for Mach numbers between 0.2 and 10, and at angles of attack from 0° to 10° . Engine-on flap deflections are shown at centre of gravity locations corresponding to full-fuel, full conical tank, and empty conditions with the third stage included, and engine-off flap deflections are shown at the centre of gravity corresponding to a fuel-empty condition after third stage release. The flap deflections are designated as negative up. Negative flap deflection necessary for trim indicates that the centre of pressure is aft of the centre of gravity, and that the vehicle has positive static margin. It can be observed that while the cylindrical fuel tanks are being used, the SPARTAN is generally stable at low angles of attack, and the static margin is close to 0, requiring only small flap deflections for trim. As the fuel in the conical tank is depleted, the centre of gravity moves aft, and the SPARTAN develops a negative static margin, requiring larger flap deflections to trim at high Mach numbers. These large flap deflections indicate that the SPARTAN may experience instability issues at the end of its acceleration, however, determining the controllability of the SPARTAN is outside the scope of this study.

Once the flap deflections necessary to trim the SPARTAN are calculated, the additional lift and drag produced by the flaps are added to the aerodynamic database, ensuring that the SPARTAN is trimmed at every flight condition. Trimmed aerodynamic databases are calculated for engine on and engine off conditions, as well as at all centre of gravity locations listed previously.

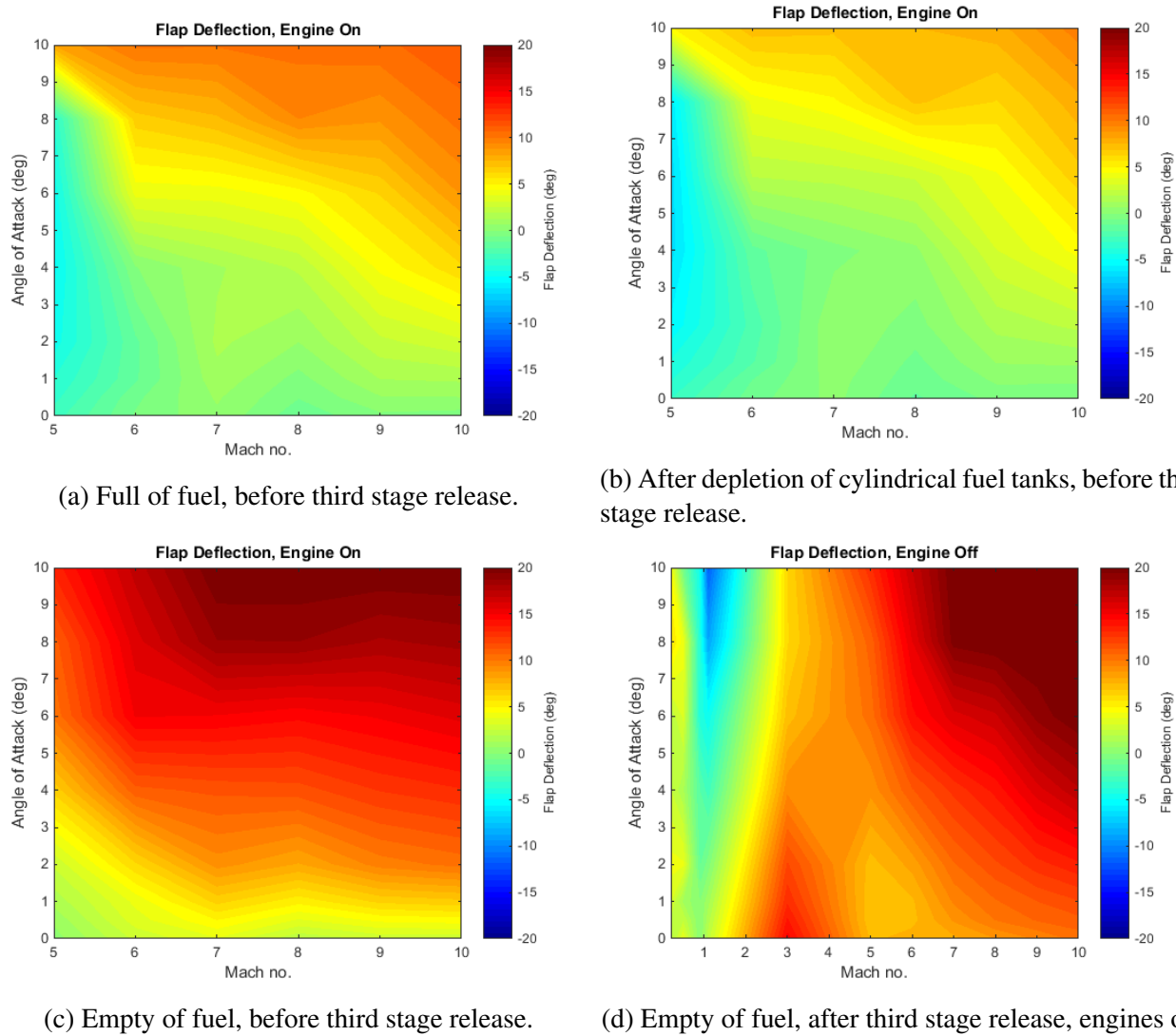


Figure 3.18: Flap deflection required for trim of the SPARTAN. Negative up.

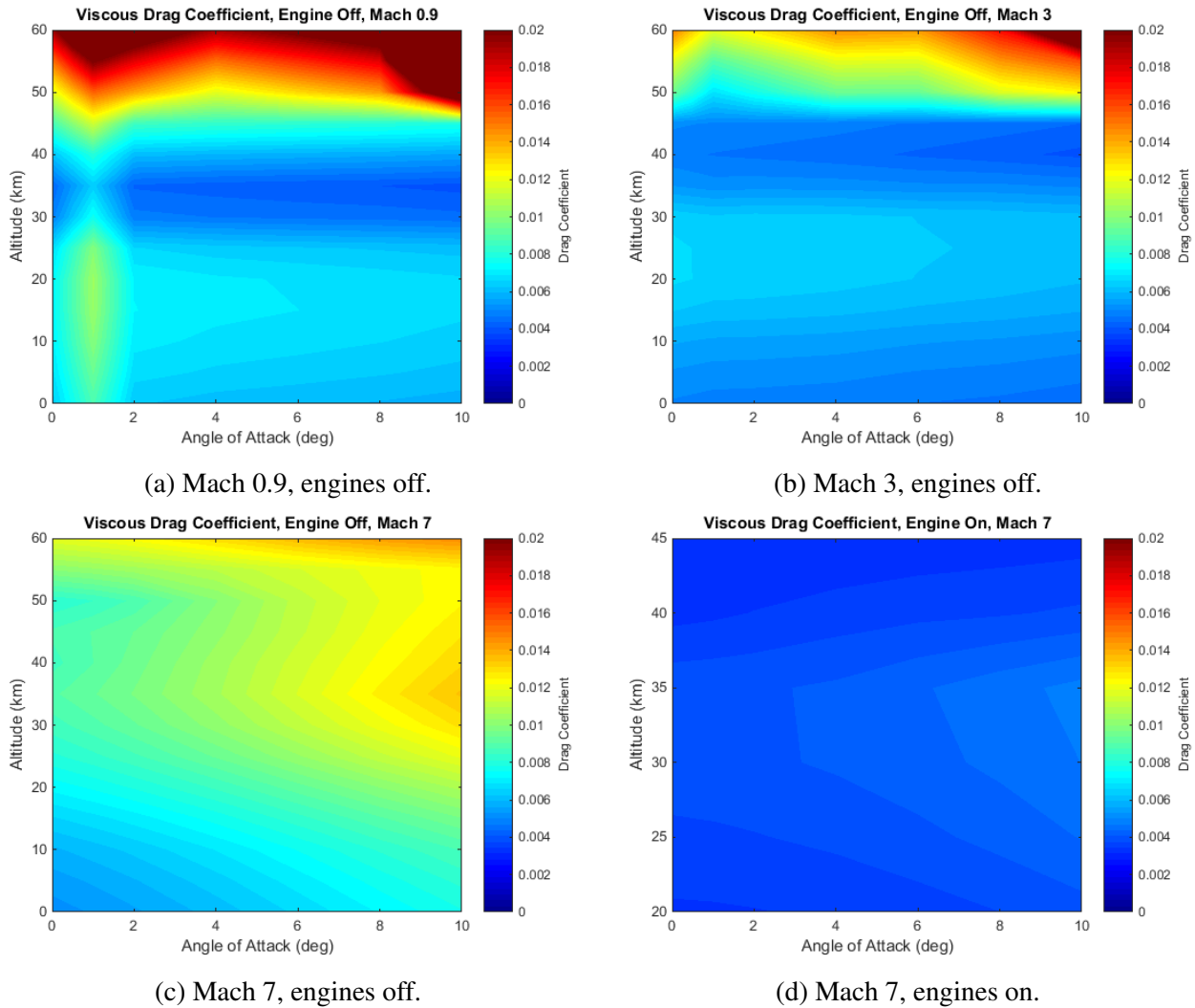


Figure 3.19: Viscous drag coefficient across various Mach numbers.

Viscous Correction

As Cart3D is an inviscid solver, the aerodynamic database generated by Cart3D lacks the forces generated by skin friction drag. In order for the aerodynamic model to more closely approximate realistic dynamics, a correction for the viscous forces on the SPARTAN is calculated, using the inviscid Cart3D cases. This inviscid correction utilises flat plate correlations for skin friction on each surface cell, employing a simplified running length based on the Euclidean distance to the respective stagnation feature. Further details of this method can be found in Reference [122]. This method has been shown to significantly improve upon the accuracy of the aerodynamic coefficients calculated by Cart3D for multiple test vehicles [122]. The viscous drag coefficients are generated for the SPARTAN at every Mach number and angle of attack which are simulated in Cart3D. Viscous databases are generated for both engine-on and engine-off cases, for altitudes of 20-45km and 20-60km respectively. The viscous drag coefficients for selected flight conditions are shown in Figure 3.19.

3.1.4 Trimmed Aerodynamic Database of the SPARTAN with Engine-On

The engine-on aerodynamics of the SPARTAN are used during the simulation of the acceleration phase, when the C-REST engines are operational at all times, as well as during the fly-back phase, when the engines are operational for a short time to aid the SPARTAN in returning to its initial launch site. The external aerodynamics of the SPARTAN with the scramjet engines powered-on are calculated by removing the engine and boat tail from Cart3D simulations of the SPARTAN with engine flowpaths. Engine-on aerodynamic calculations are performed for Mach numbers 5, 7, 9 and 10. An example of a Cart3D solution of the nozzle exit and boat tail with the scramjet engines powered-on is shown in Figure 3.20, and the aerodynamics of the SPARTAN with engines powered-on are shown in Figure 3.21.

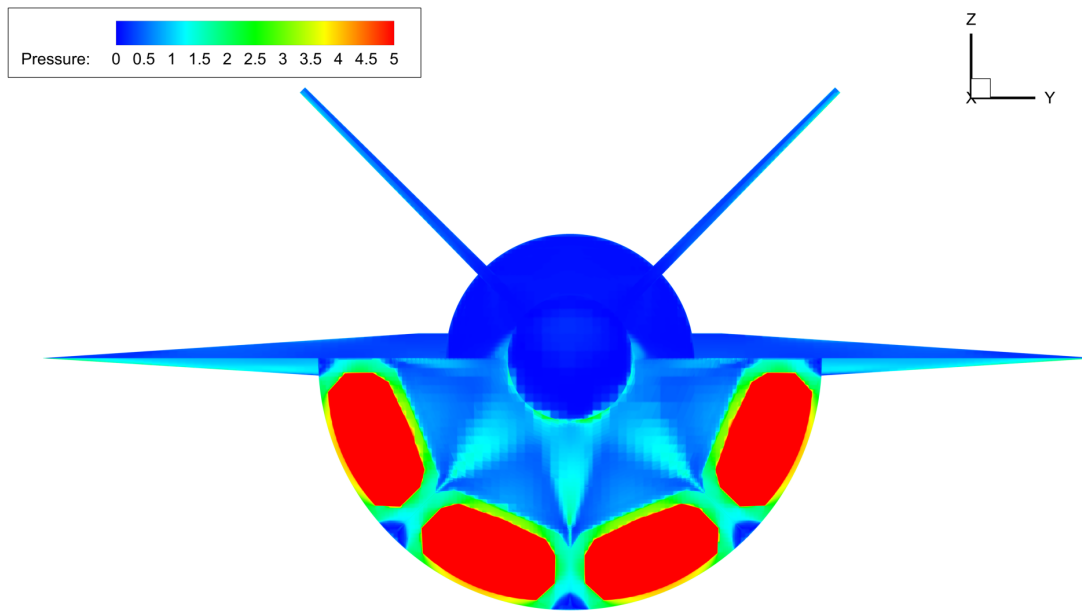


Figure 3.20: Engine-on Cart3D simulation at Mach 6, 2° angle of attack, and 25km altitude.

3.1.5 Trimmed Aerodynamic Database of the SPARTAN with Engine-Off

During the majority of the return flight, the scramjet engines are not operational, and the SPARTAN is gliding without power. The return phase takes the SPARTAN from third stage separation, at approximately Mach 9, to landing approach at low subsonic speeds. While the engines are not powered-on air flows through the flowpath without fuel injection, generating a large amount of drag. The aerodynamics of the SPARTAN are calculated using Cart3D for Mach numbers from 0.2 to 10, and angle of attack values from 0° to 10° to cover the range of flight conditions experienced during the fly-back of the SPARTAN. An example Cart3D solution is shown for a Mach 7 engine off condition in Figure 3.22. Figure 3.23 shows the engine off aerodynamic characteristics of the SPARTAN vehicle over the

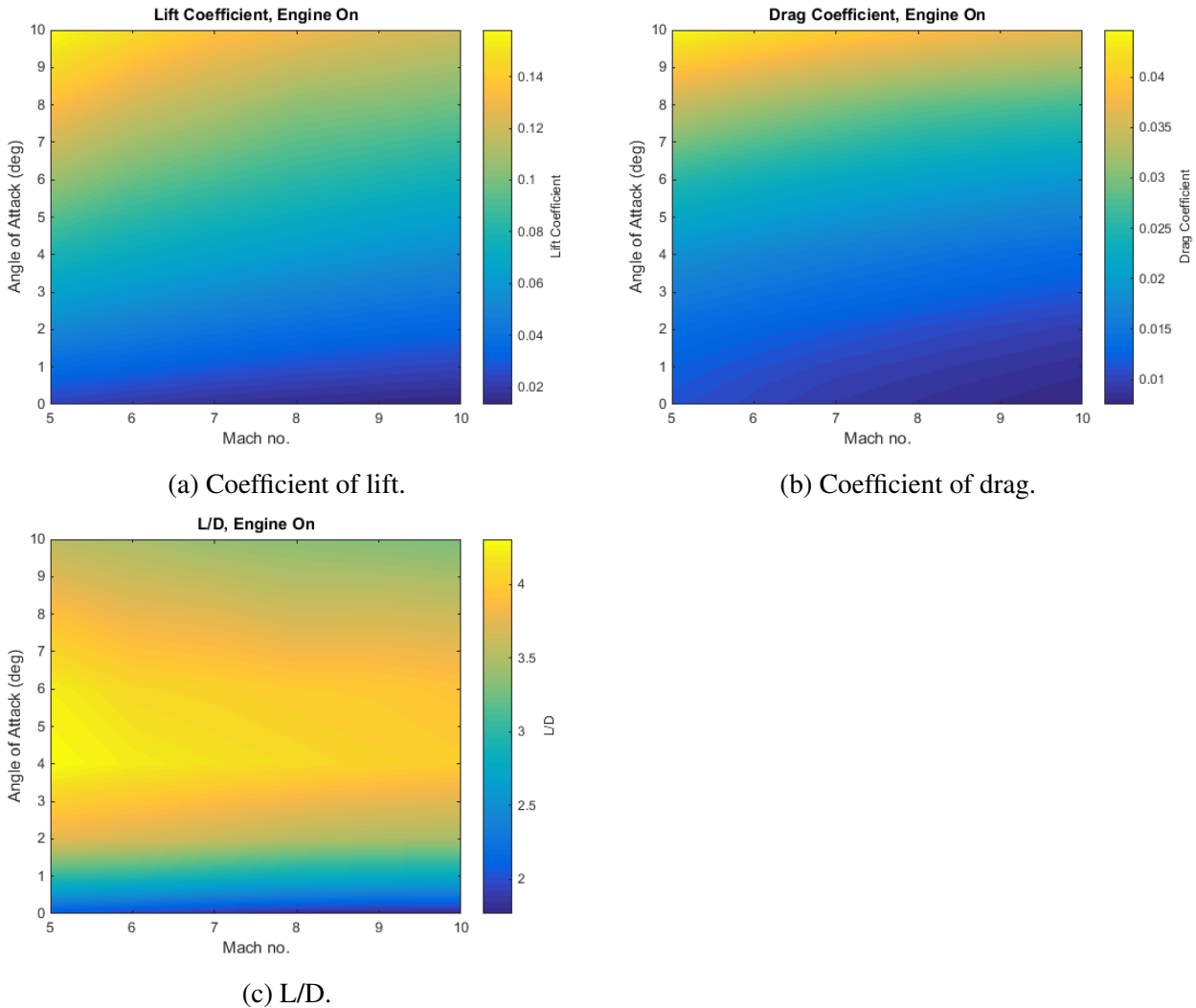
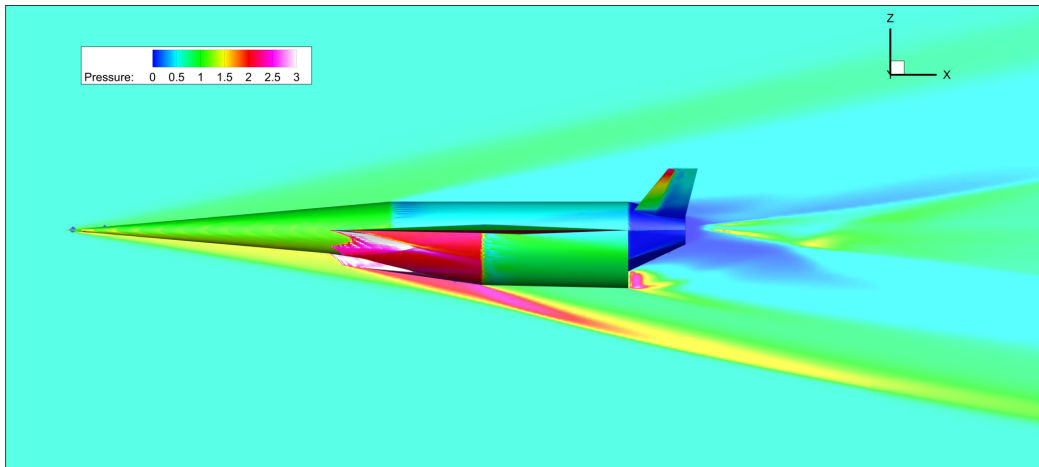
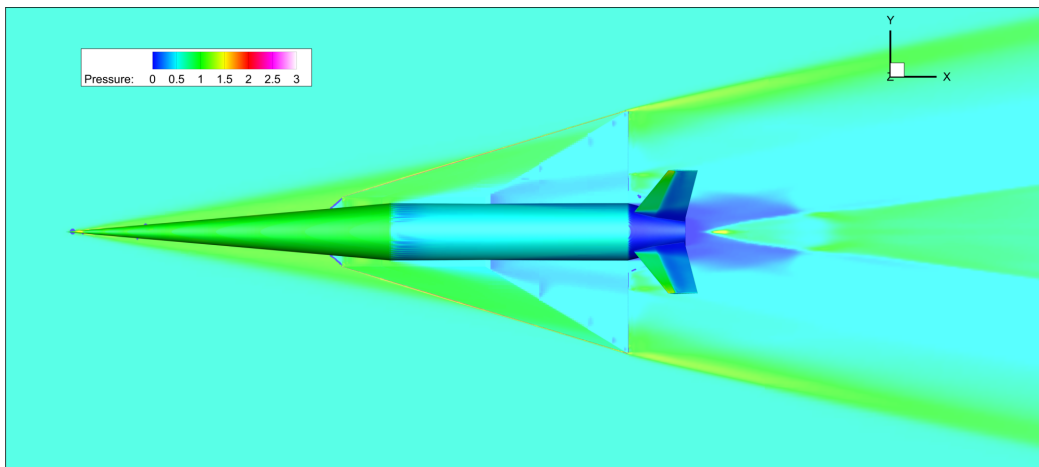


Figure 3.21: Aerodynamic coefficients with the C-REST engines powered-on. Coefficients correspond to a reference area of 62.77m^2 . **note what CG**

range of Mach numbers and angle of attack values analysed. These results show a distinct maximum region in the L/D of the SPARTAN at high Mach numbers, within the hypersonic regime. Below Mach 5, the L/D of the SPARTAN decreases sharply. This is caused by the scramjet engines unstarting, generating significant drag. The unstarted scramjet engines are shown in Figure 3.24. Below Mach 3, the L/D shows a trend of general increase, except at very low angle of attack, as the effects of the unstarted engine lessen. Below Mach 1 the L/D of the SPARTAN increases significantly, in part due to not having the significant drag induced from the engines unstarting, as observed in the supersonic regime.



(a) Side view.

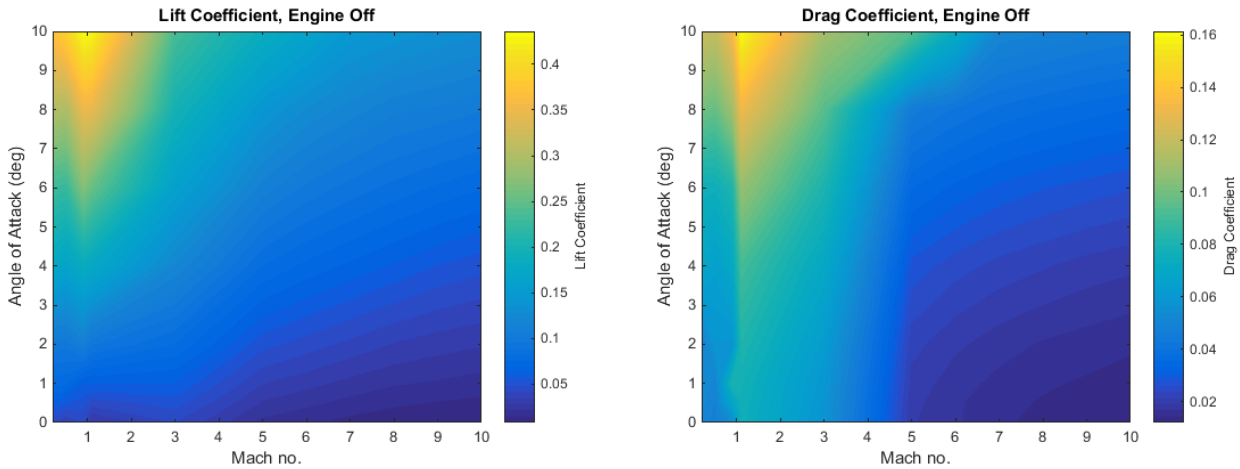


(b) Top view.

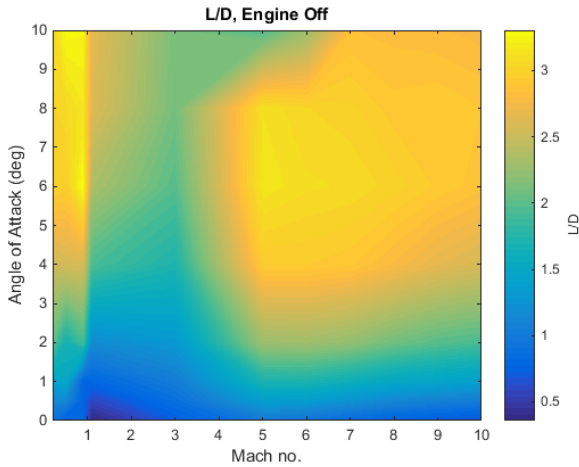
Figure 3.22: Cart3D flow result for the SPARTAN, at Mach 6, 2° angle of attack.

3.2 First Stage Rocket

The first stage rocket is required to deliver the second stage to near horizontal flight at Mach 5.1 flight conditions, after which it is discarded. To achieve this, the first stage rocket is modelled as a Falcon-1e first stage scaled down lengthwise to 8.5m, keeping the original diameter of 1.67m[145]. An additional 1m is added between the first stage and the SPARTAN to allow for any necessary stage interfacing. The Falcon-1e has been chosen due to its appropriate scale, and the proven flightworthiness of the Falcon-1. The first stage is attached to the rear of the scramjet second stage and is powered by a single LOX-kerosene Merlin 1-C engine. A connecting cowl has been modelled between the first stage rocket and the SPARTAN to improve the aerodynamic profile. The first stage has a structural mass of 1356kg, determined by scaling of the structural mass of the Falcon-1e. The engine mass of the Merlin 1-C is kept constant during scaling at 630kg[78]. The mass of the fuel in the first stage is scaled as part of the optimisation routine, as the dynamics of the vehicle, and its ability to reach a



(a) Coefficients of lift of the SPARTAN, calculated us- (b) Coefficients of drag of the SPARTAN, calculated us-
ing Cart3D.



(c) L/D of the SPARTAN.

Figure 3.23: Aerodynamic Characteristics of the SPARTAN with C-REST engine powered-off. Coefficients correspond to a reference area of 62.77m^2 .

given separation point, are very closely coupled to the available fuel mass.

The thrust and specific impulse of the Merlin 1-C are determined by interpolation between the sea level and vacuum specific impulse of the Merlin 1-C, shown in Table 3.2, with ambient pressure. Thrust scaling is determined by linear pressure scaling using nozzle exit area, $T = T_{SL} + (p_e - p_{SL})A_e$. The Merlin 1-C is throttled down to a constant 70%, a throttling value determined during the trajectory optimisation process to allow the first stage to pitch over more easily, while still allowing the first stage rocket to accelerate the SPARTAN to Mach 5.

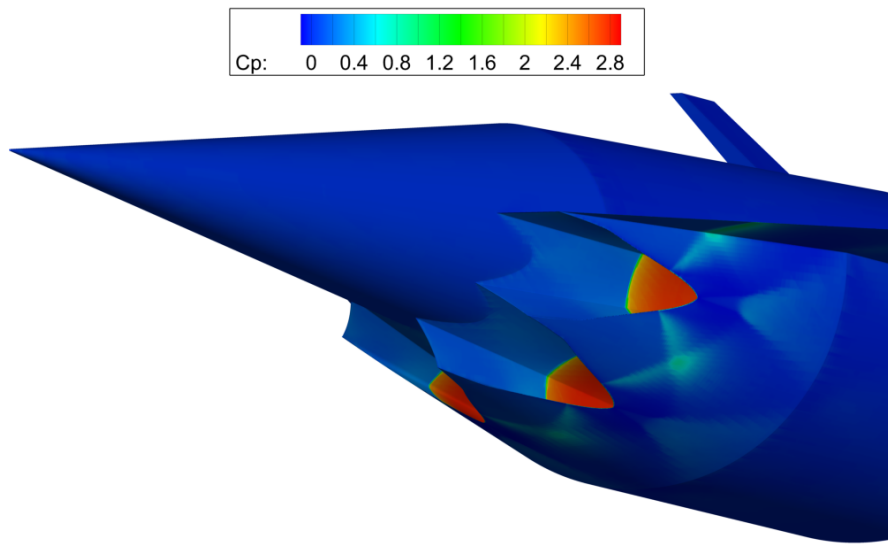


Figure 3.24: Unstarted scramjet engines at mach 3, 2° angle of attack.

$I_{SP_{SL}}$	275s
$I_{SP_{vac}}$	304s
T_{SL}	555.9kN
A_e	$0.552m^2$

Table 3.2: First Stage Engine Properties[78].

3.2.1 Aerodynamics Including First Stage

The aerodynamics of the launch system during first stage flight are calculated in a similar manner to those of the SPARTAN without the first stage rocket, as detailed in Section 3.1.3. The aerodynamics of the SPARTAN and first stage rocket are calculated using Cart3D. The first stage aerodynamics are modelled between angles of attack of 0° to -5° , as the first stage will be flying at negative angle of attack to induce faster pitch-over. Mach numbers from 0.2 to 5.1 (second stage separation velocity) are simulated. Figure 3.25 shows an example Cart3D simulation case, at Mach 2, -1° angle of attack. The coefficient of lift, drag and aerodynamic moment are tabulated for each simulation. Figure 3.26 shows the lift and drag coefficients of the first stage, as well as the lift-over-drag, across the simulated Mach Numbers and angles of attack. Above -1° angle of attack, the L/D of the first stage is generally greater than 0, meaning that lift is being gained in the positive vertical direction, and that the angle of attack must be lower than 1° to assist pitching. At Mach numbers over Mach 2, the absolute magnitude of the L/D generally increases as the Mach number increases. This is caused by the decreased effects of the engines unstarting, in turn reducing the drag of the engines at higher Mach numbers, as observed in the aerodynamics of the SPARTAN in Section 3.1. Note that absolute magnitude is the metric used for 'good' L/D, as the angles of attack are negative.

The First stage is trimmed using thrust vectoring of the Merlin 1-C engine during flight. The

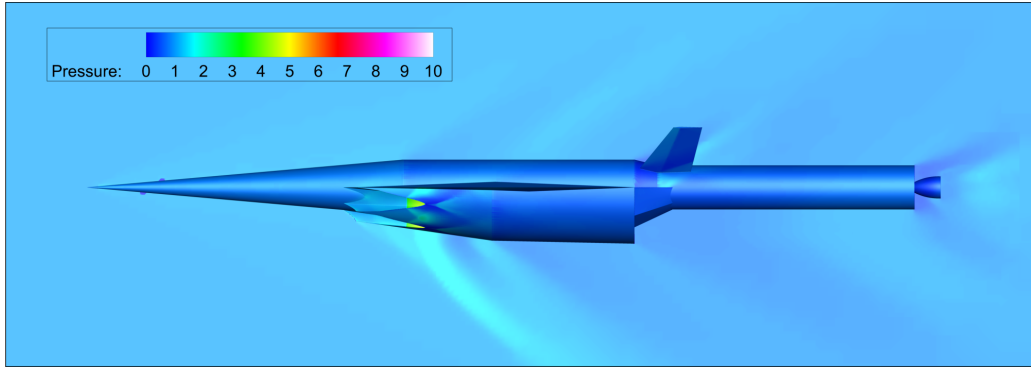


Figure 3.25: Cart3D result for the SPARTAN and first stage vehicles at Mach 2, -1° angle of attack.

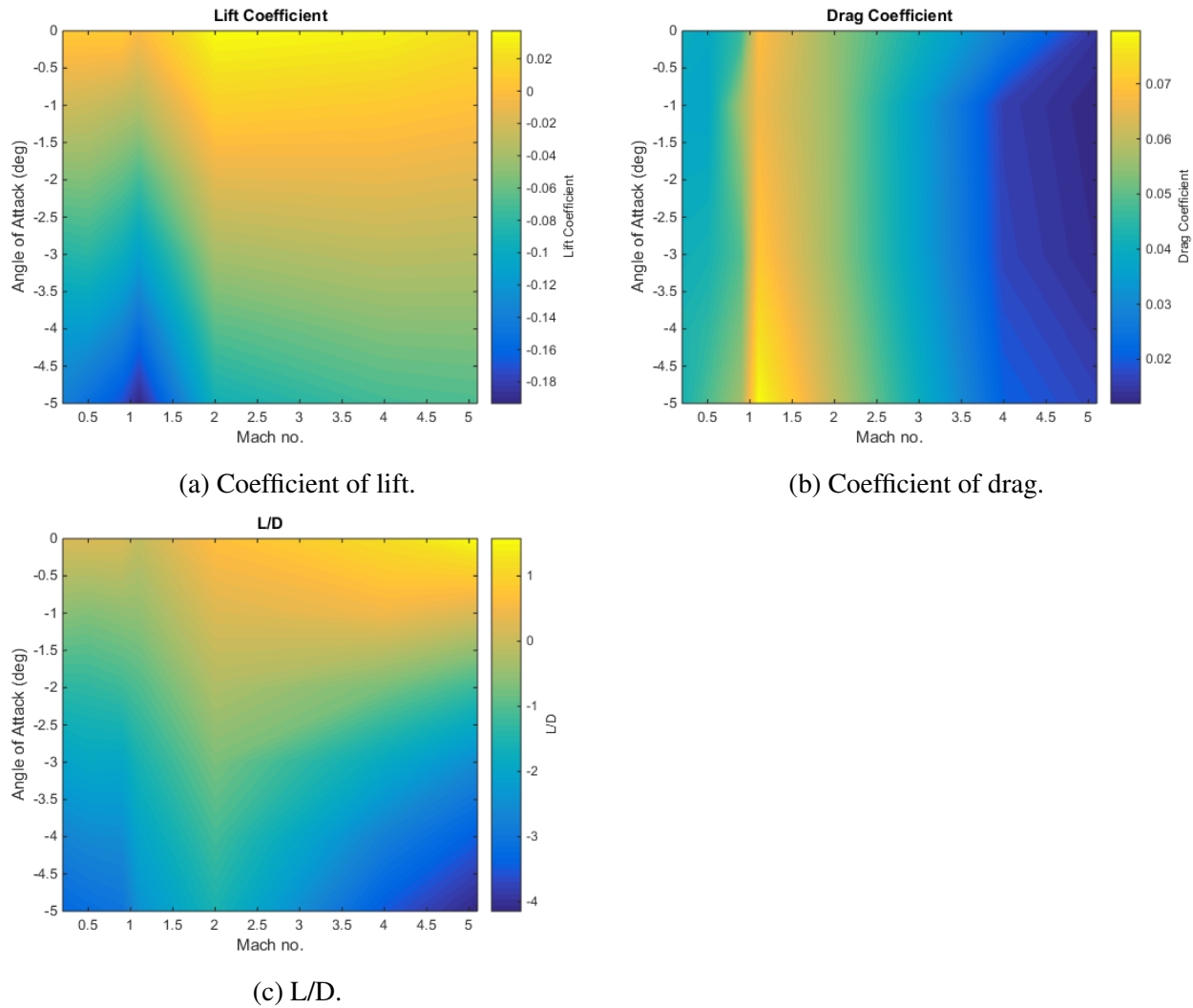


Figure 3.26: Aerodynamic characteristics of the SPARTAN including the first stage rocket.

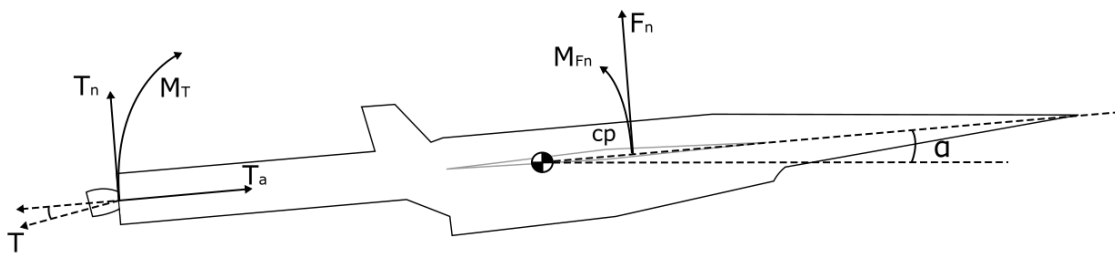


Figure 3.27: Thrust vectoring moment balancing of the first stage.



Figure 3.28: The third stage rocket, showing major internal features.

thrust vector angle of the engine is adjusted so that the moment caused by the rocket engine is equal and opposite to the moment caused by the aerodynamics of the vehicle, as illustrated in Figure 3.27, ie. $M_T = -M_{Fn}$. This thrust vectoring is calculated as the trajectory is simulated, at every flight condition.

3.3 Third Stage Rocket - Baseline

The third stage has a total length of 9m, with a 3m long nose, 4.5m long centrebody and 1.5m long engine. In this study the third stage rocket has been designed to accommodate a SpaceX Kestrel engine. In previous studies, the third stage has been designed to be powered by a Pratt & Whitney RL-10-3A pump-fed engine. The Kestrel has been used over the RL-10-3A for its cost effectiveness. As a pressure-fed engine, the Kestrel trades off specific impulse for weight and cost savings when compared to the RL-10-3A. As the only expendable portion of the system; the cost of the third stage is one of the main drivers of overall system cost. Reducing the cost of the third stage allows the cost of launch to be directly reduced.

The third stage rocket is released at the end of the scramjet accelerator burn, and lifts the payload out of the atmosphere and into the desired orbit. The third stage weighs a total of 3300kg. This has been chosen as a nominal design weight, to satisfy the fuel necessary to achieve orbit with an acceptable payload, while also allowing for ample payload volume. The internal layout of the third stage rocket is shown in Figure 3.28. The third stage has a structural mass fraction of 0.09, similar to the Falcon 1 second stage [145]. This gives a total structural mass (without heat shield) of 285.7kg.

The kestrel engine which powers the third stage is modified to have 50% increased propellant mass flow rate, giving a mass flow rate of 14.8kg/s. This is done to assist the rocket in exiting the atmosphere, as it was found during analysis that the third stage has difficulty exiting the atmosphere when powered by a standard Kestrel engine. It is likely that this mass flow increase will necessitate a heavier combustion chamber and likely heavier fuel tanks, though these effects are not considered in this study. The nozzle exit of the Kestrel engine has been kept constant at 1.1m diameter. An increase in mass flow necessitates a corresponding increase in throat area. This increase in throat area decreases the area ratio of the nozzle. The initial area ratio is 60, measured from schematics in the Falcon-1 Users Guide. A 50% mass flow increase corresponds to a 50% throat area increase, which causes the area ratio to decrease to 40. This decrease in area ratio results in a 2% loss of efficiency from the nozzle, measured from the thrust coefficient relationships shown in Figure 3.29[146]. The coefficient of thrust is calculated for a specific heat ratio of 1.20, as this is close to the specific heat ratio of oxygen and RP-1 of 1.24[146]. The modified specific impulse of the engine is 310.7s.

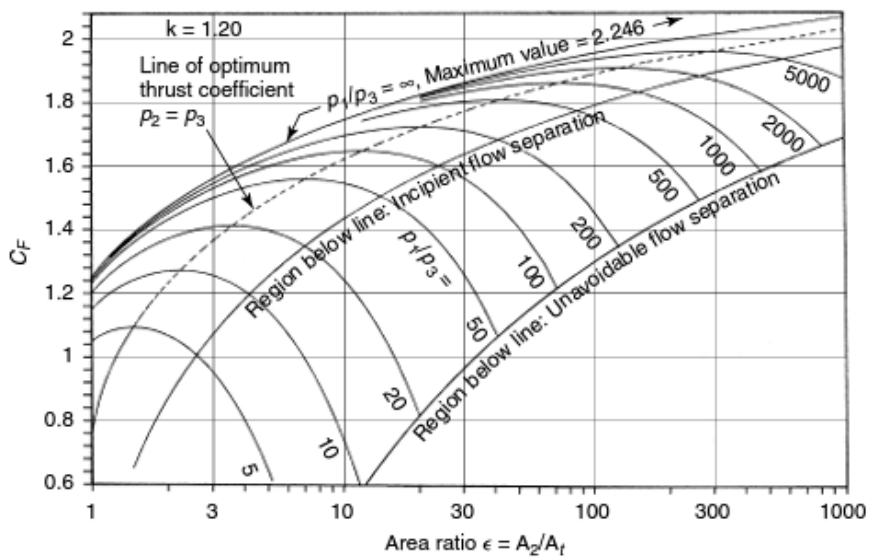


Figure 3.29: Variation in coefficient of thrust with area ratio [146].

3.3.1 Heat Shield Sizing

The third stage rocket is separated from the SPARTAN at a high dynamic pressure, after which it spends some time accelerating in-atmosphere before reaching exoatmospheric conditions. The time spent within a high dynamic pressure environment creates a large amount of heat loading, which must be mitigated by heat shielding. The heat shielding must be capable of withstanding the extremely high heat and structural loading necessary to protect the third stage rocket internals and payload, as well as being lightweight, as the payload-to-orbit is extremely sensitive to the mass of the third stage, and

cost effective, as increasing the cost of the third stage directly increases launch cost due to it being expendable.

The heat shield used to protect the third stage is constructed from a tungsten nose tip, a reinforced carbon-carbon nose cone, and a phenolic cork cylinder, weighing 130.9kg in total. This heat shield is designed to match the materials and thicknesses used by previous studies[12]. A mass breakdown is shown in Table 3.3. Tungsten is used at the tip of the nose cone, the area of maximum heat loading. Tungsten has extremely high heat resistivity, and a very low coefficient of thermal expansion[147]. However, tungsten is costly and heavy, and conducts heat well, and so is only used on the very tip of the nose where it is absolutely necessary. Reinforced carbon-carbon is used for the conical section of the heat shield, as this is an area that will be subject to high heat and structural loading. Carbon-carbon is able to withstand high temperatures, as well as being thermal shock resistant and having a low coefficient of thermal expansion[148]. Carbon-carbon is used in rocket and missile nose cones, as well as on aircraft leading edges due to its good heat resistant properties[148]. However, carbon-carbon is expensive, and is used only on the conical section of the heat shield to minimise cost. For the cylindrical section of the heat shield protecting the main body of the third stage, phenolic cork is used. Phenolic cork is a composite of ground cork and phenolic binders which is light and relatively cheap, with good heat resistivity. Phenolic cork has lower tensile strength and heat resistivity than carbon-carbon[148, 149], but is cheaper and lighter, making it appropriate for use on section of the heat shield which experiences lower heating and structural loads.

Part	Density	Geometry	mass
Tungsten Nose	$\rho_{Tungsten} = 19250 \text{ kg/m}^3$	50mm diameter cylinder, spherical tip	12.6kg
C-C Cone	$\rho_{CC} = 1800 \text{ kg/m}^3$	10mm thick, conical	93.4kg
Phenolic Cork Cylinder	$\rho_{PhenolicCork} = 320 \text{ kg/m}^3$	5mm thick, cylindrical	24.9kg

Table 3.3: Third stage heat shield breakdown.

3.3.2 Fuel Tank Sizing

The internal design of the third stage is allowed to be slightly variable as the trajectory is optimised. The third stage mass is fixed at 3300kg, and the calculated payload-to-orbit varies by exchanging leftover fuel mass for effective payload mass. To calculate the dynamics of the third stage, the fuel tanks have been approximately sized, assuming 160kg of payload-to-orbit. Realistically the exchange between fuel and payload mass would cause the fuel tanks to be resized slightly, however, for the purposes of this study the fuel tanks are assumed to be of constant size for simplicity. Currently this is a reasonable assumption as the internals of the rocket are very simplified. The structural mass is held constant at 9%. With a payload mass of 160kg, the third stage carries a total propellant mass of 2736.7kg. Table 3.4 breaks shows the component break-down of the LOX oxidiser and RP1 for this

fuel weight. The total mass and volumes of these fuels will change slightly as the trajectory of the launch system is optimised, and fuel is traded for payload mass. However, the ratio between the fuel and oxidiser will stay constant.

	LOX	RP1
Ratio	2.56	1
Density	1141kg/m ³	813kg/m ³ [150]
Volume	1.7248m ³	0.9455m ³
Mass	1968.0 kg	768.7 kg

Table 3.4: Third stage fuel distribution.

3.3.3 The Aerodynamics of the Third Stage Rocket

The third stage aerodynamics have been calculated using Missile DATCOM [114], a preliminary design tool for estimating the aerodynamic characteristics of missile and rocket vehicles. Missile DATCOM utilises empirical methods, along with various estimation techniques, to compute the aerodynamics of missile and rocket-like vehicles across the subsonic, supersonic and hypersonic regimes. The aerodynamic coefficients of the third stage rocket are shown in Figure 3.30.

Thrust Vectoring

The third stage rocket is controlled via thrust vectoring. The centre of pressure is calculated using missile Datcom. The thrust vector is set so that the moment generated by the engine matches the lift force acting at the centre of pressure, as shown in Figure 3.31, ie $M_T = -M_{F_n}$. This thrust vector is calculated at each flight condition during the trajectory simulations. The maximum thrust vector limit has been set to 8° . As no data on the maximum thrust vectoring capabilities of the kestrel engine was able to be found, this was set to the maximum gimbal range of the Aestus pressure-fed engine and Orbital Manoeuvring Engine (OME), which are similarly sized engines [78].

The centre of gravity is determined using CREO, and is located at 4.53m from the nose when the rocket is full of fuel, and 5.4m from the nose when the rocket is empty. It is assumed that the mass of the structure of the rocket (excluding fuel tanks, heat shielding, engine and payload) is distributed homogeneously for simplicity. The third stage rocket is statically unstable. Flying this rocket at an angle of attack will require an advanced automatic controller, as the only control available is produced by thrust vectoring. This study assumes that the third stage rocket controllable as long as the thrust vector limits of the vehicle are not exceeded.

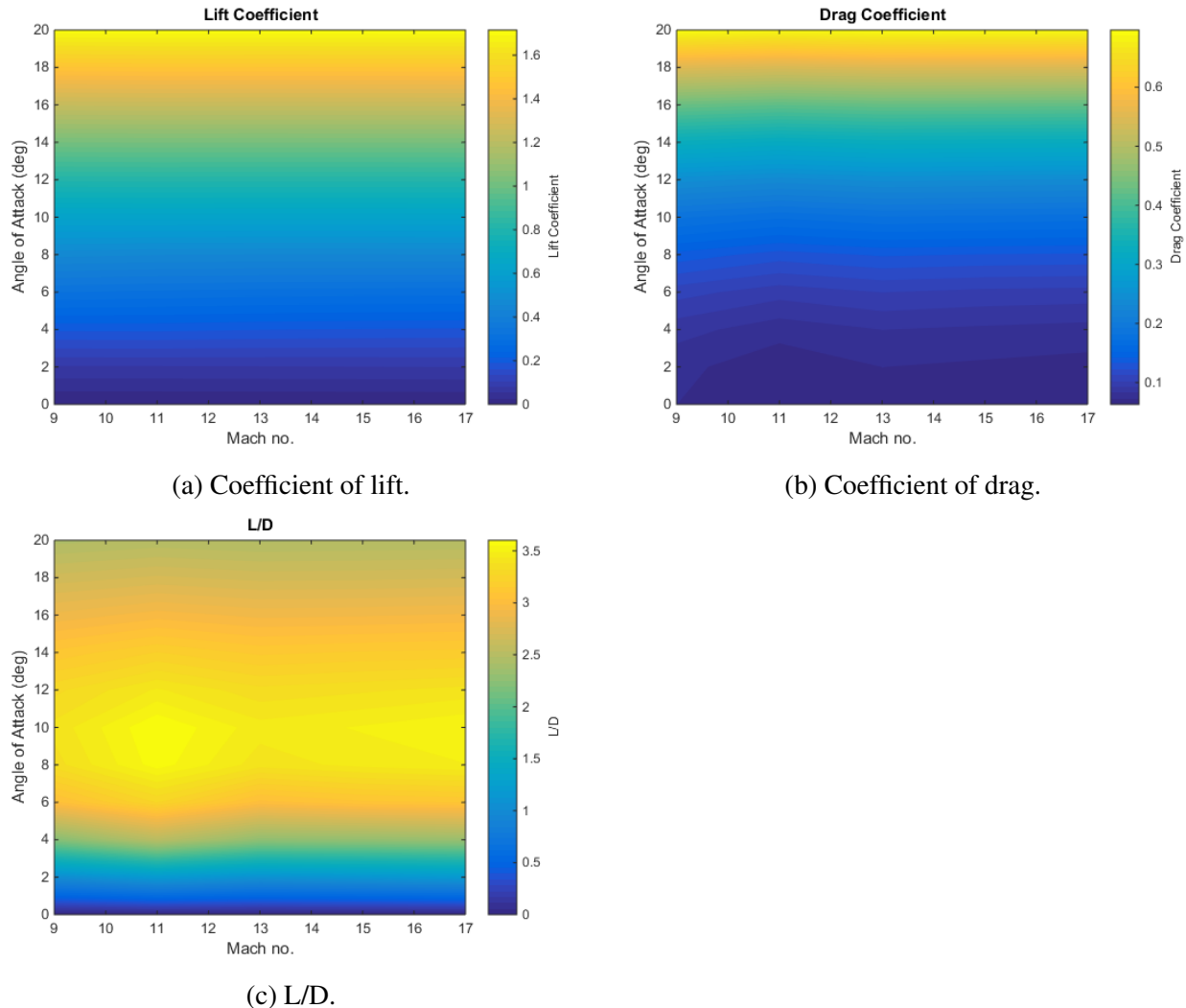


Figure 3.30: Aerodynamic characteristics of the third stage rocket, for a reference area of 0.95m^2 .

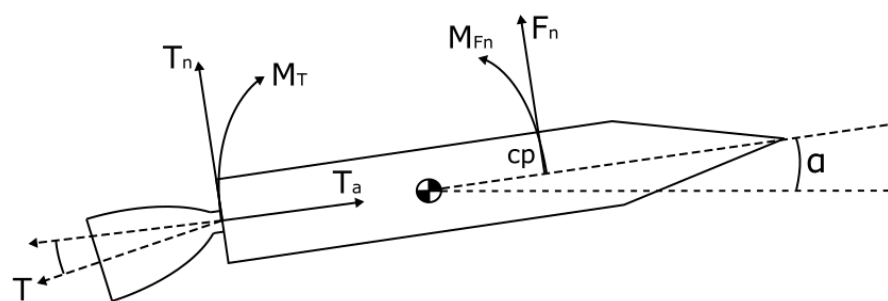


Figure 3.31: Thrust vector moment balancing of the third stage.

3.4 Summary

In this chapter, the design and simulation of a rocket-scramjet-rocket launch system was presented, based on the SPARTAN scramjet-powered accelerator. The design of the first stage is based on the first stage of the Falcon-1e, scaled down to 8.5m, and throttled down to 70%. The third stage is designed around the SpaceX Kestrel engine, with the fuel tanks of the SPARTAN resized to accommodate for the new third stage size. Mass breakdowns and key design features have been detailed for all three stages, including fuel ratios and structural mass fractions. The aerodynamic databases of all three stages were presented and analysed, and the process for generating these databases was detailed. The CFD simulations of the first stage and SPARTAN in Cart3D have been detailed, including the process of verifying the convergence of each solution. The propulsion modelling of the C-REST scramjet engines was presented, along with the schemes used to generate smooth, second order continuous interpolations of the engine data. The process for generating the trimmed aerodynamic databases for the SPARTAN has been presented, including the calculation of the control surface aerodynamics, and the calculation of the variable centre of gravity of the SPARTAN. The thrust vectoring for the first and third stages was detailed, along with the relevant limitations to thrust vector angle.

CHAPTER 4

LODESTAR

The calculation of the maximum payload-to-orbit trajectory profile for a rocket-scramjet-rocket launch system is a complex task, and specialised packages for this purpose are not widely available. This chapter presents the package LODESTAR (Launch Optimisation and Data Evaluation for Scramjet Trajectory Analysis Research), which has been developed to calculate the optimal trajectories of satellite launch systems by simulating the dynamics of the launch system, and interfacing appropriately with an optimal control solver. LODESTAR optimises a trajectory towards a user-defined objective function, such as maximum payload-to-orbit, subject to constraints that bound the operational region of a vehicle. LODESTAR is developed in MATLAB and utilises GPOPS-2[151] a proprietary pseudospectral method optimisation package, which uses an hp-adaptive version of the Radau pseudospectral method, described in further detail in Section 2.9. LODESTAR performs multiple functions which facilitate the optimisation of launch trajectories, including:

- providing a smooth, continuous interpolation of the aerodynamic and engine performance databases,
- calculating the dynamics of each vehicle in six degree of freedom,
- interfacing with GPOPS-2 to provide the configuration of the multi-stage optimisation problem,
- adaptively calculating an initial guess for the initialisation of the optimal control solution,
- performing the simulation of the uncontrolled segments of the trajectory,
- parallelising the optimal solution process,
- assessing and validating the optimised trajectory solution,
- and visualising the optimised trajectory solution along with key vehicle performance indicators.

Within this chapter, the structure of LODESTAR is presented, as well as the set-up of LODESTAR for the rocket-scramjet-rocket trajectory optimisation, and the verification methods used to determine if a solution has converged correctly.

Figure 4.1 illustrates a simplified iteration of the pseudospectral solver. GPOPS-2 provides an initial guess of the solution to the external modules, over an initial mesh of nodes. The external modules calculate the aerodynamic and engine performance of the launch system at each point along the trajectory, along with atmospheric conditions. This data is then used to calculate the dynamics of the vehicle along the trajectory. The constraints and cost function are then evaluated by GPOPS-2 and passed through to the IPOPT nonlinear optimisation package[106], which updates the guess of the state and control variables. This process is repeated for a set number of iterations, with the solution evaluated at each iteration to compute the feasibility and optimality of the solution. This process repeats until the solver reaches a predefined tolerance of optimality, or a predefined number of iterations. At this point, GPOPS-2 updates the node mesh, clustering nodes and creating mesh segments around key sections of the trajectory to improve accuracy. The process repeats for a number of mesh iterations defined by the user.

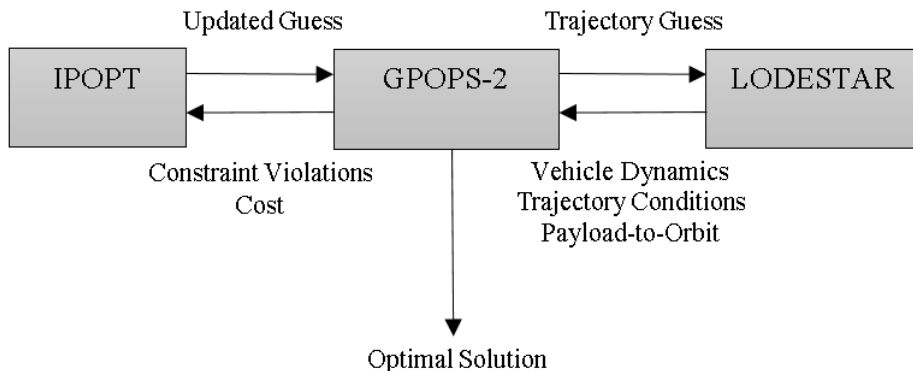


Figure 4.1: The simplified optimisation process.

Due to the nature of the pseudospectral method, it is possible that GPOPS-2 will not be able to converge to a physically valid or optimal solution. LODESTAR contains a number of verification modules that assess the optimised trajectory solution to ensure that the solution has converged sufficiently, and that the dynamics of the solution are accurate. To aid in ensuring that an optimal solution is reached, GPOPS-2 is initiated from four separate initial guesses, with final altitude guess varied by 1km between each guess. These iterations of GPOPS-2 are run in parallel, using Matlab's Parfor function. After all iterations of GPOPS-2 have completed, the state feasibility is calculated for each solution. The 'best' solution is chosen as the solution with the most accurately modelled dynamics.

4.1 Vehicle Simulation

Each of the vehicles within the rocket-scramjet-rocket launch system are simulated by establishing a set of dynamic equations that fully describe the motion of the vehicle in terms of the time, states (\mathbf{x}), and controls (\mathbf{u}) of the system;

$$\dot{\mathbf{x}}(t) = f[t, \mathbf{x}(t), \mathbf{u}(t)]. \quad (4.1)$$

The states and controls are the variables that define the time dependent physical characteristics of the system. The state variables are dependent on the controls and the system dynamics, while the control variables are the variables that drive the behaviour of the system and are independently variable. The state variables are defined by the coordinate system, and the outputs of each vehicle model. These are nonlinear functions that depend on the interpolation of data sets, which supply the atmospheric, aerodynamic and propulsion characteristics of each vehicle. The methods used to interpolate these data sets must be as smooth and continuous as possible, and cover the entire possible operational range of the vehicle. Even if the solution is well within the range of all input data sets, the solver will potentially explore all regions within the user-defined bounds. If there are large discontinuities or inaccurate extrapolation effects within the possible solution space of a particular vehicle, the solver may be unable to converge, or converge to a physically invalid solution. Discontinuities within the aerodynamics or engine properties of a particular vehicle must be mitigated through the careful application of interpolation techniques. Discontinuities that are unable to be mitigated, such as stage separations, must be separated into distinct phases within the optimal control solution, connected by linkage constraints.

4.1.1 6DOF Equations of Motion

The dynamics of the vehicle are calculated in six degrees of freedom, illustrated in Figures 4.2 and 4.3, with yaw constrained to zero. The dynamics of all stages are calculated using an geodetic rotational reference frame, written in terms of the angle of attack α , bank angle η , radius from centre of Earth r , longitude ξ , latitude ϕ , flight path angle γ , velocity v and heading angle ζ . The equations of motion are given from [96]:

$$\dot{r} = v \sin \gamma \quad (4.2)$$

$$\dot{\xi} = \frac{v \cos \gamma \cos \zeta}{r \cos \phi} \quad (4.3)$$

$$\dot{\phi} = \frac{v \cos \gamma \sin \zeta}{r} \quad (4.4)$$

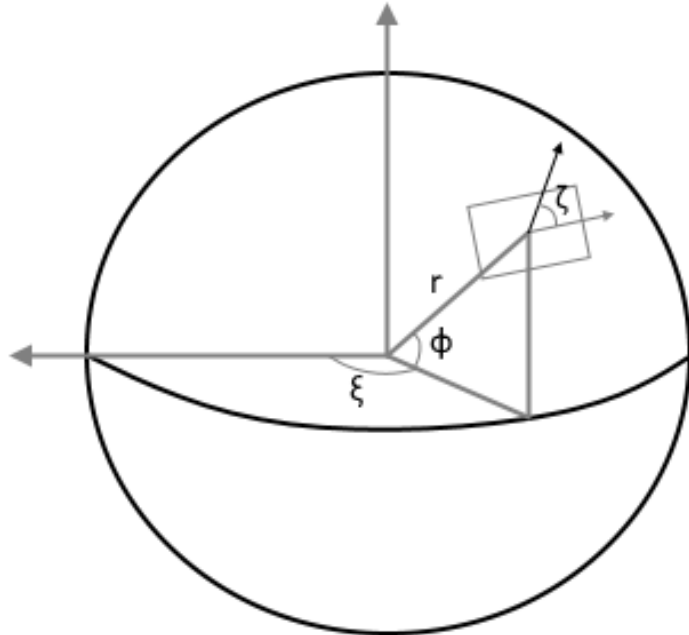


Figure 4.2: The Earth-fixed components of the geodetic rotational coordinate system.

$$\dot{\gamma} = \frac{T \sin \alpha \cos \eta}{mv} + \left(\frac{v}{r} - \frac{\mu_E}{r^2 v} \right) \cos \gamma + \frac{L}{mv} + \cos \phi [2\omega_E \cos \zeta + \frac{\omega_E^2 r}{v} (\cos \phi \cos \gamma + \sin \phi \sin \gamma \sin \zeta)] \quad (4.5)$$

$$\dot{v} = \frac{T \cos \alpha}{m} - \frac{\mu_E}{r^2} \sin \gamma - \frac{D}{m} + \omega_E^2 r \cos \phi (\cos \phi \sin \gamma - \sin \phi \cos \gamma \sin \zeta) \quad (4.6)$$

$$\dot{\zeta} = \frac{T \sin \alpha \sin \eta}{mv \cos \gamma} - \frac{v}{r} \tan \phi \cos \gamma \cos \zeta + 2\omega_E \cos \phi \tan \gamma \sin \zeta - \frac{\omega_E^2 r}{v \cos \gamma} \sin \phi \cos \phi \cos \zeta - 2\omega_E \sin \phi \quad (4.7)$$

4.2 Mission Definition

LODESTAR is able to simulate any mission desired of a rocket-scramjet-rocket launch system. However, the configuration of the optimal control routines must be tailored towards the specific mission profile desired. The nominal mission of the rocket-scramjet-rocket is presented here in order to provide a suitable reference for the configuration specifications, detailed in the following sections.

The mission chosen for the optimal trajectory calculation is a launch to sun synchronous orbit. A satellite in sun synchronous orbit is close to polar inclination, regressing so that it keeps its orbital alignment to the sun. The sun synchronous is one of the most commonly used types of orbit for space

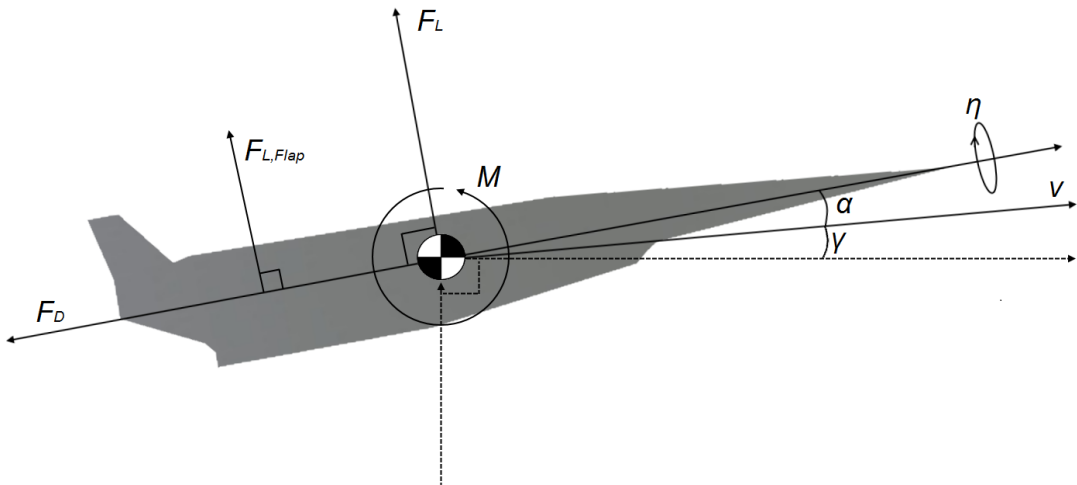


Figure 4.3: The vehicle-based components of the coordinate system.

science missions, as it has many useful properties[152]. A sun synchronous orbit allows for global coverage, passing over each latitude at the same time each day, illustrated in Figure 4.4. It also allows for a satellite to either have full sun and have consistent power generation, or alternatively, allows for a satellite to have a consistent ‘dark side’ each day to alleviate thermal issues[152]. A sun synchronous orbit at 566km has been used in previous studies as the target orbit[12], and this orbit is also used for the current work.

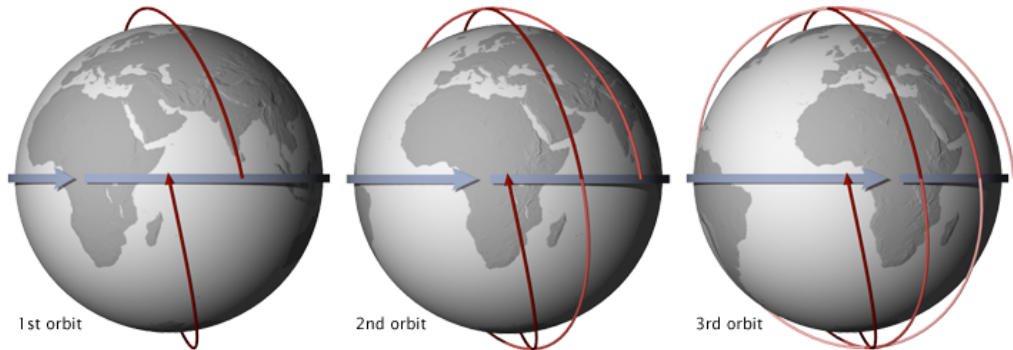


Figure 4.4: Sun synchronous orbit illustration, passing over the equator at the same time each day[153].

The launch site selected for the simulation is the proposed Equatorial Launch Australia launch site near Nhulunbuy in the Northern Territory, Australia[154]. This proposed launch site looks to take advantage of the remoteness of northern Australia, as well as its close proximity to the equator. While the proximity to the equator of this launch site is slightly disadvantageous for launch to sun synchronous orbits, the possibility of launch directions from this location, and its active development, make it an appropriate choice as a practical launch location within Australia. The site is ‘about 30km south of Nhulunbuy’[154] which places it within the approximate region indicated in Figure 4.5.



Figure 4.5: Approximate location of the ELA launch site. Image from Google maps.

4.3 Optimal Control Problem Structure

One of the primary functions of LODESTAR is to interface with the optimal control solver GPOPS-2. GPOPS-2 is a generic optimal control solver that utilises the pseudospectral method of optimal control, described in detail in Section 2.8. Practically, the implementation of optimal control involves the specification of the dynamics of the system to be optimised, as well as the set of constraints and objectives that define the optimisation problem. Together, these define the optimisation problem being solved.

Cost Function

The cost function, J , defines the target of the optimisation problem. This cost function may be any function which is defined by the states or controls of the optimisation problem. The cost function is defined as follows:

$$J(t, \mathbf{x}(t), \mathbf{u}(t)) = M[t, \mathbf{x}(t_f), \mathbf{u}(t_f)] + \int_{t_0}^{t_f} P[\mathbf{x}(t), \mathbf{u}(t)] dt, \quad t \in [t_0, t_f], \quad (4.8)$$

where M is the terminal cost function and P is the time integrated cost.

Dynamic Constraints

The constraints impose various conditions on the optimisation problem. The optimisation problem is

subject to a set of dynamic constraints, which describe the behaviour of the system over the solution space:

$$\dot{\mathbf{x}}(t) - f[t, \mathbf{x}(t), \mathbf{u}(t)] = 0. \quad (4.9)$$

These dynamic constraints ensure that the polynomial approximations of the state variables match the physical dynamics of the system, determined by the state variables of each vehicle. Implementing the dynamics as constraints allows each state variable to be approximated separately, and gives the optimiser some freedom to explore each state variable independently, greatly increasing the robustness of the optimal control problem.

Bounds and Path Constraints

Inequality constraints define the bounds of each state, as well as any path constraints. The bounds directly confine the state and control variables to prescribed values. This serves the purpose of limiting the search space to the physically possible (eg. constraining altitude to be greater than ground level), constraining the vehicle within its performance limits (eg. limiting the angle of attack), and improving computational efficiency by ensuring that the optimiser is constrained to a reasonable solution space:

$$\mathbf{b}_{min} \leq \mathbf{x}(t), \mathbf{u}(t) \leq \mathbf{b}_{max}. \quad (4.10)$$

The path constraints are inequality constraints which consist of functions based on the states and controls of the system. Path constraints place adaptive bounds on the system, which vary over time with the state of the system:

$$\lambda[t, \mathbf{x}(t), \mathbf{u}(t)] \leq \mathbf{0}. \quad (4.11)$$

Path constraints are generally used to impose physical limitations on the system such as structural, aerothermodynamic, pathing, and control limits.

Event Constraints

The event constraints constrain the states at the start and end points of a trajectory or phase:

$$\psi_0[\mathbf{x}(t_0), t_0] = \mathbf{0}, \quad (4.12)$$

$$\psi_f[\mathbf{x}(t_f), t_f] = \mathbf{0}. \quad (4.13)$$

These constraints determine the initial and terminal conditions of the optimisation problem, such as the initial location and velocity, and the starting fuel mass. Additionally, if the problem has multiple phases, these constraints are used to couple the states and time of each phase to the preceding and following phases as follows:

$$\mathbf{x}_{f,1} - \mathbf{x}_{0,2} = 0, \quad (4.14)$$

$$\mathbf{t}_{f,1} - \mathbf{t}_{0,2} = 0. \quad (4.15)$$

Together, these objectives, constraints, and variables describe the optimal control problem being solved, and form the inputs into GPOPS-2. GPOPS-2 uses these inputs, along with a pseudospectral method transcription, to form the constrained optimisation problem that is solved using IPOPT.

4.3.1 Trajectory Connection Points

The optimisation of a large, multi-vehicle launch trajectory requires that the optimal control problem be broken down into multiple segments, or phases[151]. This segmentation is performed in order to assist the convergence of the optimal control solver, by ensuring that the dynamics of the underlying model are as smooth and continuous as possible across each segment. For a launch system, discontinuities in the system dynamics generally arise when the aerodynamics, mass and propulsion mode of a launch vehicle change significantly between stages or flight modes. If a vehicle model with large discontinuities is implemented directly into a single phase application of the pseudospectral method, it is likely to cause significant convergence issues, as the system dynamics will be unable to be approximated by the underlying polynomial of the pseudospectral method.

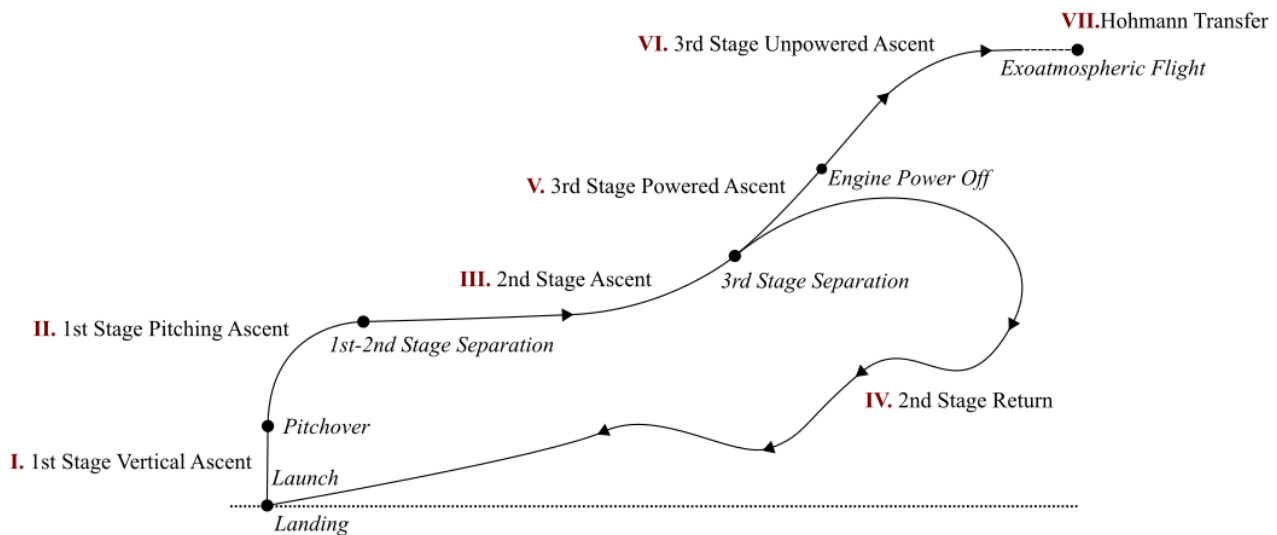


Figure 4.6: Illustration of the segmented launch profile.

To allow the trajectory profile to be formulated as an optimal control problem, the trajectory of the rocket-scramjet-rocket launch system has been broken down into the seven segments shown in Figure 4.6. The segments have been separated into two groups; controlled segments which take the form of phases within the optimal control problem; and segments without control which are either forward simulated at each iteration of the optimiser, or simulated externally to the optimal control problem. If the unpowered segments are simulated within the optimiser, they may be included in the cost and constraint functions of the optimisation problem. The unpowered segments are implemented in this

way in order to increase computational efficiency and improve the convergence of the optimal control solver.

Segments **II-V** are controlled by various combinations of angle of attack, bank angle and throttle, and are implemented as the phases of the optimisation problem. These phases are; The 1st stage pitching ascent; the 2nd stage ascent; the 2nd stage return flight; and the 3rd stage powered ascent. Segments **I, VI** and **VII** are segments without direct control, which are simulated using forward time stepping methods. These phases are; the pre-pitch segment of the first stage; the unpowered section of the third stage ascent; and the final Hohmann transfer to orbit. Each segment is connected through a set of conditions, which ensure that the trajectory of the vehicle is continuous, and that the trajectory that is being simulated is the one that is intended. The optimal control problem phases are connected through the use of initial and end discontinuity constraints on each phase to be coupled, ie $\mathbf{x}_{f1} = \mathbf{x}_{02}, t_{f1} = t_{02}$, while the forward simulated segments are simply initiated and terminated at set conditions. The segment coupling conditions are described in Table 4.1.

The following sections describe the setup of each individual phase of the optimal control problem, including the variables and constraints for the optimised phases. The bounds on the state dynamics are chosen to encompass the solution space, while not being overly expansive, to assist with the convergence and scaling of the optimal control solver. Across all optimised phases, the bounds on the latitude and longitude are chosen to cover the possible solution space, and are kept consistent across each phase to ensure that the position of the vehicle is not being unreasonably constrained between segments. The velocity constraints are chosen to cover the possible solution space, with the lower bound of 10m/s chosen to not allow the velocity to approach 0m/s, which produces singularities within the system dynamics.

4.3.2 **I. First Stage Vertical Ascent**

LODESTAR optimises the ascent of the first stage rocket in two segments; pre and post-pitchover. These aerodynamics of flight during these segments are simulated using spline interpolation of the databases generated using the method described in Section 3.2.1, and the engine properties are determined using linear pressure scaling as described in Section 3.2.

The pre-pitchover phase is the segment of flight immediately after vertical launch. During this phase, the launch system continues vertically for a short time in order to clear the launch tower and stabilise the vehicle. The pre-pitchover section is prescribed, and is simulated externally to the optimisation to allow the dynamics of the system to behave appropriately during the pitching ascent. During vertical flight, the heading angle (Equation 4.7) is meaningless, and vertical flight is allowed during the pitching ascent, the heading angle change rate can tend towards infinity, causing mathematical and scaling errors. Simulating this segment after the optimisation has been completed makes the starting mass and altitude of the first stage slightly variable, but this variation is negligible. The

Section	Initial Conditions	End Conditions	Controlled
I: 1 st Stage Vertical Ascent	Launches from rest, at the predefined launch site.	Fly until pitchover conditions are met.	no
II: 1 st Stage Pitching Ascent	Start at pitchover conditions	-	yes
III: 2 nd Stage Ascent	Must begin at 1 st stage pitching ascent end conditions.	-	yes
IV: 2 nd Stage Return	Must begin at 2 nd stage ascent end conditions.	Must approach landing conditions at the initial launch site.	yes
V: 3 rd Stage Powered Ascent	Must begin at 2 nd stage ascent end conditions.	Must produce exoatmospheric flight at the termination of stage VI.	yes
VI: 3 rd Stage Unpowered Ascent	Must begin at 3 rd stage powered ascent end conditions.	Terminates when flight is parallel with Earth's surface.	no
VII: 3 rd Stage Hohmann Transfer	Must begin at 3 rd stage unpowered ascent end conditions.	Must attain prescribed orbit.	no

Table 4.1: Segment coupling conditions for combined trajectory optimisation.

pitchover is defined to occur at 90m altitude and 15m/s velocity. During the vertical launch the rocket is assumed to need no control, and is held at 0° angle of attack.

4.3.3 II. First Stage Pitching Ascent

At 90m altitude and 15m/s velocity, pitchover occurs. The pitchover is a very minor amount of instantaneous pitching (0.01°) which is introduced in order to begin the pitching ascent, allowing the heading angle of the vehicle to resolve correctly. The first stage pitching ascent trajectory is an angle of attack controlled phase in the optimisation routine, which is simulated from pitchover until second stage separation. Table 4.2 shows the optimisation setup of this phase. During this phase, the launch system is allowed to fly at negative angles of attack, to assist in pitching. The control for this phase is the second derivative of angle of attack, which is chosen as the control variable to assist in mitigating the first stage's sensitivity to angle of attack, ie. when the trajectory angle is near 90° and at low velocities, the effect of changes in angle of attack is very large. Using the second derivative of angle of attack as the control variable smooths the angle of attack change rate and ensures a physically attainable solution. The initial fuel mass of the first stage rocket is unconstrained, as small variations in the initial fuel mass can have an important effect on the capabilities of the first stage. The fuel mass can influence the velocity achievable at first to second stage separation, as well as the rate at which the

rocket is able to pitch, and consequentially, the altitude and flight path angle range of the first stage. Allowing the initial fuel mass to vary increases the flexibility of the optimal control solver, and allows the optimal sizing of the first stage to be investigated.

Variable Group	Associated Variables	Values
Initial Constraints	Velocity Altitude Latitude Longitude Trajectory Angle Angle of Attack	30m/s 90m -12.16° 136.75° 89.9° 0°
Terminal Constraints	$\mathbf{x}_{f,\text{II}} - \mathbf{x}_{0,\text{III}}$ $t_{f,\text{II}} - t_{0,\text{III}}$	0 0
Path Constraints	Dynamic Pressure	0kPa - 50kPa
Control Variables	$\ddot{\alpha}$	$\pm 0.029^\circ/s^2$
State Variables	Altitude Velocity Trajectory Angle Latitude Longitude Heading Angle Total Mass Angle of Attack (α) $\dot{\alpha}$	0 - 30km 10 - 3000m/s $-5.7^\circ - 89.9^\circ$ $\pm 28.6^\circ$ $114.6^\circ - 171.9^\circ$ $\pm 360^\circ$ 11453 - 29388kg $-5^\circ - 0^\circ$ $\pm 5.7^\circ/s$

Table 4.2: Optimisation setup of the first stage phase.

4.3.4 III. Second Stage Ascent Trajectory

The second stage ascent phase consists of the acceleration of the SPARTAN scramjet-powered vehicle. The ascent trajectory of the SPARTAN is controlled using angle of attack and bank angle. The aerodynamics of the SPARTAN are calculated from an interpolation of the database described in Section 3.1. The engine properties are determined as described in Section 3.1.2. During the ascent, the engines are assumed to be operating at the maximum equivalence ratio at all times. This equivalence ratio is 1 in most sections of the trajectory, except at low mach numbers where the possibility of unstart and choking necessitates a reduction in equivalence ratio. This trajectory is constrained to a maximum dynamic pressure of 50kPa, corresponding to the maximum structural limits of the vehicle. Aerodynamic and propulsion databases are generated as described in Sections 3.1.2 and 3.1.3. The lift and drag of the vehicle is interpolated from the trimmed aerodynamics database and the propulsion is determined from interpolation of the C-REST database. The control variables are set as angle of attack and bank angle change rate. Using the derivatives of the angle of attack and bank

Variable Group	Associated Variables	Values
Initial Constraints	Fuel Mass	1562kg
Terminal Constraints	Altitude Trajectory Angle Bank Angle η $\mathbf{x}_{f,\text{III}} - \mathbf{x}_{0,\text{IV}}$ $t_{f,\text{III}} - t_{0,\text{IV}}$	0 - 45km 0 - 15° 0° 0 0
Path Constraints	Dynamic Pressure	0 - 50kPa
Target Cost	Dynamic Pressure*	$(q - 50000)^2 / 50000$
Control Variables	$\dot{\alpha}$ $\dot{\eta}$	$\pm 0.5^\circ/\text{s}$ $\pm 1^\circ/\text{s}$
State Variables	Altitude Velocity Trajectory Angle Latitude Longitude Heading Angle Fuel Mass Angle of Attack (α) Bank Angle η	0 - 50km 10 - 3000m/s -28.6° - 15° $\pm 28.6^\circ$ 114.6° - 171.9° -240° - 360° 0 - 1562kg 0° - 10° -1° - 90°

Table 4.3: Optimisation setup of the second stage ascent. * This is only used in the constant dynamic pressure simulation.

angle as the control variables serves to smooth the angle of attack and bank angle by constraining the change rates to reasonable values. The angle of attack is constrained to 10°, approximated as a reasonable upper bound to the angle of attack, and the limit to which the aerodynamic characteristics of the SPARTAN are modelled. The bank angle is constrained to a maximum of 90°, as it is assumed that the SPARTAN is not able to invert. The bank angle is also constrained to positive values only (ie. that the heading angle may only increase) as the SPARTAN is launched from the ELA launch site at Nhulunbuy, and must be launched to the northeast or east to avoid overflying populated areas.

A cost function can be included during this phase, shown in Table 4.3, when flying a constant dynamic pressure trajectory is desired. This cost function is smooth and approaches 0 at the target dynamic pressure, allowing the third stage cost function of payload mass to still be active, while prioritising flying at constant dynamic pressure.

4.3.5 IV. Second Stage Return Trajectory

After releasing the third stage rocket, the scramjet-powered second stage must return back to the initial launch site. During this return flight, the SPARTAN is able to use its engines if necessary to ensure that it is able to return successfully. The aerodynamics of the SPARTAN during fly-back are determined by interpolation of the engine-on and engine-off trimmed data sets described in Section 3.1.3.

As the scramjet engines are throttled on, the aerodynamics are assumed to vary linearly between the aerodynamics calculated by the engine-off and engine-on datasets. During the fly-back, the SPARTAN cannot exceed its dynamic pressure limit of 50kPa. The end state is constrained to a minimum of -20° trajectory angle, which is assumed to be an appropriate lower bound on the trajectory angle for approach to a landing strip. The altitude is constrained to less than 1km at the end point to ensure that the SPARTAN is approaching landing altitude. The velocity is left unconstrained at the end point. Constraining the end velocity may over constrain the optimisation problem, and it is assumed that for a payload-to-orbit optimised trajectory the SPARTAN will end its return at a low velocity, so that the energy necessary for return is small.

During the return, the C-REST engines are able to be throttled on and off. The throttle is set as a state variable, variable between 0 and 1, where 1 represents the maximum equivalence ratio at that point. The fuel mass flow rate is scaled linearly with the throttle:

$$\dot{m}_{fuel} = \dot{m}_{fuel,max} \text{throttle}, \quad (4.16)$$

and the thrust of the engine is assumed to scale linearly with the fuel mass flow rate. A control variable of throttle change rate is added, to smooth the throttle in the same was as angle of attack and bank angle.

Variable Group	Associated Variables	Values
Initial Constraints	Bank Angle η	0°
Terminal Constraints	Latitude Longitude	-12.16° 136.75°
Path Constraints	Dynamic Pressure	0 - 50kPa
Control Variables	$\dot{\alpha}$ $\dot{\eta}$ <i>Throttle</i>	$\pm 0.5^\circ/\text{s}$ $\pm 1^\circ/\text{s}$ $\pm 0.2/\text{s}$
State Variables	Altitude Velocity Trajectory Angle Latitude Longitude Heading Angle Fuel Mass Angle of Attack (α) Bank Angle (η) Throttle	0 - 70km 10 - 5000m/s $\pm 80^\circ$ $\pm 28.6^\circ$ $114.6^\circ - 171.9^\circ$ $60^\circ - 500^\circ$ 0kg - 500kg $0^\circ - 10^\circ$ $0^\circ - 90^\circ$ 0 - 1

Table 4.4: Optimisation setup of the second stage return.

4.3.6 **V.** Third Stage Powered Ascent

The trajectory of the third stage rocket is separated into the powered and unpowered phases of ascent. During the powered ascent phase, the third stage is manoeuvred out of the atmosphere using one continuous burn of the Kestrel engine. The powered phase is controlled using angle of attack, and trimmed using thrust vectoring of the engine, as described in Section 3.3.3. The aerodynamics of the third stage are determined using interpolation of the aerodynamic dataset developed as described in Section 3.3.3.

The third stage rocket is constrained to an angle of attack of less than 20° . This is assumed to be the maximum controllable angle of attack possible for the third stage rocket. Additionally, a maximum normal force restriction is placed on the third stage, to limit the angle of attack of the third stage by the normal force on the vehicle. However, as a detailed structural study of the third stage has not been conducted, the maximum allowable normal force on the third stage is not known. For consistency, the maximum allowable normal force was calculated from the conditions of previous studies. Previous studies flew the third stage rocket at a constant 10° angle of attack, and initially released the rocket at 50kPa[12]. It is assumed that this condition of 10° angle of attack and 50kpa dynamic pressure produces the maximum allowable normal force to prevent the rocket from being released into an environment which could exceed its structural limitations. The maximum allowable normal force is calculated at the release Mach number, and is set as a path constraint.

The end angle of attack is constrained to 0° , as the angle of attack will not be able to be controlled during the unpowered ascent. The other terminal constraints of this phase correspond to end constraints imposed after the third stage unpowered ascent has been simulated. The altitude at the end of the unpowered ascent (Phase VI) is constrained to a lower limit of 90km, in order to ensure that the circularisation burn is exoatmospheric. The final heading angle is also constrained at this point, so that the orbit of the third stage is circularised into the correct inclination for sun synchronous orbit.

4.3.7 **VI.** Third Stage Unpowered Ascent

After the burn of the Kestrel engine is complete, the engine is cut and the third stage coasts to a point where it is able to be circularised into a low orbit. The unpowered phase of the ascent is not controlled. After the engine is cut, the third stage does not have sufficient aerodynamic control to manoeuvre, and the trajectory of the third stage is a coast at 0° angle of attack. The trajectory of the third stage rocket is only directly optimised during the powered section of its trajectory, the unpowered section of the trajectory is simulated from the end of the controlled section of the trajectory, using a second order Taylor series approximation. This integration ceases when the flight path angle reaches 0° . During this phase, the heat shield is released once the rocket has reached a dynamic pressure of 10Pa, where it is assumed that atmospheric effects will have ceased to have a major thermal effect. As the third stage is required to deliver the payload into heliosynchronous orbit, the third stage must achieve an

Variable Group	Associated Variables	Values
Initial Constraints	Total Mass $\mathbf{x}_{f,\text{III}} - \mathbf{x}_{0,\text{V}}$ $t_{f,\text{III}} - t_{0,\text{V}}$	3300kg 0 0
Terminal Constraints	Altitude, $\zeta_{f,\text{VI}}$ Heading Angle, $\zeta_{f,\text{VI}}$ Angle of Attack (α)	$\geq 90\text{km}$ 97.64° 0°
Path Constraints	Angle of Attack (α) Thrust Vector Angle	Maximum F_N $\pm 8^\circ$
Target Cost	Payload-to-Orbit	Payload Calculated in Phase VII
Control Variables	$\dot{\alpha}$	$\pm 1^\circ$
State Variables	Altitude Velocity Trajectory Angle Latitude Heading Angle Total Mass Angle of Attack (α)	30 - 84km 10 - 8000m/s $-5^\circ - 30^\circ$ $\pm 28.6^\circ$ $80^\circ - 120^\circ$ 0kg - 3300kg $-5^\circ - 0^\circ$

Table 4.5: Optimisation setup of the third stage powered ascent.

inclination of 97.63° at the end of this phase[152]. These terminal constraints are implemented in Phase V.

4.3.8 VII. Hohmann Transfer

After the rocket has attained exoatmospheric flight parallel to the Earth's surface, a circularisation burn is performed. This circularisation burn takes the third stage rocket into low orbit around the Earth. However, in order to reach a heliosynchronous orbit of 567km, the orbit of the third stage rocket must be raised. To this end, the final manoeuvre performed by the third stage rocket is a Hohmann transfer. A Hohmann transfer is the most fuel efficient way to raise a spacecraft from one circular orbit to another[155]. The orbit of the third stage is first circularised into a low orbit:

$$\Delta V_{12} = \sqrt{\frac{\mu}{r_2}} - V_1. \quad (4.17)$$

Following circularisation, the third stage engine is reignited (or remains ignited) and the third stage manoeuvres into an appropriate elliptical orbit:

$$\Delta V_{23} = \sqrt{\frac{\mu}{r_2}} \left(\sqrt{\frac{2r_4}{r_2 + r_4}} - 1 \right). \quad (4.18)$$

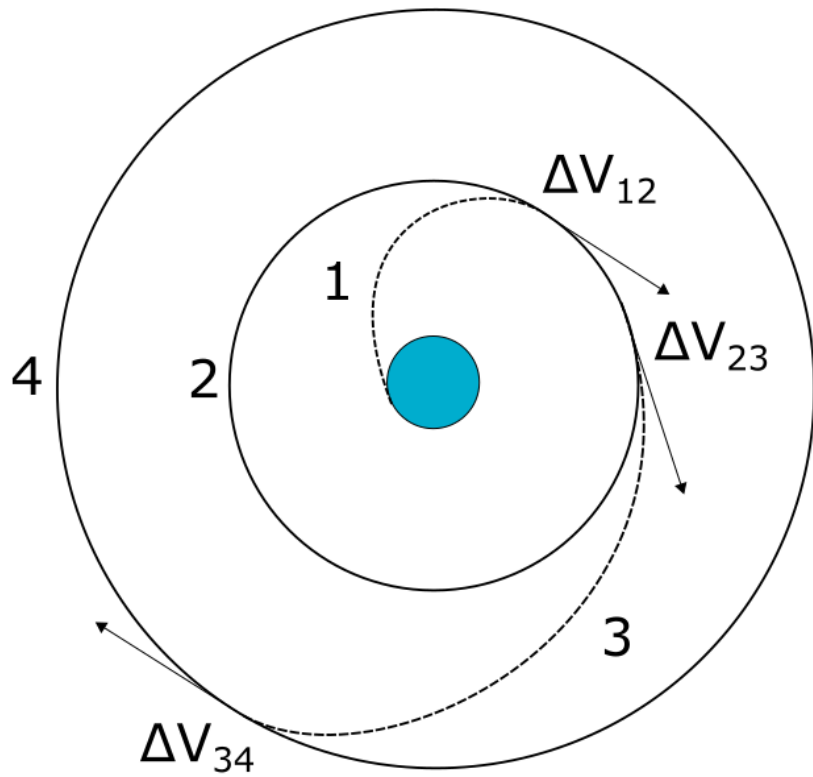


Figure 4.7: The Hohmann transfer manoeuvre.

At the apogee of the transfer orbit, corresponding to the desired orbital radius, an insertion burn is performed, and the orbit is circularised:

$$\Delta V_{34} = \sqrt{\frac{\mu}{r_4}} \left(1 - \sqrt{\frac{2r_2}{r_2 + r_4}} \right). \quad (4.19)$$

At this point, the payload is separated from the third stage rocket.

The mass of the third stage rocket after each burn is calculated using the Tsiolkovsky rocket equation:

$$m_2 = \frac{m_{1f}}{\exp^{\frac{V_{12}}{I_{SP} \cdot g_0}}} \quad (4.20)$$

$$m_3 = \frac{m_2}{\exp^{\frac{V_{23}}{I_{SP} \cdot g_0}}} \quad (4.21)$$

$$m_4 = \frac{m_3}{\exp^{\frac{V_{34}}{I_{SP} \cdot g_0}}} \quad (4.22)$$

Finally, the payload-to-orbit is determined by removing the structural mass from the total mass of the vehicle at the end of the Hohmann transfer. The remaining mass is taken to be the payload-to-orbit

capability of the vehicle.

$$m_{payload} = m_4 - m_{struct} \quad (4.23)$$

4.4 Optimal Solution Analysis

LODESTAR provides the capacity to analyse the optimal solution provided by the pseudospectral method solver to assist in determining whether the pseudospectral method solver has converged close to an optimal solution of the nonlinear programming problem. It is particularly useful to verify that the optimality and constraint tolerances that have been chosen are sufficiently small, or to check whether the pseudospectral method solver has approached an optimal solution in the case that the defined tolerances are not able to be reached. Checking the solution is achieved through the examination of five key parameters: the IPOPT constraint violation and dual infeasibility parameters; the Hamiltonian necessary condition for optimality; the state derivatives; and finally a forward simulation.

The first metrics to be checked are the IPOPT constraint violation (*inf-pr*) and dual infeasibility parameter (*inf-du*)[156]. The constraint violation parameter is a measure of the infinity-norm (L_∞ -norm) of the constraints of the problem[156]. This factor must be suitably small in order to indicate that the constraints of the problem have been met. While the permissible magnitude of this factor changes with each individual problem, it is always desirable for this factor to be as small as possible. The dual infeasibility provides an indication of the optimality of the solution. A low dual infeasibility indicates that the solution is dual feasible and is likely to have approached an optimal solution. A dual feasible solution indicates that the dual problem is at least a lower bound on the optimal solution, p^* , ie. $p^* \geq g(\lambda, \nu)$. For more details on duality see Reference [157]. Again, the magnitude of this value is variable with each problem, though as a problem becomes more complex, the ability to converge towards an optimal solution diminishes. It should generally be observable that the *inf-du* term is decreasing by multiple orders of magnitude and is stable at the completion of optimisation for a solution to be approaching optimality. In this study it is accepted that a given solution may not approach the global optimum, and multiple solutions are calculated to mitigate the error caused by the problem complexity, with the 'most optimal' solution selected.

The Hamiltonian of the optimal control problem is defined as

$$H(x(t), u(t), \lambda(t), t) = \lambda^T(t) f(x(t), u(t)) + L(x(t), u(t)). \quad (4.24)$$

The Hamiltonian of the optimal control problem is calculated using LODESTAR, and investigated as a partial verification that the first order necessary conditions hold. Due to the unconstrained end time of the trajectory problems, the Hamiltonian necessary condition for an optimal solution is $H = 0$ [158]. A sufficiently small Hamiltonian indicates that the end solution is likely to have approached an optimal solution.

The pseudospectral method considers the dynamics of the system as constraints on the optimal control problem, and solves across the entire trajectory simultaneously. This causes the physical system dynamics to have an associated margin of error, ie. $\dot{x} = f(x)$ will only hold to a certain degree of accuracy. For a well converged solution, this margin of error will be negligibly small, and the dynamics of the system will be consistent with realistic Newtonian dynamics. However, when the problem is not well converged, the dynamics of the system may have a large error. A check is performed on each state to affirm that the derivative of the approximated state is equal to the derivative supplied by the vehicle model. This checks that the solver has converged to a solution which satisfies the vehicle dynamics at each individual node. The state feasibility of the solution is checked through a verification of the state derivatives of each stage, $\dot{x} = f(x, u)$. \dot{x} is first determined through numerical differentiation of the state variables over the solution time, differentiated at the node points created by GPOPS-2. Then $f(x, u)$ is determined using the dynamics of the system and vehicle model, in the same way that $f(x, u)$ is input to the pseudospectral solver. Examination of the error between the ‘expected’ state derivatives, and the numerical approximation of the derivatives, $\dot{x} - f(x, u)$, allows the accuracy of the system dynamics to be assessed.

The final verification check is a full forward simulation. This forward simulation starts at the initial conditions of the optimal control problem, and propagates the dynamics of the system forward in time using the Runge-Kutta method, through Matlab’s ODE45 function. The forward simulation uses the optimised control variables as the only input. This checks that the flight path will follow the path computed by GPOPS-2, using only the calculated control inputs. This is the most complete test of the optimal solution. However, in some cases calculating a forward solution may be problematic. The pseudospectral method has a limited number of nodes, potentially spread across relatively large time steps. Due to the high accuracy of the polynomial approximation, the pseudospectral method is able to maintain accuracy over large time steps[86, 90]. However, a forward simulation necessarily has less accuracy than the spectral method, and may interpolate differently when applied to the optimal solution, causing minor deviations. These variations are usually negligibly small, however, this is problematic during the return phase, due to the way the throttling of the engines is modelled, ie. the specific impulse of the engines is set to 0 under Mach 5 or 20kPa inlet conditions during the optimisation process. As the engines are often throttled close to the minimum operable conditions, these restrictions can intensify the effects of otherwise minor deviations in the forward simulation. For this reason, the forward simulation of the return stage is split into three segments, with divisions at 1/6th and 1/3rd of the total trajectory length, chosen to separate the first major ‘skip’ and bank, and split the ‘skipping’ section of the trajectory. A forward simulation is initiated at each of these segments, mitigating some of the effects of the engines throttling on and off in the forward simulation. Splitting the forward simulation allows the forward simulation of the return stage to be assessed without the effects of the throttle model having an unreasonably large effect.

4.5 The Optimisation Process

Figure 4.8 shows the flow chart of the optimisation process, including the external simulation modules. The main process is run multiple times, with varying initial guesses, in order to be able to select the most converged solution. This process is parallelised, with green and red arrows in Figure 4.8 indicating the initiation and termination of the parallel loop respectively.

4.6 Summary

This chapter presented a tool for optimising the trajectory of launch systems, designated LODESTAR. LODESTAR simulates each stage of a rocket-scramjet-rocket launch system, and interfaces with the optimal control solver GPOPS-2, to generate a maximum payload-to-orbit trajectory solution. Each stage of the launch system is simulated individually within LODESTAR, either as a separate phase of the optimal control problem, connected by event constraints, or as a forward simulation. The set-up of LODESTAR for the launch of a small satellite to sun synchronous orbit has been detailed. The bounds of each stage have been chosen so as to provide suitable limits to the dynamics of the system, and the payload-to-orbit capability of the system has been set as the end cost function of the optimal control problem. The state and control variables of each stage were detailed, along with the state, event and path constraints. The capability of LODESTAR to verify the optimised solution was presented, including analysis using the necessary conditions of optimality, as well as forward simulation comparisons.

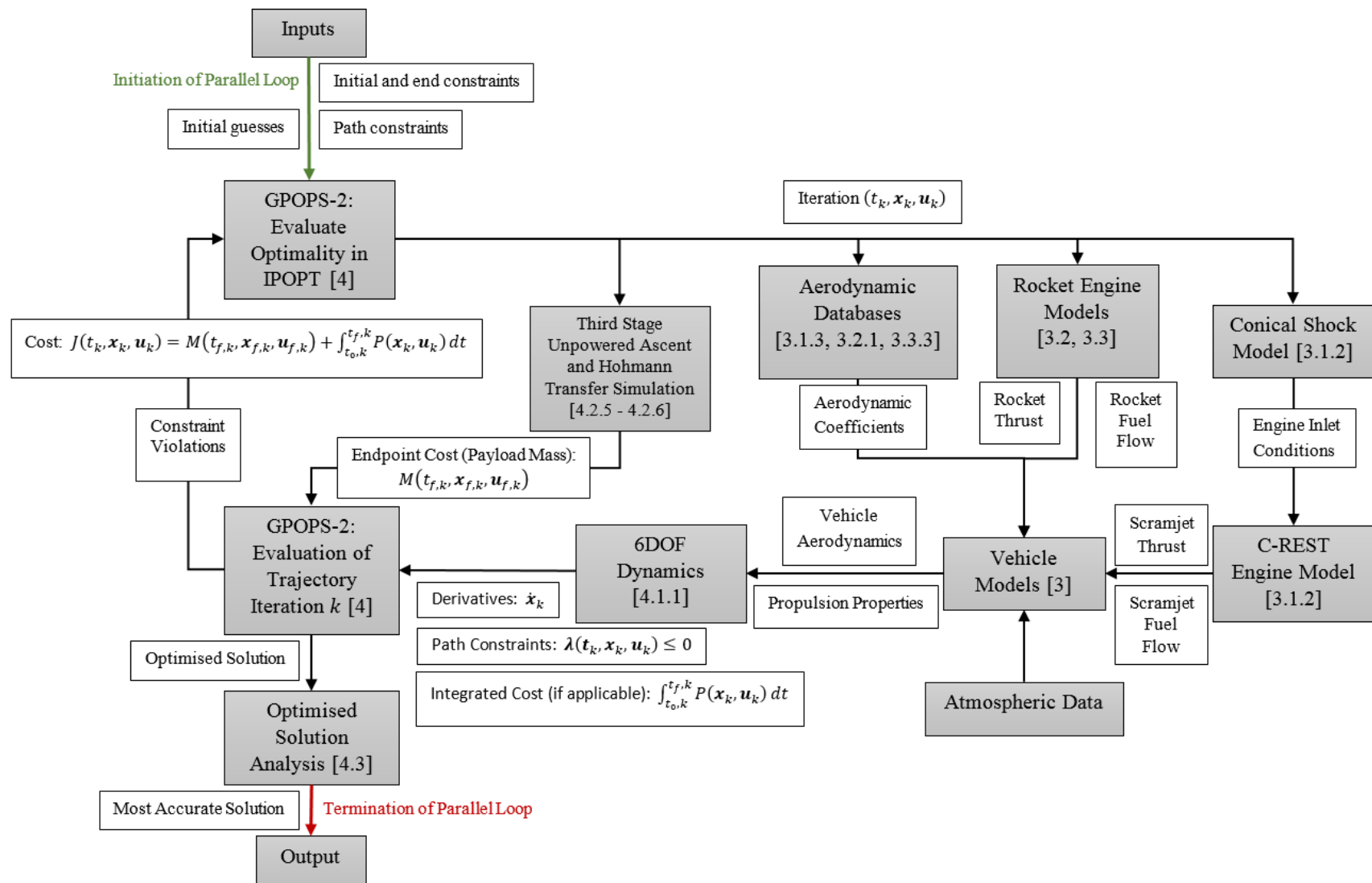


Figure 4.8: The process of the rocket-scramjet-rocket trajectory optimisation. Relevant sections are indicated in square brackets at each process step.

CHAPTER 5

OPTIMISED ASCENT TRAJECTORY

This chapter presents a maximum payload-to-orbit trajectory optimisation for the rocket-scramjet-rocket launch system incorporating the SPARTAN scramjet-powered accelerator. This launch system is simulated as being launched from the Equatorial Launch Australia launch site in East Arnhem Land (Detailed in Section 4.2), and delivers a small satellite into sun synchronous orbit. LODESTAR is used to calculate the maximum payload-to-orbit trajectory solutions for this launch system. First, a trajectory solution is calculated in which the SPARTAN flies at constant dynamic pressure. This trajectory is calculated to serve as a baseline for comparisons to be made, as previous studies have assumed that flying the SPARTAN at its maximum allowable dynamic pressure would produce the best overall system performance[12]. An optimal payload-to-orbit trajectory is then developed, and the trajectory shape compared and contrasted to the constant dynamic pressure trajectory. Lastly, a sensitivity study is performed, varying key performance parameters of the launch system and investigating the effects of each parameter on the performance of the launch system.

The following trajectories are developed:

- Case 1: $q = 50\text{kPa}$ fixed SPARTAN trajectory.
 - This trajectory provides a baseline trajectory for comparison purposes.
- Case 2: Trajectory optimised for payload-to-orbit, $q_{max} = 50\text{kPa}$.
 - This trajectory demonstrates improved performance through trajectory optimisation.
- Case 3: Variation of maximum allowable dynamic pressure between $q_{max} = 40\text{kPa}$ & $q_{max} = 60\text{kPa}$.
 - Comparison of these simulations allows an investigation into the influence of the SPARTAN's ability to withstand aerodynamic forces on the performance of the launch vehicle.

- Case 4: Variation of the coefficient of drag of the SPARTAN between $C_d = 90\%$ & $C_d = 110\%$.
→ Comparison of optimal trajectories with drag variation allows investigation of the effects of the SPARTAN's aerodynamic design on launch system performance.
- Case 5: Variation of the specific impulse of the SPARTAN's C-REST engines between $I_{SP} = 90\%$ & $I_{SP} = 110\%$.
→ Comparison of optimal trajectories with C-REST specific impulse variation allows investigation of the effects of the efficiency of the C-REST engines on the performance of the launch system.
- Case 6: Variation of the mass of the SPARTAN between $m_2 = 95\%$ & $m_2 = 105\%$.
→ Comparison of optimal trajectories with SPARTAN mass variation allows investigation of the effects of the internal design of the SPARTAN on the launch system performance.
- Case 7: Variation of the fuel mass of the SPARTAN between $m_{fuel} = 90\%$ & $m_{fuel} = 110\%$.
→ Comparison of optimal trajectories with SPARTAN fuel mass variation allows investigation of the effects of the amount of fuel which the SPARTAN is able to carry on the launch system efficiency.
- Case 8: Variation of the mass of the third stage rocket between $m_3 = 90\%$ & $m_3 = 110\%$.
→ Comparison of optimal trajectories with third stage mass variation allows investigation of the effects of the third stage internal design on the efficiency of the system.
- Case 9: Variation of the specific impulse of the third stage rocket between $I_{SP,3} = 95\%$ & $I_{SP,3} = 105\%$.
→ Comparison of optimal trajectories with third stage specific impulse variation allows investigation of the effects of the efficiency of the third stage engine on the overall efficiency of the launch system.
- Case 10: Variation of the coefficient of drag of the third stage rocket between $C_d = 80\%$ & $C_d = 120\%$.
→ Comparison of optimal trajectories with third stage drag variation allows investigation of the effects of the aerodynamic design of the third stage on the performance of the launch system.

These optimised trajectory cases allow the benefits of flying an optimised trajectory to be quantified, and enable the key design parameters of the SPARTAN and third stage rocket to be characterised. Comparisons between the sensitivity studies allow for the relative impact of each design parameter on the performance of the launch system to be assessed.

The performance of launch system, as well as each individual stage, is quantified using exergy analysis. Exergy expresses how much useful work is available to a system, and exergy efficiency

quantifies how well a system utilises the available work. Exergy is lost due to inefficiencies within a launch system. These inefficiencies arise from many sources, including the energy being lost due to the inability of the propulsion system to convert all of the combustion energy to thrust, the energy which must be used to overcome drag, and energy being lost due to manoeuvring. Exergy efficiency is an important parameter for analysing launch vehicles, allowing the relative efficiencies of each stage to be compared when the design or trajectory of a launch system is varied[159]. The exergy efficiency of a stage of a launch system is expressed as the fraction of the fuel combustion energy which is turned into kinetic and potential energy during flight:

$$\eta_{exergy,stage} = 1 - \frac{\Delta m_{fuel} H_{fuel} - \Delta KE - \int mgdz}{\Delta m_{fuel} H_{fuel}}, \quad (5.1)$$

where H_{fuel} is the heating value of the fuel, KE is the change in the kinetic energy of the stage, and $\int mgdz$ is the change in potential energy of the stage over its trajectory. This exergy efficiency expresses how efficiently each stage utilises its available fuel over each individual trajectory. However, this stage-based exergy efficiency does not account for the effects of the unused mass of each stage on the performance of the launch system. The total exergy efficiency of the launch system is calculated as the fraction of the total available energy which goes directly into placing the payload into orbit:

$$\eta_{exergy} = \frac{\Delta KE_{payload} + \Delta PE_{payload}}{\sum_{stage} \Delta m_{fuel} H_{fuel}}. \quad (5.2)$$

This total exergy efficiency expresses how efficiently the launch system as a whole is able to accelerate the payload to orbit. Within this work, exergy efficiency is expressed as the percentage of total exergy utilised, $\% \eta$, ie. $\eta_{exergy} \times 100$.

5.1 Case 1: Constant Dynamic Pressure Trajectory

The first trajectory which is produced using LODESTAR is a maximum payload-to-orbit trajectory in which the SPARTAN flies a constant dynamic pressure path, at its maximum allowable dynamic pressure of 50kPa. In order to drive the SPARTAN towards a constant dynamic pressure path, the cost function described in Table 4.3 is utilised. In addition to the dynamic pressure cost function, the maximum payload-to-orbit cost function is also active on the third stage phase, so that when the SPARTAN is close to 50kPa, the third stage will fly a maximum payload-to-orbit trajectory from the termination of the SPARTAN's constant dynamic pressure path. Previous studies have assumed that flying the SPARTAN at constant dynamic pressure will produce the best possible system performance[12]. Because of this assumption, a constant dynamic pressure trajectory is produced to serve as a baseline for comparison with the maximum payload-to-orbit optimised trajectory. Producing a constant dynamic pressure trajectory also serves to verify that LODESTAR is able to calculate a tra-

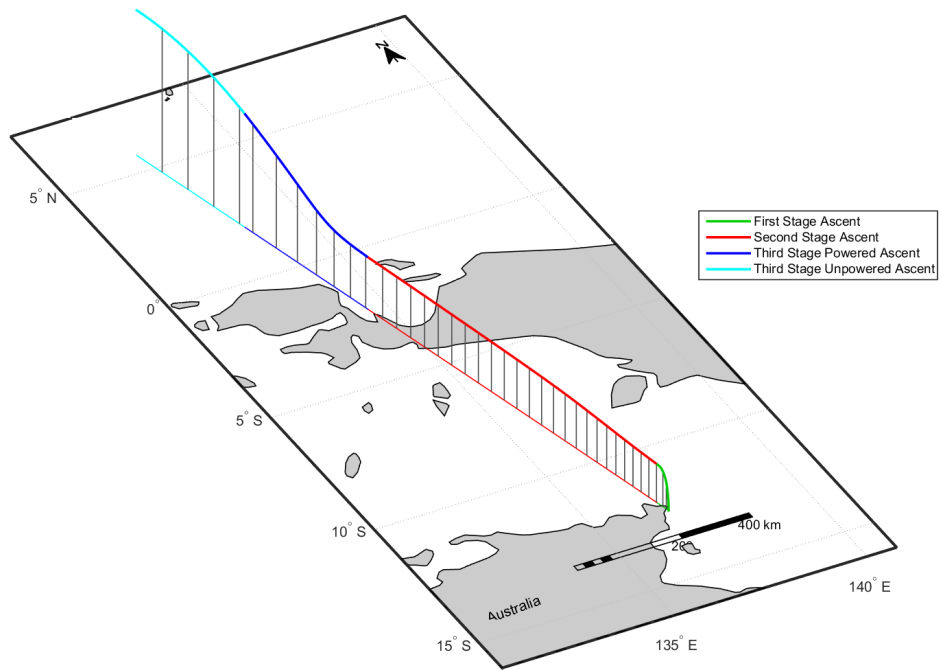


Figure 5.1: Maximum payload-to-orbit trajectory path with the SPARTAN flying at constant dynamic pressure (Case 1). Initial heading angle 92.6° .

jectory in which the SPARTAN flies at the maximum possible dynamic pressure for the duration of its flight. In addition, the simulation of the aerodynamics and design of the launch system has been improved in this work, compared to previous studies[12]. In this work, Cart3D is used for aerodynamic calculations, the internal design of the SPARTAN is modified, the third stage design is modified significantly, and the first stage is included. Due to these changes and additions, it must be confirmed that the launch system is able to fly mission which involves the SPARTAN maintaining maximum dynamic pressure, to ensure that any deviations from the SPARTAN's maximum dynamic pressure in the maximum payload-to-orbit trajectory serve to improve the performance of the system, rather than being a result of the problem setup or design constraints.

LODESTAR is successfully used to simulate the trajectory of the rocket-scramjet-rocket system, with the SPARTAN flying at constant dynamic pressure, achieving a payload-to-orbit of 158.4kg. Figure 5.1 shows the simulated trajectory path, and Table 5.1 provides a summary of the key parameters

Trajectory Condition	Value
Payload to Orbit (kg)	158.4
Total η_{exergy} (%)	1.432
1st Stage η_{exergy} (%)	8.010
Separation Alt, 1→2 (km)	23.78
Separation v, 1→2 (m/s)	1445
Separation γ, 1→2 (m/s)	0.7
2nd Stage η_{exergy} (%)	12.260
Separation Alt, 2→3 (km)	32.25
Separation v, 2→3 (m/s)	2803
Separation γ, 2→3 (deg)	0.4
Separation q, 2→3(kPa)	49.9
2nd Stage L/D, 2→3	5.1
2nd Stage Flight Time (s)	619.4
3rd Stage η_{exergy} (%)	16.865
3rd Stage $t, q > 5\text{kPa}$ (s)	99.2
3rd Stage max α (deg)	13.2
3rd Stage Fuel Mass (kg)	2856.4

Table 5.1: Summary of the key results from a maximum payload-to-orbit trajectory with the SPARTAN constrained to 50kPa.

of the trajectory, including the exergy efficiency of each stage. The rocket-scramjet-rocket system launches vertically, flying a fixed vertical trajectory for 3.9s, after which a pitchover is initiated at a heading angle of 92.6°. Under power of the first stage rocket, the launch system begins pitching, flying north-west, over the Arafura Sea. After pitchover the angle of attack stays constant at 0° for 49.1s, as shown in Figure 5.2. At this point, the angle of attack is reduced, reaching a minimum of -4.89°, before increasing back up to 0° for stage separation. The SPARTAN is separated at a trajectory angle of 0.7° at an altitude of 23.78km, a total flight time of 120.9s, with a total ground distance of 45.7km covered under power of the first stage rocket. In order to release the SPARTAN at a lower trajectory angle, the first stage must launch with a lower fuel mass, to allow it to pitch in the correct manner. To achieve a constant dynamic pressure trajectory, the first stage launches with a fuel mass of 17010kg. This is significantly lower than the full amount of allowable fuel mass, 17934kg, indicating that the launch system is unable to achieve 50kPa first stage-SPARTAN conditions using the full fuel mass. The first stage rocket achieves an exergy efficiency of 8.010% η when separating the SPARTAN onto a constant dynamic pressure trajectory.

The constant dynamic pressure trajectory for the SPARTAN stage is shown in Figure 5.3 with key results summarised in Table 5.1. After the separation of the first stage rocket, the SPARTAN flies north west over the Arafura Sea, and crosses West Papua before releasing the third stage rocket. Due to the clear objective of a constant dynamic pressure trajectory, any deviations from the target dynamic pressure are readily apparent, allowing the efficacy of the optimiser to be verified. The constant

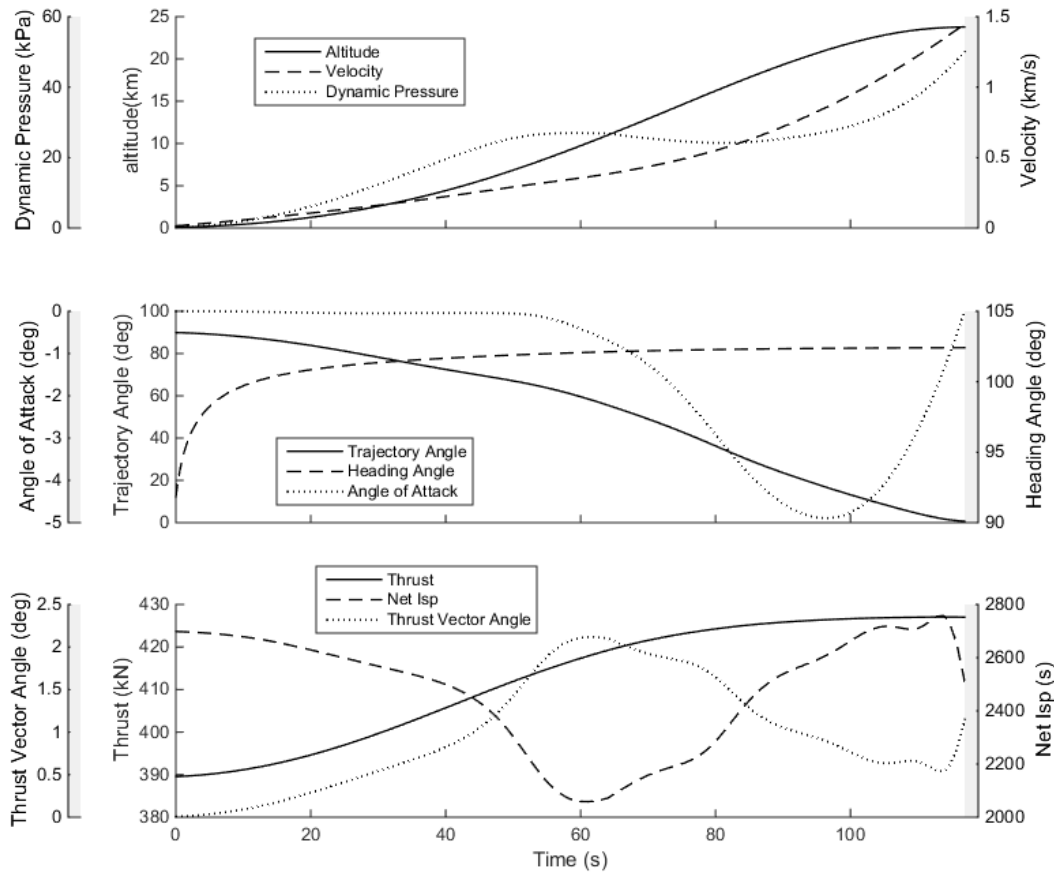


Figure 5.2: The first stage trajectory of the launch system, with the SPARTAN constrained to flight at constant dynamic pressure (Case 1).

dynamic pressure simulation, shown in Figure 5.3, shows very close adherence to 50kPa dynamic pressure (maximum 0.2% deviation). Third stage release occurs at 619.4s at 32.25km altitude. Over the trajectory, the Mach no. increases from 4.85 to 9.23, the velocity increases from 1445m/s to 2803m/s, and the flap deflection increases from -3.2° to 4.7° . At the beginning of the trajectory the equivalence ratio increases as the capture limitations are relaxed with increasing Mach number. This causes the net specific impulse to increase, to a maximum of 1481s, during the first 169.3s flight time. After this initial increase, the net specific impulse ($I_{sp,net} = \frac{T-D}{\dot{m}_fg}$) decreases over the trajectory, as the efficiency of the scramjet engines decreases. The exergy efficiency of the SPARTAN is 12.260η over its trajectory, 4.250% η higher than the exergy efficiency of the first stage rocket. This increased exergy efficiency compared to the first stage rocket is due to the high specific impulse of the scramjet engines, utilising the available fuel more effectively.

Figure 5.4 shows the corresponding third stage atmospheric exit trajectory after release, evaluated as described in Chapter 4. The third stage released from a constant dynamic pressure trajectory, shown

5.1. CASE 1: CONSTANT DYNAMIC PRESSURE TRAJECTORY

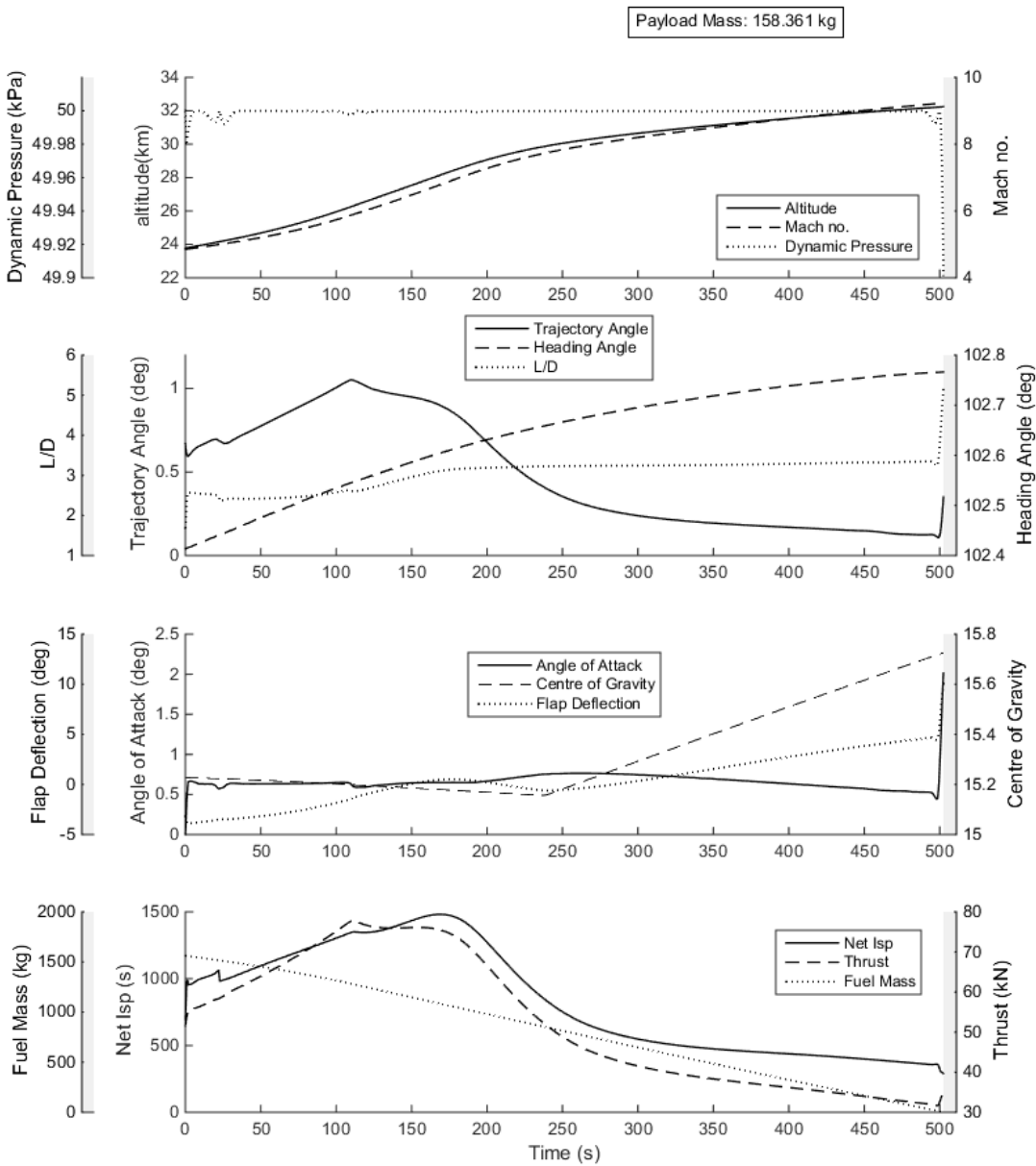


Figure 5.3: The constant dynamic pressure flight path of the SPARTAN (Case 1).

in Figure 5.4, is limited by the maximum thrust vector angle for the first 37.3s of flight. This places significant limitations on the maximum allowable angle of attack. This angle of attack limitation reduces the lift of the rocket, causing the flight path angle to stay close to horizontal for the first 20s of flight. This slow ascent leads to the rocket spending a large amount of time at low altitude, in a high drag environment, spending 99.2s over 5kPa dynamic pressure. The angle of attack increases gradually to a maximum of 13.2° at 62.5s before decreasing until burnout at 130.4s. The dynamic pressure of the third stage rocket reduces to 10kPa at 171.4s, and the heat shield is discarded. The

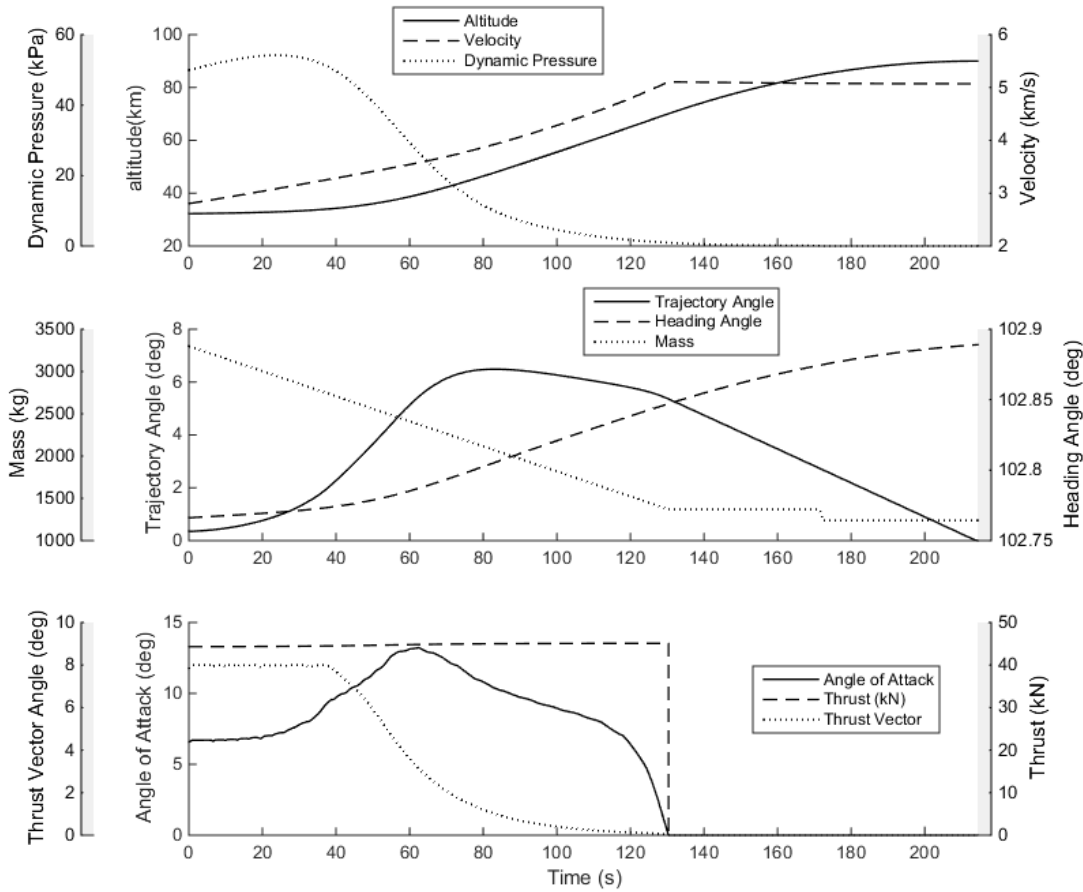


Figure 5.4: The third stage trajectory of the launch system, with the SPARTAN constrained to flight at constant dynamic pressure (Case 1).

rocket coasts to a trajectory angle of 0° , which is reached at a total flight time of 214.4s. The trajectory terminates at 90km, the lowest allowable altitude for circularisation. When this altitude is reached, the trajectory is circularised and performs a Hohmann transfer manoeuvre to reach sun synchronous orbit. The exergy efficiency of the third stage rocket over its trajectory is significantly lower than the preceding two stages, at only $16.865\% \eta$. This low efficiency is a consequence of the third stage rocket spending large amounts of time within the atmosphere, at low trajectory angle. A significant portion of the available energy of the third stage must be used to overcome the high drag and aerodynamic moments present at low altitude, as well as being used to provide additional lift to the third stage rocket.

5.2 Case 2: Optimised Ascent Trajectory

This section presents the maximum payload-to-orbit trajectory for the rocket-scramjet-rocket launch system. The optimal trajectory shape for a $q = 50\text{kPa}$ limited, maximum payload-to-orbit trajectory is shown in Figure 5.5 with key results summarised in Table 5.2. The maximum payload-to-orbit trajectory shape involves the SPARTAN performing altitude raising manoeuvres, where the dynamic pressure of the SPARTAN is lowered from its maximum of 50kPa. These manoeuvres serve either to increase the net specific impulse of the SPARTAN, or to trade-off the efficiency of the SPARTAN in order to increase the efficiency of the first and third stages. This payload-to-orbit optimised trajectory is able to deliver 189.2kg of payload to heliocentric orbit, an increase of 16.3% over the constant, 50kPa dynamic pressure result (Case 1).

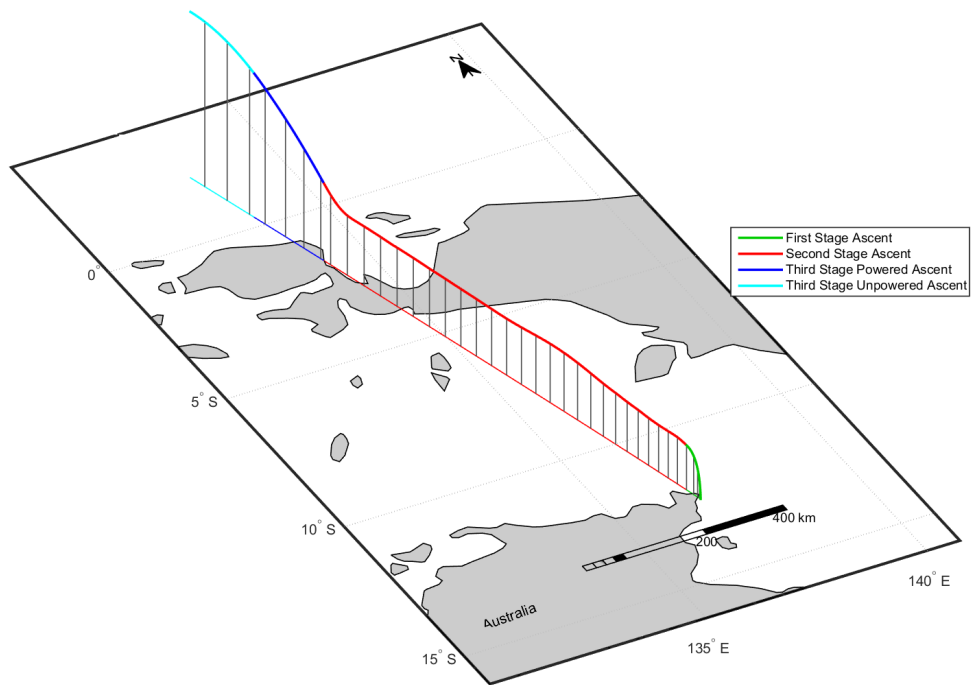


Figure 5.5: The optimised maximum payload-to-orbit trajectory of the launch system (Case 2).

The first stage trajectory, shown in Figure 5.6, has a very similar trajectory shape to that of the first stage releasing the SPARTAN onto a constant dynamic pressure trajectory. However, the trajectory

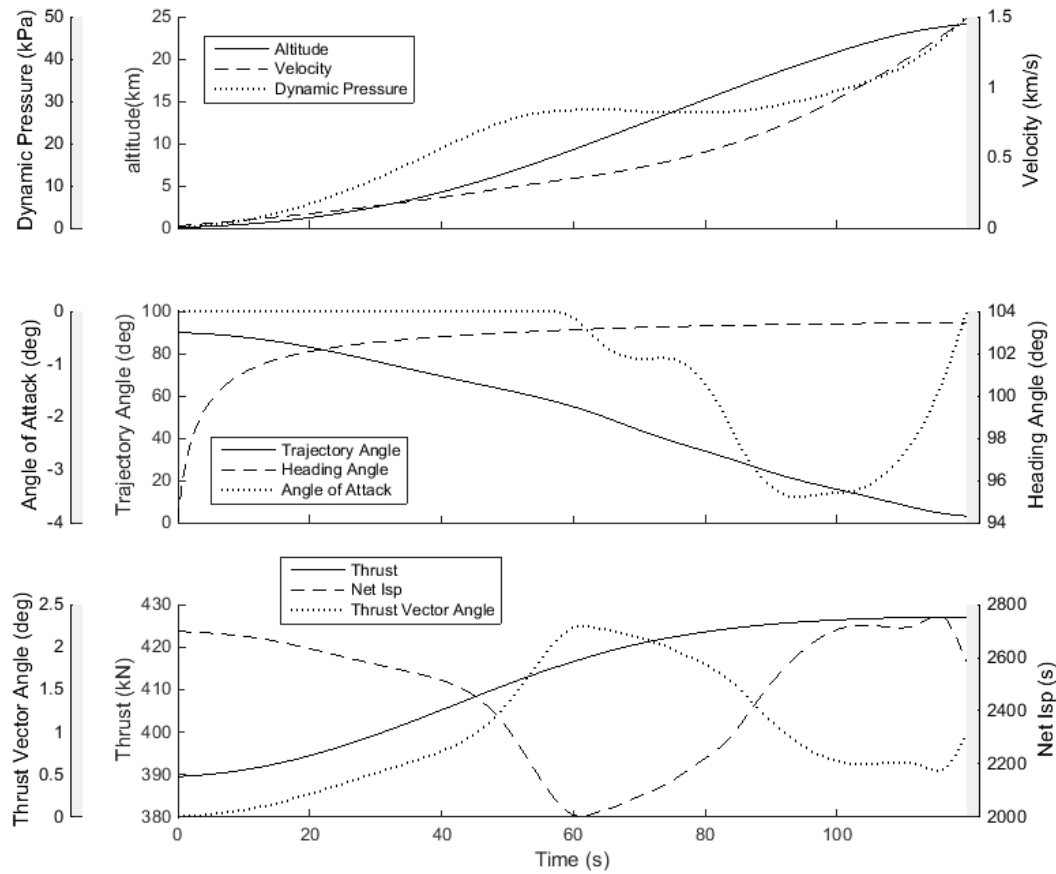


Figure 5.6: The optimised maximum payload-to-orbit trajectory of the launch system under power of the first stage rocket (Case 2).

angle at the separation of the SPARTAN is 10.8° , rather than the trajectory angle of 0.4° required for the SPARTAN to fly a constant dynamic pressure trajectory. Additionally, the altitude at first stage-SPARTAN separation is raised to 24.12km, an increase of 0.34km compared to the separation point of a SPARTAN flying at constant 50kPa dynamic pressure. This higher release angle and altitude causes the altitude of the SPARTAN to immediately increase, and consequently for its dynamic pressure to decrease. This trajectory angle at release is the consequence of a trade-off between the efficiency of the SPARTAN and the first stage efficiency. The efficiency of the first stage is increased to $8.171\%\eta$, an overall improvement of $+0.161\%\eta$ (+2.0%) compared to the first stage separating the SPARTAN at 50kPa conditions.

In addition to improving the exergy efficiency of the first stage, the higher release angle and altitude conditions also allow the first stage to launch with more fuel. In order to release the SPARTAN at a trajectory angle conducive to flying at 50kPa, the first stage must launch with a low fuel mass, to allow it to pitch in the correct manner. When the SPARTAN release angle and altitude are increased

during the maximum payload-to-orbit trajectory, the first stage is able to launch with a fuel mass of 17185kg, an increase of 1.0% compared to the constant dynamic pressure trajectory in Case 1. During the maximum payload-to-orbit trajectory, the first stage rocket releases the SPARTAN at a velocity of 1484.3m/s, an increase of 2.7% compared to the first stage releasing the SPARTAN onto a constant dynamic pressure trajectory. Neither first stage utilises the full amount of allowable fuel mass, 17934kg, indicating that using the full fuel mass would necessitate separation conditions which would reduce the efficiency of the SPARTAN unfavourably. These results indicate that the fuel mass utilised by the first stage has a distinct optimal magnitude, and that including additional fuel over the optimal amount does not increase the performance of the system. This implies that the size of the first stage is closely linked to the optimal trajectory of the system, and that future first stage designs should be sized so that optimal pitching is achieved.

Trajectory Condition	Value
Payload to Orbit (kg)	189.2
Total η_{exergy} (%)	1.693
1st Stage η_{exergy} (%)	8.171
Separation Alt, 1→2 (km)	24.12
Separation v, 1→2 (m/s)	1484
Separation γ, 1→2 (m/s)	3.1
2nd Stage η_{exergy} (%)	10.942
Separation Alt, 2→3 (km)	41.73
Separation v, 2→3 (m/s)	2687
Separation γ, 2→3 (deg)	10.8
Separation q, 2→3(kPa)	10.8
2nd Stage L/D, 2→3	4.0
2nd Stage Flight Time (s)	648.1
3rd Stage η_{exergy} (%)	20.321
3rd Stage $t, q > 5\text{kPa}$ (s)	14.2
3rd Stage max α (deg)	16.2
3rd Stage Fuel Mass (kg)	2825.6

Table 5.2: A summary of key results from the maximum payload-to-orbit trajectory (Case 2).

After the initial deviation from the maximum dynamic pressure, the SPARTAN returns to 50kPa dynamic pressure for a time. At 122.5 seconds, the altitude of the trajectory is again raised, and the dynamic pressure decreased, to a minimum of 35.6kPa. In this region the net specific impulse of the SPARTAN is relatively homogeneous with respect to changes in dynamic pressure. This homogeneous region can be observed in the specific impulse of the C-REST engines in Figure 5.9, between inlet Mach number (M1) values of 6 and 7, and in Figure 5.8, in the flight Mach number 7 and 8 plots of net specific impulse. This homogeneity means that the variation in engine performance with flight conditions is small and that flying at the maximum dynamic pressure in this region does not maximise the specific impulse from the C-REST engines. Figure 5.8 shows that while the optimised trajectory

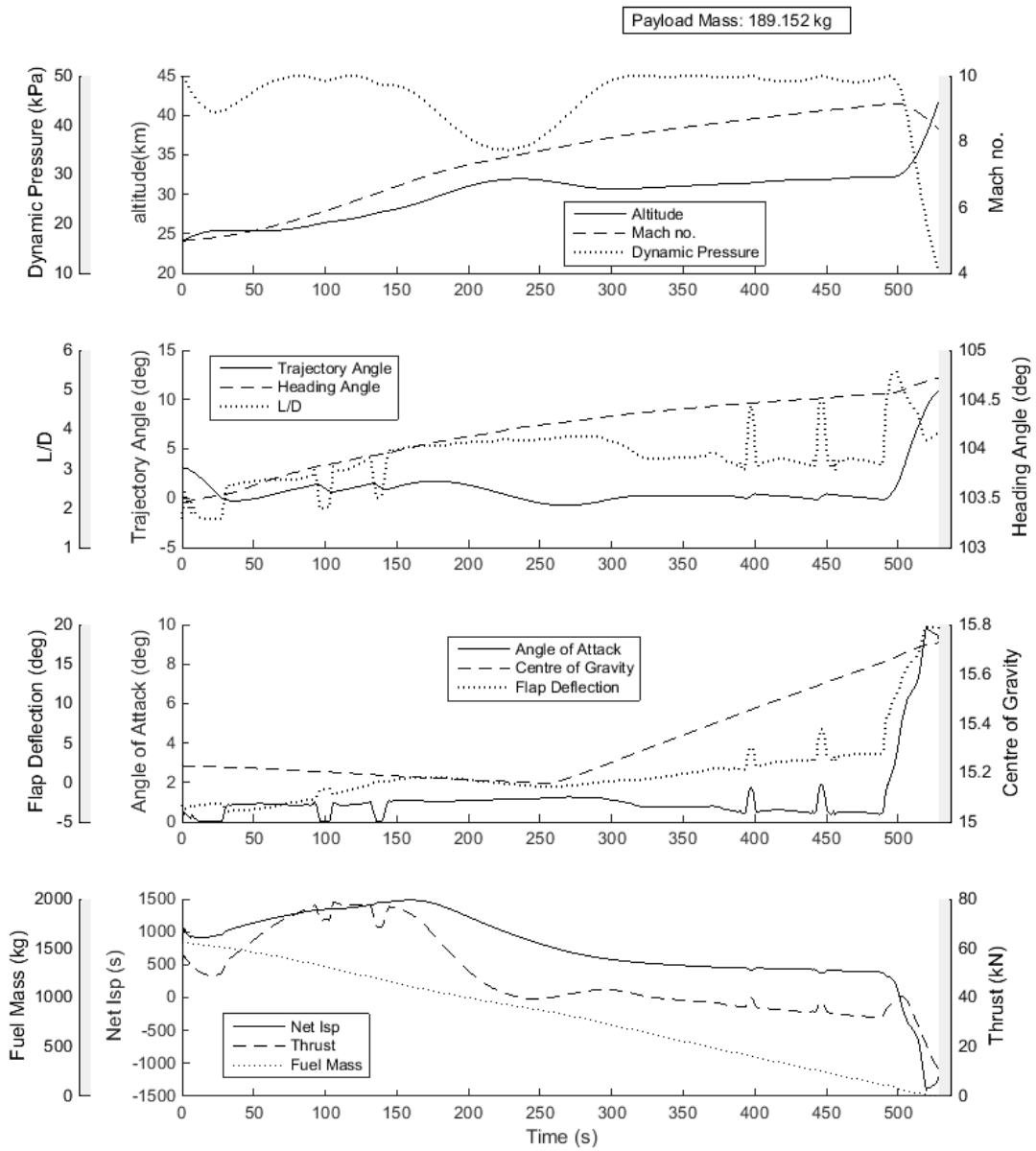


Figure 5.7: The optimised maximum payload-to-orbit trajectory of the SPARTAN (Case 2).

differs significantly from a constant dynamic pressure trajectory, both achieve similar net specific impulses with no detectable variations, with the exception of the initial trajectory conditions at Mach 5, where the efficiency of the SPARTAN is traded for first stage rocket performance. Appendix C.1 details a maximum payload-to-orbit trajectory in which the SPARTAN is constrained to 50kPa between Mach 6-8, to prevent the altitude raising manoeuvre from taking place. This constrained trajectory allows for the magnitude of the performance gain from the altitude raising manoeuvre to be quantified. The altitude raising manoeuvre increases the combined total efficiency launch system from $1.690\% \eta$

to $1.693\%\eta$ (calculated including the energy lost due to stage separations). This is a relatively minor variation, and the payload-to-orbit benefits of this altitude raising manoeuvre are correspondingly small. The optimised trajectory exhibits a payload-to-orbit increase of 0.4kg compared to the trajectory constrained to 50kPa between Mach 6-8, a difference of only 0.2%. However, it is important to note that, while its benefits are small, the altitude raising manoeuvre is consistently observed in every maximum payload-to-orbit optimised trajectory. Also, despite its small benefit to payload-to-orbit, this altitude raising manoeuvre is significant as it reduces the heating and structural loading on the SPARTAN, though it is beyond the scope of this study to quantify these benefits.

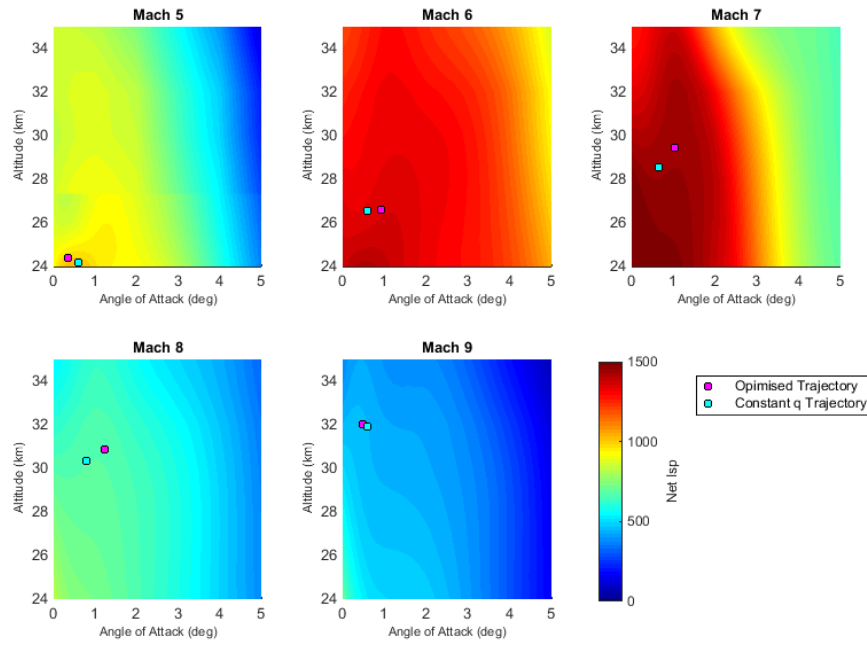


Figure 5.8: Net Isp contours for the SPARTAN at Mach numbers from 5-9, showing optimised trajectory and constant dynamic pressure trajectory.

At 314.3s, the SPARTAN returns to flight at close to 50kPa dynamic pressure until 494.1s at which point a pull-up manoeuvre is performed, gaining altitude until the third stage rocket is released at 528.4s SPARTAN flight time. The point at which the pull-up manoeuvre begins is the location that takes into account the best combination of velocity, altitude and release angle for the trade-off between the scramjet stage performance and the release of the third stage rocket. This pull-up indicates the region at which increasing altitude and release angle becomes more important than extracting maximum thrust from the scramjet (which is generally attained at high q and low flight angle at an equivalence ratio of 1). At high Mach numbers, flight in a lower dynamic pressure environment results in less thrust output from the scramjet engines, as well as an increase in angle of attack and flap deflection angle to compensate for the additional lift required. Due to this, less overall acceleration is obtained compared to the constant dynamic pressure result with minimum pull-up. Separation oc-

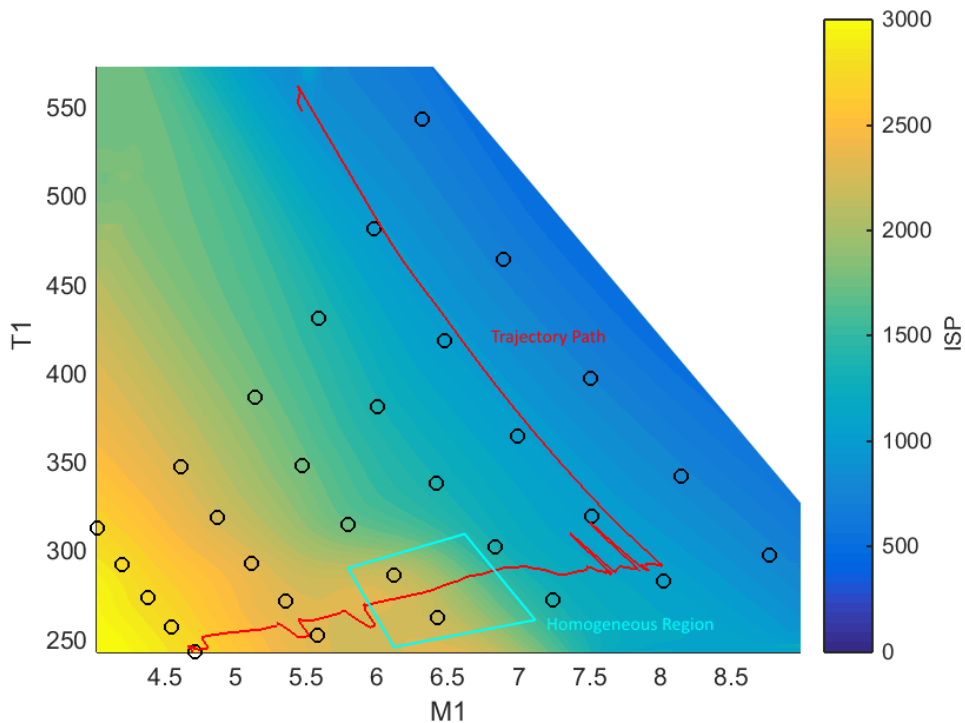


Figure 5.9: The specific impulse of the C-REST engines, plotted for inlet temperature (T_1) and inlet Mach number (M_1). Data points are shown in black.

curs at a velocity of 2687m/s, a decrease of 116.2m/s (-4.1%). However, at the same time separation altitude increases by 9.48km (+29.4%) to 41.73km, resulting in a decrease in separation dynamic pressure to 10.8kPa. The larger scramjet stage pull-up assists the rocket in manoeuvring to exoatmospheric altitude by increasing the altitude and angle at separation, utilising the superior aerodynamics and manoeuvrability of the scramjet vehicle. The increase in release angle, to the optimal angle of 10.8°, significantly reduces the turning that is required by the rocket as evident from comparing Fig 5.4 and 5.10. Overall, the altitude raising manoeuvres which the SPARTAN performs result in a decrease in the exergy efficiency of the SPARTAN to $10.942\%\eta$, a total decrease of $1.318\%\eta$ compared to the SPARTAN flying at a constant dynamic pressure. However, the optimised trajectory drastically increases the exergy efficiency of the third stage, to $20.321\%\eta$, an overall increase of $6.72\%\eta$ compared to the third stage released from the SPARTAN flying a constant dynamic pressure trajectory. This leads to the total exergy efficiency of the launch system increasing from $1.432\%\eta$ to $1.693\%\eta$.

The trajectory of the third stage rocket after release from an optimised scramjet trajectory is shown in Figure 5.10. Release at a higher, more optimal angle, reduces the aerodynamic moment necessary to trim the vehicle. In turn, this reduced moment reduces the necessary thrust vector angle, so that the thrust vector limit is not reached. The third stage rocket is released at a high trajectory angle, and continuously gains altitude, avoiding the close-to-horizontal flight required by the fixed dynamic

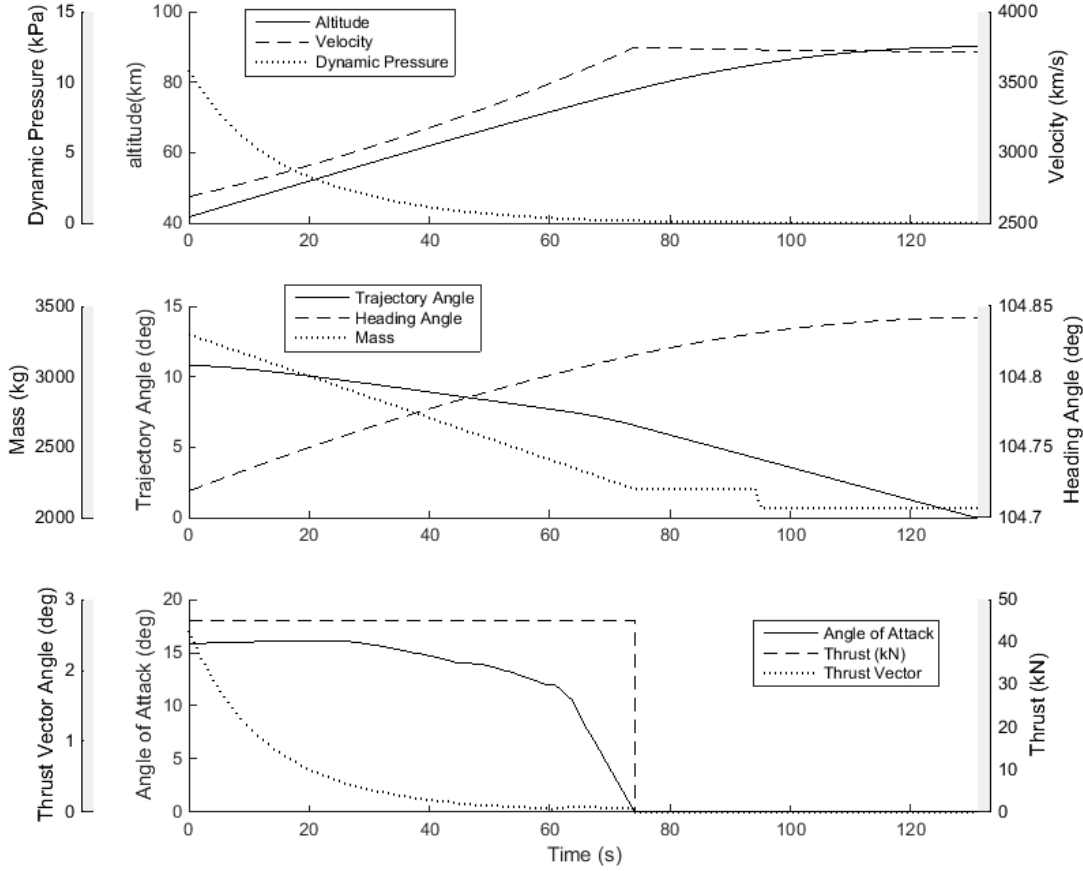


Figure 5.10: The third stage trajectory of the launch system flying the maximum payload-to-orbit trajectory (Case 2).

pressure release (Case 1). Due to the higher altitude and release angle, the third stage rocket is released at a lower dynamic pressure, 10.8kPa compared to 49.9kPa, and spends much less time flying in a high dynamic pressure environment, 13.3s at over 5kPa dynamic pressure rather than 99.2s. The reduced time that the rocket must spend in a high dynamic pressure environment and decrease in the maximum dynamic pressure that the rocket stage experiences may allow the structural mass and heat shielding necessary to achieve exoatmospheric flight to be decreased. This may enable higher payload to orbit, though it is beyond the scope of this study to investigate these design changes.

Previous studies considering the optimised trajectory of vehicles with multiple propulsion methods within a single stage show airbreathing-rocket transitions at, or close to, exoatmospheric flight[28, 58, 67]. compared to these studies, the maximum payload to orbit trajectory of the multi-stage system shows a scramjet-rocket transition point at much lower altitudes. This lower transition point is a consequence of the stage separation creating an energy trade-off between the stages, which does not occur in a single stage vehicle. Single-stage vehicles must necessarily transport all components

to exoatmosphere, and so utilise the scramjet engines until higher altitude to take advantage of their high efficiency. A multi-stage vehicle is able to separate the scramjet stage. This separation occurs when the performance benefits provided by the superior aerodynamics and engine efficiency of the scramjet stage are offset by the energy required to lift the extra mass to higher altitude. The beneficial ability to separate the scramjet stage results in a lower altitude scramjet-rocket transition point, when compared to single stage vehicle designs.

5.3 Sensitivity Analysis

A sensitivity analysis is conducted, in which selected design parameters of the launch system are varied, and the effects on the optimised maximum payload-to-orbit trajectory of the launch system are investigated. Appendix D shows comparison plots of the second and third stage trajectories for each parameter variation study, however, the first stage rocket trajectories are very similar and are not compared graphically. Key results including performance factors of each stage and separation conditions are summarised within this section. This study is performed in order to determine the relative importance of the design parameters on the efficiency of the system, as well as investigating changes in the maximum payload-to-orbit trajectory as the performance of the launch system is varied. The investigation of the key design parameters of the launch system provides a metric which is used to quantify the relative impact of the vehicle design on the performance of the launch system. The performance trade-offs between the stages are investigated by studying the variation in the optimised trajectory, particularly the stage separation conditions, as the parameters of the launch system design are changed. Trends are developed for each parameter study, quantifying how much the performance factors of the launch system vary per percentage of variation of each design parameter ($\Delta\%$). This percentage variation gives a general metric for how much each design parameter effects the performance factors of the launch system, however, the relative magnitude of one percent variation of each individual design parameter must be taken into account when making comparisons. The information obtained from this parameter variation study can be used to inform future launch system designs. In addition to investigating the trends in the performance of the launch system, this sensitivity study serves to verify the ability of LODESTAR to generate optimal trajectories with varied vehicle designs, as well as investigating the robustness of the optimised solution.

When necessary for the trajectory simulations within this section, it is assumed that the scramjet engines are operable at velocities slightly under Mach 5. This assumption is made in order to allow meaningful assessment of parameters which effect the first stage-SPARTAN separation velocity, without modification of the first stage rocket. All optimised trajectories within this section use the full amount of fuel available to the SPARTAN vehicle.

5.3.1 Case 3: Dynamic Pressure Sensitivity

Trajectory Condition	q_{max} :	40kPa	45kPa	50kPa	55kPa	60kPa	$\Delta/\Delta\%q$
Payload to Orbit (kg)	181.4	185.7	189.2	192.8	196.4	0.4	
Payload Variation (%)	-4.11	-1.82	0.00	1.90	3.82	0.2	
Total η_{exergy} (%)	1.624	1.662	1.693	1.726	1.758	3e-05	
1st Stage η_{exergy} (%)	8.235	8.204	8.171	8.128	8.103	-0.003	
Separation Alt, 1→2 (km)	25.49	24.77	24.12	23.51	23.00	-0.06	
Separation v, 1→2 (m/s)	1480	1483	1484	1483	1485	-	
Separation γ, 1→2 (m/s)	5.5	4.4	3.1	1.1	0.8	-0.13	
2nd Stage η_{exergy} (%)	10.571	10.760	10.942	11.168	11.366	0.02	
Separation Alt, 2→3 (km)	42.00	41.90	41.73	41.61	41.39	-0.02	
Separation v, 2→3 (m/s)	2657	2673	2687	2703	2720	1.56	
Separation γ, 2→3 (deg)	10.1	10.5	10.8	11.0	11.2	0.03	
Separation q, 2→3(kPa)	10.2	10.4	10.8	11.1	11.6	0.04	
2nd Stage L/D, 2→3	3.9	3.9	4.0	4.0	4.3	-	
2nd Stage Flight Time (s)	731.6	686.1	648.1	611.2	587.8	-3.62	
3rd Stage η_{exergy} (%)	20.309	20.367	20.321	20.321	20.296	-	
3rd Stage $t, q > 5\text{kpa}$ (s)	12.7	12.4	14.2	12.6	13.3	-	
3rd Stage max α (deg)	17.8	16.6	16.2	15.5	14.7	0	
3rd Stage Fuel Mass (kg)	2833.4	2829.1	2825.6	2822.0	2818.4	-0.37	

Table 5.3: Comparison of key trajectory parameters with variation in the maximum dynamic pressure of the SPARTAN.

To investigate the sensitivity of the vehicle to changes in q_{max} , the maximum dynamic pressure is varied by $\pm 10\text{kPa}$ in 5kPa increments, and the flight trajectory optimised, with results shown in Table 5.3, and comparison plots shown in Appendix D.1.1. The variation in maximum dynamic pressure has only a small effect on the total exergy efficiency of the system, and hence only a small effect on the payload mass delivered to heliocentric orbit. Varying the maximum dynamic pressure by $\pm 20\%$ causes a variation of only $+0.065\%\eta$ or $-0.069\%\eta$ in exergy efficiency and a corresponding $+7.2\text{kg}$ ($+3.8\%$) or -7.8kg (-4.1%) variation in payload to orbit. Separation altitudes of 42.00km and 41.39km are reached for the 40kPa and 60kPa limited cases respectively, with separation velocities of 2657m/s and 2720m/s . The 40kPa limited case flies for 731.6s , significantly longer than the 60kPa case which flies for 587.8s . As the dynamic pressure decreases, the size of the altitude raising manoeuvre in the middle of the trajectory lessens. This is due to the increased altitude and angle of attack moving the flight conditions into a region where the specific impulse of the C-REST engines is not homogeneous, so that it is beneficial to fly at maximum dynamic pressure. All trajectories pull-up to similar altitudes, with relatively small variation in separation velocity. This small variation in velocity is despite the increase in air density and decrease in angle of attack required for flight at higher dynamic pressures, both of which increase the mass flow into the engine. Although the thrust output of the C-REST engines increases with dynamic pressure, so does the drag on the vehicle, and the net increase in

performance is relatively small ($0.02 \Delta\eta_{exergy}/\Delta\%q$). The trade-off between the exergy efficiency of the first and second stages shifts as the dynamic pressure limit is increased, with the first stage rocket becoming less efficient (varying from an η_{exergy} of $8.235\%\eta$ at 40kPa to $8.103\%\eta$ at 60kPa), while the exergy efficiency of the SPARTAN increases (varying from an η_{exergy} of $10.571\%\eta$ at 40kPa to $11.366\%\eta$ at 60kPa). The decreased altitude of first stage-SPARTAN separation requires the first stage to pitch more to reach the optimal staging conditions, resulting in a less efficient first stage trajectory, which partially offsets some of the increased SPARTAN performance gained from the flight at higher dynamic pressure.

5.3.2 Case 4: SPARTAN Drag Sensitivity

Trajectory Condition	$C_{d,2}$:	90%	95%	100%	105%	110%	$\Delta/\Delta\%C_{d,2}$
Payload to Orbit (kg)	209.8	198.1	189.2	180.4	172.0	-1.9	
Payload Variation (%)	10.92	4.74	0.00	-4.61	-9.05	-0.99	
Total η_{exergy} (%)	1.875	1.772	1.693	1.618	1.546	-0.00016	
1st Stage η_{exergy} (%)	8.570	8.383	8.171	7.971	7.762	-0.041	
Separation Alt, 1→2 (km)	25.24	25.00	24.12	23.89	23.65	-0.09	
Separation v, 1→2 (m/s)	1528	1505	1484	1457	1430	-4.87	
Separation γ, 1→2 (m/s)	5.1	4.8	3.1	1.9	1.2	-0.22	
2nd Stage η_{exergy} (%)	11.939	11.360	10.942	10.558	10.202	-0.086	
Separation Alt, 2→3 (km)	41.04	41.20	41.73	41.47	40.85	-	
Separation v, 2→3 (m/s)	2804	2741	2687	2637	2589	-10.69	
Separation γ, 2→3 (deg)	10.7	10.7	10.8	11.0	11.1	-	
Separation q, 2→3(kPa)	13.0	12.1	10.8	10.8	11.4	-	
2nd Stage L/D, 2→3	4.2	4.1	4.0	3.9	3.8	-0.02	
2nd Stage Flight Time (s)	668.8	661.5	648.1	650.6	653.3	-	
3rd Stage η_{exergy} (%)	19.841	20.093	20.321	20.573	20.779	0.047	
3rd Stage $t, q > 5\text{kpa}$ (s)	16.1	14.1	14.2	14.4	14.6	-	
3rd Stage max α (deg)	14.7	15.7	16.2	16.0	16.1	-	
3rd Stage Fuel Mass (kg)	2805.0	2816.7	2825.6	2834.3	2842.7	1.86	

Table 5.4: Comparison of key trajectory parameters with variation in the drag of the SPARTAN.

To investigate the effect of the vehicle design and uncertainty in aerodynamic performance on the optimal trajectory the drag of the SPARTAN is varied by $\pm 10\%$, and an optimised trajectory calculated with dynamic pressure limited to 50kpa. The drag of the SPARTAN is varied during both the first stage ascent, as well as the acceleration of the SPARTAN. Results are compared to the 100% drag result in Table 5.4 with a trajectory path comparison shown in Appendix D.1.3.

The drag variation of the SPARTAN shows a significant effect on the overall exergy efficiency of the system ($+0.182\%\eta$ at 90% drag, and $-0.147\%\eta$ at 110% drag) and correspondingly, on the maximum payload-to-orbit, +19.6kg at 90% drag, a variation of +10.4% and -17.2kg at 110% drag, a

variation of -9.1%. The exergy efficiencies of the first stage rocket and the SPARTAN are decreased significantly as the drag is increased, from $8.570\%\eta$ and $11.939\%\eta$ respectively at 90% drag, to $7.762\%\eta$ and $10.202\%\eta$ respectively at 110% drag. This reduction in efficiency is due to the energy which must be used to overcome the added drag. The velocity and trajectory angle at first stage-SPARTAN separation decrease significantly as the drag is increased. This indicates that the first stage is able to pitch more during the trajectory, as a consequence of accelerating more slowly as the drag increases. The SPARTAN trajectory results show that when drag is varied, the optimal trajectories are similar to the base-line case, with a similarly sized pull-up, though as the drag is increased (ie. L/D is decreased), the second stage follows a slightly slower and hence lower flight path, and the SPARTAN generally pulls-up to a higher trajectory angle. The similar shape of the optimal trajectory with variation in the aerodynamics of the SPARTAN suggests that sacrificing velocity to increase separation altitude in a pull-up manoeuvre is optimal for multiple vehicle designs, and that the size of this pull-up is consistent with variation in the aerodynamics of the SPARTAN. As the drag of the SPARTAN increases, the exergy efficiency of the third stage shows a corresponding increase, from $19.841\%\eta$ at 90% drag, to $20.779\%\eta$ at 110% drag. This indicates that as the performance of the SPARTAN is decreased, it is beneficial to trade-off more of the SPARTAN's performance for an increase in third stage efficiency, resulting in similarly sized pull-ups.

5.3.3 Case 5: C-REST Engine Specific Impulse Sensitivity

The specific impulse of the C-REST scramjet engines is varied by $\pm 10\%$ to directly investigate the effects of the efficiency of the scramjet engines on the performance of the launch vehicle. The comparison of key trajectory parameters is shown in Table 5.5, with comparison plots presented in Appendix D.1.2. The maximum payload-to-orbit varies by +24.2kg (12.8%) to -20.5kg (-10.8%), and the total exergy efficiency varies by $+0.220\%\eta$ to $-0.183\%\eta$ at 110% I_{SP} and 90% I_{SP} respectively. The increased C-REST specific impulse does not vary the first stage performance significantly, and the first stage-SPARTAN separation point stays relatively constant for all cases excepting 110% I_{SP} , where the altitude and trajectory angle of the first stage-SPARTAN separation increase. The small variations in first stage release point indicate that the efficiency trade-off between the first stage and the SPARTAN is not significantly affected by the efficiency of the SPARTAN, and is primarily driven by the capabilities of the first stage rocket. It is likely that this variation in release point at 110% I_{SP} is simply due to the optimiser converging to an optimal trajectory with slightly different trade-offs between the first stage and SPARTAN efficiency, but with similar overall efficiency. This is supported by the variability in the first stage-SPARTAN separation point when the mass or drag of the SPARTAN are changed, in Sections 5.3.2 and 5.3.4, parameters which affect the ability of the first stage to pitch.

The additional efficiency provided by increases the exergy efficiency of the SPARTAN considerably, by $+1.724\%\eta$ at 110% I_{SP} to $-1.558\%\eta$ at 90% I_{SP} . Increasing the specific impulse of the

Trajectory Condition	$I_{SP,2}$:	90%	95%	100%	105%	110%	$\Delta/\Delta\%I_{SP,2}$
Payload to Orbit (kg)		168.7	179.1	189.2	199.5	213.4	2.2
Payload Variation (%)	-10.81	-5.34	0.00	5.49	12.81	1.16	
Total η_{exergy} (%)	1.510	1.602	1.693	1.787	1.913	0.0002	
1st Stage η_{exergy} (%)	8.171	8.170	8.171	8.168	8.222	-	
Separation Alt, 1→2 (km)	24.12	24.12	24.12	24.12	25.28	-	
Separation v, 1→2 (m/s)	1484	1484	1484	1484	1480	-	
Separation γ, 1→2 (m/s)	3.2	3.4	3.1	3.3	5.5	-	
2nd Stage η_{exergy} (%)	9.384	10.174	10.942	11.698	12.666	0.162	
Separation Alt, 2→3 (km)	41.58	41.64	41.73	41.07	41.53	-	
Separation v, 2→3 (m/s)	2553	2622	2687	2752	2831	13.74	
Separation γ, 2→3 (deg)	11.9	11.3	10.8	10.6	10.2	-0.08	
Separation q, 2→3(kPa)	10.0	10.4	10.8	12.5	12.4	-	
2nd Stage L/D, 2→3	3.9	4.2	4.0	3.9	3.8	-	
2nd Stage Flight Time (s)	677.1	665.6	648.1	645.9	668.0	-	
3rd Stage η_{exergy} (%)	21.068	20.676	20.321	20.002	19.580	-0.073	
3rd Stage t, q > 5kpa (s)	10.7	11.7	14.2	14.9	14.8	-	
3rd Stage max α (deg)	15.6	16.0	16.2	15.9	15.8	-	
3rd Stage Fuel Mass (kg)	2846.1	2835.7	2825.6	2815.2	2801.4	-2.2	

Table 5.5: Comparison of key trajectory parameters with variations in the specific impulse of the C-REST engines.

C-REST engines allows the SPARTAN to accelerate more over the flight time, increasing the velocity at SPARTAN-third stage separation significantly. The velocity added to the end of the SPARTAN’s trajectory directly contributes to the final velocity of the third stage at circularisation. Varying the specific impulse does not change the optimal SPARTAN-third stage separation altitude significantly, however the increased velocity allows this altitude to be reached by the SPARTAN with less trajectory angle variation during the pull-up. Increasing the specific impulse allows the third stage to successfully reach orbit from a lower trajectory angle release point, as low as 10.2° (-5.6%) at 110% I_{SP} , while decreasing the specific impulse requires a higher release point, up to 11.9° (+10.2%) at 90% I_{SP} . The exergy efficiency of the third stage is decreased as the specific impulse of the SPARTAN increases, varying by $-0.741\%\eta$ at 110% I_{SP} to $+0.747\%\eta$ at 90% I_{SP} . As was observed in Case 4, this decrease in efficiency again indicates that as the efficiency of the SPARTAN is improved, the optimal trade-off between the efficiencies of the SPARTAN and the third stage rocket is shifted more in favour of the SPARTAN, and vice versa.

5.3.4 Case 6: SPARTAN Mass Sensitivity

The mass of the SPARTAN is varied by $\pm 5\%$ ($\pm 247.9\text{kg}$), to investigate the effects of the structural, thermal shielding, and system mass of the SPARTAN on the performance of the launch system. Only

Trajectory Condition	$m_2:$	95%	97.5%	100%	102.5%	105%	$\Delta/\Delta\%m_2$
Payload to Orbit (kg)	196.6	192.5	189.2	185.2	181.3	-1.5	
Payload Variation (%)	3.95	1.77	0.00	-2.07	-4.16	-0.8	
Total η_{exergy} (%)	1.750	1.719	1.693	1.665	1.637	-0.00011	
1st Stage η_{exergy} (%)	8.480	8.323	8.171	8.036	7.872	-0.06	
Separation Alt, 1→2 (km)	25.70	25.06	24.12	23.86	23.55	-0.22	
Separation v, 1→2 (m/s)	1540	1509	1484	1454	1418	-11.97	
Separation γ, 1→2 (m/s)	5.1	4.7	3.1	2.7	1.8	-0.34	
2nd Stage η_{exergy} (%)	10.609	10.790	10.942	11.072	11.238	0.062	
Separation Alt, 2→3 (km)	41.56	41.75	41.73	41.71	41.77	-	
Separation v, 2→3 (m/s)	2733	2709	2687	2662	2637	-9.54	
Separation γ, 2→3 (deg)	10.6	10.6	10.8	11.0	11.1	0.06	
Separation q, 2→3(kPa)	11.4	10.9	10.8	10.6	10.4	-0.1	
2nd Stage L/D, 2→3	3.9	4.0	4.0	4.0	4.1	-	
2nd Stage Flight Time (s)	671.5	674.4	648.1	650.8	652.6	-	
3rd Stage η_{exergy} (%)	20.074	20.208	20.321	20.454	20.596	0.052	
3rd Stage $t, q > 5\text{kpa}$ (s)	14.4	14.3	14.2	13.3	11.9	-0.24	
3rd Stage max α (deg)	16.1	16.2	16.2	16.0	16.0	-	
3rd Stage Fuel Mass (kg)	2818.2	2822.3	2825.6	2829.5	2833.5	1.52	

Table 5.6: Comparison of key trajectory parameters with variation in the structural mass of the SPARTAN.

a total mass variation of 5% is used, in order to prevent the first stage-SPARTAN separation velocity from dropping unacceptably low. A summary of the key parameters of each trajectory is detailed in Table 5.6, with comparison plots shown in Appendix D.1.4. Variation in the mass of the SPARTAN causes the maximum payload-to-orbit of the launch system to vary by +7.4kg (+3.9%) at 95% structural mass and by -7.9kg (-4.2%) at 105% structural mass. The exergy efficiency of the first stage rocket decreases as the mass of the SPARTAN is increased (-0.300% η at 105% structural mass) and increases as the mass of the SPARTAN is decreased (+0.309% η at 95% structural mass). Accelerating the additional SPARTAN mass is counted as 'useful' work during the first stage trajectory. However, as the mass of the SPARTAN increases, the acceleration of the first stage decreases, and the first stage spends a larger time in high density conditions, causing the efficiency of the system to be reduced. Additionally, the altitude and trajectory angle at first stage-SPARTAN separation are decreased significantly. This change in separation conditions, along with the decreased exergy efficiency of the first stage, indicates that as the mass of the SPARTAN increases, it becomes beneficial to trade-off more of the exergy efficiency of the first stage to increase the performance of the SPARTAN. This variation in the optimal trade-off is due in part to the first stage being able to pitch more easily with added SPARTAN mass, so that it is physically able to achieve a wider range of separation conditions. Another factor which contributes to the variation in the optimal trade-off is the efficiency of the SPARTAN. As the SPARTAN's mass increases, the first stage-SPARTAN separation velocity decreases significantly.

This results in the SPARTAN maintaining high specific impulse for a longer time at the beginning of its trajectory. As well as this initial increase in efficiency, the higher SPARTAN structural mass causes the SPARTAN to stay at relatively lower velocities over its trajectory, which results in a higher specific impulse throughout. The increased specific impulse of the SPARTAN means that the a larger trade-off of the first stage efficiency for the efficiency of the SPARTAN is beneficial. The increased efficiency of the C-REST engines, as well as the favourable trade-off from the first stage causes the exergy efficiency of the SPARTAN to rise as the structural mass increases (by $+0.296\%\eta$ at 105% mass) and to decrease as the structural mass decreases (by $-0.333\%\eta$ at 95% mass). However, as the SPARTAN mass is increased, more work must be used accelerating the additional mass, which is then separated, causing the overall efficiency of the launch system to decrease.

Variation in the structural mass of the SPARTAN does not significantly affect the altitude at the end of the pull-up manoeuvre, however, as the mass of the SPARTAN is varied, the velocity at SPARTAN-third stage separation does change significantly, by +46m/s (+17.1%) at 95% structural mass, and -50m/s (-18.6%) at 105% structural mass. In order to reach similar altitudes at the end of pull-up, the trajectory angle at the SPARTAN-third stage separation increases as the structural mass is increased (by $+0.3^\circ$, +2.8% at 105% structural mass) and decreases as the structural mass is decreased (by -0.2° , -1.9%, at 95% structural mass). As the mass of the SPARTAN increases, the exergy efficiency of the third stage is increased, varying by $+0.275\%\eta$ at 105% structural mass, and as the SPARTAN mass is decreased the exergy efficiency of the third stage is decreased, varying by $-0.247\%\eta$ at 95% structural mass. This indicates that the trade-off between the efficiency of the SPARTAN and the third stage rocket is shifted in favour of the third stage rocket as the structural mass of the SPARTAN increases. This seemingly runs counter to the results of Cases 4 and 5, which show the trade-off between the efficiencies of the SPARTAN and third stage shifting towards the SPARTAN as the exergy efficiency of the SPARTAN increases. However, the exergy efficiency of the SPARTAN does not take into account the energy wasted accelerating the additional mass of the SPARTAN. This additional energy causes the overall exergy efficiency of the launch system to decrease as the mass of the SPARTAN increases. This additional mass effectively reduces the 'useful' energy available to the SPARTAN, and causes the optimal trade-off between the exergy efficiencies of the SPARTAN and the third stage to shift towards the third stage.

5.3.5 Case 7: SPARTAN Fuel Mass Sensitivity

The available fuel mass of the SPARTAN is varied by $\pm 10\%$, to investigate the effects of variations of the fuel tank size within the SPARTAN. Comparison plots are shown in Appendix D.1.5, with a summary of key trajectory parameters detailed in Table 5.7. The fuel mass causes the maximum payload to orbit to vary by +6.9kg (+3.6%) at 110% fuel mass, and by -7.3kg (3.9%) at 90% fuel mass. In every case, the SPARTAN utilises the full amount of fuel available to it, so that the addition

Trajectory Condition	$m_{F,2}:$	90%	95%	100%	105%	110%	$\Delta/\Delta\%m_{F,2}$
Payload to Orbit (kg)		181.9	185.6	189.2	192.6	196.1	0.7
Payload Variation (%)		-3.81	-1.90	0.00	1.80	3.67	0.37
Total η_{exergy} (%)		1.695	1.695	1.693	1.691	1.690	0
1st Stage η_{exergy} (%)		8.373	8.291	8.171	8.085	8.003	-0.019
Separation Alt, 1→2 (km)		25.21	25.06	24.12	23.95	23.80	-0.08
Separation v, 1→2 (m/s)		1520	1501	1484	1465	1446	-3.65
Separation γ, 1→2 (m/s)		4.7	4.7	3.1	2.9	2.9	-
2nd Stage η_{exergy} (%)		11.270	11.076	10.942	10.798	10.656	-0.03
Separation Alt, 2→3 (km)		41.76	41.79	41.73	41.20	41.59	-
Separation v, 2→3 (m/s)		2639	2662	2687	2712	2734	4.78
Separation γ, 2→3 (deg)		11.2	11.0	10.8	10.6	10.4	-0.04
Separation q, 2→3(kPa)		10.4	10.5	10.8	11.9	11.4	-
2nd Stage L/D, 2→3		3.9	3.9	4.0	3.9	4.0	-
2nd Stage Flight Time (s)		611.9	637.9	648.1	674.7	703.8	4.41
3rd Stage η_{exergy} (%)		20.611	20.476	20.321	20.173	20.042	-0.029
3rd Stage $t, q > 5\text{kpa}$ (s)		11.8	14.1	14.2	14.3	14.3	0.11
3rd Stage max α (deg)		15.9	16.0	16.2	16.0	16.4	-
3rd Stage Fuel Mass (kg)		2832.8	2829.2	2825.6	2822.2	2818.7	-0.71

Table 5.7: Comparison of key trajectory parameters with variation in the fuel mass of the SPARTAN.

of extra fuel mass allows the SPARTAN to accelerate for longer.

As was observed in Case 6, the addition of extra mass to the SPARTAN causes the first stage separation altitude and velocity to decrease, and also for the first stage exergy efficiency to decrease. At 110% fuel mass, the first stage-SPARTAN separation altitude decreases by -0.32km (-1.3%), the separation velocity decreases by -38m/s (-2.6%) and the exergy efficiency of the first stage by $-0.168\%\eta$ (-2.1%), while at 90% fuel mass, the first stage-SPARTAN separation altitude increases by +1.09km (+4.5%), the separation velocity increases by +36m/s (+2.4%) and the efficiency increases by $+0.202\%\eta$ (+2.5%). All cases exhibit similar trajectory shapes, with the SPARTAN pulling-up to similar altitudes, so that increasing the fuel mass directly increases the velocity at SPARTAN-third stage separation and requires slightly less pull-up angle. The SPARTAN-third stage velocity is increased by +47m/s (+17.5%) and the trajectory angle is decreased by -0.4° (-3.7%) at 110% fuel mass, while the velocity is decreased by -48m/s (-17.9%) and the trajectory angle is increased by $+0.4^\circ$ (+3.7%) at 90% fuel mass. As the increased fuel mass directly increases the velocity at the end of the SPARTAN’s trajectory, the beneficial effects of additional fuel exhibit diminishing returns as the velocity at the end of the SPARTAN’s trajectory increases, and Isp decreases. This diminishing specific impulse causes the exergy efficiency of the SPARTAN to decrease by $-0.296\%\eta$ (-2.7%) at 110% fuel mass, and to increase by $+0.318\%\eta$ (+2.9%) at 90% fuel mass. While the exergy efficiency decreases, the addition of extra fuel mass means that there is more total energy available, and so the SPARTAN is able to accelerate more over its trajectory. For this reason the total exergy efficiency of

the system also decreases as the fuel mass is increased, although the payload mass is increasing.

The exergy efficiency of the third stage is decreased as the fuel mass is increased. This indicates that as the fuel mass is increased, the optimal performance trade-off between the SPARTAN and third stage rocket shifts to favour the SPARTAN. In the previous cases it was shown that increasing, rather than decreasing, the efficiency of the SPARTAN shifted the efficiency trade-off towards SPARTAN. However, as the fuel mass is increased, the SPARTAN has more total energy from burning a greater amount of fuel. The decreasing efficiency trend of the third stage rocket in the current case, which occurs as the fuel mass of the SPARTAN is increased, implies that the more total energy which the SPARTAN is able to put towards 'useful' work, the more the efficiency trade-off between the SPARTAN and the third stage favours the SPARTAN.

5.3.6 Case 8: Third Stage Mass Sensitivity

Trajectory Condition	m_3 :	90%	95%	100%	105%	110%	$\Delta/\Delta\%m_3$
Payload to Orbit (kg)	179.0	184.4	189.2	193.3	196.6	0.9	
Payload Variation (%)	-5.36	-2.50	0.00	2.20	3.96	0.47	
Total η_{exergy} (%)	1.603	1.651	1.693	1.733	1.765	8e-05	
1st Stage η_{exergy} (%)	8.614	8.389	8.171	7.993	7.789	-0.041	
Separation Alt, 1→2 (km)	27.05	25.41	24.12	23.77	23.39	-0.18	
Separation v, 1→2 (m/s)	1556	1521	1484	1444	1400	-7.78	
Separation γ, 1→2 (m/s)	7.1	4.9	3.1	2.6	1.9	-0.25	
2nd Stage η_{exergy} (%)	10.514	10.767	10.942	11.064	11.204	0.033	
Separation Alt, 2→3 (km)	41.38	41.49	41.73	41.91	41.97	0.03	
Separation v, 2→3 (m/s)	2752	2722	2687	2649	2612	-7.09	
Separation γ, 2→3 (deg)	10.4	10.5	10.8	11.3	11.7	0.07	
Separation q, 2→3(kPa)	11.9	11.5	10.8	10.2	9.9	-0.11	
2nd Stage L/D, 2→3	3.9	3.9	4.0	4.0	4.1	0.01	
2nd Stage Flight Time (s)	682.5	666.6	648.1	652.5	657.0	-	
3rd Stage η_{exergy} (%)	20.004	20.121	20.321	20.575	20.792	0.041	
3rd Stage $t, q > 5\text{kpa}$ (s)	14.6	13.8	14.2	11.3	10.6	-	
3rd Stage max α (deg)	14.5	15.7	16.2	16.0	16.5	-	
3rd Stage Fuel Mass (kg)	2535.5	2680.2	2825.6	2971.6	3118.4	29.15	

Table 5.8: Comparison of key trajectory parameters with variation in the mass of the third stage.

The total mass of the third stage rocket is varied by $\pm 10\%$ to investigate the effects of having greater mass density within the third stage rocket. The mass which is added or subtracted from the third stage is a combination of payload, fuel and structural mass. Table 5.8 details key trajectory parameters, and Appendix D.1.6 presents comparison plots of each trajectory. The mass of the heat shield is unchanged at 130.9kg, and the structural mass is assumed to contribute to 9% of the remaining mass (so that the structural mass varies by $\pm 10\%$). The remaining mass which is varied consists

of a flexible combination of fuel and payload mass, ie. the optimiser may use the available mass as fuel, and the mass leftover when orbit is reached is assumed to be payload in the usual manner. This mass variation investigates the effects of the third stage internal layout on the trajectory of the launch system, quantifying the consequences of fitting additional fuel, payload and structure within the available space.

Varying the mass of the third stage rocket by $\pm 10\%$ varies the maximum payload-to-orbit by +7.4kg (3.9%) and -10.2kg (-5.4%). The majority of the additional mass is used for fuel and structural mass, with only 2.1% of the added mass utilised for payload. This mass fraction change rate is less than the payload mass fraction of the standard third stage without heat shield, 6.0%, indicating that as mass is added to the internals of the third stage, the efficiency of the third stage decreases. As the mass of the third stage increases, the altitude and trajectory angle of the first stage-SPARTAN separation point decrease, as was observed previously when the mass of the SPARTAN is increased. The SPARTAN pulls-up to similar altitudes as the third stage mass is varied, however, the velocity at the SPARTAN-third stage separation is decreased by -75m/s (-2.8%) at 110% third stage mass, and increased by +65m/s (+2.4%) at 90% third stage mass. Consequently, a larger trajectory angle is required during SPARTAN pull-up, increasing by $+0.9^\circ$ (+8.3%) when the third stage mass is increased, and decreasing by -0.4° (3.7%) when the third stage mass is decreased. As the mass of the third stage is varied by $\pm 10\%$, the exergy efficiency of the SPARTAN varies by $+0.262\%\eta$ and $-0.428\%\eta$, and the exergy efficiency of the third stage varies by $+0.471\%\eta$ and $-0.379\%\eta$. The exergy efficiency variation of the SPARTAN is due to the SPARTAN flying at lower velocity when the third stage mass is higher, resulting in higher specific impulse from the scramjet engines. The increase in the exergy efficiency of the third stage rocket as its mass increases is primarily due to a smaller fraction of the fuel mass of the third stage being used during the in-atmosphere portion of its trajectory, 40.83% of the total fuel mass at 90% m_3 , compared to 40.21% at 110% m_3 . Within the atmosphere, the atmospheric drag, the angle of attack necessary for increasing altitude, and the thrust vector angle needed for aerodynamic trim combine to decrease the exergy efficiency of the third stage. In addition, a smaller percentage of the overall mass is dedicated to the heat shield, which is discarded, 'wasting' energy. As the mass of the heat shield becomes a significantly smaller overall percentage of the third stage mass, its exergy efficiency increases.

5.3.7 Case 9: Third Stage Specific Impulse Sensitivity

The specific impulse of the third stage rocket is varied between 95-105% in order to investigate the effect of the rocket engine on the payload-to-orbit. Appendix D.1.7 presents comparison plots of the optimised trajectories, and Table 5.9 details key trajectory parameters. The specific impulse variation has a significant effect on the trajectory of the system, and the payload-to-orbit, increasing the payload by +45.9kg (+24.26%) at 105% I_{sp} , and decreasing the payload by -45.9kg (-24.26%) at 95% I_{sp} .

Trajectory Condition	$I_{SP,3}$:	95%	97.5%	100%	102.5%	105%	$\Delta/\Delta\%I_{SP,3}$
Payload to Orbit (kg)	143.3	166.4	189.2	212.3	235.1	4.6	
Payload Variation (%)	-24.26	-12.05	0.00	12.21	24.26	2.43	
Total η_{exergy} (%)	1.282	1.488	1.693	1.901	2.107	0.00041	
1st Stage η_{exergy} (%)	8.168	8.175	8.171	8.179	8.169	-	
Separation Alt, 1→2 (km)	24.12	24.13	24.12	24.13	24.12	-	
Separation v, 1→2 (m/s)	1484	1485	1484	1486	1484	-	
Separation γ, 1→2 (m/s)	3.2	3.3	3.1	3.2	3.1	-	
2nd Stage η_{exergy} (%)	10.907	10.919	10.942	10.946	11.014	0.005	
Separation Alt, 2→3 (km)	41.75	41.64	41.73	41.60	41.38	-	
Separation v, 2→3 (m/s)	2684	2686	2687	2689	2694	0.48	
Separation γ, 2→3 (deg)	11.0	10.9	10.8	10.8	10.6	-	
Separation q, 2→3(kPa)	10.8	10.9	10.8	11.0	11.4	-	
2nd Stage L/D, 2→3	4.0	4.0	4.0	4.0	4.0	-	
2nd Stage Flight Time (s)	647.6	648.4	648.1	647.7	647.3	-	
3rd Stage η_{exergy} (%)	15.119	17.697	20.321	23.031	25.693	0.53	
3rd Stage $t, q > 5\text{kpa}$ (s)	11.9	14.3	14.2	13.2	13.6	-	
3rd Stage max α (deg)	16.1	16.0	16.2	15.8	15.9	-	
3rd Stage Fuel Mass (kg)	2871.4	2848.4	2825.6	2802.5	2779.7	-4.59	

Table 5.9: Comparison of key trajectory parameters with variation in the third stage specific impulse.

Though the effect of the specific impulse of the third stage on the maximum payload-to-orbit is large, the majority of the improved efficiency comes from the circularisation and Hohmann transfer manoeuvres, where increasing the specific impulse results in significantly less mass usage, which directly translates to additional payload. Varying the specific impulse of the third stage only changes the in-atmosphere trajectory of the third stage slightly, varying the velocity of the third stage before circularisation by only +55.7m/s (+1.5%) at 105% I_{sp} and -28.1m/s (-0.7%) at 95% I_{sp} . The third stage specific impulse variation has no direct influence on the trajectory of the first stage rocket, and the first stage-SPARTAN separation conditions are relatively consistent across the thrust levels simulated. As the specific impulse of the third stage is varied, the size and shape of the pull-up manoeuvre are only slightly affected by the specific impulse of the rocket engine, and in no consistent manner. However, the exergy efficiency of the SPARTAN increases as the third stage specific impulse is increased, by +0.072% η (+0.66%) at 105% I_{sp} , and decreases as the third stage specific impulse is decreased, by -0.035% η (-0.032%) at 95% I_{sp} . This variation in the exergy efficiency of the SPARTAN is small, indicating that as the specific impulse of the third stage increases, the trade-off between the efficiencies of the SPARTAN and the third stage shifts in favour of the SPARTAN. This trade-off shift is small because most of the effect of the third stage specific impulse is during the exoatmospheric burns. The third stage specific impulse has a relatively minor effect of within the atmosphere, where the trade-off occurs.

5.3.8 Case 10: Third Stage Drag Sensitivity

Trajectory Condition	$C_{d,3}$:	80%	90%	100%	110%	120%	$\Delta/\Delta\%C_{d,3}$
Payload to Orbit (kg)	190.1	189.6	189.2	188.8	188.4	0	
Payload Variation (%)	0.50	0.22	0.00	-0.21	-0.40	-0.02	
Total η_{exergy} (%)	1.702	1.697	1.693	1.690	1.687	0	
1st Stage η_{exergy} (%)	8.173	8.169	8.171	8.171	8.168	-	
Separation Alt, 1→2 (km)	24.12	24.12	24.12	24.12	24.12	-	
Separation v, 1→2 (m/s)	1485	1484	1484	1484	1484	-	
Separation γ, 1→2 (m/s)	3.1	3.2	3.1	3.1	3.2	-	
2nd Stage η_{exergy} (%)	11.091	11.006	10.942	10.911	10.850	-0.006	
Separation Alt, 2→3 (km)	40.68	41.02	41.73	41.96	42.24	0.04	
Separation v, 2→3 (m/s)	2704	2695	2687	2684	2677	-0.64	
Separation γ, 2→3 (deg)	10.2	10.6	10.8	10.9	11.2	0.02	
Separation q, 2→3(kPa)	12.7	12.0	10.8	10.4	10.0	-0.07	
2nd Stage L/D, 2→3	4.0	3.9	4.0	4.0	4.0	-	
2nd Stage Flight Time (s)	646.4	647.6	648.1	647.9	648.9	-	
3rd Stage η_{exergy} (%)	20.152	20.285	20.321	20.359	20.463	0.007	
3rd Stage $t, q > 5\text{kpa}$ (s)	16.7	14.8	14.2	11.9	11.8	-0.13	
3rd Stage max α (deg)	17.6	16.2	16.2	15.9	15.3	0	
3rd Stage Fuel Mass (kg)	2824.7	2825.2	2825.6	2826.0	2826.4	0.04	

Table 5.10: Comparison of key trajectory parameters with variation in the drag of the third stage.

The coefficient of drag of the third stage rocket is varied by $\pm 20\%$ to investigate the effects of the third stage design and sizing on the performance of the launch system. Table 5.10 details the key trajectory parameters of each optimised trajectory, and Appendix D.1.8 shows trajectory comparison plots. The third stage drag is found to have only a very small effect on the performance of the launch system, varying the payload to orbit by only +0.9kg (+0.5%) at 120% C_d and -0.8kg (-0.4%) at 80% C_d . This indicates that the aerodynamic properties of the third stage rocket do not contribute significantly to the performance of the system.

The first stage trajectory is not affected by variations in the drag of the third stage. The SPARTAN exhibits a slightly higher pull-up as the drag of the third stage is increased by 20%, increasing altitude by +0.51km (+1.2%), and trajectory angle at separation by +0.4° (+3.7%) trajectory angle, while decreasing the separation velocity by -10.0m/s (-0.37%). Conversely, decreasing the drag of the third stage by 20% decreases the altitude at SPARTAN-third stage separation by -1.0km (-2.5%), decreases the trajectory angle at separation by -0.6° (-5.6%), and increases the velocity by +17m/s (+0.6%). Increasing the drag of the third stage by 20% causes a decrease in the exergy efficiency of the SPARTAN of -0.092% η (-0.84%), and an increase in the efficiency of the third stage of +0.142% η (+0.70%), while decreasing the drag of the third stage by 20% causes an increase in the exergy efficiency of the SPARTAN of +0.149% η (+1.36%), and a decrease in the third stage efficiency

of $-0.169\% \eta$ (-0.83%). The increasing exergy efficiency of the third stage as the drag increases indicates that the trade-off between the efficiency of the SPARTAN and the third stage shifts towards the third stage significantly when the drag of the third stage is increased. The SPARTAN pulls-up to a higher altitude so that the third stage spends less time in a high dynamic pressure environment, where the increased drag has a significant effect, mitigating the energy loss due to the increased drag considerably. The higher pull-up of the SPARTAN with the third stage drag increased by 20%, decreases the time that the third stage spends above 5kPa dynamic pressure by -2.4s (-16.9%) while the lower pull-up of the SPARTAN when the third stage drag is decreased by 20% increases the time spent at greater than 5kPa dynamic pressure by +2.5s (+17.6%).

5.4 Comparison of Design Parameters

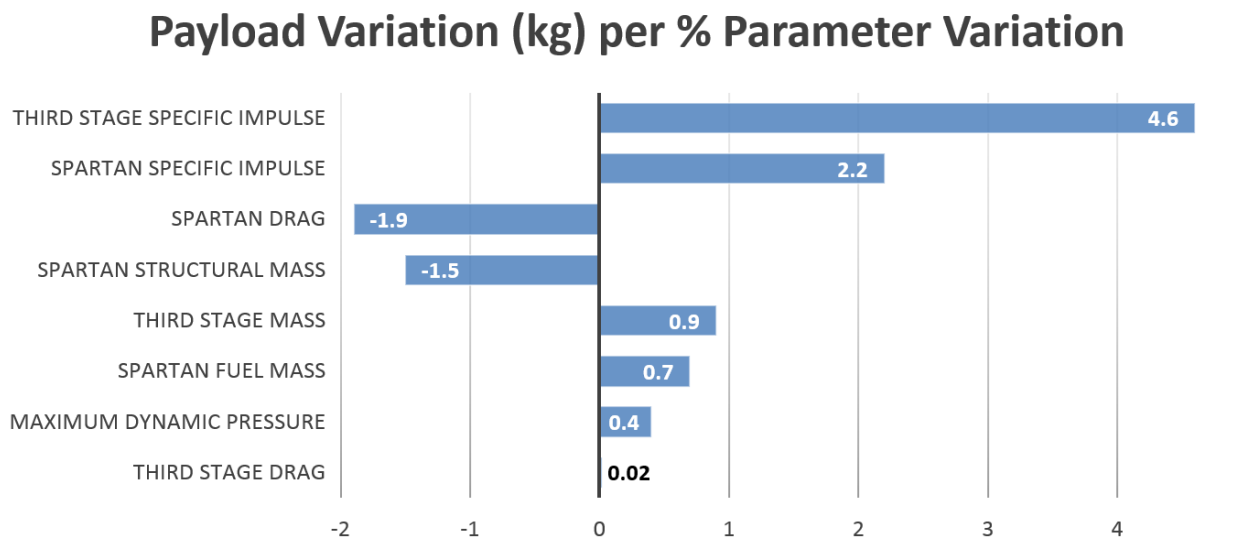


Figure 5.11: The sensitivity of the key design parameters of the launch system.

The preceding sections calculate the relative sensitivity of the launch system performance to a variety of design parameters. Comparing and contrasting the sensitivity of the launch system to each design parameter allows for the relative impact of each design parameter to be assessed. Figure 5.11 shows the change in payload mass per percentage point variation of each design parameter. This change per percentage variation indicates the magnitude by which the payload-to-orbit varies as each design parameter is varied by +1% (with sign reversed for -1% variation), and is a measure of the sensitivity of the launch system to variations in each design parameter. However, a 1% variation has a significantly different implication in the context of each individual design parameter. As such, the change per percentage is most useful when directly assessing each design parameter, and taking into account the associated effects on other, coupled design parameters.

The influence of maximum dynamic pressure on the performance of the launch system is low, particularly when compared to the influence of the closely linked the SPARTAN mass parameter. The SPARTAN's thermal protective properties and structural strength define the maximum dynamic pressure. This means that the low variance in performance with maximum dynamic pressure may be offset by the variation in the mass of the SPARTAN, ie. a lower maximum dynamic pressure requires less structural and thermal protection system mass. Comparing the relative sensitivities of the launch system dynamic pressure and SPARTAN mass ($1.5 \frac{\Delta kg}{\Delta \% kg_{SPARTAN}}$), and their absolute magnitudes (50kPa and 4957kg respectively), allows the sensitivities of these coupled effects to be directly quantified. So long as decreasing the dynamic pressure by 1kPa allows for a reduction in structural and TPS mass of greater than -26.5kg, then operating the SPARTAN at lower dynamic pressures may be preferable.

The influence of the fuel mass of the SPARTAN is also low, however, the fuel mass is only a fraction of the total mass of the SPARTAN (24.0%). This means that relatively small mass changes in fuel mass are still significant. When the fuel mass of the SPARTAN is increased, the structural mass of the tanks will require a corresponding increase. Comparing the impact of the fuel mass and structural mass of the SPARTAN along with their relative magnitudes (1562kg of fuel mass and 4957kg of structural mass), the absolute impact of each is $0.044 kg_{payload}/kg$ and $0.030 kg_{payload}/kg$ respectively. This means that so long as fuel mass can be added to the SPARTAN with less than 1.47kg of structural mass incorporated for each 1kg of fuel mass, adding additional fuel mass will be beneficial. However, the fuel mass is constrained considerably by the available internal space within the SPARTAN, which is likely to be the main limiting factor. If the size of the fuselage of the SPARTAN is increased, the aerodynamic performance of the SPARTAN may be decreased. The sensitivity of the launch system to the drag of the SPARTAN, , means that so long as 1kg of fuel can be added to the SPARTAN, with a drag increase of less than 0.024%, then the maximum payload-to-orbit will increase.

The payload-to-orbit is sensitive to the specific impulse of the C-REST engines, varying at a rate of $2.2 \frac{\Delta kg}{\Delta \% I_{SP}}$. Increasing the specific impulse of the scramjet engines is likely to require the addition of extra systems within the scramjet engines, adding weight to the SPARTAN, or a change in the shape of the scramjet engines, adding drag to the SPARTAN. The slightly lower sensitivity of the launch system to the SPARTAN mass ($1.5 \frac{\Delta kg}{\Delta \% kg_{SPARTAN}}$) compared to the sensitivity to the specific impulse, means that so long as increasing the I_{SP} of the SPARTAN by 1% causes a corresponding increase in the structural mass of the SPARTAN of less than 1.47% (72.9kg), the performance of the launch system will improve. The sensitivity of the launch system to variation of the SPARTAN drag ($1.9 \frac{\Delta kg}{\Delta \% C_d, SPARTAN}$) is similar in magnitude to the sensitivity to specific impulse. If a variation in the shape of the scramjet engines or forebody increases the I_{SP} of the SPARTAN by 1%, while increasing the drag of the SPARTAN by less than 1.16%, then the efficiency of the launch system will be improved.

The aerodynamic performance of the third stage is shown to have only a very small impact on

the performance of the launch system, with a drag sensitivity of only $0.02 \frac{\Delta kg}{\Delta \% C_{d,3}}$. This means that for any third stage shape variations, the aerodynamic sensitivity is small, and so long as the magnitude of the third stage lift force is maintained, the only significant coupled design factors are likely to be the structural and TPS mass necessary for in-atmosphere acceleration. The specific impulse of the third stage rocket has the highest percentage payload variation effect on the launch system of any of the design parameters tested, at $4.6 \frac{\Delta kg}{\Delta \% I_{SP,3}}$. Increasing the specific impulse of the third stage is likely to involve modifications to the engine, increasing the pressure within the fuel tanks, or adding a turbopump to assist fuel flow, all of which involve increasing the mass of the third stage rocket. This additional mass is subtracted directly from the available payload mass of the system. This implies that so long as the specific impulse of the third stage can be increased by 1% for less than 4.6kg additional engine and system mass, that the performance of the launch system will improve. Additionally, increasing the size of the third stage rocket is likely to require an increase in the size of the SPARTAN's fuselage. The sensitivity of the SPARTAN to drag, $1.9 \frac{\Delta kg}{\Delta \% C_{d,SPARTAN}}$, means that if the third stage can be enlarged so that the third stage mass increases by 1kg while the fuselage of the SPARTAN varied so that the increase in SPARTAN drag is less than 0.014%, the maximum payload-to-orbit will increase. However, it is likely to be cost which is the main limiting factor to variations in the third stage specific impulse. Increasing the specific impulse of the rocket engine is likely to add a large amount of cost to the third stage rocket, which is particularly important as the third stage is not reusable. This additional cost factor is likely to be the limiting factor on the specific impulse of the third stage rocket.

5.5 Summary

In this chapter, LODESTAR was used to design the trajectory of the rocket-scramjet-rocket multi-stage launch system incorporating the SPARTAN scramjet-powered accelerator. A trajectory was simulated in which the SPARTAN stage flies at a constant dynamic pressure, producing 158.4kg of payload-to-orbit. This trajectory served to verify LODESTAR and the simulation of the launch system, as well as providing a baseline trajectory for comparison. A trajectory optimised for maximum payload-to-orbit was then calculated, which increased payload mass to heliosynchronous orbit to 170.2kg (an increase of 16.3%) compared to the constant dynamic pressure trajectory. The optimal flight path indicates that the optimal scramjet flight path for a system transitioning between separate airbreathing and rocket-powered stages involves the SPARTAN flying at less than its maximum dynamic pressure at three separate points along the trajectory. Initially, the first stage-SPARTAN separation occurs at a higher trajectory angle than in the constant dynamic pressure trajectory, causing the SPARTAN to fly at lower dynamic pressure, and trading off the exergy efficiency of the SPARTAN for the exergy efficiency of the first stage, for an overall performance gain. The optimal flight path then exhibits an altitude raising manoeuvre in the middle of the trajectory, which improves the exergy

efficiency of the SPARTAN by a very minor $+0.003\%\eta$ ($+0.03\%$). Finally, the SPARTAN executes a pull-up manoeuvre before the SPARTAN-third stage separation. This optimal pull-up manoeuvre trades off velocity (a decrease of 116.2m/s) for altitude (an increase of 9.48km) and improved flight path angle (an increase of 10.45°), decreasing the exergy efficiency of the SPARTAN by $-1.32\%\eta$ (-10.7%) when compared to the constant dynamic pressure case. These conditions improve the exergy efficiency of the third stage rocket significantly, by $3.456\%\eta$, an increase of 20.5% over the third stage released from a constant dynamic pressure trajectory. The pull up manoeuvre in the payload-to-orbit optimised trajectory also reduces the maximum dynamic pressure experienced by the third stage to 10.8kPa, a decrease of 43.4kPa compared to a trajectory with minimum pull-up, which allows future design benefits due to heat shield mass reduction.

A sensitivity study was conducted, to determine the relative effects of key vehicle design parameters on the optimised trajectory. The maximum dynamic pressure, specific impulse, aerodynamic performance, structural mass, and fuel mass of the SPARTAN, were modified along with the specific impulse, mass and aerodynamic performance of the third stage, and the magnitudes of their payload-to-orbit sensitivities compared. It was observed that the efficiency trade-off between the first stage and the SPARTAN depends primarily on the pitching ability of the first stage, so that when the first stage is capable of pitching more rapidly, the trade-off shifts in favour of the SPARTAN. It was also observed that when the overall magnitude of 'useful' energy utilised during the SPARTAN acceleration is increased, the trade-off between the efficiency of the SPARTAN and the third stage rocket shifts in favour of the SPARTAN, decreasing the size of the pull-up before SPARTAN-third stage separation. The specific impulse of the third stage rocket was found to produce the most overall effect on the payload-to-orbit, increasing the payload by $+45.9\text{kg}$ ($+24.26\%$) at $105\% I_{sp}$, and decreasing the payload by -45.9kg (-24.26%) at $95\% I_{sp}$. However, increasing the specific impulse of the third stage rocket is likely to come at a high cost premium, which may be undesirable as the third stage is non-reusable. The third stage aerodynamic performance was found to have negligible effect on the payload-to-orbit, indicating this is not a significant design factor. The most easily variable design factor, the maximum dynamic pressure of the SPARTAN, was found to have a relatively small effect on the payload-to-orbit performance of the launch system, varying the payload-to-orbit by only $+24.2\text{kg}$ ($+12.8\%$) at 60kPa and -20.5kg (-10.8%) at 40kPa. The negative effect on the payload-to-orbit when flying at 40kPa is likely to be offset by the lower TPS and structural mass required by lower dynamic pressure flight. It was determined that if the TPS and structural mass decrease is greater than -26.5kg for every 1kPa reduction in the maximum dynamic pressure, then flying at lower dynamic pressure is potentially preferable.

CHAPTER 6

OPTIMISED TRAJECTORY INCLUDING FLY-BACK

This chapter presents the maximum payload-to-orbit optimised trajectory of the rocket-scramjet-rocket launch system, with the fly-back of the SPARTAN included within the optimal trajectory calculation. Flying back the SPARTAN for landing at the initial launch site allows for rapid refurbishment and re-use, and is one of the primary enabling factors in the cost efficient operation of the launch system. The fly-back of the SPARTAN requires turning-around the SPARTAN after third stage separation, covering the necessary ground distance for return, and decelerating to reduce the speed of the SPARTAN to landing approach velocity, while maintaining a suitably high trajectory angle to allow for a controlled approach. The return of the SPARTAN to the initial launch site is included in the optimisation process to asses whether it is possible for fly-back of the SPARTAN to be achieved as a part of the launch process, and to maximise the overall payload-to-orbit efficiency of the launch system. This chapter includes a sensitivity analysis, in a similar fashion to Chapter 5. This sensitivity analysis allows the influence of the fly-back of the SPARTAN on the design sensitivities of the launch system to be assessed.

6.1 Case 11: Combined SPARTAN Ascent-Descent & Third Stage

LODESTAR is used to optimise the trajectory of the rocket-scramjet-rocket launch system, including the return of the SPARTAN to its initial launch site. The optimised trajectory is shown in Figure 6.1. The rocket-scramjet-rocket launch system is shown to be able to successfully launch a small satellite, while flying-back the SPARTAN to the initial launch site location, and approaching the landing site at appropriately low altitude and velocity to allow for landing. The optimised trajectory attains a payload mass to SSO of 170.2kg. This indicates that the launch system utilising the SPARTAN is capable of successfully completing a small satellite launch mission which allows for rapid reusability

Trajectory Condition	Value
Payload to Orbit (kg)	170.2
Total η_{exergy} (%)	1.491
1st Stage η_{exergy} (%)	8.597
Separation Alt, 1→2 (km)	27.14
Separation v, 1→2 (m/s)	1548
Separation γ, 1→2 (m/s)	5.6
2nd Stage η_{exergy} (%)	9.494
Separation Alt, 2→3 (km)	40.93
Separation v, 2→3 (m/s)	2581
Separation γ, 2→3 (deg)	11.0
Separation q, 2→3(kPa)	11.2
2nd Stage L/D, 2→3	4.7
2nd Stage Flight Time (s)	525.4
2nd Stage Return Fuel (kg)	268.0
3rd Stage η_{exergy} (%)	20.786
3rd Stage $t, q > 5\text{kpa}$ (s)	13.3
3rd Stage max α (deg)	16.7
3rd Stage Fuel Mass (kg)	2844.5

Table 6.1: Selected trajectory conditions for a maximum payload-to-orbit trajectory including SPARTAN fly-back.

of the SPARTAN. The maximum payload-to-orbit is reduced by -10.0% compared to the optimised trajectory result without fly-back. The benefits of flying back the SPARTAN to its initial launch site, compared to the alternative of transporting the SPARTAN back to the launch site from a remote landing, are likely to far outweigh this associated reduction in payload.

6.2 Ascent Trajectory

After launch, the first stage pitches towards the east, beginning at a heading angle of -12.4° . Other than this heading angle difference, the first stage trajectory, shown in Figure 6.2, is very similar to that of the first stage launching the SPARTAN with no return flight, detailed in Section 5.2, with the exception of a small adjustment manoeuvre. After pitchover, the first stage gradually reduces the angle of attack to a minimum of -0.47° at 30.9s flight time, in order to make small adjustments to the pitch profile while the velocity is low. After this, the angle of attack returns to 0° at 42.9s flight time, and is maintained for 16.4s. The angle of attack is then reduced, to a minimum of -3.58° in order to adjust the altitude and trajectory angle, before increasing back to 0° at first stage-SPARTAN separation. The SPARTAN is released in an easterly direction, at a heading angle of -12.4° , an altitude of 27.14km, and a trajectory angle of 5.6° . This altitude of first stage-SPARTAN separation is 3.02km (+12.5%) higher than the first stage-SPARTAN separation point with no fly-back, with a trajectory

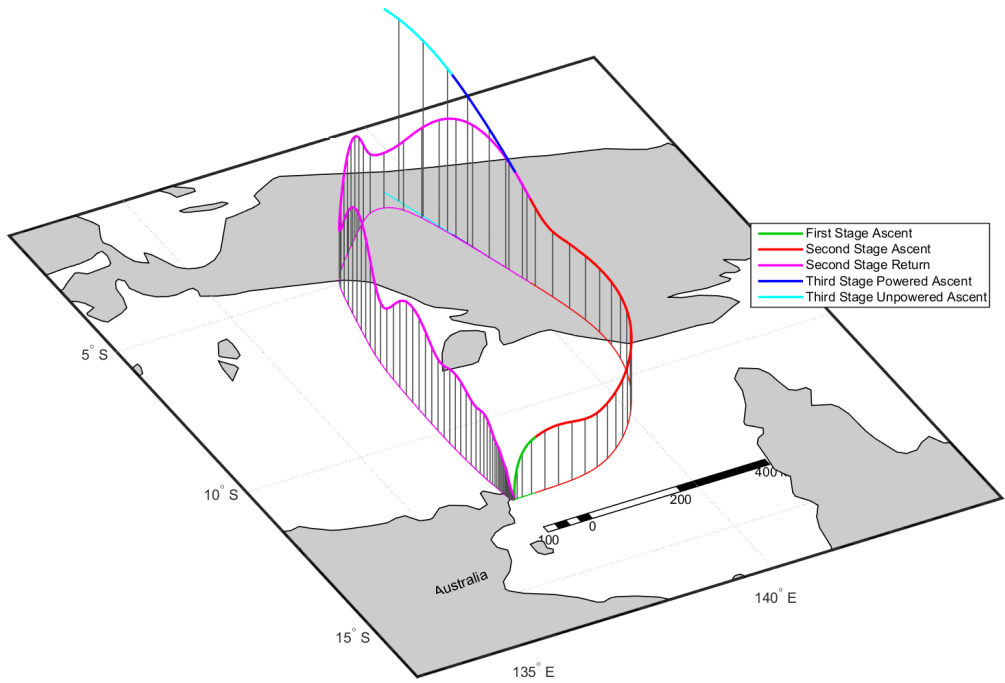


Figure 6.1: Maximum payload-to-orbit trajectory path with the inclusion of SPARTAN fly-back (Case 11). Initial heading angle of -12.44° .

angle at separation which is $+2.5^\circ$ ($+80.6\%$) higher. This higher release point increases the exergy efficiency of the first stage rocket by $+0.426\%\eta$ ($+5.2\%$), and allows the first stage to achieve a higher velocity at separation (an increase of $+64\text{m/s}$, $+4.3\%$).

The higher altitude, larger trajectory angle, and increased velocity at the first stage-SPARTAN separation point causes an altitude raising manoeuvre at the beginning of the SPARTAN's acceleration, which is significantly higher than the altitude raising manoeuvre with no fly-back. This altitude raising manoeuvre takes the SPARTAN to a height of 29.59km at 31.44s, and decreases the dynamic pressure of the SPARTAN to 29.1kPa, allowing time for the bank angle of the SPARTAN to be increased. The bank angle is initially increased, at the maximum change rate, to 44.2° after the first stage-SPARTAN separation, which aids the SPARTAN in decreasing its altitude. As the altitude of the SPARTAN begins to reduce, the bank angle stops increasing and the angle of attack is increased to 3.24° , to increase the lift, slowing the descent of the SPARTAN. The bank angle then begins to in-

crease once more, and as the SPARTAN reaches close to its maximum dynamic pressure at 109.8s, the angle of attack is reduced, and the bank angle reaches an initial maximum of 56.8° . The bank angle

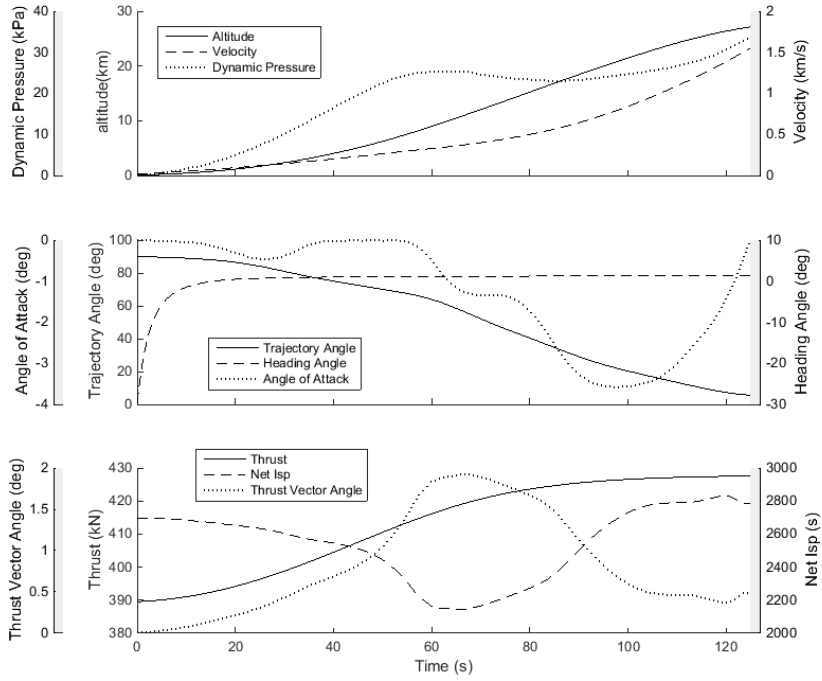


Figure 6.2: The first stage of the optimised maximum payload-to-orbit trajectory with SPARTAN fly-back (Case 11).

of the SPARTAN is then reduced, and afterwards is maintained between 50.4° and 58.6° , exhibiting higher bank angles towards the latter part of the ascent.

The angle of attack of the SPARTAN is significantly higher over the course of the maximum payload-to-orbit trajectory with fly-back inclusion, compared to maximum payload-to-orbit trajectory with no fly-back, detailed in Section 5.2. These significantly higher angles of attack result in the SPARTAN flying at close to maximum dynamic pressure for most of the duration of its trajectory, without the altitude raising manoeuvre observed in Section 5.2. The increase in angle of attack means that the SPARTAN no longer flies within the homogeneous region of the C-REST engines specific impulse, instead the flight conditions are close to a region where an increase in angle of attack causes a sharp decrease in specific impulse. This indicates that at Mach 7 and 8, the angle of attack, and consequently the allowable bank angle, of the SPARTAN is being limited by the performance of the C-REST engines. The SPARTAN stays close to its maximum dynamic pressure until a pull-up is performed at 365.8s flight time. During the pull-up, the bank angle is steadily reduced at its maximum change rate, until close to the release of the third stage rocket, which occurs at 0° bank angle.

The higher angles of attack flown by the SPARTAN also have the consequence of decreasing the net specific impulse of the SPARTAN during its acceleration, with the maximum specific impulse

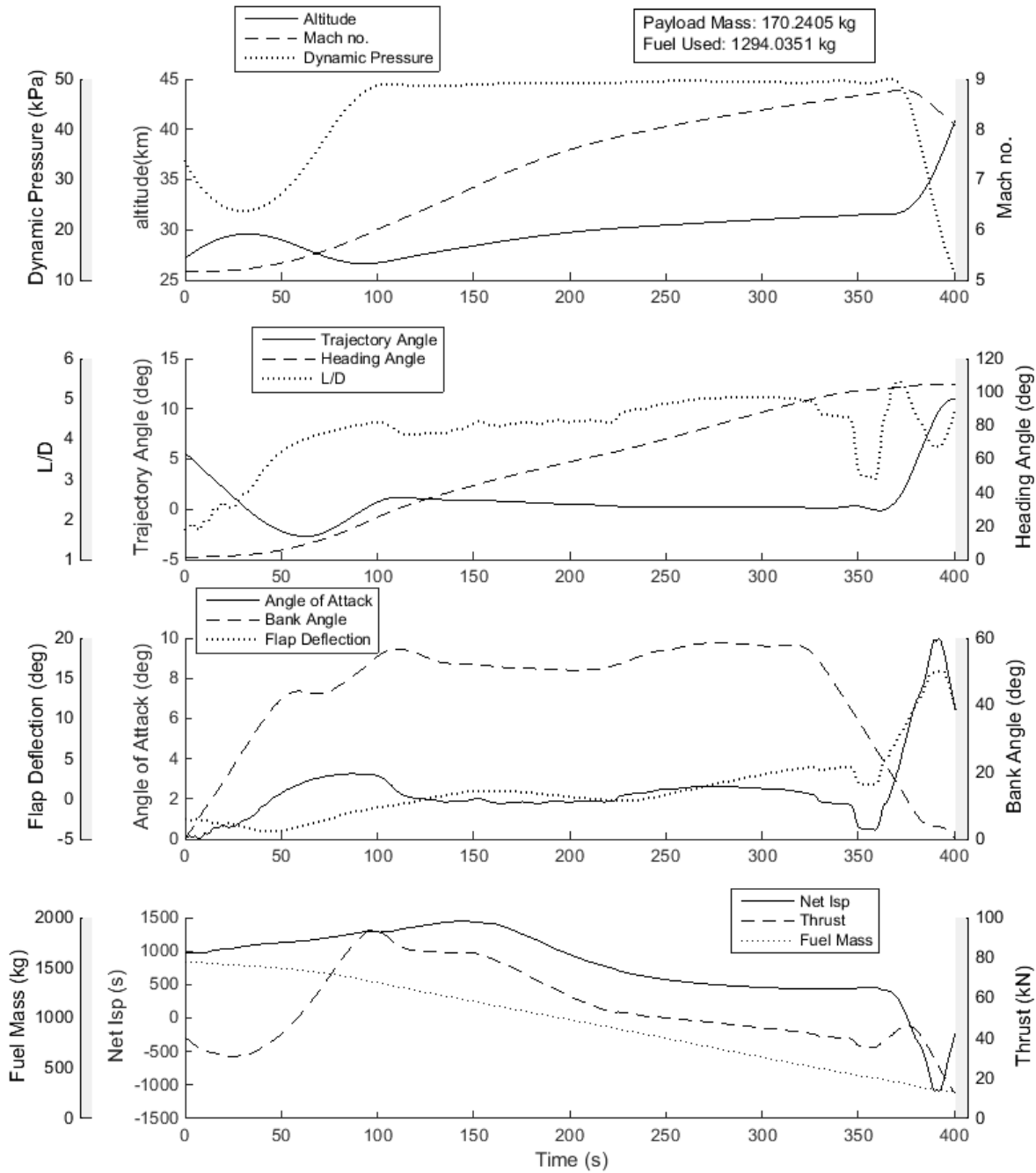


Figure 6.3: The acceleration of the SPARTAN flying an optimised maximum payload-to-orbit trajectory with SPARTAN fly-back (Case 11).

being decreased by -2.5%. The overall exergy efficiency of the SPARTAN is decreased, to $9.494\% \eta$, a decrease of $-1.448\% \eta$ (-12.2%) compared to the maximum payload-to-orbit trajectory with no fly-back. This exergy efficiency decrease is due partially to the decrease in the specific impulse of the

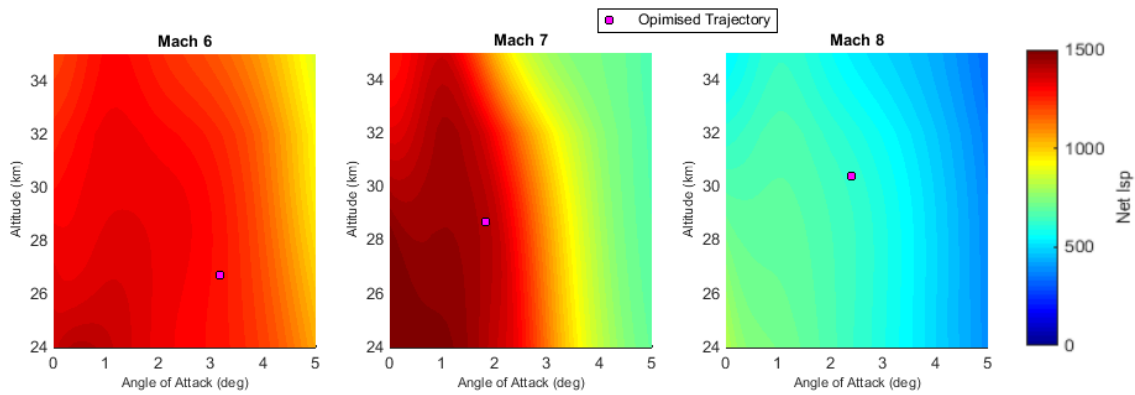


Figure 6.4: Net I_{SP} contours for the SPARTAN at Mach numbers between 6 and 8, showing the optimised trajectory path.

scramjet engines, but more significantly is attributed to the fuel necessary for the return flight resulting in less fuel being used during the ascent of the SPARTAN, and thus less 'useful' work being attained from the total fuel mass. A total fuel mass of 1294kg is used during the SPARTAN's acceleration. This reduction in fuel mass used, along with the reduction in net specific impulse due to the higher angle of attack values, reduces the velocity at SPARTAN-third stage separation by -106m/s (-3.9%) compared to the maximum payload-to-orbit case with no SPARTAN fly-back. The SPARTAN pulls up to 40.93km altitude and 11.0° before SPARTAN-third stage separation, a difference of only -0.8km (-1.9%) and $+0.2^\circ$ (+1.8%) compared to the maximum payload-to-orbit trajectory without fly-back, indicating that the inclusion of fly-back does not have a large effect on the magnitude of the pull-up manoeuvre.

The exergy efficiency of the third stage is increased by $+0.465\%\eta$ (+2.3%) when compared to the maximum payload-to-orbit trajectory with no SPARTAN fly-back. This indicates that the efficiency trade-off between the SPARTAN and the third stage favours the third stage rocket more when the fly-back of the SPARTAN is included. This supports the trend observed in Chapter 5, that as the overall 'useful' energy availability of the SPARTAN is decreased, the efficiency trade-off shifts in favour of the third stage rocket.

6.3 Fly-Back Trajectory

The optimised fly-back trajectory is shown in Figure 6.6. The SPARTAN is shown to be capable of fly-back, using 268.0kg of fuel, 17.2% of the total fuel. Throughout its fly-back the SPARTAN exhibits distinct skipping manoeuvres, and ignites the scramjet engines a total of three times. The skips are aided by the angle of attack of the SPARTAN, and are consistent with research which has shown that a periodic skipping trajectory increases the downrange distance achievable by hypersonic

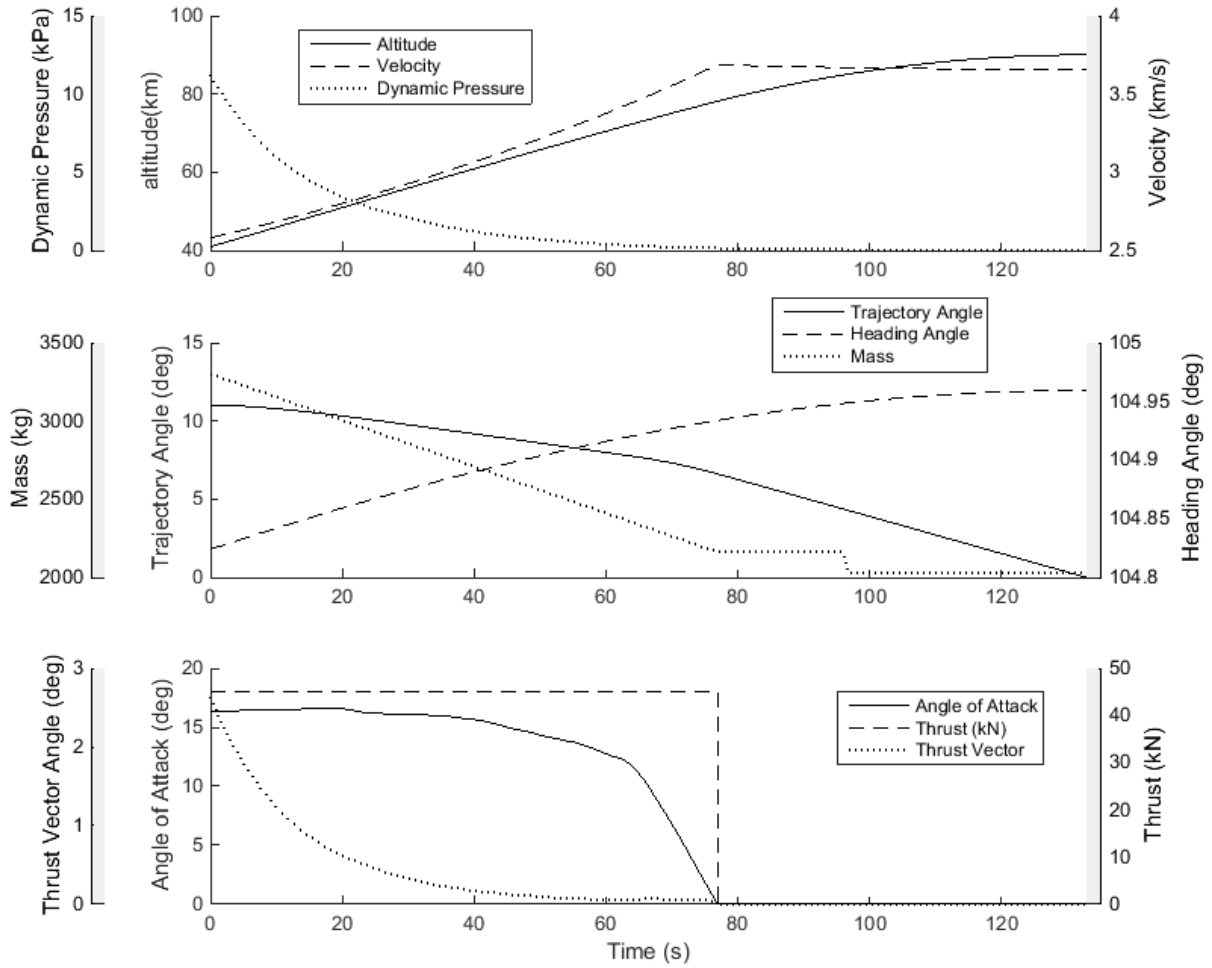


Figure 6.5: The third stage trajectory of an optimised maximum payload-to-orbit trajectory with SPARTAN fly-back (Case 11).

vehicles both during powered and unpowered flight[160, 161]. These skips serve to reduce the fuel necessary for the return flight.

It is observed that the optimised trajectory exhibits characteristics which can be separated into three distinct segments; 1. initial turn, 2. boost-skip phase, and 3. approach.

Initial Turn

The SPARTAN separates from the third stage rocket at a bank angle of 0° , and then increases its bank angle at close to the maximum change rate until 108.7s return flight time, at which point 81.7° bank angle is reached. The angle of attack is kept low during this time, in order to minimise the size of the initial skip. As the SPARTAN reaches the zenith of its initial skip, at 66.1s flight time and 60.0km

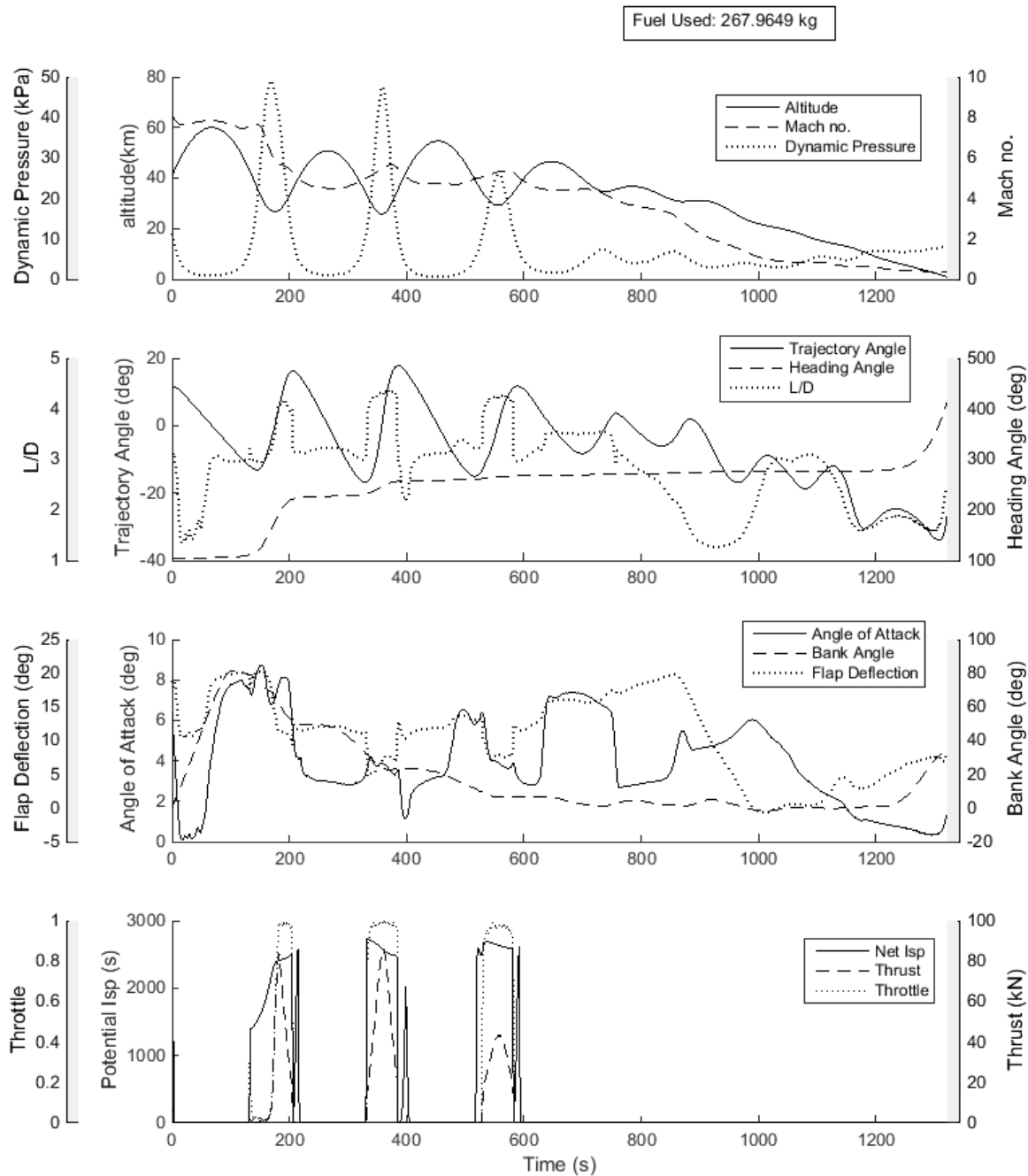


Figure 6.6: The fly-back trajectory of the SPARTAN flying an optimised maximum payload-to-orbit trajectory (Case 11).

altitude, the angle of attack is rapidly increased, up to a maximum of 8.76° . After this, the SPARTAN rapidly comes close to hitting the maximum dynamic pressure limit of 50kPa. This increase in angle of attack, along with the aid of a reduction in the bank angle to 67.5° , generates additional lift to slow

the descent of the SPARTAN. Additionally, as the angle of attack of the SPARTAN increases, the high bank angle enables a large heading angle change during the initial phase of the trajectory, particularly at the first trough between the first and second skips. The heading angle increases from 104.8° at the beginning of fly-back, to 221.7° midway through the second skip. This large heading angle change minimises the total ground distance which the SPARTAN must cover during its return, decreasing the fuel mass necessary for fly-back.

Boost-Skip Phase

At 182.8s flight time, as the bank angle is reducing, the scramjet engines are ignited. The C-REST engines are powered-on in the trough between the first and second skips, at a point of high potential specific impulse, and initially burn for 22s. During the initial burn, the lift/drag of the SPARTAN increases significantly, raising the altitude of the SPARTAN. The maximum altitude during the burn is limited by the lower inlet dynamic pressure limit of the C-REST engines of 20kPa. At 204.8s flight time the initial burn ends, the angle of attack of the SPARTAN is decreased to 3.2° , and the SPARTAN executes its second skip. As soon as the dynamic pressure is high enough for C-REST engine operation at 339.9s return flight time, the scramjet engines are once again ignited. During the second burn, the angle of attack of the SPARTAN is increased, to modify the temperature and Mach number at the inlet of the C-REST engines so that the maximum specific impulse is obtained from the C-REST engines during the burn. The angle of attack varies between 4.2° to 3.3° during the second burn, and the lift/drag is once again raised significantly, initiating the third skip. This skip raises the altitude of the SPARTAN to 54.6km, before it decreases once again. The third and last burn is initiated at 536.7s and lasts until 579.0s, when the remaining fuel has been depleted. Before the third burn, the angle of attack is decreased, so that it varies between 4.5° and 3.7° during the burn. These angle of attack values are similar to those observed during the second burn, indicating that these angle of attack values obtain a high specific impulse from the C-REST engines, this can be observed in Figure A.6, which shows the specific impulse profile of the return flight during the boost-skip phase.

After the third burn phase, the angle of attack is initially controlled so that the skipping trajectory of the SPARTAN is damped. Immediately after the third burn phase, the angle of attack is reduced, to 2.82° . This reduction coincides with the ascent portion of the fourth skip, reducing the lift, and the amount of altitude gained. As the zenith of the forth skip is reached, the angle of attack is increased to 7.2° , increasing the lift and once again counteracting the skipping manoeuvre. This high angle of attack is sustained until 748.2s at which point the angle of attack is reduced again significantly, to 2.6° , reducing the size of the fifth skip. At 871.2s, the angle of attack is again raised, to 5° , initiating the sixth and last skip. It is notable that the sixth skip is initiated in this way, as previously in the unpowered portion of the trajectory the angle of attack is being utilised to damped the skipping motion. This indicates that some degree of skipping is desirable after the final scramjet burn, and that

the angle of attack is being controlled to produce optimally sized skips.

Approach

After the final small skip, the angle of attack is adjusted, so that a gradual, controlled descent is initiated. After the skip phase, as the vehicle is approaching Mach 1, the angle of attack is reduced gradually to bring the SPARTAN down to 1km altitude, in a controlled manner. At 1227.0s, the bank angle is increased, in order to perform a final adjustment of the heading angle, to bring the SPARTAN to the desired end location. The SPARTAN reaches 1km altitude at -26.7° trajectory angle and 120.0m/s velocity. It is assumed that the SPARTAN is able to perform a landing manoeuvre after this point.

6.4 Design Sensitivity Analysis

It has been shown that the fly-back of the SPARTAN accelerator has a significant effect on the performance of the rocket-scramjet-rocket launch system, and that the maximum payload-to-orbit optimised trajectory changes significantly to compensate for the additional requirement of successfully returning the SPARTAN stage. This section investigates the sensitivity of the launch system to changes in the vehicle design, with the fly-back of the SPARTAN included. This sensitivity study varies the following:

- Case 12: Dynamic Pressure,
- Case 13: Specific Impulse,
- Case 14: SPARTAN Drag,
- Case 15: SPARTAN Mass,
- Case 16: SPARTAN Fuel Mass,
- Case 17: Third Stage Mass,
- & Case 18: Third Stage Thrust.

As in Section 5.3, the effect of third stage drag is negligible. For this reason, variation in the third stage drag is omitted from this study.

The launch system is able to successfully place a small satellite in orbit for every varied performance condition which has been tested, while returning the SPARTAN to its initial launch location for landing. Every maximum payload-to-orbit optimised trajectory exhibits considerable banking

during the SPARTAN's ascent trajectory, as well as a pull-up of the SPARTAN before third stage release. In every case the optimised return flight path exhibits an initial turn, boost and approach phase, with multiple skipping manoeuvres. However, two aspects of the optimised trajectories vary between cases, exhibiting no clear trend across the sensitivity studies which have been performed; the first stage-SPARTAN release conditions, and the size of the second skip of the return phase.

The first stage-SPARTAN separation angle and altitude shows no clear trend in any of the sensitivity studies performed, except for the third stage mass variation, in contrast to the sensitivity study with no fly-back, detailed in Section 5.3, in which the SPARTAN mass and drag parameters change the first stage separation point significantly. All of the optimised trajectory solutions show a distinct initial altitude raising manoeuvre, however, their size is inconsistent across optimised trajectory solutions, indicating that this manoeuvre is no longer solely a product of an efficiency trade-off between the first stage pitching and SPARTAN engine efficiency. In the maximum payload-to-orbit optimised trajectories calculated during the sensitivity analysis, it is observed that the trajectory angle at first-second stage release varies significantly between the optimised trajectories, with no discernible trend. When the SPARTAN is released at a high trajectory angle, there is a significant amount of time allowed for the bank angle to increase, and the high bank angle is utilised during the descent of the SPARTAN onto the maximum dynamic pressure path, where the trajectory angle is negative and the heading angle changes more rapidly. A lower release angle results in the SPARTAN banking more, and flying a slightly less efficient trajectory. However, a lower release angle also results in the SPARTAN using its fuel more rapidly, and covering less ground, which results in the fly-back requiring less fuel. The trade-off between first stage efficiency and the initial operational efficiency of the SPARTAN appears to be close, and for each particular trajectory optimisation one or the other is favoured with no clear trend.

It is also observed that there are two distinct return trajectory shapes for the return trajectory of the SPARTAN. The more common return trajectory shape has been shown in the preceding section, and consists of three or more large skips to begin the return trajectory. The second trajectory shape exhibits a small second skip, with the first two burns very closely spaced, or combined into one longer burn. An example of this second type of return trajectory is shown in Figure D.25. During the first two burns, a higher bank angle is maintained when compared to the large skip trajectory shape, however, after the first two burns are completed, the bank angle is reduced more rapidly. During simulations, it was observed that on occasion, the optimal return trajectory type would change as the initial guess or problem setup was altered, with no significant change in the payload-to-orbit capabilities of the launch system. This variability suggests that there is minimal difference between the two shapes of return trajectory.

Trajectory Condition	q_{max} :	40kPa	45kPa	50kPa	55kPa	60kPa	$\Delta/\Delta/\%q_{max}$
Payload to Orbit (kg)		162.5	168.4	170.2	176.5	179.6	0.4
Payload Variation (%)		-4.52	-1.10	0.00	3.65	5.51	0.25
Total η_{exergy} (%)		1.424	1.475	1.491	1.546	1.574	4e-05
1st Stage η_{exergy} (%)		8.554	8.532	8.597	8.642	8.651	-
Separation Alt, 1→2 (km)		26.08	25.36	27.14	28.13	28.47	-
Separation v, 1→2 (m/s)		1551	1554	1548	1546	1545	-
Separation γ, 1→2 (m/s)		3.3	2.6	5.6	7.2	7.7	-
2nd Stage η_{exergy} (%)		9.266	9.518	9.494	9.816	9.937	-
Separation Alt, 2→3 (km)		41.21	41.13	40.93	40.70	40.64	-0.02
Separation v, 2→3 (m/s)		2553	2579	2581	2619	2632	1.99
Separation γ, 2→3 (deg)		10.1	10.5	11.0	10.9	11.2	-
Separation q, 2→3(kPa)		10.5	10.9	11.2	11.9	12.1	0.04
2nd Stage L/D, 2→3		4.4	4.7	4.7	5.0	5.1	0.02
2nd Stage Flight Time (s)		569.4	532.5	525.4	515.9	498.7	-1.58
2nd Stage Return Fuel (kg)		292.4	257.0	268.0	222.6	208.8	-
3rd Stage η_{exergy} (%)		20.710	20.670	20.786	20.620	20.587	-
3rd Stage $t, q > 5\text{kpa}$ (s)		14.7	14.1	13.3	14.3	14.5	-
3rd Stage max α (deg)		18.2	17.9	16.7	16.1	15.9	0
3rd Stage Fuel Mass (kg)		2852.2	2846.4	2844.5	2838.3	2835.2	-0.42

Table 6.2: Comparison of key trajectory parameters with variation in the maximum dynamic pressure of the SPARTAN, with fly-back.

6.4.1 Case 12: Dynamic Pressure Variation with Fly-Back Inclusion

The maximum dynamic pressure allowable during flight is varied by $\pm 20\%$ in order to determine the sensitivity of the launch system to the structural and thermal limitations of the SPARTAN. No significant variation is observed between sensitivity studies with or without the fly-back included in the sensitivity of the launch system to the maximum dynamic pressure of the SPARTAN, by percentage. Table 6.2 shows a summary of the key parameters of each optimised trajectory, and trajectory comparison plots are shown in Appendix D.2.1. The variation in each trajectory parameter per % of the dynamic pressure is shown, if there is a clear trend. The payload-to-orbit of the launch system improves by +9.4kg (+5.51%) at 60kPa, and decreases by -7.7kg (-4.52%) at 40kPa. the overall exergy efficiency of the system increases as the maximum dynamic pressure increases, by +0.06% at 60kPa, and decreases as the maximum dynamic pressure decreases, by -0.062% at 40kpa.

No trends are observed in the exergy efficiencies of each stage due to maximum dynamic pressure variation, when fly-back is included. Compared to the sensitivity study with no fly-back, the trade-offs between the efficiencies of the stages include the manoeuvrability of the SPARTAN, which dictates the fuel used during the return flight. This additional factor produces more complicated energy trade-offs, resulting in differing optimal trajectory shapes. This can particularly be observed in the 45kPa maximum dynamic pressure trajectory, which exhibits significantly different trade-offs between each

stage, when compared to the other cases.

The 45kPa maximum dynamic pressure simulation shows lower exergy efficiencies for the first and third stages than would be suggested by the general exergy efficiency trends. However, the 45kPa simulation trades off the performance of the stages during ascent to achieve greater manoeuvrability at the beginning of the SPARTAN's trajectory, resulting in less fuel being used during fly-back, and a higher overall exergy efficiency for the SPARTAN. The first stage-SPARTAN separation occurs at a lower altitude and trajectory angle compared to the other simulations, allowing the acceleration to be achieved more quickly at the start of the trajectory, and enabling the SPARTAN to manoeuvre more effectively at the beginning of its trajectory. As a consequence, the 45kPa simulation uses only 257.0kg of fuel during the fly-back, against the general trend of the return fuel usage.

Excluding the 45kpa trajectory, increasing the maximum dynamic pressure improves the manoeuvring capabilities of the SPARTAN and increases the acceleration rate during ascent, which leads to a smaller flight time, and less ground coverage, reducing the amount of fuel necessary for fly-back. The exergy efficiency of the first stage is generally increased as the maximum dynamic pressure is increased, and the altitude at first stage-SPARTAN release is raised, again with the exception of the 45kpa case. The exergy efficiency of the SPARTAN is relatively consistent across the simulations, particularly when compared to the variance observed in the dynamic pressure sensitivity study with no fly-back, in Section 5.3.1. This is due to the higher maximum dynamic pressure simulations using more fuel during the acceleration of the SPARTAN, and accelerating more over the trajectory (the velocity at SPARTAN-third stage separation increases by +51m/s, 2.0%, at 60kpa maximum dynamic pressure, and decreases by -28m/s, 1.1%, at 40kPa), resulting in the specific impulse of the scramjet engines being lower at the end of the acceleration. Overall, the SPARTAN is utilising more fuel mass at similar efficiencies, so that more overall 'useful' work is being gained.

6.4.2 Case 13: SPARTAN Drag Sensitivity with Fly-Back Inclusion

The coefficient of drag is varied by $\pm 10\%$ to investigate the effect of variation in the aerodynamic design of the SPARTAN on the performance of the launch system, including the effects on the fly-back of the SPARTAN. Appendix D.2.2 presents trajectory comparison plots, and Table 6.3 compares key parameters of each trajectory. Increasing the drag of the SPARTAN by 10% decreases the payload-to-orbit by -14.0kg (-8.2%), while decreasing the drag by 10% increases the payload-to-orbit by +18.3kg (+10.8%). The sensitivity to variations in the SPARTAN's aerodynamics is decreased when compared to the sensitivity study with no fly-back inclusion, down to $-1.5 \frac{\Delta kg}{\Delta \% C_d}$ ($-0.9 \frac{\Delta \%}{\Delta \% C_d}$) compared to $-1.9 \frac{\Delta kg}{\Delta \% C_d}$ ($-0.99 \frac{\Delta \%}{\Delta \% C_d}$). This is due to the increased drag decreasing the ground distance covered during the ascent, offsetting the detrimental effects of the increased drag on the aerodynamic performance of the SPARTAN during fly-back. Because of this, the amount of fuel necessary for fly-back has no significant trend with variation in the drag coefficient of the SPARTAN. Once again, the trade-

Trajectory Condition	$C_{d,2}$:	90%	95%	100%	105%	110%	$\Delta/\Delta\%C_{d,2}$
Payload to Orbit (kg)	188.5	175.8	170.2	164.1	156.2	-1.5	
Payload Variation (%)	10.75	3.26	0.00	-3.61	-8.25	-0.9	
Total η_{exergy} (%)	1.653	1.540	1.491	1.437	1.368	-0.00013	
1st Stage η_{exergy} (%)	8.895	8.729	8.597	8.423	8.323	-0.029	
Separation Alt, 1→2 (km)	26.68	26.93	27.14	26.29	27.48	-	
Separation v, 1→2 (m/s)	1587	1566	1548	1534	1512	-3.66	
Separation γ, 1→2 (m/s)	4.5	5.1	5.6	4.2	6.4	-	
2nd Stage η_{exergy} (%)	10.368	9.820	9.494	9.152	8.716	-0.079	
Separation Alt, 2→3 (km)	41.71	41.29	40.93	40.86	40.82	-0.04	
Separation v, 2→3 (m/s)	2685	2616	2581	2538	2486	-9.5	
Separation γ, 2→3 (deg)	10.8	10.8	11.0	11.4	11.7	-	
Separation q, 2→3(kPa)	10.8	10.9	11.2	10.9	10.6	-	
2nd Stage L/D, 2→3	5.2	5.1	4.7	4.4	4.3	-0.05	
2nd Stage Flight Time (s)	522.1	520.2	525.4	511.7	527.0	-	
2nd Stage Return Fuel (kg)	211.7	283.2	268.0	269.3	293.8	-	
3rd Stage η_{exergy} (%)	20.326	20.663	20.786	21.080	21.274	0.046	
3rd Stage $t, q > 5\text{kpa}$ (s)	13.4	13.4	13.3	12.4	11.9	-	
3rd Stage max α (deg)	16.1	16.6	16.7	15.9	16.1	-	
3rd Stage Fuel Mass (kg)	2826.2	2839.0	2844.5	2850.7	2858.6	1.53	

Table 6.3: Comparison of key trajectory parameters with variation in the drag of the SPARTAN, with fly-back.

off between the exergy efficiency of the SPARTAN and the third stage rocket shifts in favour of the third stage rocket as the exergy efficiency of the SPARTAN is decreased. When the drag of the SPARTAN is increased by 10% the exergy efficiency of the first stage is reduced by $-0.274\%\eta$ (-3.19%), the efficiency of the SPARTAN is decreased by $-0.778\%\eta$ (-8.19%), and the efficiency of the third stage is increased by $+0.488\%\eta$ (+2.35%). When the drag of the SPARTAN is decreased by 10%, the the exergy efficiency of the first stage is increased by $+0.298\%\eta$ (+3.47%), the efficiency of the SPARTAN is increased by +0.874 (+9.21%), and the efficiency of the third stage is reduced by $-0.460\%\eta$ (-2.21%).

As was observed in the drag sensitivity study with no return, the SPARTAN-third stage separation angle shows a general increase as the drag is increased, increasing by $+0.7^\circ$ (+6.4%) at 110% drag, and decreasing by -0.2° (-1.8%) at 90% drag. However, in contrast to the drag variation study with no fly-back, the altitude of the SPARTAN-third stage separation shows a clear trend, decreasing slightly as the drag of the SPARTAN is increased, by -0.1km (-0.24%) at 110% drag, and increasing slightly as the drag is decreased, by +0.79km (+1.93%) at 90% drag. The release altitude and angle of attack serve to initiate the first skip of the return trajectory in a consistent manner, so that the shape of the initial skip is very similar with drag variation. In all cases the angle of attack is reduced to 0° immediately during return to lessen the size of the initial skip, and is then raised to close to the

maximum of 10° to prevent the dynamic pressure limit being exceeded. This consistency indicates that the initial skip of the return flight is driving the conditions at SPARTAN-third stage release, and that it is primarily the control and structural limitations, rather than the aerodynamics of the SPARTAN, which determine the shape of this skip.

6.4.3 Case 14: C-REST Specific Impulse Variation with Fly-Back Inclusion

Trajectory Condition	$I_{SP,2}$:	90%	90%	100%	105%	110%	$\Delta/\Delta\%I_{SP,2}$
Payload to Orbit (kg)	155.5	162.3	170.2	180.1	188.5	1.7	
Payload Variation (%)	-8.63	-4.65	0.00	5.81	10.71	0.98	
Total η_{exergy} (%)	1.362	1.422	1.491	1.578	1.652	0.00015	
1st Stage η_{exergy} (%)	8.547	8.562	8.597	8.563	8.564	-	
Separation Alt, 1→2 (km)	25.70	26.33	27.14	26.18	26.16	-	
Separation v, 1→2 (m/s)	1553	1550	1548	1552	1552	-	
Separation γ, 1→2 (m/s)	3.1	4.2	5.6	3.9	3.9	-	
2nd Stage η_{exergy} (%)	8.314	8.891	9.494	10.191	10.877	0.129	
Separation Alt, 2→3 (km)	40.91	41.34	40.93	41.18	41.46	-	
Separation v, 2→3 (m/s)	2475	2524	2581	2640	2695	11.13	
Separation γ, 2→3 (deg)	12.1	11.5	11.0	10.8	10.3	-0.09	
Separation q, 2→3(kPa)	10.3	10.1	11.2	11.3	11.3	-	
2nd Stage L/D, 2→3	4.6	4.8	4.7	4.6	4.8	-	
2nd Stage Flight Time (s)	509.8	521.5	525.4	511.4	513.8	-	
2nd Stage Return Fuel (kg)	270.1	274.8	268.0	244.2	247.4	-	
3rd Stage η_{exergy} (%)	21.382	21.160	20.786	20.491	20.182	-0.061	
3rd Stage $t, q > 5\text{kpa}$ (s)	12.0	11.4	13.3	14.1	14.7	-	
3rd Stage max α (deg)	15.6	15.9	16.7	16.5	16.8	-	
3rd Stage Fuel Mass (kg)	2859.2	2852.5	2844.5	2834.6	2826.3	-1.67	

Table 6.4: Comparison of key trajectory parameters with variation in the specific impulse of the C-REST engines, with fly-back.

The specific impulse of the SPARTAN is varied by $\pm 10\%$ in order to assess the sensitivity of the optimised trajectory to the performance of the scramjet engines. Key parameters of the trajectories are summarised in Table 6.4, and comparison plots are shown in Appendix D.2.3. The SPARTAN specific impulse increases the payload-to-orbit by +18.3kg (+10.71%) at 110% I_{SP} , and decreases the payload-to-orbit by -14.7kg (-8.63%) at 90% I_{SP} . This produces a general trend in the payload-to-orbit of $1.7 \frac{\Delta kg}{\Delta \% I_{SP}}$, lower than the trend of $2.2 \frac{\Delta kg}{\Delta \% I_{SP}}$ observed in the sensitivity study without fly-back, in Section 5.3.3. This lowered sensitivity in the payload-to-orbit is due to a correspondingly lowered sensitivity in the exergy efficiency of the SPARTAN, of $0.129 \frac{\Delta \% \eta}{\Delta \% I_{SP}}$, compared to $0.162 \frac{\Delta \% \eta}{\Delta \% I_{SP}}$ in the sensitivity study without fly-back. This lowered sensitivity is due to the larger I_{SP} increasing the acceleration of the SPARTAN, in turn increasing the ground distance covered by the SPARTAN and

the velocity at SPARTAN-third stage separation. At 110% I_{SP} , the SPARTAN covers 1670.2km during fly-back, compared to 1445.2km at 90% I_{SP} . This more difficult return flight serves to increase the energy necessary for the return flight, partially offsetting the benefits of the increased I_{SP} .

Similarly to the specific impulse sensitivity study without fly-back conducted in Section 5.3, the first stage trajectory is not significantly altered as the specific impulse of the SPARTAN is varied, and consequently the first stage-SPARTAN separation conditions, as well as the exergy efficiency of the first stage, exhibit no clear trends. Following first stage-SPARTAN separation, the shape of the SPARTAN's acceleration does not change significantly with specific impulse variation, including the pull-up location and acceleration flight times. As with the optimised trajectories with no fly-back, increasing the specific impulse of the scramjet engines by 10% increases the velocity at separation (by +114m/s, +4.4%) and decreases the trajectory angle (by -0.7°, 6.4%), while decreasing the specific impulse of the scramjet engines by 10% decreases the velocity at SPARTAN-third stage separation (by -106m/s, -4.1%), and increases the trajectory angle (by -1.1°, -10%). The exergy efficiency of the third stage rocket decreases as the exergy efficiency of the SPARTAN increases. This is in line with the trend which has been observed in all previous cases, that the efficiency trade-off between the SPARTAN and the third stage rocket shifts in favour of the SPARTAN as the useful energy of the SPARTAN increases.

6.4.4 Case 15: SPARTAN Mass Sensitivity

The mass of the SPARTAN is varied by $\pm 5\%$ to investigate the sensitivity of the launch system performance to the structural mass of the second stage, with the inclusion of the fly-back of the SPARTAN. The mass is varied by only $\pm 5\%$ in order to limit the decrease in the velocity of first stage-SPARTAN separation, consequently limiting the extrapolation of the C-REST engine conditions below Mach 5 (where they are still assumed to be functional during the ascent). Table 6.5 details key parameters of each trajectory, and Appendix D.2.4 shows comparison plots. Varying the structural mass of the SPARTAN yields a change in maximum payload-mass to orbit of +7.2kg (+4.22%) at 95% mass, and -6.0kg (-3.56%) at 105% mass.

The ascent trajectory of the first stage shows no significant trend with variation in the mass of the SPARTAN, except for a lower total acceleration due to having to accelerate a larger total mass. As the structural mass of the SPARTAN is increased, the exergy efficiency of the first stage decreases, from 8.780% η at 95% structural mass, to 8.356% η at 105% structural mass. This is due to the first stage rocket spending more time at lower altitude as the mass of the SPARTAN increases, spending 62.9s under 10km altitude at 95% SPARTAN mass, and 64.2s under 10km at 105% SPARTAN mass. While this difference is small, the lowered altitude over the trajectory causes an increased back pressure on the rocket engine, resulting in a lower net thrust, and consequently a lower I_{SP} from the rocket engine throughout the trajectory. The first stage-SPARTAN separation altitude and trajectory angle show no

Trajectory Condition	$m_2:$	95%	97.5%	100%	102.5%	105%	$\Delta/\Delta\%m_2$
Payload to Orbit (kg)	177.4	174.9	170.2	167.4	164.2	-1.4	
Payload Variation (%)	4.22	2.72	0.00	-1.66	-3.56	-0.8	
Total η_{exergy} (%)	1.555	1.532	1.491	1.466	1.438	-0.00012	
1st Stage η_{exergy} (%)	8.780	8.661	8.597	8.461	8.356	-0.042	
Separation Alt, 1→2 (km)	27.22	26.34	27.14	25.93	25.61	-	
Separation v, 1→2 (m/s)	1590	1572	1548	1532	1512	-7.84	
Separation γ, 1→2 (m/s)	5.1	4.0	5.6	3.8	3.6	-	
2nd Stage η_{exergy} (%)	9.364	9.460	9.494	9.605	9.709	0.033	
Separation Alt, 2→3 (km)	41.38	41.02	40.93	40.93	40.66	-0.06	
Separation v, 2→3 (m/s)	2624	2606	2581	2559	2541	-8.52	
Separation γ, 2→3 (deg)	10.8	11.0	11.0	11.3	11.3	-	
Separation q, 2→3(kPa)	10.8	11.3	11.2	11.0	11.3	-	
2nd Stage L/D, 2→3	4.8	4.7	4.7	4.7	4.6	-	
2nd Stage Flight Time (s)	522.5	510.5	525.4	510.7	509.4	-	
2nd Stage Return Fuel (kg)	260.8	251.6	268.0	281.3	282.6	-	
3rd Stage η_{exergy} (%)	20.523	20.736	20.786	20.865	20.967	0.041	
3rd Stage $t, q > 5\text{kpa}$ (s)	13.6	13.8	13.3	13.0	13.7	-	
3rd Stage max α (deg)	17.7	16.0	16.7	16.5	16.6	-	
3rd Stage Fuel Mass (kg)	2837.4	2839.9	2844.5	2847.4	2850.6	1.36	

Table 6.5: Comparison of key trajectory parameters with variation in the structural mass of the SPARTAN, with fly-back.

consistent trend as the mass of the SPARTAN is varied. Additionally, the sensitivity of the exergy efficiency of the first stage rocket to variation in the mass of the SPARTAN is lower when compared to the sensitivity study with no fly-back, at $-0.042 \frac{\Delta\%\eta}{\Delta\%m_{SPARTAN}}$, compared to $-0.060 \frac{\Delta\%\eta}{\Delta\%m_{SPARTAN}}$ with no fly-back. This lowered exergy efficiency sensitivity of the first stage, along with the lack of a trend in the trajectory angle and altitude at separation, indicates that there is no distinguishable variation in the trade-off between the exergy efficiency of the first stage and the SPARTAN. The exergy efficiency variation in the first stage is likely to be entirely due to I_{SP} variation, indicating that the performance of the SPARTAN does not affect the first stage-SPARTAN efficiency trade-off when fly-back is included.

The lower velocity of first stage-SPARTAN separation means that when the SPARTAN is heavier, it is flying at lower velocities, which is beneficial for the specific impulse of the C-REST engines. For this reason, when the SPARTAN mass is increased, the specific impulse of the SPARTAN stays high for longer, above 500s I_{SP} for 278.8s of its trajectory at 105% mass, compared to 254.4s of its trajectory at 95% mass. No significant trend is shown in the fuel necessary for return flight, indicating that the effects of the additional mass of the SPARTAN during the return flight are offset by the increased structural mass reducing the ground distance which the SPARTAN must cover during its return, from 1562.2km at 95% structural mass, to 1505.5km at 105% structural mass. As was observed in Section 5.3.4, the exergy efficiency of the SPARTAN shows an increase as the SPARTAN

mass is increased, while the exergy efficiency of the third stage rocket also shows a corresponding increase. Once again, this trend is due to additional structural mass being accelerated, which decreases the overall exergy efficiency of the stage when the 'wasted' energy from the additional structural mass is taken into account. When the structural mass of the SPARTAN is excluded from the exergy calculations, an increase in the mass of the SPARTAN decreases the useful energy usage, to 7.363GJ at 105% structural mass, compared to 7.643GJ at 95% structural mass. The third stage exergy efficiency increases as the mass of the SPARTAN is increased, by $+0.181\%\eta$ (+0.9%) at 105% SPARTAN mass, and decreases as the mass of the SPARTAN is decreased, by $-0.263\%\eta$ (-1.2%) at 95% SPARTAN mass. This indicates that the trade-off between the exergy efficiency of the SPARTAN and the third stage shifts in favour of the SPARTAN as the useful work obtained from the SPARTAN increases, further supporting the trend observed in every case previously.

6.4.5 Case 16: SPARTAN Fuel Mass Sensitivity

Trajectory Condition	$m_{F,2}$:	90%	95%	100%	105%	110%	$\Delta/\Delta\%m_{F,2}$
Payload to Orbit (kg)		165.6	169.3	170.2	175.2	179.8	0.7
Payload Variation (%)		-2.73	-0.55	0.00	2.94	5.61	0.4
Total η_{exergy} (%)		1.515	1.515	1.491	1.503	1.511	-
1st Stage η_{exergy} (%)		8.614	8.563	8.597	8.497	8.515	-
Separation Alt, 1→2 (km)		24.92	24.93	27.14	25.83	27.60	-
Separation v, 1→2 (m/s)		1580	1567	1548	1540	1523	-2.82
Separation γ, 1→2 (m/s)		1.8	2.0	5.6	3.6	6.7	-
2nd Stage η_{exergy} (%)		10.027	9.843	9.494	9.474	9.362	-0.034
Separation Alt, 2→3 (km)		41.03	40.97	40.93	41.15	41.21	-
Separation v, 2→3 (m/s)		2546	2571	2581	2611	2644	4.73
Separation γ, 2→3 (deg)		11.4	11.2	11.0	10.8	10.5	-0.04
Separation q, 2→3(kPa)		10.7	11.1	11.2	11.1	11.3	-
2nd Stage L/D, 2→3		4.8	4.8	4.7	4.7	4.8	-
2nd Stage Flight Time (s)		459.8	480.1	525.4	531.6	577.2	5.73
2nd Stage Return Fuel (kg)		252.3	248.6	268.0	265.5	241.5	-
3rd Stage η_{exergy} (%)		20.996	20.868	20.786	20.665	20.451	-0.026
3rd Stage $t, q > 5\text{kpa}$ (s)		12.3	14.6	13.3	13.9	14.9	-
3rd Stage max α (deg)		16.1	16.2	16.7	16.5	17.0	-
3rd Stage Fuel Mass (kg)		2849.2	2845.5	2844.5	2839.5	2835.0	-0.69

Table 6.6: Comparison of key trajectory parameters with variation in the fuel mass of the SPARTAN, with fly-back.

The fuel mass of the SPARTAN is varied by $\pm 10\%$, to investigate the sensitivity of the performance of the launch system to variations in the size of the fuel tanks within the SPARTAN. Appendix D.2.5 shows plots comparing each trajectory, and Table 6.6 details comparisons of key trajectory

parameters. When the fuel mass within the SPARTAN is increased by 10%, the payload to orbit increases by +9.6kg (+5.6%) and when the fuel mass is decreased by 10%, the payload mass reduces by -4.6kg (-2.7%). The magnitude of the payload-to-orbit sensitivity is very similar to the sensitivity observed without fly-back, in Section 5.3.5.

The first stage shows no significant trend in its trajectory when the fuel mass of the SPARTAN is varied, besides a decrease in the overall acceleration due to the additional mass. As the fuel mass of the SPARTAN is increased, the SPARTAN shows a decrease in exergy efficiency, by $-0.132\%\eta$ (-1.4%) at 110% fuel mass, and as the fuel mass of the SPARTAN decreases, its exergy efficiency increases significantly, by $0.533\%\eta$ (+5.6%) at 90% fuel mass. Additionally, the overall exergy efficiency of the system shows no distinct trend. As in Section 5.3.5, this is due to the increased period of acceleration causing the specific impulse of the C-REST engines to decrease. However, the overall energy availability is increased, resulting in more overall useful energy, so that the acceleration of the SPARTAN is increased, as well as the payload-to-orbit. Once again, as the amount of useful energy available to the SPARTAN increases, the trade-off between the SPARTAN and the third stage rocket shifts in favour of the SPARTAN. For this reason, the exergy efficiency of the third stage is decreased by $-0.335\%\eta$ (-1.6%) at 110% SPARTAN fuel mass, and increased by +0.210 (+1.0%) at 90% SPARTAN fuel mass.

6.4.6 Case 17: Third Stage Mass Sensitivity

The mass of the third stage rocket is varied by $\pm 10\%$. Table 6.7 details key trajectory parameters, and Appendix D.2.6 shows trajectory comparison plots. As in Section 5.3.6, the varied mass is a combination of the fuel, structural and payload mass of the third stage, representing the density of the components within the third stage. The heat shield mass is not varied, and the structural mass held at 9% of the total, non-heat shield mass. The remaining mass variation is the combination of fuel and payload mass, which the optimiser utilises interchangeably to optimise the trajectory.

Increasing the third stage mass by 10% causes a corresponding increase in the payload-to-orbit of +9.9kg (+5.8%), while decreasing the third stage mass by 10% causes a decrease in payload-to-orbit of -9.4kg (-5.5%). This payload-to-orbit mass sensitivity is very similar when compared to the third stage mass sensitivity study without fly-back, in Section 5.3.6. However, due to the payload-to-orbit being lower when the fly-back of the SPARTAN is included, the overall percentage payload increase is higher, at $0.56 \frac{\Delta\%m_{payload}}{\Delta\%m_3}$, compared to $0.47 \frac{\Delta\%m_{payload}}{\Delta\%m_3}$ without fly-back. Similarly to the sensitivity study without fly-back, the SPARTAN-third stage separation angle increases as the third stage mass is increased, by $+0.6^\circ$ (+5.4%) at $110\%m_3$, and decreases as the third stage mass is decreased, by -1.2° (-10.9%) at $90\%m_3$. The exergy efficiency of the SPARTAN increases as the mass of the third stage increases, by $+0.289\%\eta$ (+1.4%) at $110\% m_3$, and decreases when the third stage mass is decreased, by $-0.567\%\eta$ (-2.7%) at $90\% m_3$. This trend in third stage exergy efficiency is very similar

Trajectory Condition	$m_3:$	90%	95%	100%	105%	110%	$\Delta/\Delta\%m_3$
Payload to Orbit (kg)		160.8	167.2	170.2	176.7	180.1	1
Payload Variation (%)		-5.54	-1.76	0.00	3.81	5.76	0.56
Total η_{exergy} (%)		1.420	1.471	1.491	1.542	1.565	7e-05
1st Stage η_{exergy} (%)		8.856	8.742	8.597	8.428	8.290	-0.029
Separation Alt, 1→2 (km)		27.73	27.73	27.14	25.77	25.32	-0.14
Separation v, 1→2 (m/s)		1602	1575	1548	1526	1500	-5.06
Separation γ, 1→2 (m/s)		5.7	6.1	5.6	3.6	3.2	-
2nd Stage η_{exergy} (%)		9.464	9.470	9.494	9.683	9.808	0.018
Separation Alt, 2→3 (km)		40.36	41.01	40.93	41.27	41.29	-
Separation v, 2→3 (m/s)		2656	2621	2581	2559	2531	-6.25
Separation γ, 2→3 (deg)		9.8	10.6	11.0	11.5	11.6	0.09
Separation q, 2→3(kPa)		12.9	11.4	11.2	10.5	10.2	-0.13
2nd Stage L/D, 2→3		5.0	4.9	4.7	4.6	4.6	-
2nd Stage Flight Time (s)		525.8	530.6	525.4	514.5	514.6	-
2nd Stage Return Fuel (kg)		257.2	235.8	268.0	253.4	271.5	-
3rd Stage η_{exergy} (%)		20.219	20.524	20.786	20.885	21.075	0.041
3rd Stage $t, q > 5\text{kpa}$ (s)		17.0	14.2	13.3	11.5	12.4	-
3rd Stage max α (deg)		16.5	16.2	16.7	17.0	17.7	-
3rd Stage Fuel Mass (kg)		2553.7	2697.4	2844.5	2988.2	3135.0	29.07

Table 6.7: Comparison of key trajectory parameters with variation in the mass of the third stage, with fly-back.

to the corresponding trend observed with no fly-back, in Section 5.3.6. As with the trend observed in Section 5.3.6, this increase in third stage exergy efficiency as the mass of the third stage is increased is caused by a lower portion of the third stage fuel being utilised in-atmosphere when the third stage mass is increased, consisting of 41.89% of the total fuel when m_3 is set to 110% of the baseline mass, compared to 43.32% of the total fuel when m_3 is set to 90% of the baseline mass. In addition, the heat shield is once again a lower fraction of the overall mass, resulting in a lower fraction of the third stage mass being discarded.

6.4.7 Case 18: Third Stage I_{SP} Sensitivity

The specific impulse of the third stage rocket is varied by $\pm 5\%$ to investigate the sensitivity of the launch system to the performance of the third stage rocket when the fly-back of the SPARTAN is included. Table 6.8 shows selected performance indicators, while Appendix D.2.7 shows comparison plots of the maximum payload-to-orbit trajectory at each magnitude of third stage specific impulse. The sensitivity of the optimal trajectory with SPARTAN fly-back to the third stage specific impulse is very similar to that observed in Section 5.3.7 with no SPARTAN fly-back. The specific impulse of the third stage has the most significant effect on the payload-to-orbit capability of the launch system, with a sensitivity of 4.6kg per % I_{SP} variation. This indicates that the fly-back does not considerably

Trajectory Condition	$I_{SP,3}$:	95%	97.5%	100%	102.5%	105%	$\Delta/\Delta\%I_{SP,3}$
Payload to Orbit (kg)	126.5	149.5	170.2	195.0	217.9	4.6	
Payload Variation (%)	-25.71	-12.20	0.00	14.55	28.00	2.68	
Total η_{exergy} (%)	1.107	1.309	1.491	1.709	1.911	0.0004	
1st Stage η_{exergy} (%)	8.561	8.562	8.597	8.602	8.604	0.003	
Separation Alt, 1→2 (km)	26.09	26.07	27.14	27.01	27.03	-	
Separation v, 1→2 (m/s)	1552	1552	1548	1550	1550	-	
Separation γ, 1→2 (m/s)	3.7	3.8	5.6	5.3	5.4	-	
2nd Stage η_{exergy} (%)	9.519	9.541	9.494	9.610	9.701	-	
Separation Alt, 2→3 (km)	41.18	41.13	40.93	41.01	40.63	-	
Separation v, 2→3 (m/s)	2583	2585	2581	2595	2606	-	
Separation γ, 2→3 (deg)	11.3	11.3	11.0	10.9	10.5	-	
Separation q, 2→3(kPa)	10.8	10.9	11.2	11.2	11.9	-	
2nd Stage L/D, 2→3	4.7	4.6	4.7	4.8	4.8	-	
2nd Stage Flight Time (s)	510.1	510.8	525.4	525.0	526.3	-	
2nd Stage Return Fuel (kg)	249.9	251.6	268.0	239.0	232.7	-	
3rd Stage η_{exergy} (%)	15.548	18.222	20.786	23.386	25.913	0.518	
3rd Stage $t, q > 5\text{kpa}$ (s)	12.1	12.3	13.3	13.7	14.9	0.14	
3rd Stage max α (deg)	17.7	16.2	16.7	16.3	16.9	-	
3rd Stage Fuel Mass (kg)	2888.3	2865.3	2844.5	2819.8	2796.9	-4.57	

Table 6.8: Comparison of key trajectory parameters with variation in the specific impulse of the third stage, with fly-back.

effect the sensitivity of the launch system to variations in the third stage specific impulse, and that the third stage specific impulse has a consistent magnitude of effect at lower separation velocities. The trajectory of the first stage does not change significantly as the specific impulse of the third stage is varied. The exergy efficiency of the first stage shows a slight trend, however, this is very small. The trajectory SPARTAN shows no distinct trends as the specific impulse of the third stage is varied. This lack of distinct trends indicates that the performance of the third stage has no bearing on the magnitude of the pull-up of the SPARTAN, and does not effect the efficiency trade-off between the SPARTAN and the third stage in a significant way. As the specific impulse of the third stage is increased, the angle of attack schedule of the third stage is modified, so that 90km altitude is reached at circularisation conditions in all cases. This causes an increase in specific impulse to result in more time spent in-atmosphere, with the third stage spending 14.9s at dynamic pressures greater than 5kPa at 105% I_{SP} , compared to 12.1s at 95% I_{SP} .

6.5 Comparison of Sensitivities

The sensitivities of the launch system to a variety of design parameters have been presented in the preceding sections. Figure 6.7 shows a relative comparison of the payload-to-orbit sensitivity for

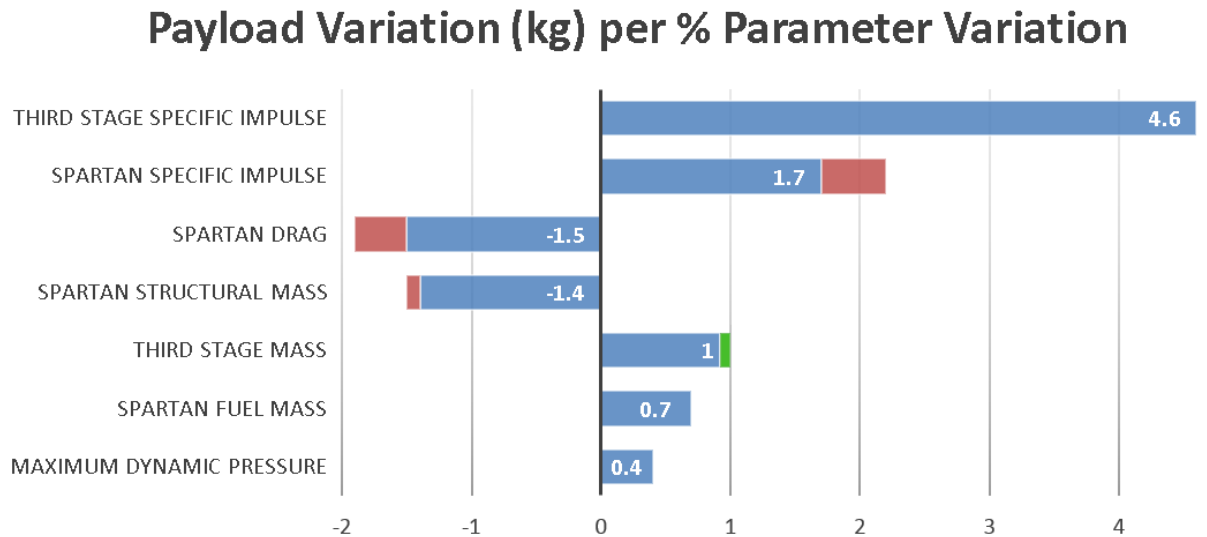


Figure 6.7: The sensitivity of the key design parameters of the launch system, including SPARTAN fly-back. Red and green coloured areas indicate decreases or increases in the magnitude of sensitivity respectively, compared to the sensitivity study without SPARTAN fly-back in Section 5.4.

each parameter which has been tested, by percentage. When the fly-back of the SPARTAN is included, the sensitivity of the launch system to the specific impulse, drag, and mass of the SPARTAN decreases. This is due to the fly-back of the SPARTAN partially offsetting the effects of variations in the performance of the SPARTAN. As the performance of the SPARTAN improves, the velocity at SPARTAN-third stage separation increases, as well as the ground distance which the SPARTAN covers during its ascent. These effects are beneficial to the payload-to-orbit, but result in a more challenging fly-back, in turn necessitating the SPARTAN to trade-off performance in order to successfully return to the initial launch site.

The sensitivity of the launch system to the maximum dynamic pressure is unchanged when fly-back is included. However, the slight decrease in the sensitivity of the launch system to the structural mass of the SPARTAN, to $-1.4 \frac{\Delta kg}{\Delta \% m_{SPARTAN}}$, means that the potential beneficial effects of reducing the maximum dynamic pressure of the SPARTAN are reduced slightly. So long as the mass of the SPARTAN reduces by 28.3kg for each 1kPa reduction in the maximum dynamic pressure, the performance of the launch system will improve.

For the specific impulse of the SPARTAN to be increased, it is likely that the shape of the C-REST engines or forebody will need to be modified, or extra systems will need to be added. The sensitivity of the launch system to the specific impulse of the SPARTAN is decreased significantly when the fly-back of the SPARTAN is included, to $1.7 \frac{\Delta kg}{\Delta \% I_{SP,SPARTAN}}$, a decrease of $-0.5 \frac{\Delta kg}{\Delta \% I_{SP,SPARTAN}}$ (-22.7%) compared to the sensitivity without fly-back. The sensitivity of the launch system to the SPARTAN's structural mass is also decreased, to $-1.4 \frac{\Delta kg}{\Delta \% m_{SPARTAN}}$. Comparing these sensitivities, it is apparent that if the specific impulse of the SPARTAN can be increased by 1% with less than 1.21% (60.0kg) in-

crease in the total mass of the SPARTAN, then the overall performance of the launch system will be improved. Similarly, the sensitivity of the launch system to variation in the drag of the SPARTAN is reduced, to $-1.5 \frac{\Delta kg}{\Delta \% C_d, SPARTAN}$. Comparing this sensitivity with the sensitivity to the structural mass of the SPARTAN, it can be seen that if the specific impulse of the C-REST engines can be improved by 1%, while increasing the drag of the SPARTAN by less than 1.13% due to shape variation, that the overall performance change will be beneficial. The decreased sensitivity of the launch system performance to the structural mass of the SPARTAN, along with the unchanged fuel mass sensitivity, means that so long as 1kg of fuel mass can be added with less than 1.59kg of structural mass added, the performance of the launch system will improve. Additionally, the decreased sensitivity of the launch system to the drag of the SPARTAN means that so long as 1kg of fuel can be added to the SPARTAN, with a drag increase of less than 0.030%, then the maximum payload-to-orbit will increase. Comparing the increased third stage mass sensitivity, of $1 \frac{\Delta kg}{\Delta \% m_3}$, with the decreased SPARTAN drag sensitivity, shows that if the size of the third stage can be increased so that the third stage mass increases by 1kg while the fuselage of the SPARTAN varied so that the increase in SPARTAN drag is less than 0.020%, the maximum payload-to-orbit will be improved.

6.6 Summary

In this chapter, the maximum payload-to-orbit trajectory for a rocket-scramjet-rocket system has been calculated, with the inclusion of the fly-back of the SPARTAN scramjet-powered stage. It was found that it is possible for 170.2kg of payload to be delivered to sun synchronous orbit, while successfully returning the scramjet-powered stage to the initial launch site. During the return flight, the scramjet engines are powered on three times, in total using 268.0kg of fuel for the return flight, 17.2% of the SPARTAN's total fuel.

It was found that when the fly-back of the SPARTAN is included in the optimal trajectory calculation, the first stage of the launch system pitches in an easterly direction. The launch system exhibits a first stage-SPARTAN separation point of 27.14km, an increase of 3.0km when compared to the maximum payload-to-orbit trajectory with no fly-back, and a trajectory angle of 5.6° , an increase of 2.5° . This higher separation point serves to increase the efficiency of the first stage, to $8.597\% \eta$, an increase of $0.426\% \eta$ when compared to the maximum payload-to-orbit trajectory with no fly-back. In addition to increasing the exergy efficiency of the first stage, the higher first stage-SPARTAN separation serves to increase the altitude of the SPARTAN at the beginning of its trajectory. The SPARTAN banks heavily immediately after release, and descends, allowing for the heading angle to change rapidly. The SPARTAN maintains a high bank angle throughout its trajectory, executing a banking manoeuvre, and staying close to its maximum dynamic pressure. This banking manoeuvre decreases the exergy efficiency of the SPARTAN by $-1.448\% \eta$ (-12.2%), but also reduces the ground distance necessary for the return of the SPARTAN, decreasing the amount of fuel necessary for fly-back, and

increasing the overall efficiency of the SPARTAN. At the end of its acceleration, the SPARTAN was found to exhibit a pull-up manoeuvre before the separation of the third stage, in a similar fashion to the maximum payload-to-orbit trajectory with no fly-back.

The fly-back of the SPARTAN is found to be separated into three stages; an initial turn, a boost phase, and an approach. The initial turn takes place immediately after separation, and consists of the SPARTAN banking heavily in order to manoeuvre the heading angle back towards the initial launch site. During the boost-skip phase the SPARTAN exhibits multiple 'skipping' manoeuvres. These skipping manoeuvres have been shown in previous literature to extend the flight range of hypersonic vehicles[70–73], and serve to reduce the amount of fuel used during the fly-back. In addition, the skipping manoeuvres allow the scramjet engines to be powered on at the points where the specific impulse of the C-REST engines are highest, maximising the performance of the SPARTAN, and minimising the fuel necessary for return. During the approach phase, the trajectory of the SPARTAN is smoothed, and the SPARTAN glides to the landing point. The optimal trajectory terminates when SPARTAN reaches 1km altitude at a velocity of 120m/s. After this point, it is assumed that the SPARTAN lands on a traditional runway. This result indicates that it is feasible to return a hypersonic launch vehicle from a high Mach number separation, to its initial launch site.

The sensitivity of the launch system to various design parameters has been investigated. As was observed in the sensitivity study with no fly-back, it has been observed that in all cases the exergy efficiency trade-off between the SPARTAN and the third stage rocket shifts in favour of the SPARTAN as the amount of 'useful' work available to the SPARTAN is increased, and vice versa. The sensitivity of the launch system to variations in the specific impulse, drag and structural mass of the SPARTAN was found to decrease when fly-back is included, compared to the sensitivity study with no fly-back. This decreased sensitivity indicates that the fly-back of the SPARTAN offsets some of the payload-to-orbit variation due to changes in these parameters.

CHAPTER 7

CONCLUSIONS

The purpose of this work was to design and investigate the launch trajectory for a partially-reusable, rocket-scramjet-rocket, small satellite launch system. The trajectory of this launch system was optimised for maximum payload-to-orbit, and characterised in order to determine the key performance parameters of the launch system. This aim was achieved through the completion of the set of objectives detailed as follows:

Development of a detailed design and aerodynamic simulation for a rocket-scramjet-rocket launch system.

In order to create a representative model for a trajectory simulation, the design of a rocket-scramjet-rocket launch system was developed, structured around the SPARTAN scramjet-powered accelerator, which is in development at The University of Queensland. A first stage rocket was designed to accelerate the SPARTAN to its minimum operating of Mach 5. This first stage is based upon the Falcon-1e, scaled down lengthwise to 8.5m and throttled down to a constant 70% to assist in pitching. A third stage rocket was designed, based around the Kestrel upper stage rocket motor, for cost effectiveness. This third stage was sized to fit within the fuselage of the SPARTAN, to be 9m long, and 1.5m wide. The internal layout of the SPARTAN was modified, to accommodate the redesigned third stage. The fuel tanks of the SPARTAN were sized to hold a total of 1562kg of LH₂ fuel.

The aerodynamics of the first stage and the SPARTAN were calculated using Cart3D, an inviscid CFD package, and the aerodynamics of the SPARTAN were modified using a viscous correction for accuracy. The aerodynamics of the launch system were calculated across the operable regimes of the vehicles, which for the SPARTAN included both engine-on and engine-off conditions, across a range of Mach numbers from 0.2 to 10. The control surfaces of the SPARTAN were modelled, and the aerodynamics of the SPARTAN simulated with flaps deployed. A variable centre of gravity model

CHAPTER 7. CONCLUSIONS

was created for the SPARTAN, to model the changes in the vehicle dynamics during flight. The aerodynamics of the SPARTAN were calculated at multiple centre of gravity positions, and a trimmed aerodynamic database created. The aerodynamics of the third stage were modelled using Missile Datcom, a partially empirical tool for estimating the aerodynamics of missile and rocket vehicles.

Calculation of the maximum payload-to-orbit trajectory for a rocket-scramjet-rocket launch system using optimal control, with and without fly-back.

In order to calculate the maximum payload-to-orbit trajectory of the launch system, a software package was created to simulate and optimise launch system trajectories, designated LODESTAR. LODESTAR utilises GPOPS-2, a pseudospectral method optimal control solver. LODESTAR simulates the trajectory of each stage of the launch system in six degrees of freedom, in a geodetic rotational reference frame. LODESTAR optimises the entire trajectory of the launch system simultaneously, so that the performance trade-offs between the stages are captured accurately.

A mission profile has been developed for the rocket-scramjet-rocket launch system, launching a satellite to sun synchronous orbit from the Northern Territory, Australia. Initially, the trajectory of the launch system was simulated without taking into account the fly-back of the SPARTAN, assuming that the SPARTAN lands at a location downrange. A mission case was developed in which the scramjet stage of the launch vehicle was constrained to flight at its maximum dynamic pressure, and providing a baseline trajectory case for comparison. This constant dynamic pressure trajectory was found to be capable of delivering 158.4kg to sun synchronous orbit. The maximum payload-to-orbit trajectory of the launch system was then calculated. It was found that when flying the payload-optimised trajectory, the launch system is capable of delivering 189.2kg of payload to sun synchronous orbit, an increase of 16.3% over the simulation with the SPARTAN constrained to constant dynamic pressure. This improvement in payload-to-orbit was found to be primarily a result of favourable trade-offs, between the efficiency of the stages of the launch system. Three key features were observed in the trajectory; a high first stage-SPARTAN separation point, an altitude raising manoeuvre in the centre of the SPARTAN's trajectory, and a pull-up before SPARTAN-third stage separation. The higher first stage-SPARTAN separation point was found to decrease the amount of turning which the first stage must perform, resulting in an overall increase in performance. Similarly, a pull-up before SPARTAN-third stage separation decreases the amount of turning which the third stage must perform, and enables the third stage to gain altitude much more rapidly, causing it to spend significantly less time at high dynamic pressure. Increasing the altitude of the stage separations was found to trade off the efficiency of the SPARTAN, which is reduced by $-1.318\%\eta$, for an increase in the efficiency of the first and third stages, by $+0.161\%\eta$ (+2.0%) and $+6.72\%\eta$ (+39.8%) respectively. The altitude raising manoeuvre in the centre of the SPARTAN's trajectory was observed occur in a region of homogeneity in the performance of the SPARTAN, increasing the efficiency of the SPARTAN very slightly (by only $+0.003\%\eta$).

The optimised maximum payload-to-orbit was calculated with the addition of the fly-back of the SPARTAN, to the initial launch site. It was found that the launch system is capable of delivering 170.2kg of payload to sun synchronous orbit, while returning the SPARTAN to the initial launch site. The fly-back of the SPARTAN was found to alter the shape of the ascent trajectory significantly. When the fly-back was included, the first stage was found to initially pitch towards the east, exhibiting a significantly higher first stage-SPARTAN separation at 27.14km. The SPARTAN was then observed to bank heavily, executing a heading angle change manoeuvre during its acceleration. No altitude raising manoeuvre is present during the acceleration of the SPARTAN. This is due to the angle of attack values being higher during the SPARTAN's acceleration, resulting in flight at the SPARTAN's maximum dynamic pressure being optimal. When the fly-back was included, the SPARTAN was still observed to perform a pull-up manoeuvre before third stage separation, of a similar magnitude the pull-up manoeuvre performed with no fly-back. The optimal fly-back of the SPARTAN was found to require the ignition of the scramjet engines, and was observed to exhibit three distinct phases, an initial turn, a boost-skip, and an approach. During the initial turn, the bank angle of the SPARTAN is increased rapidly, in order to manoeuvre the heading angle of the SPARTAN back towards its initial launch site. After this initial turn, the boost-skip phase is initiated, consisting of multiple skipping manoeuvres. These skipping manoeuvres serve both to increase the range of the SPARTAN during its return, minimising the fuel necessary for the fly-back, as well as improving the specific impulse of the scramjet engines. The scramjet engines were observed to be ignited at the trough of each skip, as the SPARTAN accelerates to the minimum operable Mach number. This is the point of the skipping manoeuvres at which the specific impulse of the scramjet engines is highest, so that igniting the scramjet engines at this point minimises the fuel necessary for the return flight. After the scramjets were ignited a total of three times, the size of the skips were observed to decrease. Finally, the skips ceased entirely, beginning a steady descent and approach to the landing site. In total, 268.0kg of fuel was used during the fly-back, 17.2% of the SPARTAN's total fuel mass.

Analysis of the sensitivity of the maximum payload-to-orbit trajectory to variations in key design parameters of the launch system.

Eight key design parameters of the launch system were modified, and the variation in the maximum payload-to-orbit trajectory of the launch system was studied, for cases with and without SPARTAN fly-back. The parameters varied were: the maximum dynamic pressure of the SPARTAN, the fuel mass within the SPARTAN, the drag of the SPARTAN, the specific impulse of the SPARTAN, the mass of the SPARTAN, the drag of the third stage, the specific impulse of the third stage, and the mass of the third stage. It was found that in the cases with no fly-back, the ability of the first stage to pitch, determined by the overall system mass or drag, is the primary driver of the first stage-SPARTAN separations conditions. The efficiency trade-off was observed to shift towards the SPARTAN when the first stage accelerated more slowly, due to the better pitching ability of the first stage. However,

CHAPTER 7. CONCLUSIONS

this trend was not observed when the fly-back of the SPARTAN was included. The disappearance of this trend indicates that when the fly-back of the SPARTAN is included, the first stage-SPARTAN separation point is determined by a more complex trade-off, involving the fly-back trajectory. Across all cases it was found that the trade-off was determined by the 'useful' energy available to the SPARTAN, which is increased due to improving the efficiency of the SPARTAN, adding fuel mass, or reducing structural mass. The more 'useful' energy available to the SPARTAN, the more the trade-off between the SPARTAN and the third stage favours the SPARTAN (ie. the pull-up before separation is smaller). However, variations in the efficiency of the third stage were found to produce no significant variation in the trajectory of the SPARTAN.

Out of the modified design parameters, it was found that the specific impulse of the third stage had by far the largest effect on the performance of the launch system, varying the payload-to-orbit by 4.6kg for each percent of additional specific impulse. This large sensitivity is due to the particular importance of the specific impulse during the Hohmann transfer, which is significant in determining the final payload mass. The sensitivities of all significantly coupled design parameters are compared, and their relative quantities assessed to provide meaningful insights into the design of the launch system. Of these comparisons, the relationship between the maximum dynamic pressure and the structural mass of the SPARTAN was found to be of particular interest. It was found that the sensitivity of the launch system to the maximum dynamic pressure of the SPARTAN is relatively low, indicating that it may be advantageous to fly the SPARTAN at a lower maximum dynamic pressure, in order to reduce heat shielding and structural mass. It was found that if the mass of the SPARTAN can be reduced by greater than -26.5kg per -1Kpa reduction in maximum dynamic pressure (or -28.4kg per 1kPa when fly-back is included) then a larger payload-to-orbit will be achieved.

The investigation of the optimised trajectory with variations in key design parameters of the launch vehicle has provided insights into the shape of the optimised trajectory, while the comparative sensitivities have allowed the effects of the modified design parameters of the launch vehicle to be quantified. These findings can be used to predict the maximum payload-to-orbit trajectories of future launch systems, as well as how design changes may affect the performance of the launch system utilised in this study.

CHAPTER 8

RECOMMENDATIONS FOR FUTURE WORK

This work on the calculation of a maximum payload-to-orbit trajectory for a rocket-scramjet-rocket launch system was carried out to determine the behaviour and sensitivities of such a launch system, in order to inform future launch vehicle designs. In addition to improvements in the design of the launch system, a number of outstanding research questions were identified during the course of this work. In order to build upon this work and advance our knowledge of partially-airbreathing launch systems, the following research directions are suggested:

Controllability studies of all three vehicles of the launch system.

During this work, the controllability of the vehicles within the launch system were constrained to values which were estimated to represent the realistic control limits of each vehicle. A controllability study of all three stages would improve the accuracy of the vehicle simulation model and introduce more realistic control limits to the trajectory optimisation.

Design of a fly-back first stage booster.

During this work, the first stage booster is assumed to be expendable, to enable a simple design process. However, in the future it is likely that the first stage of the launch system will be required to be reusable for the launch system to be economically feasible. As such, a first stage booster must be designed and sized which is capable of accelerating the SPARTAN to operational speeds, as well as returning to the initial launch site after separation.

Cost analysis of the launch system.

A primary driver for a realistic launch system is its overall performance, as a function of payload-to-orbit and launch flexibility, and launch cost. In order for a new style of launch system to be properly characterised, a bottom-up cost model estimate is necessary. A bottom-up cost model estimate allows for the primary cost drivers to be identified, down to a subsystem level.

Multi-disciplinary design optimisation sizing of the launch system.

During this work, the first and third stages of the launch system were designed around the previously sized SPARTAN vehicle. The development and characterisation of the maximum payload-to-orbit trajectory of the rocket-scramjet-rocket launch system paves the way for a multi-disciplinary design optimisation, of all three stages concurrently. A multi-disciplinary design optimisation of the system would allow the sizing of the three stages to be optimised, taking into account the variation in the maximum payload-to-orbit trajectory path.

REFERENCES

- [1] S. O. Forbes-Spyratos, M. P. Kearney, M. K. Smart, and I. H. Jahn. “Trajectory Design of a Rocket-Scramjet-Rocket Multi-Stage Launch System”. In: *Journal of Spacecraft and Rockets* (2018). DOI: [10.2514/1.A34107](https://doi.org/10.2514/1.A34107).
- [2] S. Forbes-Spyratos, M. Kearney, M. Smart, and I. Jahn. “Trajectory design of a rocket-scramjet-rocket multi-stage launch system”. In: *21st AIAA International Space Planes and Hypersonics Technologies Conference, Hypersonics 2017*. Xiamen, China, 2017. ISBN: 9781624104633.
- [3] S. O. Forbes-Spyratos, M. P. Kearney, M. K. Smart, and I. H. Jahn. “Fly-back of a scramjet-powered accelerator”. In: *AIAA Scitech, 2018*. Orlando, FL, 2018. ISBN: 9781624105241. DOI: [10.2514/6.2018-2177](https://doi.org/10.2514/6.2018-2177).
- [4] J. Chai, M. Smart, S. Forbes-Spyratos, and M. Kearney. “Fly Back Booster Design for Mach 5 Scramjet Launch”. In: *68th International Astronautical Congress*. Aelade, Australia, 2017.
- [5] Federal Aviation Administration. *The Annual Compendium of Commercial Space Transportation: 2018*. Tech. rep. January. Washington, DC, 2018, p. 255. URL: https://www.faa.gov/about/office_org/headquarters_offices/ast/media/2018_AST_Compendium.pdf.
- [6] C. Niederstrasser and W. Frick. “Small Launch Vehicles A 2015 State of the Industry Survey”. In: *Proceedings of the 29th Annual AIAA/USU Conference on Small Satellites*. Logan, UT, 2015.
- [7] M. K. Smart and M. R. Tetlow. “Orbital Delivery of Small Payloads Using Hypersonic Air-breathing Propulsion”. In: *Journal of Spacecraft and Rockets* 46.1 (2009), pp. 117–125. ISSN: 0022-4650. DOI: [10.2514/1.38784](https://doi.org/10.2514/1.38784).

REFERENCES

- [8] A. D. Ketsdever, M. P. Young, J. B. Mossman, and A. P. Pancotti. “Overview of Advanced Concepts for Space Access”. In: *Journal of Spacecraft and Rockets* 47.2 (2010), pp. 238–250. ISSN: 0022-4650. DOI: [10.2514/1.46148](https://doi.org/10.2514/1.46148).
- [9] M. Smart. *Scramjet Inlets*. Tech. rep. 9. Defense Technical Information Center, 2010. DOI: [10.2514/5.9781600866609.0447.0511](https://doi.org/10.2514/5.9781600866609.0447.0511).
- [10] F. Curran, J. Hunt, N. Lovell, G. Maggio, and V. Bilardo. “The Benefits of Hypersonic Airbreathing Launch Systems for Access to Space”. In: *39th AIAA/ASME/SAE/ASEE Joint Propulsion Conference and Exhibit* July (2003), pp. 1–14. DOI: [10.2514/6.2003-5265](https://doi.org/10.2514/6.2003-5265). URL: <http://arc.aiaa.org/doi/10.2514/6.2003-5265>.
- [11] J. D. Shaughnessy, S. Z. Pinckney, and J. D. McMinn. “Hypersonic Vehicle Simulation Configuration Model : Winged-Cone Configuration”. In: (1990).
- [12] D. Preller and M. K. Smart. “Reusable Launch of Small Satellites Using Scramjets”. In: *Journal of Spacecraft and Rockets* 54.6 (2017), pp. 1–13. ISSN: 0022-4650. DOI: [10.2514/1.A33610](https://doi.org/10.2514/1.A33610). URL: <https://doi.org/10.2514/1.A33610>.
- [13] Heiser H. H. and D. T. Pratt. *Hypersonic Airbreathing Propulsion*. Washington, D.C: American Institute of Aeronautics and Astronautics, 1994, p. 11. ISBN: 1-56347-035-7. DOI: [10.2514/4.470356](https://doi.org/10.2514/4.470356).
- [14] A. Rao. “A survey of numerical methods for optimal control”. In: *Advances in the Astronautical Sciences* 135 (2009), pp. 497–528. URL: <http://vdol.mae.ufl.edu/ConferencePublications/trajectorySurveyAAS.pdf>.
- [15] J. T. Betts. “Survey of Numerical Methods for Trajectory Optimization”. In: *Journal of Guidance, Control, and Dynamics* 21.2 (1998), pp. 193–207. ISSN: 0731-5090. DOI: [10.2514/2.4231](https://doi.org/10.2514/2.4231).
- [16] *Australia’s hypersonic plane for a new space race*. URL: <http://www.bbc.com/future/story/20161117-australias-hypersonic-spaceplane-for-a-new-space-race> (visited on 06/21/2018).
- [17] F. S. Billig. “Research on supersonic combustion”. In: *Journal of Propulsion and Power* 9.4 (1993), pp. 499–514. ISSN: 0748-4658. DOI: [10.2514/3.23652](https://doi.org/10.2514/3.23652).
- [18] S. Cook and U. Hueter. “NASA’s Integrated Space Transportation Plan 3rd generation reusable launch vehicle technology update”. In: *Acta Astronautica* 53.4-10 (2003), pp. 719–728. ISSN: 00945765. DOI: [10.1016/S0094-5765\(03\)00113-9](https://doi.org/10.1016/S0094-5765(03)00113-9).
- [19] E. T. Curran. “Scramjet Engines: The First Forty Years”. In: *Journal of Propulsion and Power* 17.6 (2001), pp. 1138–1148. ISSN: 0748-4658. DOI: [10.2514/2.5875](https://doi.org/10.2514/2.5875). URL: <http://arc.aiaa.org/doi/10.2514/2.5875>.

- [20] M. K. Smart. “How Much Compression Should a Scramjet Inlet Do?” In: *AIAA Journal* 50.3 (2012), pp. 610–619. ISSN: 0001-1452. DOI: [10.2514/1.J051281](https://doi.org/10.2514/1.J051281). URL: <http://arc.aiaa.org/doi/10.2514/1.J051281>.
- [21] E. T. Curran. “Scramjet Engines: The First Forty Years”. In: *Journal of Propulsion and Power* 17.6 (2001), pp. 1138–1148. ISSN: 0748-4658. DOI: [10.2514/2.5875](https://doi.org/10.2514/2.5875).
- [22] A Paull, R. Stalker, and D Mee. “Thrust Measurements of a Complete Axisymmetric Scramjet in an Impulse Facility”. In: *5th International Space Planes and Hypersonics Conference*. Munich,Germany, 1993.
- [23] E. Curran. *Scramjet Propulsion*. Progress in Astronautics and Aeronautics, 2001. ISBN: 978-1-60086-660-9.
- [24] W. Heiser, D. Pratt, D. Daley, and U. Mehta. *Hypersonic Airbreathing Propulsion*. the American Institute of Aeronautics and Astronautics, 1994. ISBN: 978-1-56347-035-6.
- [25] R. S. Fry. “A Century of Ramjet Propulsion Technology Evolution”. In: *Journal of Propulsion and Power* 20.1 (2004), pp. 27–58. ISSN: 0748-4658. DOI: [10.2514/1.9178](https://doi.org/10.2514/1.9178). URL: <http://arc.aiaa.org/doi/10.2514/1.9178>.
- [26] M Smart. “Scramjets”. In: 3219 (2007).
- [27] D. J. Dalle, S. M. Torrez, J. F. Driscoll, M. a. Bolender, and K. G. Bowcutt. “Minimum-Fuel Ascent of a Hypersonic Vehicle Using Surrogate Optimization”. In: *Journal of Aircraft* 51.6 (2014), pp. 1973–1986. ISSN: 0021-8669. DOI: [10.2514/1.C032617](https://doi.org/10.2514/1.C032617). URL: <http://arc.aiaa.org/doi/10.2514/1.C032617>.
- [28] J. Bradford, J. Olds, R. Bechtel, T. Cormier, and D. Messitt. “Exploration of the design space for the ABLV-GT SSTO reusable launch vehicle”. In: *Space 2000 Conference and Exposition* September (2000). DOI: [doi:10.2514/6.2000-5136](https://doi.org/10.2514/6.2000-5136). URL: <http://dx.doi.org/10.2514/6.2000-5136>.
- [29] D. Dalle, S. Torrez, and J. Driscoll. “Turn Performance of an Air-Breathing Hypersonic Vehicle”. In: *AIAA Atmospheric Flight Mechanics Conference* August (2011). DOI: [10.2514/6.2011-6300](https://doi.org/10.2514/6.2011-6300). URL: <http://arc.aiaa.org/doi/10.2514/6.2011-6300>.
- [30] R. Kendall and P. Portanova. *Launch Vehicles Then and Now: 50 Years of Evolution*. 2010. URL: <http://www.aerospace.org/crosslinkmag/spring-2010/launch-vehicles-then-and-now-50-years-of-evolution/> (visited on 06/21/2018).
- [31] R. D. Launius. “Assessing the legacy of the Space Shuttle”. In: *Space Policy* 22.4 (2006), pp. 226–234. ISSN: 02659646. DOI: [10.1016/j.spacepol.2006.08.008](https://doi.org/10.1016/j.spacepol.2006.08.008).

REFERENCES

- [32] J. Foust. *SpaceX achievements generate growing interest in reusable launchers*. 2018. URL: <http://spacenews.com/spacex-achievements-generate-growing-interest-in-reusable-launchers/> (visited on 06/21/2018).
- [33] D. Mosher. *SpaceX faces a growing list of competitors in the new space race*. 2018. URL: <https://www.businessinsider.com.au/spacex-elon-musk-competition-companies-rockets-2018-3> (visited on 06/21/2018).
- [34] S. Clark. *Ariane 6 Rocket Holding to Schedule for 2020 Maiden Flight*. 2016. URL: <https://spaceflightnow.com/2016/08/13/ariane-6-rocket-holding-to-schedule-for-2020-maiden-flight/>.
- [35] S. Lewin. *Blue Origin Announces Big 'New Glenn' Rocket for Satellite & Crew Launches*. 2016. URL: <https://www.space.com/34034-blue-origin-new-glenn-rocket-for-satellites-people.html> (visited on 06/21/2018).
- [36] H. Pettit. *The galaxy's fastest car*. 2018. URL: <http://www.dailymail.co.uk/sciencetech/article-5361789/Ride-Elon-Musks-Starman-travels-space.html> (visited on 06/21/2018).
- [37] To Challenge SpaceX, Rockets Get Wings. 2016. URL: <http://www.spacesafetymagazine.com/news/to-challenge-spacex-rockets-get-wings/> (visited on 06/21/2018).
- [38] Richard Webb. “Is It Worth It? The Economics of Reusable Space Transportation”. In: *ICEAA 2016 International Training Symposium, Bristol, UK* (2016), pp. 1–19.
- [39] S. Clark. *Falcon 9 rocket launching Sunday sports fin upgrade*. 2018. URL: <https://spaceflightnow.com/2017/06/25/falcon-9-rocket-launching-sunday-sports-fin-upgrade/> (visited on 06/21/2018).
- [40] M. Sarigul-Klijn and N. Sarigul-Klijn. “Flight Mechanics of Manned Sub-Orbital Reusable Launch Vehicles with Recommendations for Launch and Recovery”. In: *41st Aerospace Sciences Meeting and Exhibit, Aerospace Sciences Meetings*. Reno, NV, 2003.
- [41] Rocket Lab. *Electron*. 2016. URL: <https://www.rocketlabusa.com/electron/> (visited on 11/30/2017).
- [42] Zero2Infinity. *Bloostar*. 2016. URL: <http://www.zero2infinity.space/bloostar/> (visited on 11/30/2017).
- [43] M. Gilmour. *Gilmour Space Secures AUD 19 Million to Launch Next-Generation Hybrid Rockets to Space*. 2018. URL: <https://www.gspacetech.com/single-post/2018/09/28/Gilmour-Space-secures-AUD-19-million-to-launch-next-gen-hybrid-rockets> (visited on 10/06/2018).

- [44] RocketCrafters. *Intrepid-1*. 2017. URL: <http://rocketcrafters.space/products-services/intrepid-launcher-family/intrepid-1/> (visited on 12/01/2017).
- [45] China Launches New Rocket. 2018. URL: <http://www.spacelaunchreport.com/kz.html>.
- [46] Vector Space. *Vector Launch Vehicle Family*. 2017. URL: <https://vectorspacesystems.com/technology/> (visited on 12/01/2017).
- [47] M. Kuhn, I. Müller, I. Petkov, B. Oving, A. J. van Kleef, C. J. Verberne, B. Haemmerli, and A. Boiron. “Innovative European Launcher Concept SMILE”. In: *21st AIAA International Space Planes and Hypersonics Technologies Conference* March (2017), pp. 1–14. DOI: [10.2514/6.2017-2441](https://arc.aiaa.org/doi/10.2514/6.2017-2441). URL: <https://arc.aiaa.org/doi/10.2514/6.2017-2441>.
- [48] Firefly. *Firefly*. 2017. URL: <http://www.fireflyspace.com/> (visited on 11/30/2017).
- [49] VirginOrbit. *LauncherOne*. 2017. URL: <https://virginorbit.com/> (visited on 11/30/2017).
- [50] D. Outreach. *DARPA Picks Design for Next-Generation Spaceplane*. 2017. URL: <https://www.darpa.mil/news-events/2017-05-24> (visited on 11/16/2017).
- [51] Orbital Access. *The Orbital 500R*. 2017. URL: <http://www.orbital-access.com/the-orbital-500/> (visited on 12/01/2017).
- [52] M. K. Smart and M. R. Tetlow. “Orbital Delivery of Small Payloads Using Hypersonic Air-breathing Propulsion”. In: *Journal of Spacecraft and Rockets* 46.1 (2009), pp. 117–125. ISSN: 0022-4650. DOI: [10.2514/1.38784](https://arc.aiaa.org/doi/abs/10.2514/1.38784). URL: [http://arc.aiaa.org/doi/abs/10.2514/1.38784](https://arc.aiaa.org/doi/abs/10.2514/1.38784).
- [53] R. W. Powell, J. D. Shaughnessy, C. I. Cruz, and J. C. Naftel. “Ascent performance of an air-breathing horizontal-takeoff launch vehicle”. In: *Journal of Guidance, Control, and Dynamics* 14.4 (1991), pp. 834–839. ISSN: 0731-5090. DOI: [10.2514/3.20719](https://arc.aiaa.org/doi/abs/10.2514/3.20719).
- [54] A. W. Wilhite, W. C. Engelund, D. O. Stanley, and J. C. Naftel. “Technology and staging effects on two-stage-to-orbit systems”. In: *Journal of Spacecraft and Rockets* 31.1 (1991), pp. 31–39. ISSN: 0022-4650. DOI: [10.2514/3.26399](https://arc.aiaa.org/doi/abs/10.2514/3.26399).
- [55] R. Varvill and A. Bond. “The Skylon Spaceplane: Progress to Realisation”. In: *Journal of the British Interplanetary Society* 61 (2008), pp. 412–418.
- [56] T. Tsuchiya and T. Mori. “Optimal Design of Two-Stage-To-Orbit Space Planes with Air-breathing Engines”. In: *Journal of Spacecraft and Rockets* 42.1 (2005), pp. 90–97. ISSN: 0022-4650. DOI: [10.2514/1.8012](https://arc.aiaa.org/doi/abs/10.2514/1.8012).
- [57] U. B. Mehta and J. V. Bowles. “Two-Stage-to-Orbit Spaceplane Concept with Growth Potential”. In: *Journal of Propulsion and Power* 17.6 (2001), pp. 1149–1161. ISSN: 0748-4658. DOI: [10.2514/2.5886](https://arc.aiaa.org/doi/abs/10.2514/2.5886).

REFERENCES

- [58] C. Trefny. “An Air-Breathing Concept Launch Vehicle for Single-Stage-to-Orbit”. In: *35th Joint Propulsion Conference and Exhibit*. May. Los Angeles, CA, 1999. DOI: [10.2514/6.1999-2730](https://doi.org/10.2514/6.1999-2730).
- [59] J. M. Roche and D. N. Kosareo. *Structural Sizing of a 25000-Lb Payload , Air-Breathing Launch Vehicle for Single-Stage-To-Orbit*. Tech. rep. January 2001. 2000.
- [60] D. Young, T. Kokan, C. Tanner, I. Clark, C. Tanner, and A. Wilhite. “Lazarus: A SSTO Hypersonic Vehicle Concept Utilizing RBCC and HEDM Propulsion Technologies”. In: *14th AIAA/AHI Space Planes and Hypersonic Systems and Technologies Conference*. 2006, pp. 1–15. ISBN: 978-1-62410-050-5. DOI: [10.2514/6.2006-8099](https://doi.org/10.2514/6.2006-8099). URL: <http://arc.aiaa.org/doi/10.2514/6.2006-8099>.
- [61] C. Gong, B. Chen, and L. Gu. “Design and Optimization of RBCC Powered Suborbital Reusable Launch Vehicle”. In: *19th AIAA International Space Planes and Hypersonic Systems and Technologies Conference* June (2014), pp. 1–20. DOI: [10.2514/6.2014-2361](https://doi.org/10.2514/6.2014-2361). URL: <http://arc.aiaa.org/doi/abs/10.2514/6.2014-2361>.
- [62] K. W. Flaherty, K. M. Andrews, and G. W. Liston. “Operability Benefits of Airbreathing Hypersonic Propulsion for Flexible Access to Space”. In: *Journal of Spacecraft and Rockets* 47.2 (2010), pp. 280–287. ISSN: 0022-4650. DOI: [10.2514/1.43750](https://doi.org/10.2514/1.43750). URL: <http://arc.aiaa.org/doi/abs/10.2514/1.43750>.
- [63] J. Olds and I. Budianto. “Constant Dynamic Pressure Trajectory Simulation with POST”. In: *Aerospace Sciences Meeting & Exhibit*. Reno, NV, 1998, pp. 1–13. DOI: [10.2514/6.1998-302](https://doi.org/10.2514/6.1998-302). URL: <http://citeseerx.ist.psu.edu/viewdoc/download?doi=10.1.1.25.6506&rep=rep1&type=pdf>.
- [64] D. Preller and M. K. Smart. “Longitudinal Control Strategy for Hypersonic Accelerating Vehicles”. In: *Journal of Spacecraft and Rockets* 52.3 (2015), pp. 1–6. ISSN: 0022-4650. DOI: [10.2514/1.A32934](https://doi.org/10.2514/1.A32934). URL: <http://dx.doi.org/10.2514/1.A32934>.
- [65] L. S. Punnoose, M. Lal, and V Brinda. “On-Line Trajectory Optimization of a Typical Air-Breathing Launch Vehicle using Energy State Approximation Approach”. In: *Advances in Control and Optimization of Dynamical Systems* (2007), pp. 296–302.
- [66] T. Kanda and K. Kudo. “Payload to Low Earth Orbit by Aerospace Plane with Scramjet Engine Summary”. In: *Journal of Propulsion and Power Technical Notes* 13.1 (1996), pp. 164–166. ISSN: 0748-4658. DOI: [10.2514/2.7641](https://doi.org/10.2514/2.7641).
- [67] P. Lu. “Inverse dynamics approach to trajectory optimization for an aerospace plane”. In: *Journal of Guidance, Control, and Dynamics* 16.4 (1993), pp. 726–732. ISSN: 0731-5090. DOI: [10.2514/3.21073](https://doi.org/10.2514/3.21073). URL: <http://arc.aiaa.org/doi/abs/10.2514/3.21073>.

- [68] F. Pescetelli, E. Minisci, C. Maddock, I. Taylor, and R. Brown. “Ascent Trajectory Optimisation for a Single-Stage-to-Orbit Vehicle with Hybrid Propulsion”. In: *18th AIAA/3AF International Space Planes and Hypersonic Systems and Technologies Conference*. September. 2012, pp. 1–18. ISBN: 978-1-60086-931-0. DOI: [10.2514/6.2012-5828](https://doi.org/10.2514/6.2012-5828). URL: <http://arc.aiaa.org/doi/abs/10.2514/6.2012-5828>.
- [69] B. M. Hellman. *Comparison of Return to Launch Site Options for a Reusable Booster Stage*. Tech. rep. Space Sytems Design Lab, Georgia Institute of technology, 2005, pp. 1–18.
- [70] M. R. Tetlow, U. M. Sch-ograve, Ttle, and G. M. Schneider. “Comparison of Glideback and Flyback Boosters”. In: *Journal of Spacecraft and Rockets* 38.5 (1992), pp. 752–758. ISSN: 0022-4650. DOI: [10.2514/2.3742](https://doi.org/10.2514/2.3742). URL: <http://dx.doi.org/10.2514/2.3742>.
- [71] N. D. Moshman and R. J. Proulx. “Range Improvements in Gliding Reentry Vehicles from Thrust Capability”. In: *Journal of Spacecraft and Rockets* 51.5 (2014), pp. 1681–1694. ISSN: 0022-4650. DOI: [10.2514/1.A32764](https://doi.org/10.2514/1.A32764). URL: <http://arc.aiaa.org/doi/10.2514/1.A32764>.
- [72] C. L. Darby, W. W. Hager, and A. V. Rao. “Direct Trajectory Optimization Using a Variable Low-Order Adaptive Pseudospectral Method”. In: *Journal of Spacecraft and Rockets* 48.3 (2011), pp. 433–445. ISSN: 0022-4650. DOI: [10.2514/1.52136](https://doi.org/10.2514/1.52136).
- [73] F. Toso, A. Riccardi, E. Minisci, C. Maddock, and Ristie. “Optimisation of ascent and descent trajectories for lifting body space access vehicles”. In: *66th International Astronautical Congress*. Jerusalem, 2015.
- [74] D. Chai, Y. W. Fang, Y. L. Wu, and S. H. Xu. “Boost-skipping trajectory optimization for air-breathing hypersonic missile”. In: *Aerospace Science and Technology* 46 (2015), pp. 506–513. ISSN: 12709638. DOI: [10.1016/j.ast.2015.09.004](https://doi.org/10.1016/j.ast.2015.09.004). URL: <http://dx.doi.org/10.1016/j.ast.2015.09.004>.
- [75] T. Jazra, D. Preller, and M. K. Smart. “Design of an Airbreathing Second Stage for a Rocket-Scramjet-Rocket Launch Vehicle”. In: *Journal of Spacecraft and Rockets* 50.2 (2013), pp. 411–422. ISSN: 0022-4650. DOI: [10.2514/1.A32381](https://doi.org/10.2514/1.A32381). URL: <http://arc.aiaa.org/doi/abs/10.2514/1.A32381>.
- [76] M. K. Smart and E. G. Ruf. “Free-jet testing of a {REST} scramjet at off-design conditions”. In: *Collection of Technical Papers - 25th AIAA Aerodynamic Measurement Technology and Ground Testing Conference* AIAA 2006-2955 (2006), pp. 190–201. DOI: [doi:10.2514/6.2006-2955](https://doi.org/10.2514/6.2006-2955).
- [77] D. Preller. “Multidisciplinary Design and Optimisation of a Pitch Trimmed Hypersonic Air-breathing Accelerating Vehicle”. Ph.D Dissertation. The University of Queensland, 2018.

REFERENCES

- [78] M. Wade. *Encyclopedia Astronautica*. 2017. URL: <http://www.astronautix.com/> (visited on 07/24/2018).
- [79] R Bulirsch, E Nerz, H. J. Pesch, and O von Stryk. “Combining direct and indirect methods in optimal control: Range maximization of a hang glider”. In: *Optimal Control (Calculus of Variations, Optimal Control Theory and Numerical Methods)* 111 (1993), pp. 273–288.
- [80] O. Stryk and R. Bulirsch. “Direct and indirect methods for trajectory optimization”. In: *Annals of Operations Research* 37 (1992), pp. 357–373. ISSN: 0254-5330. DOI: [10 . 1007 / BF02071065](https://doi.org/10.1007/BF02071065).
- [81] M. S. Bazaraa, H. D. Sherali, and C. M. Shetty. *Nonlinear Programming: Theory and Algorithms*. John Wiley & Sons, 2013.
- [82] P. Boggs and J. Tolle. “Sequential quadratic programming for large-scale nonlinear optimization”. In: *Journal of Computational and Applied Mathematics* 124.1-2 (2000), pp. 123–137. ISSN: 03770427. DOI: [10 . 1016 / S0377-0427\(00\)00429-5](https://doi.org/10.1016/S0377-0427(00)00429-5). URL: <http://linkinghub.elsevier.com/retrieve/pii/S0377042700004295> \$ \backslash backslash \$ <http://www.sciencedirect.com/science/article/pii/S0377042700004295>.
- [83] M. P. Kelly. “Transcription Methods for Trajectory Optimization A beginners tutorial”. In: *Arxiv* (2015), pp. 1–14.
- [84] G. Fasano and J. Pinter. *Modelling and Optimisation in Space Engineering*. New York, NY: Springer, 2013. DOI: [10 . 1007 / 978-1-4614-4469-5](https://doi.org/10.1007/978-1-4614-4469-5).
- [85] D. Jezewski. “An Optimal, Analytic Solution to the Linear-Gravity, Constant-Thrust Trajectory Problem”. In: *Journal of Spacecraft and Rockets* July (1971), pp. 793–796.
- [86] I. M. Ross and F. Fahroo. “Pseudospectral Knotting Methods for Solving Nonsmooth Optimal Control Problems”. In: *Journal of Guidance, Control, and Dynamics* 27.3 (2004), pp. 397–405. ISSN: 0731-5090. DOI: [10 . 2514 / 1 . 3426](https://doi.org/10.2514/1.3426).
- [87] F. Fahroo and I. Ross. “Direct trajectory optimization by a Chebyshev pseudospectral method”. In: *Proceedings of the 2000 American Control Conference*. Chicago, IL, 2000, pp. 3860–3864. ISBN: 0-7803-5519-9. DOI: [10 . 1109 / ACC . 2000 . 876945](https://doi.org/10.1109/ACC.2000.876945).
- [88] H.-O. Kreiss and J. Oliger. “Comparison of accurate methods for the integration of hyperbolic equations”. In: *Tellus A* 1971 (1972). ISSN: 0280-6495. DOI: [10 . 3402 / tellusa . v24i3 . 10634](https://doi.org/10.3402/tellusa.v24i3.10634).

- [89] G. Huntington, D. Benson, and A. Rao. “A Comparison of Accuracy and Computational Efficiency of Three Pseudospectral Methods”. In: *AIAA Guidance, Navigation and Control Conference and Exhibit* (2007), pp. 1–43. DOI: [10.2514/6.2007-6405](https://doi.org/10.2514/6.2007-6405). URL: <http://arc.aiaa.org/doi/abs/10.2514/6.2007-6405>.
- [90] C. L. Darby, W. W. Hager, and A. V. Rao. “An hp-adaptive pseudospectral method for solving optimal control problems”. In: *Optimal Control Applications and Methods* 32.3 (2011), pp. 476–502. DOI: [10.1002/oca.957](https://doi.org/10.1002/oca.957). URL: <http://doi.wiley.com/10.1002/oca.957>.
- [91] D Garg, M. Patterson, and W. Hager. “An Overview of Three Pseudospectral Methods for the Numerical Solution of Optimal Control Problems”. In: *Advances in the Astronautical Sciences* 135 (2009), pp. 1–17. URL: <http://vdol.mae.ufl.edu/ConferencePublications/unifiedFrameworkAAS.pdf>.
- [92] Q. Gong, I. M. Ross, and F. Fahroo. “Costate Computation by a Chebyshev Pseudospectral Method”. In: *Journal of Guidance, Control, and Dynamics* 33.2 (2010), pp. 623–628. ISSN: 0731-5090. DOI: [10.2514/1.45154](https://doi.org/10.2514/1.45154).
- [93] F. Fahroo and I. M. Ross. “Costate Estimation by a Legendre Pseudospectral Method”. In: *Journal of Guidance, Control, and Dynamics* 24.2 (2001), pp. 270–277. ISSN: 0731-5090. DOI: [10.2514/2.4709](https://doi.org/10.2514/2.4709).
- [94] N. Bedrossian, B. Technologies, and L. N. Nasa. “Zero Propellant Manoeuvre Flight Results For 180 Degree ISS Rotation”. In: *20th International Symposium on Space Flight Dynamics*. Annapolis, MD, 2007.
- [95] H. Li, R. Zhang, Z. Li, and R. Zhang. “Footprint problem with angle of attack optimization for high lifting reentry vehicle”. In: *Chinese Journal of Aeronautics* 25.2 (2012), pp. 243–251. ISSN: 10009361. DOI: [10.1016/S1000-9361\(11\)60384-1](https://doi.org/10.1016/S1000-9361(11)60384-1). URL: [http://dx.doi.org/10.1016/S1000-9361\(11\)60384-1](http://dx.doi.org/10.1016/S1000-9361(11)60384-1).
- [96] S. Josselyn and I. M. Ross. “Rapid Verification Method for the Trajectory Optimization of Reentry Vehicles”. In: *Notes* 26.3 (2002), pp. 505–508. ISSN: 0731-5090. DOI: [10.2514/2.5074](https://doi.org/10.2514/2.5074).
- [97] J. Zhao and R. Zhou. “Reentry trajectory optimization for hypersonic vehicle satisfying complex constraints”. In: *Chinese Journal of Aeronautics* 26.6 (2013), pp. 1544–1553. ISSN: 10009361. DOI: [10.1016/j.cja.2013.10.009](https://doi.org/10.1016/j.cja.2013.10.009). URL: <http://dx.doi.org/10.1016/j.cja.2013.10.009>.

REFERENCES

- [98] B. Tian and Q. Zong. “Optimal guidance for reentry vehicles based on indirect Legendre pseudospectral method”. In: *Acta Astronautica* 68.7-8 (2011), pp. 1176–1184. ISSN: 00945765. DOI: [10.1016/j.actaastro.2010.10.010](https://doi.org/10.1016/j.actaastro.2010.10.010). URL: <http://linkinghub.elsevier.com/retrieve/pii/S0094576510003899>.
- [99] S. T.U. I. Rizvi, L. S. He, and D. J. Xu. “Optimal trajectory and heat load analysis of different shape lifting reentry vehicles for medium range application”. In: *Defence Technology* 11.4 (2015), pp. 350–361. ISSN: 22149147. DOI: [10.1016/j.dt.2015.06.003](https://doi.org/10.1016/j.dt.2015.06.003). URL: <http://dx.doi.org/10.1016/j.dt.2015.06.003>.
- [100] S. Yang, T. Cui, X. Hao, and D. Yu. “Trajectory optimization for a ramjet-powered vehicle in ascent phase via the Gauss pseudospectral method”. In: *Aerospace Science and Technology* 67 (2017), pp. 88–95. ISSN: 12709638. DOI: [10.1016/j.ast.2017.04.001](https://doi.org/10.1016/j.ast.2017.04.001). URL: <http://dx.doi.org/10.1016/j.ast.2017.04.001>.
- [101] M. Kodera, H. Ogawa, S. Tomioka, and S. Ueda. “Multi-Objective Design and Trajectory Optimization of Space Transport Systems with RBCC Propulsion via Evolutionary Algorithms and Pseudospectral Methods”. In: *52nd Aerospace Sciences Meeting January* (2014), pp. 1–14. DOI: [10.2514/6.2014-0629](https://doi.org/10.2514/6.2014-0629). URL: <http://arc.aiaa.org/doi/10.2514/6.2014-0629>.
- [102] Astos Solutions. *Astos Solutions*. 2018. URL: <https://www.astos.de/> (visited on 07/24/2018).
- [103] A. V. Rao, D. a. Benson, C. Darby, M. a. Patterson, C. Francolin, I. Sanders, and G. T. Huntington. “Algorithm 902”. In: *ACM Transactions on Mathematical Software* 37.2 (2010), pp. 1–39. ISSN: 00983500. DOI: [10.1145/1731022.1731032](https://doi.org/10.1145/1731022.1731032).
- [104] Y. Nie, O. Faqir, and E. Kerrigan. *ICLOCS2*. 2018. URL: <http://www.ee.ic.ac.uk/ICLOCS/> (visited on 07/24/2018).
- [105] T. Lipp and S. Boyd. “Minimum-time speed optimisation over a fixed path”. In: *International Journal of Control* 87.January 2015 (2014), pp. 1297–1311. ISSN: 0020-7179. DOI: [10.1080/00207179.2013.875224](https://doi.org/10.1080/00207179.2013.875224). URL: <http://www.tandfonline.com/doi/abs/10.1080/00207179.2013.875224>.
- [106] a Wächter and L. T. Biegler. *On the Implementation of a Primal-Dual Interior Point Filter Line Search Algorithm for Large-Scale Nonlinear Programming*. Vol. 106. 1. 2006, pp. 25–57. ISBN: 1010700405.
- [107] I. M. Ross and F Fahroo. “A direct method for solving nonsmooth optimal control problems”. In: *Proceedings of the 2002 {IFAC} World Congress* (2002).
- [108] P. E. Rutquist and M. M. Edvall. “PROPT - Matlab Optimal Control Software”. In: *Tomlab Optimization Inc* 260 (2010), pp. –.

- [109] W. Colson. *Program to Optimize Simulated Trajectories 2*. 2017. URL: <https://post2.larc.nasa.gov/> (visited on 07/24/2018).
- [110] R. Falck. *OTIS*. 2016. URL: <https://otis.grc.nasa.gov/index.html> (visited on 07/24/2018).
- [111] D. Wassel, F. Wolff, J. Vogelsang, and C. Büskens. “the Esa Nlp-Solver Worhp Recent Developments and Applications”. In: *Modeling and Optimization in Space Engineering* (2013).
- [112] B Houska, H. Ferrau, and M. Diehl. “ACADO Toolkit – An Open Source Framework for Automatic Control and Dynamic Optimization”. In: *Optimal Control Applications and Methods* 32.3 (2011), pp. 298–312.
- [113] JModelica.org. URL: <https://jmodelica.org/> (visited on 07/24/2018).
- [114] C. Rosema, J. Doyle, L. Auman, M. Underwood, and W. B. Blake. *Missile DATCOM User’s Manual - 2011 Revision*. Tech. rep. Army Aviation and Missile Research Development, 2011. DOI: [10.21236/ad1000581](https://doi.org/10.21236/ad1000581).
- [115] D. Kinney. “Aero-Thermodynamics for Conceptual Design”. In: *42nd AIAA Aerospace Sciences Meeting and Exhibit*. January. Reno, NV, 2004, pp. 1–11. ISBN: 978-1-62410-078-9. DOI: [10.2514/6.2004-31](https://doi.org/10.2514/6.2004-31). URL: <http://www.aric.or.kr/treatise/journal/content.asp?idx=53932>.
- [116] U Reisch and Y Anseaume. *Validation of the Approximate Calculation Procedure HOTSOSE For Aerodynamic and Thermal Loads in Hypersonic Flow with Existing Experimental and Numerical Results*. Tech. rep. DLR-Forschungsbericht, 1998.
- [117] T. Eggers. “Aerodynamic Analysis of the Dual-Mode Ramjet Vehicle JAPHAR”. In: *Notes on Numerical Fluid Mechanics and Multidisciplinary Design*. Vol. 115. 2011, pp. 137–140. ISBN: 9783642177699.
- [118] M. J. Aftosmis, M. J., Berger and G. Adomavicius. “A Parallel Multilevel Method for Adaptively Refined Cartesian Grids with Embedded Boundaries”. In: *38th Aerospace Sciences Meeting and Exhibit*. Reno NV, 2000. DOI: [10.2514/6.2000-808](https://doi.org/10.2514/6.2000-808).
- [119] F. Manual, R. T. Biedron, J. M. Derlaga, P. A. Gnoffo, D. P. Hammond, W. T. Jones, B. Kleb, E. M. Lee-rausch, E. J. Nielsen, M. A. Park, C. L. Rumsey, J. L. Thomas, and W. A. Wood. *FUN3D Manual: 13.3*. Tech. rep. February. Langley Research Center, Hampton, Virginia: NASA, 2018.
- [120] NASA Glenn Research Center. *Euler Equations*. URL: <https://www.grc.nasa.gov/WWW/k-12/airplane/eulereqs.html> (visited on 07/24/2018).

REFERENCES

- [121] D. Almosnino. “A Low Subsonic Study of the NASA N2A Hybrid Wing-Body Using an Inviscid Euler-Adjoint Solver”. In: *34th AIAA Applied Aerodynamics Conference* June (2016), pp. 1–18. DOI: [doi:10.2514/6.2016-3267](https://doi.org/10.2514/6.2016-3267). URL: <http://dx.doi.org/10.2514/6.2016-3267>.
- [122] A. D. Ward, M. K. Smart, and R. J. Gollan. “Development of a Rapid Inviscid/Boundary-Layer Aerodynamics Tool”. In: *22nd AIAA International Space Planes and Hypersonics Systems and Technologies Conference*. September. Orlando, FL, 2018, pp. 1–14. ISBN: 978-1-62410-577-7. DOI: [10.2514/6.2018-5270](https://doi.org/10.2514/6.2018-5270). URL: <https://arc.aiaa.org/doi/10.2514/6.2018-5270>.
- [123] R Gollan and P Jacobs. “About the formulation, verification and validation of the hypersonic flow solver Eilmer”. In: *International Journal for Numerical Methods in Fluids* 73 (2013). ISSN: 02712091. DOI: [10.1002/fld](https://doi.org/10.1002/fld). arXiv: [fld.1 \[DOI: 10.1002\]](https://arxiv.org/abs/1302.0001).
- [124] Ansys. *Fluent Bruchure*. Tech. rep. Ansys, 2014, p. 2. URL: <http://ansys.com/staticassets/ANSYS/staticassets/resourcelibrary/brochure/ansys-fluent-brochure-14.0.pdf>.
- [125] AEA Technology. *Itroduction to CFX-TASCflow*. URL: <http://hmf.enseeiht.fr/travaux/CD0102/travaux/optmfn/micp/reports/s19cfx2/pages/frame2.htm>.
- [126] COMSOL. *Product: CFD Module*. URL: <https://www.comsol.com/cfd-module\#cfd-software>.
- [127] D. Schwamborn, T. Gerhold, and R. Heinrich. “The DLR TAU-Code: Recent Applications in Research and Industry”. In: *European Conference on Computational Fluid Dynamics, EC-COMAS CFD 2006* (2006), pp. 1–25.
- [128] The OpenFOAM Foundation. *OpenFOAM*. URL: <https://openfoam.org/>.
- [129] C. Segal. *The Scramjet Engine: Processes and Characteristics*. Cambridge, UK: Cambridge University Press, 2009, p. 229. ISBN: 9780521838153.
- [130] D. G. Sagerman, M. P. Rumpfkeil, B. M. Hellman, and N. Dasque. “Comparisons of Measured and Modeled Aero-thermal Distributions for Complex Hypersonic Configurations”. In: *55th AIAA Aerospace Sciences Meeting* January (2017), pp. 1–22. DOI: [10.2514/6.2017-0264](https://doi.org/10.2514/6.2017-0264). URL: <http://arc.aiaa.org/doi/10.2514/6.2017-0264>.
- [131] D. Abeynayake and A. Agon. “Comparison of computational and semi-empirical aerodynamics tools for making fit-for-purpose modelling decisions”. In: *20th International Congress on Modelling and Simulation*. Adelaide, Australia, 2013, pp. 1–6.

- [132] M. J. Aftosmis, M. Nemec, and S. E. Cliff. “Adjoint-based low-boom design with Cart3D”. In: *29th AIAA Applied Aerodynamics Conference 2011*. June. 2011, pp. 1–17. ISBN: 9781624101458. DOI: [doi:10.2514/6.2011-3500](https://doi.org/10.2514/6.2011-3500). URL: <http://www.scopus.com/inward/record.url?eid=2-s2.0-84872373928&partnerID=tZ0tx3y1>.
- [133] D Almosnino. “Assessment of an inviscid euler-adjoint solver for prediction of aerodynamic characteristics of the NASA HL-20 lifting body”. In: *34th AIAA Applied Aerodynamics Conference, 2016* June (2016). DOI: [10.2514/6.2016-3266](https://doi.org/10.2514/6.2016-3266). URL: <https://www.scopus.com/inward/record.uri?eid=2-s2.0-84980371959&partnerID=40\&md5=1b304aabaaad2976daf4d0742d5bdc6ba>.
- [134] U. Mehta, M. Aftosmis, J. Bowles, and S. Pandya. “Skylon Aerospace Plane and Its Aerodynamics and Plumes”. In: *Journal of Spacecraft and Rockets* 53.2 (2016), pp. 340–353. ISSN: 0022-4650. DOI: [10.2514/1.A33408](https://doi.org/10.2514/1.A33408). URL: <http://arc.aiaa.org/doi/10.2514/1.A33408>.
- [135] R. Kimmel, D. Adamczak, K Berger, and M Choudhari. “HIFiRE-5 flight vehicle design”. In: *AIAA paper* July (2010), pp. 1–17. DOI: [10.2514/6.2010-4985](https://doi.org/10.2514/6.2010-4985). URL: <http://arc.aiaa.org/doi/pdf/10.2514/6.2010-4985>.
- [136] R. Gomez, D. Vicker, S. Rogers, M. Aftosmis, W. Chan, R. Meakin, S. Murman, and S. Murman. “STS-107 Investigation Ascent CFD Support”. In: *34th AIAA Fluid Dynamics Conference and Exhibit* (2004), pp. 1–15. DOI: [10.2514/6.2004-2226](https://doi.org/10.2514/6.2004-2226). URL: <http://arc.aiaa.org/doi/10.2514/6.2004-2226>.
- [137] T. J. Sooy and R. Z. Schmidt. “Aerodynamic Predictions, Comparisons, and Validations Using Missile DATCOM (97) and Aeroprediction 98 (AP98)”. In: *Journal of Spacecraft and Rockets* 42.2 (2005), pp. 257–265. ISSN: 0022-4650. DOI: [10.2514/1.7814](https://doi.org/10.2514/1.7814).
- [138] M Suraweera and M. K. Smart. “Shock Tunnel Experiments with a Mach 12 {REST} Scramjet at Off-Design Conditions”. In: *Journal of Propulsion and Power* 25.3 (2009), pp. 555–564. ISSN: 0748-4658. DOI: [10.2514/1.37946](https://doi.org/10.2514/1.37946).
- [139] NASA. *U.S. Standard Atmosphere, 1976*. U.S. Government Printing Office, Washington, D.C., 1976, pp. 1–243. URL: <http://ntrs.nasa.gov/archive/nasa/casi.ntrs.nasa.gov/19770009539.pdf>.
- [140] J. W. MacColl. “The Conical Shock Wave Formed by a Cone Moving at a High Speed”. In: *Proceedings of the Royal Society A: Mathematical, Physical and Engineering Sciences* 159.898 (1937), pp. 459–472. ISSN: 1364-5021. DOI: [10.1098/rspa.1937.0083](https://doi.org/10.1098/rspa.1937.0083). URL: <http://rspa.royalsocietypublishing.org/cgi/doi/10.1098/rspa.1937.0083>.
- [141] Pointwise. www.pointwise.com. 2017. URL: <http://www.pointwise.com/> (visited on 02/01/2017).

REFERENCES

- [142] S. Pandya, S. Murman, and M. Aftosmis. “Validation of Inlet and Exhaust Boundary Conditions for a Cartesian Method”. In: *22nd Applied Aerodynamics Conference and Exhibit* January (2004), pp. 1–16. ISSN: 10485953. DOI: [10.2514/6.2004-4837](https://doi.org/10.2514/6.2004-4837). URL: <http://arc.aiaa.org/doi/10.2514/6.2004-4837>.
- [143] Desktop Aeronautics. *Specifying Power BCs for Rocket Plumes*. Tech. rep. NASA, pp. 9–11. URL: <https://www.nas.nasa.gov/publications/software/docs/cart3d/pages/howto/howTo_RocketPlumes_08.11.pdf>.
- [144] U. Mehta, M. Aftosmis, J. Bowles, and S. Pandya. “Skylon Aerodynamics and SABRE Plumes”. In: *20th AIAA International Space Planes and Hypersonic Systems and Technologies Conference*. July. Glasgow, Scotland, 2015, pp. 1–21. ISBN: 9781624103209. DOI: [10.2514/6.2015-3605](https://doi.org/10.2514/6.2015-3605).
- [145] Space Exploration technologies. *Falcon 1 Launch Vehicle Payload Users Guide*. Tech. rep. Hawthorne, CA: Space Exploration Technologies, 2008, p. 65.
- [146] G. Sutton and O. Biblarz. *Rocket propulsion Elements*. 8th. John Wiley & Sons, 2010, p. 67. ISBN: 978-0470080245. DOI: [10.1017/S0001924000034308](https://doi.org/10.1017/S0001924000034308).
- [147] International Tungsten Industry Association. *Tungsten Properties*. URL: <https://www.itia.info/tungsten-properties.html>.
- [148] E. Fitzer and L. Manocha. *Carbon Reinforcements and Carbon/Carbon Composites*. Berlin, Heidelberg: Springer Berlin Heidelberg, 1998. ISBN: 3-642-58745-3.
- [149] Amorim. *Reinventing Thermal Protection*. Tech. rep. Regency Park SA: Amorim Cork Composites, 2018. URL: <http://pdf.nauticexpo.com/pdf/amorim-cork-composites/tps/39162-105388.html>.
- [150] J. W. Magee Bruno, T.J., Friend, D. G., Huber, M.L., Laesecke, A., Lemmon, E.W., McLinden, M.O., Perkins, R.A., Baranski, J., Widegren, J.A. *Thermophysical Properties Measurements and Models for Rocket Propellant RP-1: Phase I, NIST-IR 6644, National Institute of Standards and Technology (U.S.)* Tech. rep. 2006.
- [151] M. a. Patterson, D Ph, A. V. Rao, and D Ph. *GPOPS-II manul: A General-Purpose MATLAB Software for Solving Multiple-Phase Optimal Control Problems Version 2 . 1*. Tech. rep. October. 2015, pp. 1–72.
- [152] R. J. Boain. “A-B-Cs of Sun-Synchronous Orbit Mission Design 14 AAS / AIAA Space Flight Mechanics Conference”. In: *14th AAS/AIAA Space Flight Mechanics Conference* (2004), pp. 1–19.
- [153] R. Simmon. *Three Classes of Orbit*. 2009. URL: <https://earthobservatory.nasa.gov/Features/OrbitsCatalog/page2.php> (visited on 08/22/2018).

- [154] M. Palin. *Australias first commercial space base to launch rockets within a year*. 2017. URL: <https://www.news.com/technology/science/space/australias-first-commercial-space-base-to-launch-rockets-within-a-year/news-story/eb7841c5b39e04fd31302e8b1056e3ab>.
- [155] B Barrar. *An Analytic Proof That the Hohmann-Type Transfer is the True Minimum Tro-Impulse Transfer*. Tech. rep. Fort Belvoir, VA: Defense Technical Information Center, 1962.
- [156] Y. Kawajir, C. D. Laird, and A. Waechter. “Introduction to IPOPT: A tutorial for downloading, installing, and using IPOPT .” In: *Most* (2010), pp. 1–68. ISSN: 00981354. DOI: http://web.mit.edu/ipopt_v3.8/doc/documentation.pdf. arXiv: [arXiv:1011.1669v3](https://arxiv.org/abs/1011.1669v3).
- [157] H. Hindi. “A tutorial on convex optimization II: duality and interior point methods”. In: *2006 American Control Conference* 1 (2006), 11 pp. ISSN: 07431619. DOI: [10.1109/ACC.2006.1655436](https://doi.org/10.1109/ACC.2006.1655436). URL: <http://ieeexplore.ieee.org/document/1655436/>.
- [158] P. Pucci and J. B. Serrin. *The maximum principle*. Vol. 73. Springer, 2007, pp. 80–104. ISBN: 978-3-7643-8145-5.
- [159] A. Gilbert, B. Mesmer, and M. D. Watson. “Exergy analysis of rocket systems”. In: *9th Annual IEEE International Systems Conference, SysCon 2015*. Vancouver, British Columbia, Canada, 2015, pp. 283–288. ISBN: 9781479959273. DOI: [10.1109/SYSCON.2015.7116765](https://doi.org/10.1109/SYSCON.2015.7116765).
- [160] B. A. J. Eggers, H. J. Allen, and S. E. Neice. “Technical Note 4046”. In: October (1957).
- [161] T. Kanda and T. Hiraiwa. “Evaluation of Effectiveness of Periodic Flight by a Hypersonic Vehicle”. In: *Journal of Aircraft* 44.6 (2007), pp. 2076–2077. ISSN: 0021-8669. DOI: [10.2514/1.31143](https://doi.org/10.2514/1.31143).
- [162] H. W. Carlson and D. J. Maglieri. “Review of Sonic Boom Generation Theory and Prediction Methods”. In: *The Journal of the Acoustical Society of America* 51.2C (1972), pp. 675–685. ISSN: 0001-4966. DOI: [10.1121/1.1912901](https://doi.org/10.1121/1.1912901). URL: <http://asa.scitation.org/doi/10.1121/1.1912901>.
- [163] R. L. Hershey and T. H. Higgins. *Statistical Model of Sonic Boom Structural Damage*. Tech. rep. July. U.S. Department of Transportation, 1976.
- [164] J. Hentschke. *Ordinary Meeting Agenda*. Streaky Bay, SA, Australia, 2017. URL: <https://www.streakybay.sa.gov.au/webdata/resources/minutesAgendas/CouncilAgenda-Report-October2017.pdf>.

APPENDIX A

MODELLING AND SIMULATION

A.1 Propulsion Interpolation Scheme

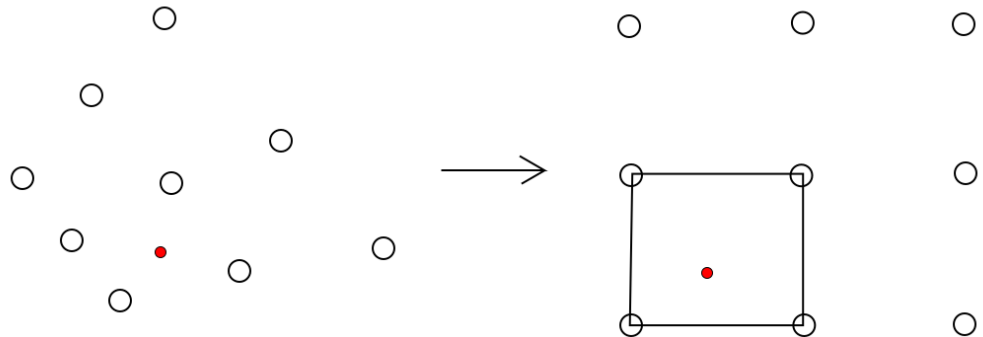


Figure A.1: The transformation to a normalised interpolation scheme.

The C-RESTM10 engine database consists of a set of engine conditions, including specific impulse, ordered by the inlet Mach number and temperature. This data set must be interpolated between, to calculate the performance of the engine at each flight condition. However, no inlet Mach number and temperature values are repeated between any of the C-RESTM10 data points. This makes for a scattered data set which particularly complicates the process of interpolating for specific impulse. It was observed that when interpolating for specific impulse, a scattered interpolation produces particularly poor results, and that fitting splines to the data set is the only way to produce an appropriate interpolation scheme. However, even when splines were fit, and the general trends of the specific impulse were matched, minuscule oscillations were still present in the interpolated values. These

oscillations do not significantly affect a forward simulation, however, when the vehicle model is accessed by an optimal control solver, they can cause gradients which affect the convergence process. Consequently, it was necessary to craft a bespoke interpolation scheme in order to accurately interpolate the specific impulse of the vehicle.

This interpolation begins by designating a new coordinate system, normalised to [0 1], running from data point with the lowest inlet temperature [0,0], to the data point with the highest inlet temperature [1,1]. Each data point is then given a set of normalised coordinates, and a cubic spline is fit to this set of normalised points using MATLAB's `griddedInterpolant` function. This cubic spline is smooth, with no oscillations present. In order to interpolate at a specific location, each data point bounding the interpolation region is set as the corner of a square of data points in normalised coordinates. This is illustrated in Figure A.1. The distance of the location to be interpolated to each of these bounding data points is calculated, and the location to be interpolated is assigned a set of normalised coordinates. This set of normalised coordinates is used, along with the cubic spline interpolant, to calculate a specific impulse.

This process is accurate, but time consuming, and would increase the computation time of the optimisation process significantly if implemented directly within the vehicle model. In order to expedite the interpolation process, interpolations are performed for the specific impulse over a grid of inlet conditions, determined by the C-RESTM10 data points, ie. for every combination of inlet Mach number and temperature present in the C-RESM10 database. This grid of linearly interpolated specific impulse values is then used as a new data set, which is now in meshgrid form, by which the specific impulse is interpolated. A bivariate spline is fitted to this grid of data points, using MATLAB's `griddedInterpolant` function, which is accessed by the vehicle model to determine specific impulse during flight.

A.2 SPARTAN Flow Results

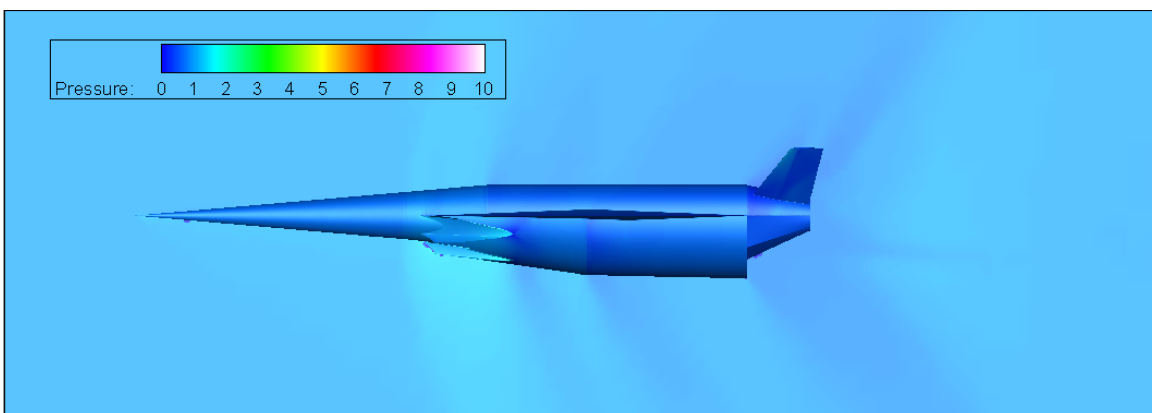


Figure A.2: CART3D flow result for the SPARTAN, at Mach 1.1, 6° angle of attack.

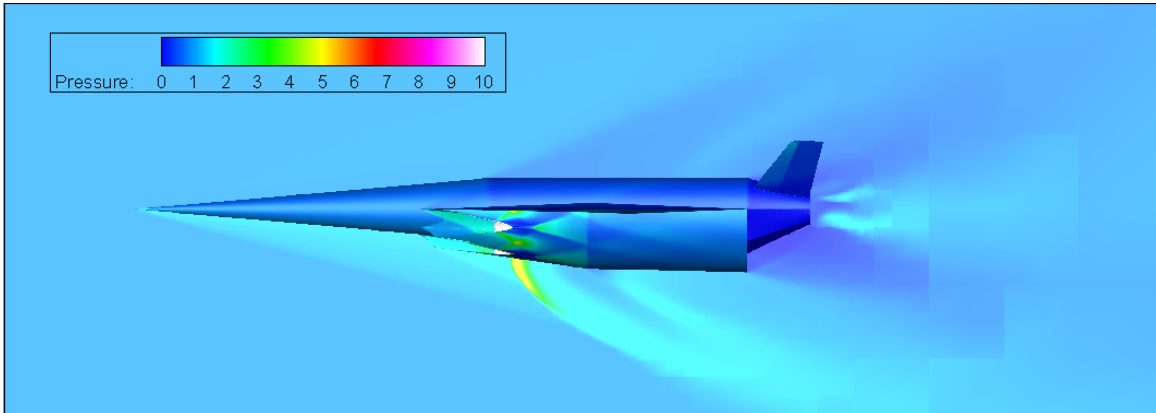


Figure A.3: CART3D flow result for the SPARTAN, at Mach 3, 6° angle of attack.

Figures A.2 and A.3 show flow results for the SPARTAN, at Mach numbers of 1.1 and 3 respectively. It can be observed that at Mach 1.1, the bow shock is not significant, and the shock structure that is evident at higher speeds has not yet formed. At Mach 3, the unstarted C-REST engines are evident, causing significant amounts of the air entering the inlet to be expelled. Shock-shock interaction structures are evident on the cowl of the engines, causing areas of localised high pressure.

A.3 Cart3D Mesh

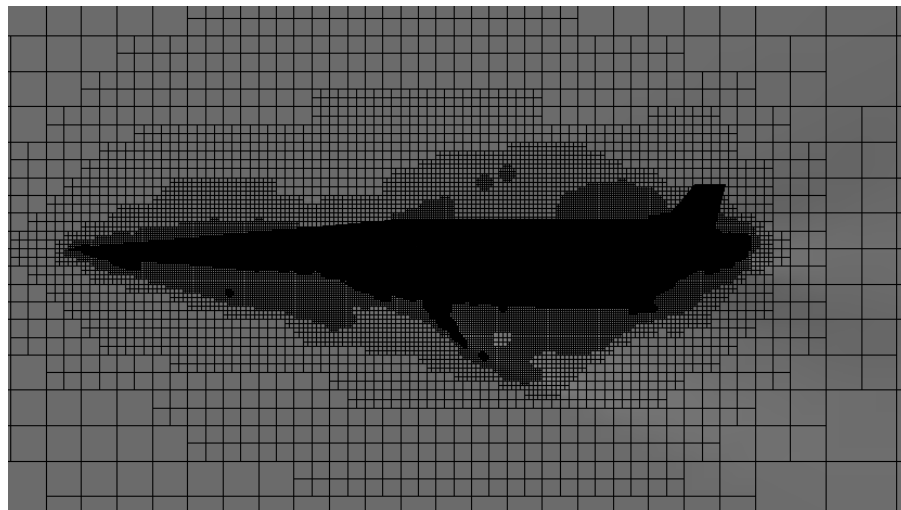


Figure A.4: Adapted mesh of the SPARTAN at Mach 6 3° angle of attack.

Figures A.4 and A.5 show adapted meshes for Cart3D solutions of the SPARTAN, and the SPARTAN and first stage. These meshes have been generated adaptively by Cart3D during the solution process. It can be observed that the mesh clusters around the vehicle, particularly in regions where strong shocks are present, where the clusters at the shock front.

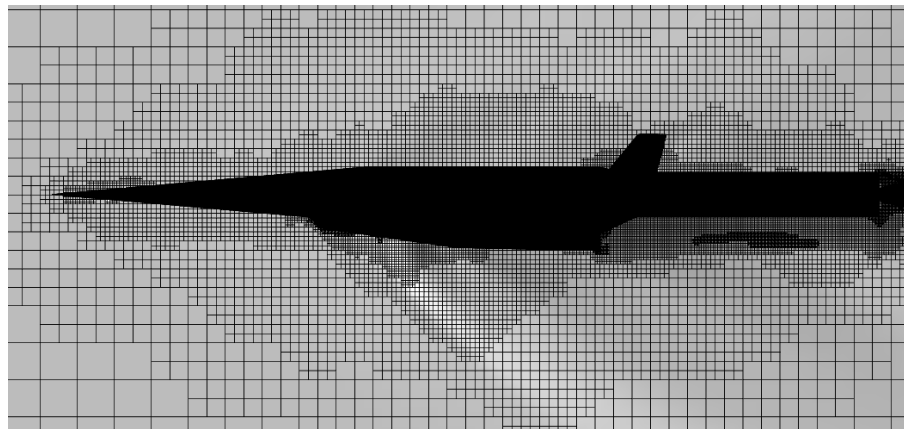


Figure A.5: Adapted mesh around the SPARTAN and first stage vehicles, flying at Mach 2, -1° angle of attack.

A.4 Performance of the SPARTAN During Fly-Back

Figure A.6 shows the performance of the SPARTAN during the boost phase, described in Section 6.3.

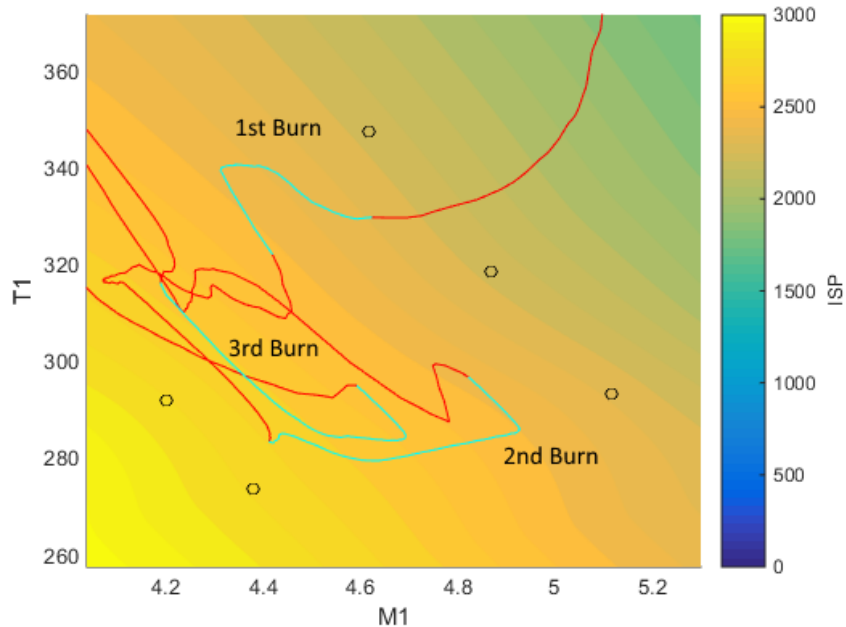


Figure A.6: The performance of the SPARTAN during the boost phase. Light blue indicates that the scramjet engines are turned on.

APPENDIX B

EXAMPLE AND VERIFICATION

B.1 GPOPS-2 Example - Brachistochrone Problem

This section describes a short example of an optimal control problem solved in GPOPS-II. The purpose of this example is to demonstrate the effectiveness of the pseudospectral method and GPOPS-II, and to provide a simple example case to establish the terminology of an optimal control problem.

The brachistochrone (from the Greek for 'shortest time') problem is a simple optimal control problem, which describes a ball rolling in two dimensions under gravity. The objective is to find the curve of descent which will minimise the time from point a , where the ball is at rest, to point b . It is assumed that gravity is constant and that there is no forces other than gravity acting on the ball. The analytical solution of this problem can be computed using the Euler-Lagrange equation as the equations describing a cycloid:

$$x = A(\theta + \sin \theta),$$

$$y = A(1 - \cos \theta)$$

This problem is included within GPOPS-2 as an example problem, and has been solved to illustrate the GPOPS-2 solution set-up[103]. Table B.1 describes the set-up of the optimal control problem in GPOPS-2. The dynamic equations for the Brachistochrone problem are:

$$\dot{x} = v * \cos(u),$$

$$\dot{y} = v * \sin(u),$$

$$\dot{v} = g * \sin(u).$$

These equations are provided to GPOPS-2 as the time-variant system model in this form. The control variable is set to be the descent angle. The initial constraints are defined to initiate the ball at rest at the origin, and the terminal constraints are defined to terminate the problem at coordinates of [2,2]. The cost is set to minimum time, so that the solution will be the descent angle which minimises the

Primal Variables	x Position y Position Velocity
Control Variables	Angle of Descent
Initial Constraints	Velocity x Position y Position
Terminal Constraints	x Position y Position
Path Constraints	None
Target Cost	Minimum Time

Table B.1: Optimisation setup of the Brachistochrone problem.

time to get from the initial position, to the end position.

The GPOPS-2 solution to the Brachistochrone problem is shown in Figure B.1, matching the analytical solution almost exactly. This is expected in this case, as the dynamics of the basic Brachistochrone problem are very simple. As the dynamics become more complex, it is no longer possible to obtain an analytical solution.

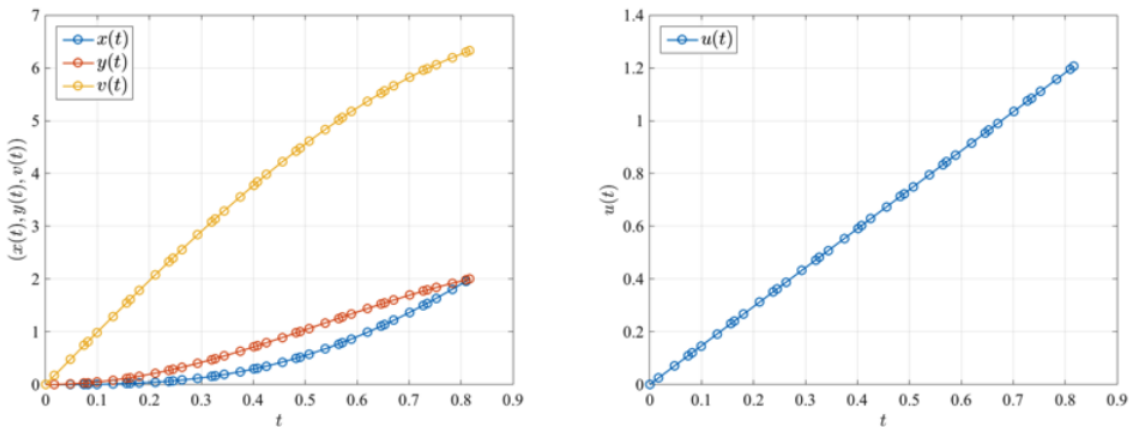


Figure B.1: The solution to the Brachistochrone problem, solved in GPOPS-2[103].

B.2 Optimised Trajectory Analysis

This section presents the an example of the convergence and verification of a maximum payload-to-orbit trajectory solution, with SPARTAN fly-back.

B.2.1 Mesh History

The mesh history of the optimal trajectory solution is shown in Figure B.2. The mesh is updated by GPOPS-2 in each iteration of the optimal solution. It can be observed that the mesh of the first and third stage rockets contains significantly less node points at the final iteration than the SPARTAN's acceleration or return. This is due to the relatively simple dynamics and shorter flight time of the first and third stages. The first stage shows a cluster of nodes at the beginning of its trajectory, in the subsonic, transonic and low Mach regimes. In these regions the aerodynamics are changing rapidly, and the nodes are clustered to accurately capture the dynamic behaviour of the vehicle. After transition occurs to supersonic flight, the aerodynamic and performance of the vehicle change more slowly, and the nodes become more widely spaced. The acceleration of the SPARTAN shows significant node density throughout. The operation of the SPARTAN is complex, as the dynamics of the vehicle and the performance of the scramjet engines vary significantly, even during relatively level flight. For this reason, the nodes of the return flight show even greater density. The trajectory conditions change significantly as the SPARTAN performs skipping manoeuvres, and transitions through the various return phases, necessitating high node density to capture the vehicle dynamics, particularly between powered and unpowered flight. The trajectories of the SPARTAN also last for a significantly longer time than the rocket trajectories, requiring more total nodes to accurately capture the vehicle dynamics. The third stage shows the least nodes at the final mesh iteration, as the dynamics of the third stage are relatively simple. Some node clustering is observed in the first part of the trajectory, this is when the atmospheric density is still significant, and changing as the altitude of the third stage is increased.

B.2.2 Verification

After the optimal trajectory has been calculated, it must be verified to ensure that the optimal control solver has converged correctly. Details on this verification are provided in Section 4.4. Figure B.3 shows the Hamiltonian time history for the optimised trajectory solution. For an optimal solution to be found, the Hamiltonian should be equal to 0 at all points over every phase. In a practical solution, a Hamiltonian close to 0 is acceptable, which is observable over all phases in the optimised solution. A small deviation from 0 is shown at the end of the SPARTAN's acceleration, this is the region in the pull-up where the angle of attack limit is close to being reached. The Hamiltonian being close to 0 at all points of the trajectory indicates that an optimal solution has been found.

The next step in the verification process is to ensure that the dynamic constraint of the optimal control problem holds across the entire solution, ie. $\dot{\mathbf{x}}(t) = f[t, \mathbf{x}(t), \mathbf{u}(t)]$. This is the most important step in the verification process, which checks that the optimal control solver has converged correctly, so that the physical dynamic of the vehicle are being correctly represented by the polynomial approximation. The dynamic constraint is tested by first calculating the dynamics of the vehicle at every node of the solution. The dynamics of the system are then integrated over time using trapezoidal

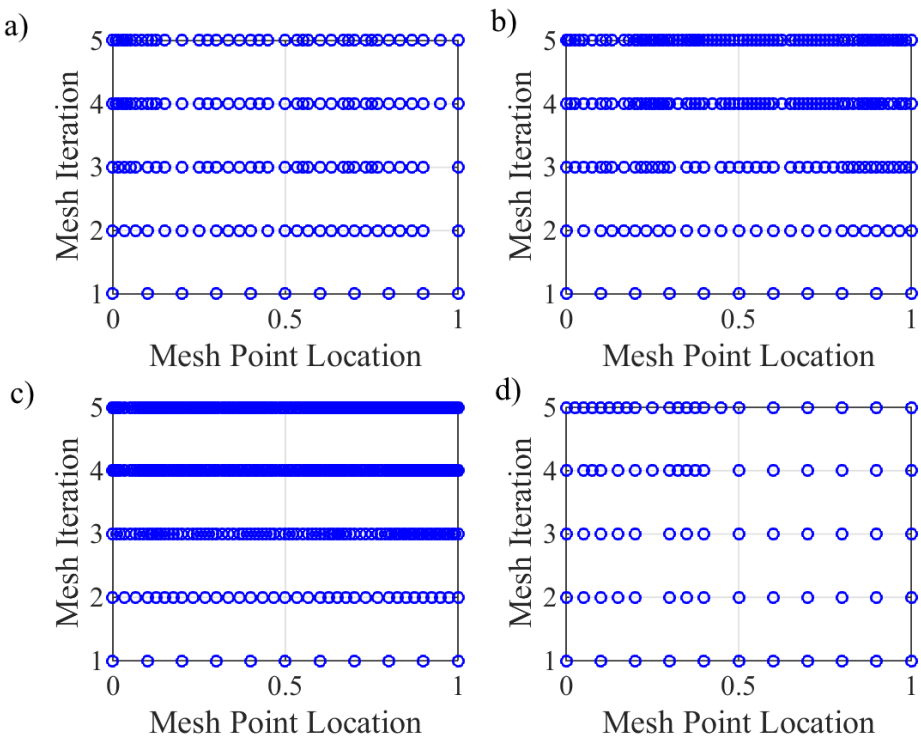


Figure B.2: The mesh history of each phase of the optimised, maximum payload-to-orbit trajectory with SPARTAN fly-back. the phases are shown in each subfigure as follows: a) first stage rocket, b) SPARTAN acceleration, c) SPARTAN fly-back and d) third stage.

*

integration, starting at the initial conditions of each phase. If the dynamic constraint holds, then the integrated dynamics of the system will be equal to the state variables of the solution. The error in the dynamic constraint is shown in Figure B.4, calculated as the difference between the integrated dynamics and each state variable, normalised to the range of the state variable. It can be observed that all errors in the dynamic constraint are very small. The error that is present is likely to be due to the inaccuracies of the trapezoidal method, which is significantly less accurate than the approximating polynomials of the pseudospectral method. This is supported by substantial increases in the error of the dynamic constraint being observable in the regions of rapid state changes, such as the heading angle when the first stage is near vertical, and the states of the return phase when the scramjet engines are throttled on.

The final verification step is a forward simulation of each phase. This forward simulation compares the solution state with a simulation which is forward integrated using only the controls of each stage. This is the most stringent method of checking the validity of the solution dynamics. However, it is expected that this verification will have significantly higher errors than the check which verifies the dynamics each state independently, as the interdependencies of each state come into play, and small errors are compounded. Figure B.5 shows the error between the forward simulation and the solution

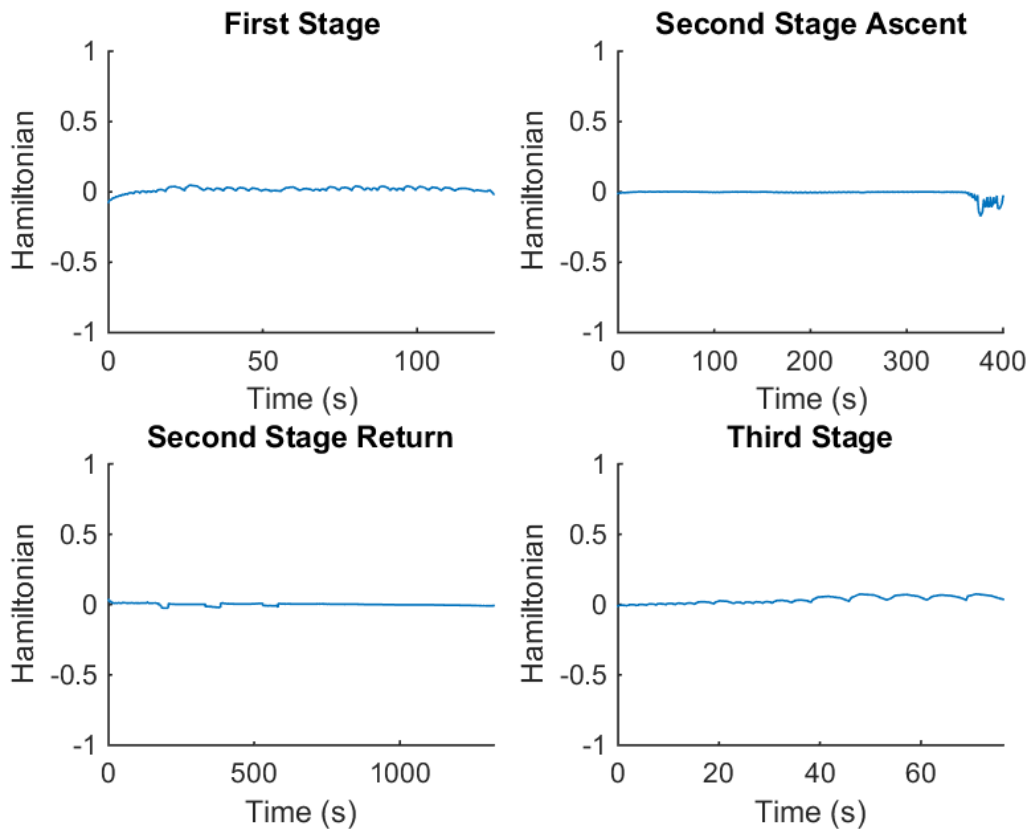


Figure B.3: The Hamiltonian time history of each phase of the optimised solution.

states. As described in Section 4.4, the forward simulation of the return flight is separated into three segments, at 1/6th and 1/3rd of the flight time. The errors in the forward simulation of each stage are observed to be acceptably small, significantly under 1% in all cases, with evident compounding errors being the cause of the most extreme deviations.

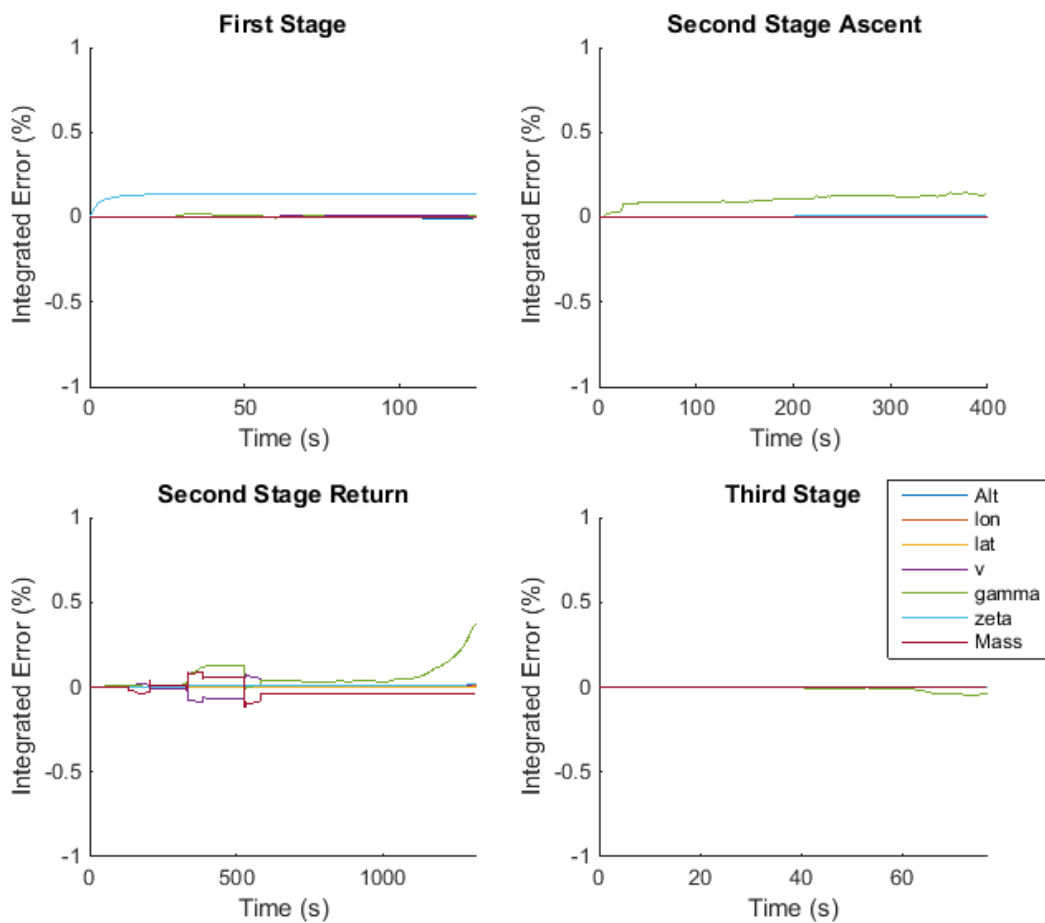


Figure B.4: The error between the integrated dynamics of the system, and the solution states. Normalised to the range of each state.

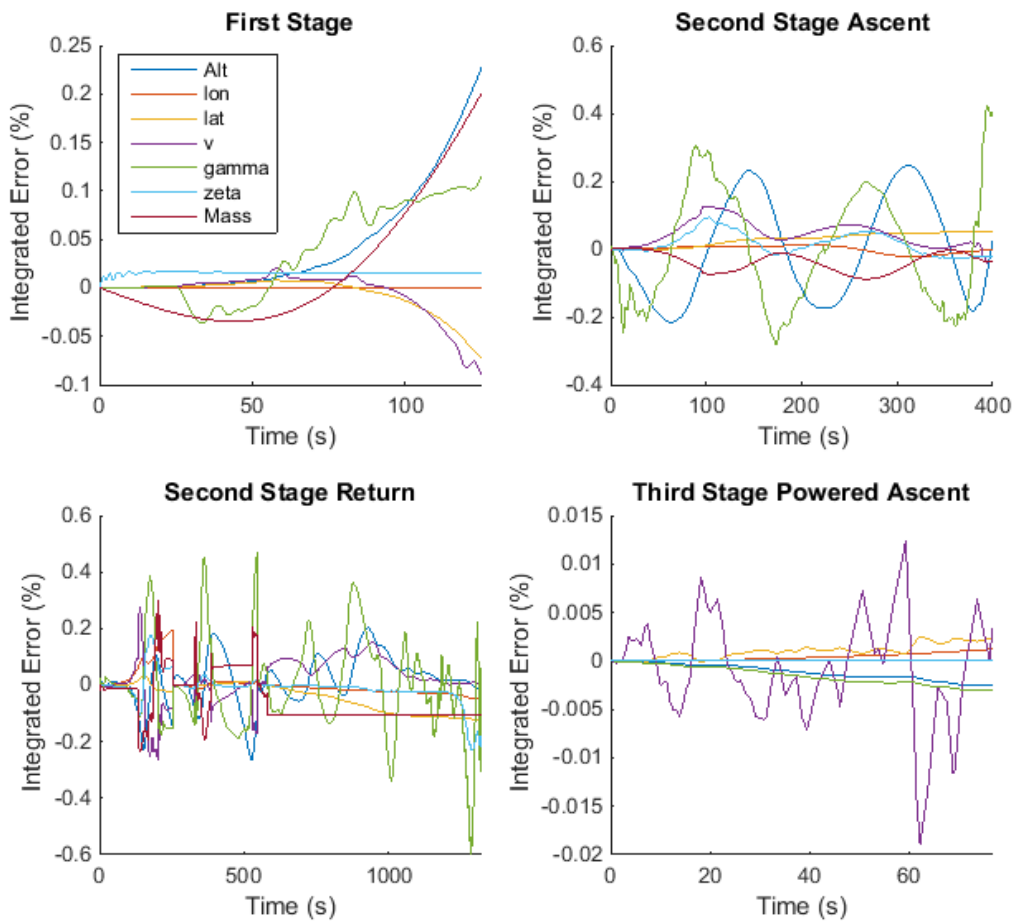


Figure B.5: The error between the forward simulated states, and the solution states. Normalised to the range of each state.

APPENDIX C

ALTERNATE TRAJECTORY CASES

C.1 Maximum Payload-To-Orbit Trajectory With Dynamic Pressure Constraint

The maximum payload-to-orbit trajectory of the launch system with no SPARTAN fly-back (Case 2) was found to involve a significant altitude raising manoeuvre in the middle of the acceleration trajectory of the SPARTAN. Discerning the benefits of this altitude raising manoeuvre proved complex, requiring a trajectory to be calculated in which the altitude raising manoeuvre was prevented from occurring. This trajectory was optimised for maximum payload-to-orbit, with a 50kPa dynamic constraint between Mach numbers of 6 and 8, the region in which the altitude raising manoeuvre was observed to occur. This constraint successfully removed the altitude raising manoeuvre from the maximum payload-to-orbit optimised trajectory, allowing for a comparison to be made to quantify the benefits of the altitude raising manoeuvre. This comparison is made in Section 5.2. Figures C.1, C.2 and C.3 show the maximum payload-to-orbit trajectory constrained to 50kPa between Mach numbers 6 to 8, and Table C.1 details key parameters of the trajectory.

C.2 Sonic Boom Ground Effects

The flight of a hypersonic vehicle has the potential to create significant overpressures on the ground due to sonic booms. Even when the vehicle is flying at high altitudes, the overpressures on the ground may still be large enough to have detrimental effects on any populated areas being overflowed. The overpressure from sonic booms can cause significant annoyance to the populace, or in more extreme cases, long term damage to building structures or peoples health. When the SPARTAN is launched to a sun synchronous orbit from the Equatorial Launch Australia launch site, it flies over

Trajectory Condition	Value
Payload to Orbit (kg)	188.8
Total η_{exergy} (%)	1.690
1st Stage η_{exergy} (%)	8.174
Separation Alt, 1→2 (km)	24.12
Separation v, 1→2 (m/s)	1485
Separation γ, 1→2 (m/s)	3.2
2nd Stage η_{exergy} (%)	10.878
Separation Alt, 2→3 (km)	42.44
Separation v, 2→3 (m/s)	2679
Separation γ, 2→3 (deg)	10.9
Separation q, 2→3(kPa)	9.7
2nd Stage L/D, 2→3	4.5
2nd Stage Flight Time (s)	629.8
3rd Stage η_{exergy} (%)	20.403
3rd Stage $t, q > 5\text{kPa}$ (s)	10.8
3rd Stage max α (deg)	16.0
3rd Stage Fuel Mass (kg)	2826.0

Table C.1: A summary of key results from the maximum payload-to-orbit trajectory, constrained to 50kPa between Mach numbers 6 to 8.

a significant portion of Papua. Fortunately, Papua is sparsely populated, and the number of towns flown over by the SPARTAN will be low, however the effects on these population centres may still be significant. Although it is flying at high altitude, the SPARTAN is flying at hypersonic speeds, and creates significant sonic boom effects. In order to assess the impact of the SPARTAN's flight, the magnitude of the overpressure from its sonic booms must be calculated.

The sonic boom overpressures are estimated using the 'first cut' estimation technique [162]. This estimation technique can approximate sonic boom overpressures moderately well, and is useful as a first approximation to the sonic boom overpressures generated by an aerospace vehicle. The overpressures generated by the SPARTAN are calculated over its trajectory, shown in Figure C.5. It is found that overpressures of up to 375.3Pa occur during flight over land during the maximum payload-to-orbit trajectory of the SPARTAN. These overpressures have a low but significant probability of causing cosmetic damage to structures (1.5% for plaster and 0.4% for glass)[163]. In addition, overpressures of these magnitudes have been rated as unacceptably annoying to the majority populace being overflowed, as shown in Figure C.4. These overpressures indicate that overflight of populated areas may not be reasonable for the SPARTAN flying its maximum payload-to-orbit trajectory.

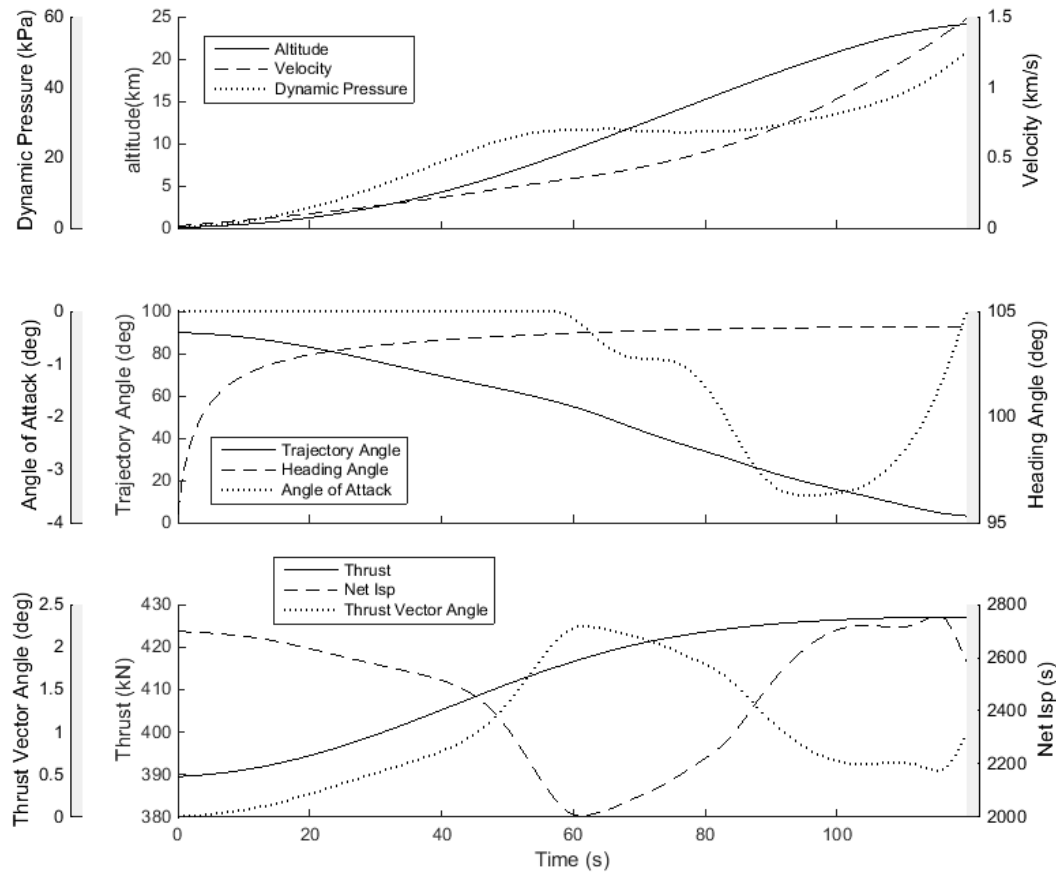


Figure C.1: The optimised maximum payload-to-orbit trajectory of the launch system constrained to 50kPa between Mach numbers 6 to 8, under power of the first stage rocket.

C.3 Alternate Launch Locations

An alternate southerly launch is investigated for the rocket-scramjet-rocket launch system, in the case that flight over Papua is not possible. This launch occurs from Streaky Bay, the possible location of a launch site being developed by Southern Launch Australia[164]. The maximum payload-to-orbit has been calculated from this launch site using LODESTAR. Figure C.6 shows the ground track of this optimised trajectory, and Table C.2 details a summary of the key trajectory parameters. The shape of this optimised trajectory is very similar to the optimal trajectory of the launch system launched from the Northern Territory. The first stage initially pitches towards the west, separating the SPARTAN in a westerly direction. The SPARTAN then performs a banking manoeuvre, and a pull-up before third stage release. After separation, the SPARTAN exhibits initial turn, boost-skip and approach phases during fly-back, with the scramjet engine igniting three times at the troughs of the first three skips. A higher payload to orbit is achieved when launching from a southerly location, attaining a total

APPENDIX C. ALTERNATE TRAJECTORY CASES

Trajectory Condition	Value
Payload to Orbit (kg)	175.2
Total η_{exergy} (%)	1.535
1st Stage η_{exergy} (%)	8.531
Separation Alt, 1→2 (km)	25.64
Separation v, 1→2 (m/s)	1552
Separation γ, 1→2 (m/s)	3.4
2nd Stage η_{exergy} (%)	9.588
Separation Alt, 2→3 (km)	41.30
Separation v, 2→3 (m/s)	2581
Separation γ, 2→3 (deg)	11.1
Separation q, 2→3(kPa)	10.6
2nd Stage L/D, 2→3	4.7
2nd Stage Flight Time (s)	500.8
2nd Stage Return Fuel (kg)	280.9
3rd Stage η_{exergy} (%)	20.691
3rd Stage $t, q > 5\text{kpa}$ (s)	12.1
3rd Stage max α (deg)	16.4
3rd Stage Fuel Mass (kg)	2839.6

Table C.2: A summary of key trajectory parameters of the maximum payload-to-orbit trajectory launched in a southerly direction.

of 175.2kg of payload-to-orbit, an increase of +2.9% compared to northerly launch. This payload increase is caused by the rotation of the Earth hindering, rather than assisting, launch when launching into a retrograde orbit.

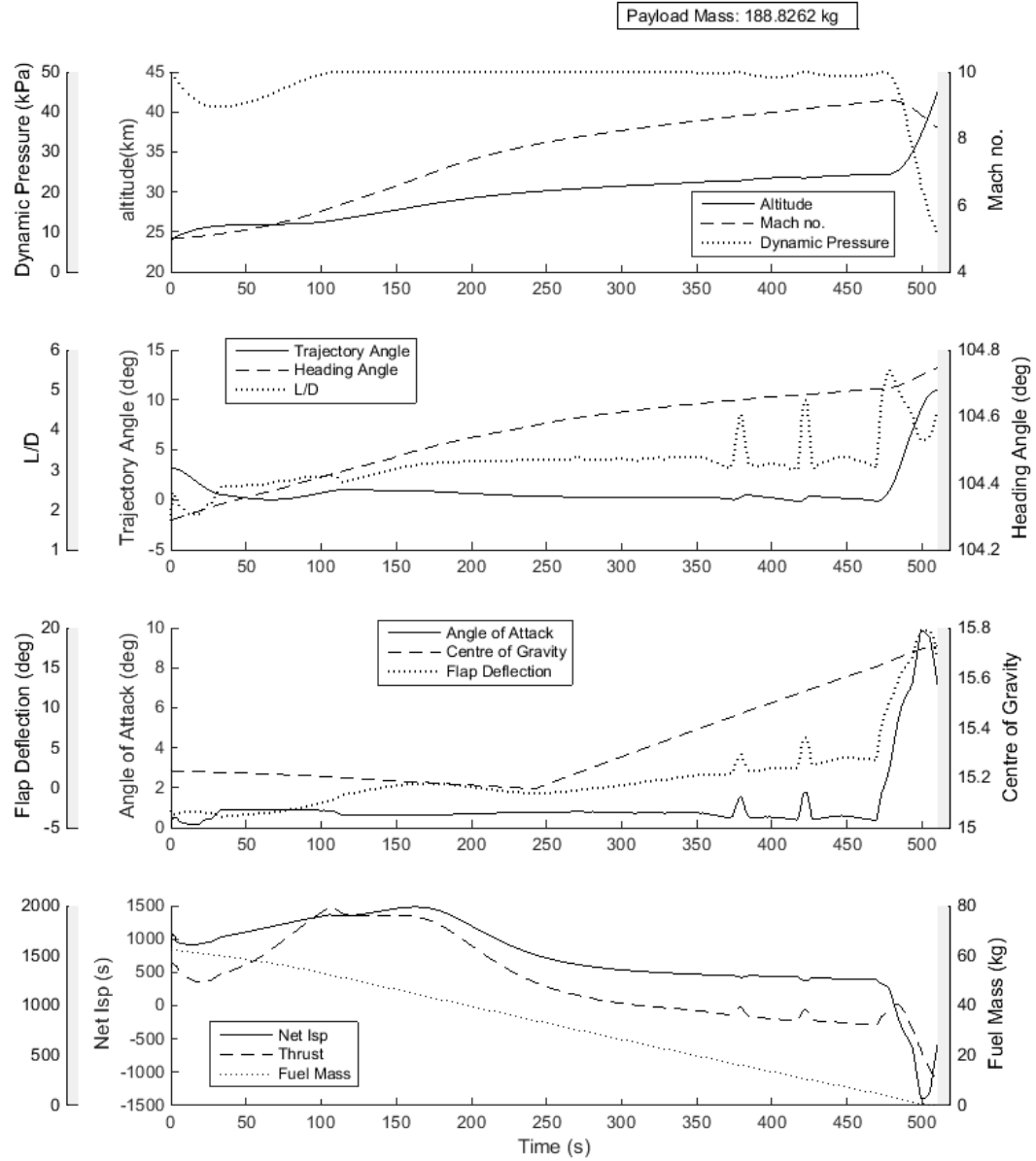


Figure C.2: The optimised maximum payload-to-orbit trajectory of the SPARTAN, constrained to 50kPa between Mach numbers 6 to 8.

APPENDIX C. ALTERNATE TRAJECTORY CASES

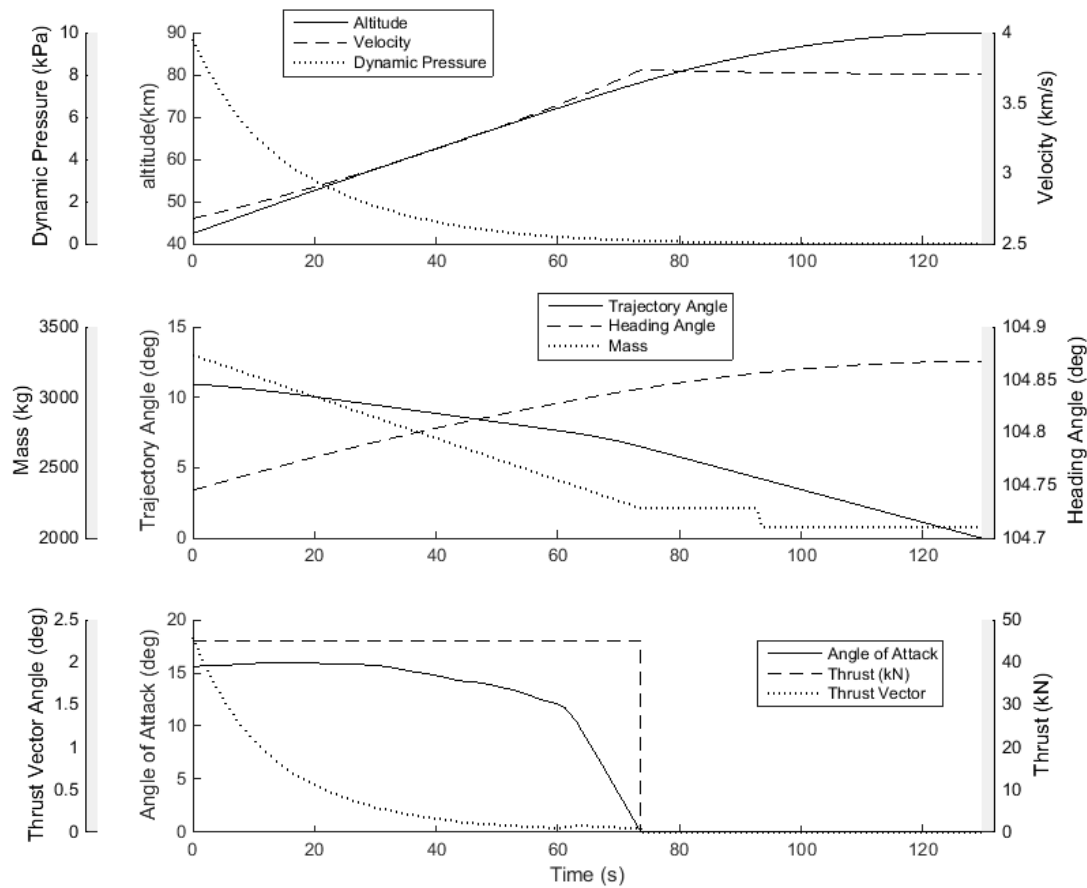


Figure C.3: The third stage trajectory of the launch system flying the maximum payload-to-orbit trajectory, constrained to 50kPa between Mach numbers 6 to 8.

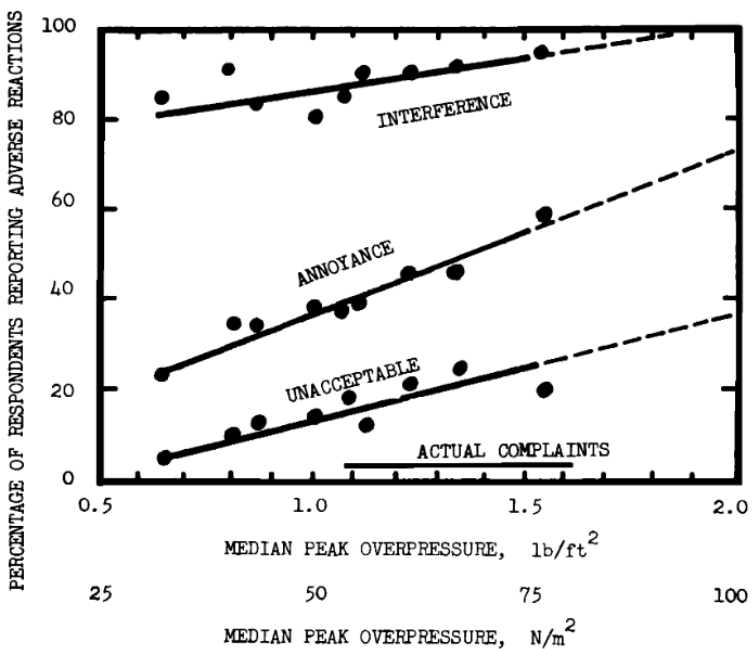


Figure C.4: The level of population annoyance with increasing overpressure.

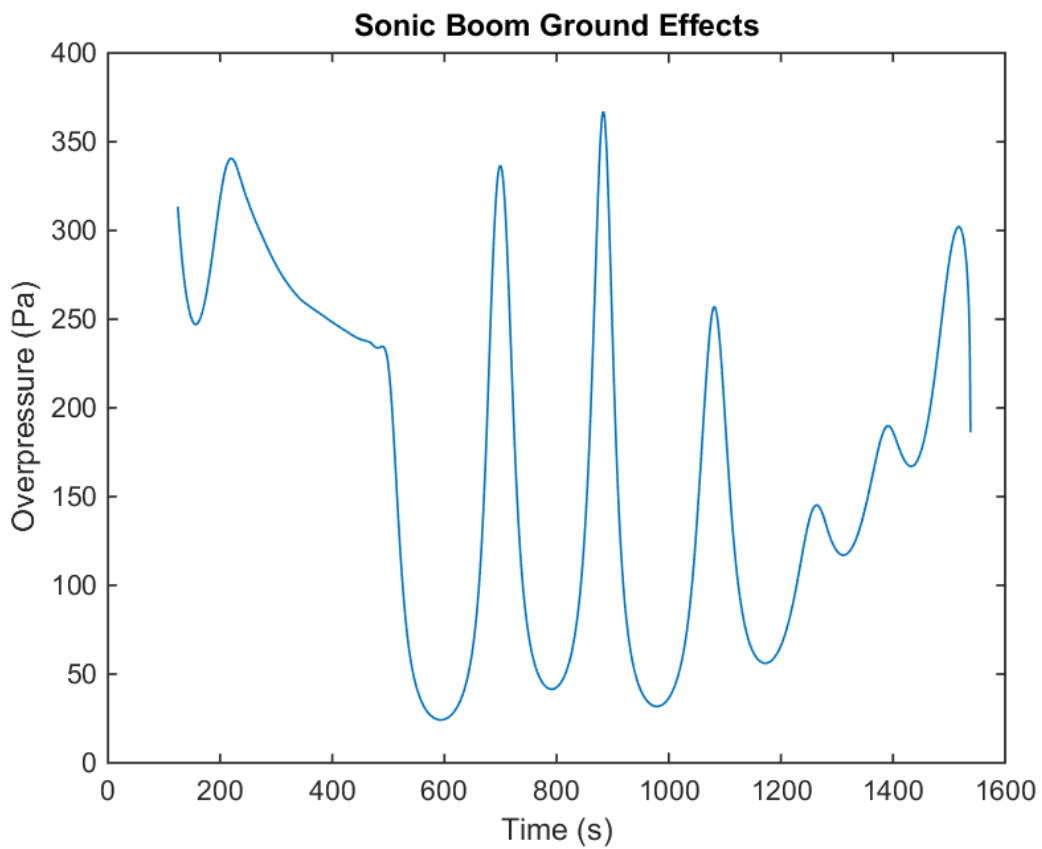


Figure C.5

APPENDIX C. ALTERNATE TRAJECTORY CASES

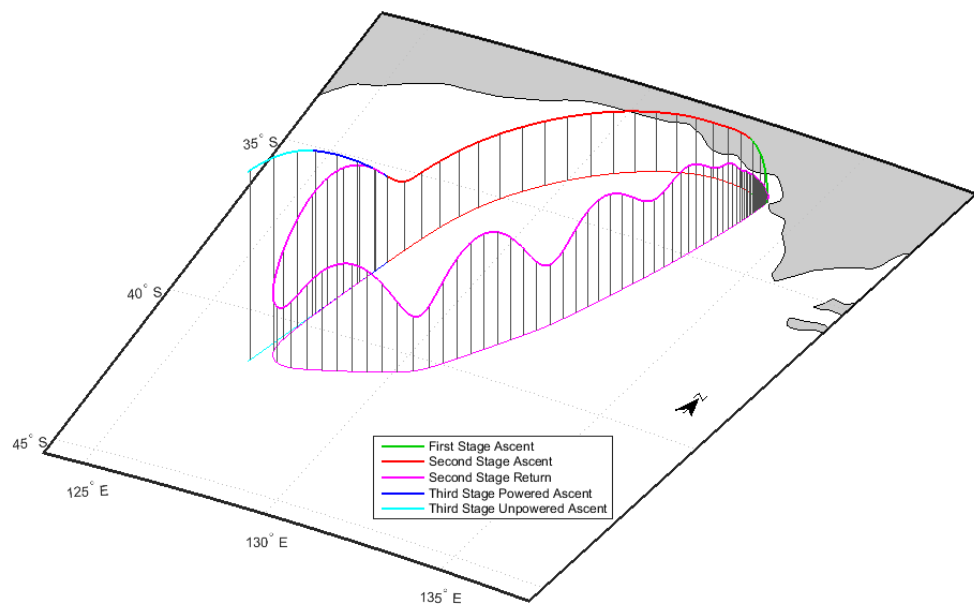


Figure C.6: The optimised maximum payload-to-orbit trajectory of the launch system launching onto a southerly orbit, from Streaky Bay.

APPENDIX D

TRAJECTORY PLOT COMPARISONS

This section contains trajectory plot comparisons for the sensitivity studies performed in Section [5.3](#) and [6.4](#). Comparisons and analyses between these trajectories are performed in the relevant sections.

D.1 Optimised Ascent Trajectory Comparisons With No Fly-Back

D.1.1 Case 3: Maximum Dynamic Pressure Sensitivity Comparison

APPENDIX D. TRAJECTORY PLOT COMPARISONS

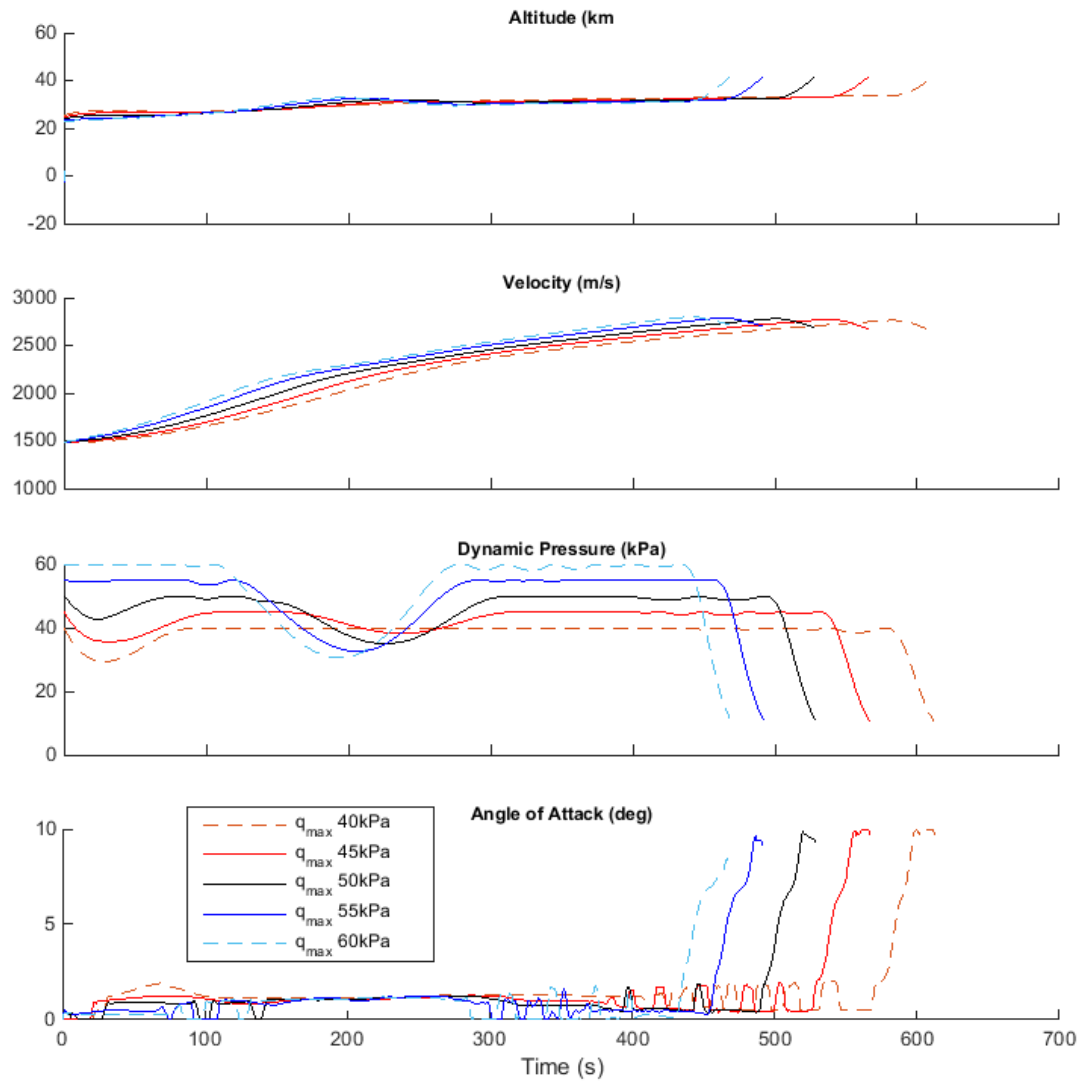


Figure D.1: Comparison of SPARTAN ascent trajectories with variation in the maximum dynamic pressure of the SPARTAN.

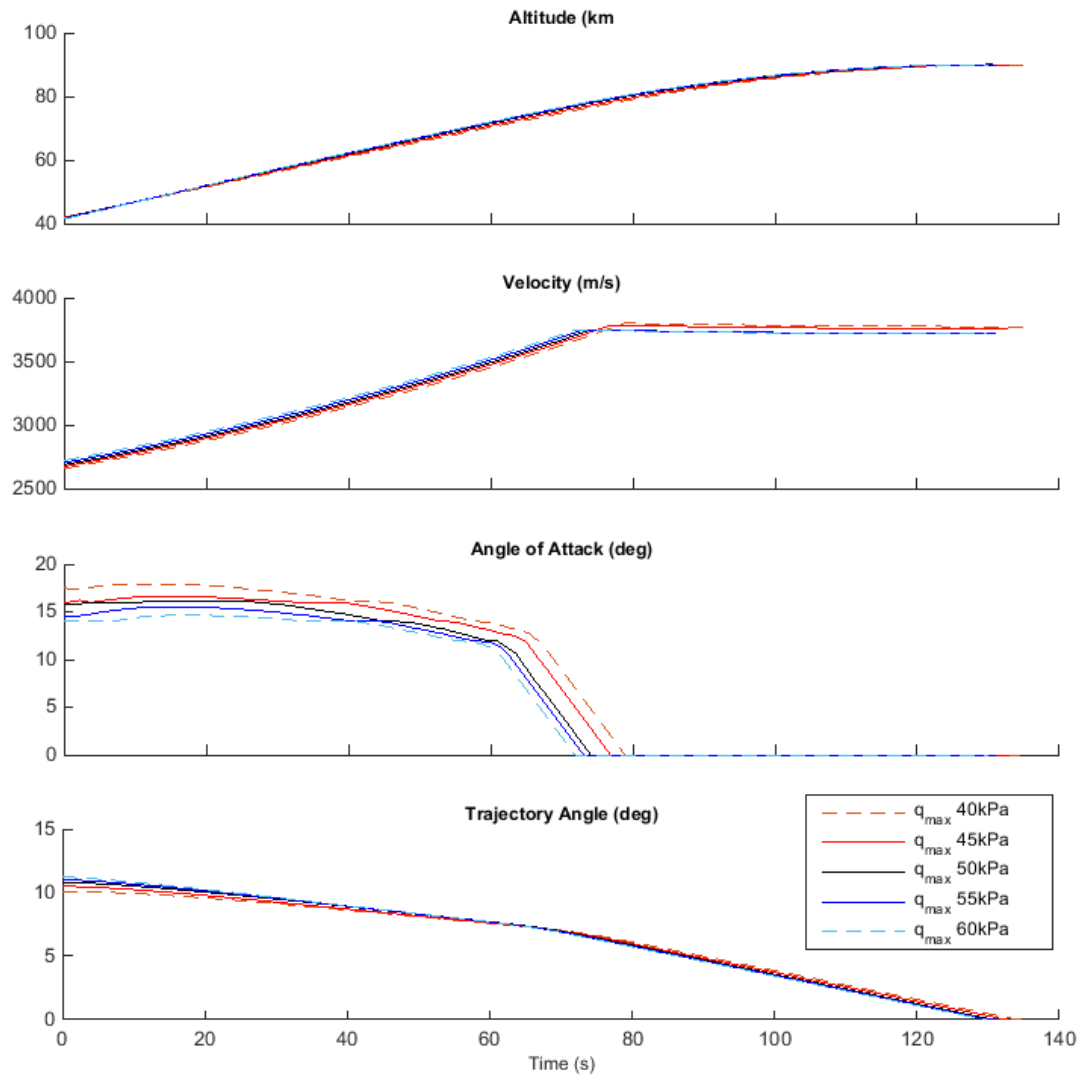


Figure D.2: Comparison of third stage rocket ascent trajectories with variation in the maximum dynamic pressure of the SPARTAN.

D.1.2 Case 4: SPARTAN Specific Impulse Sensitivity Comparison

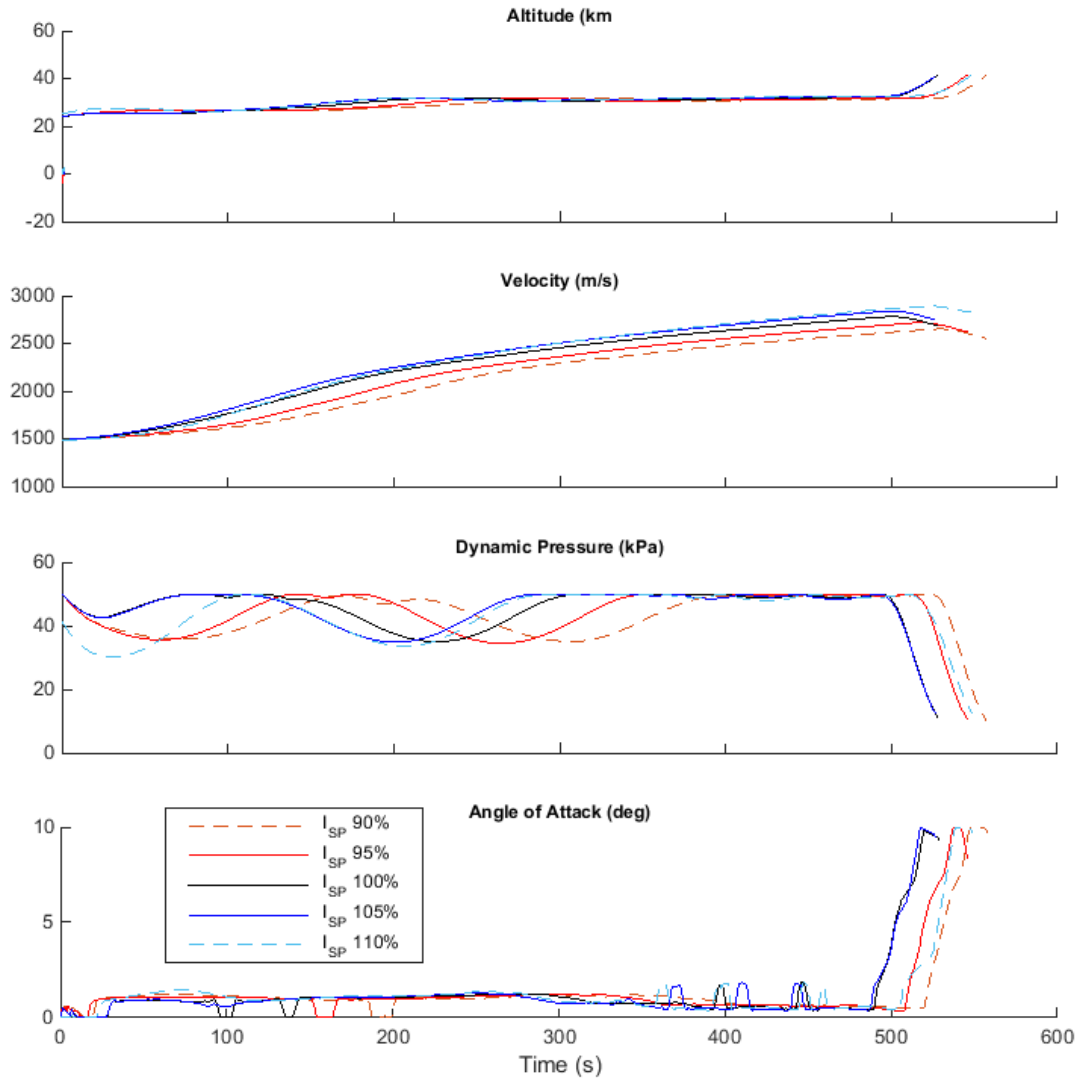


Figure D.3: Comparison of SPARTAN ascent trajectories with variation in the specific impulse of the SPARTAN.

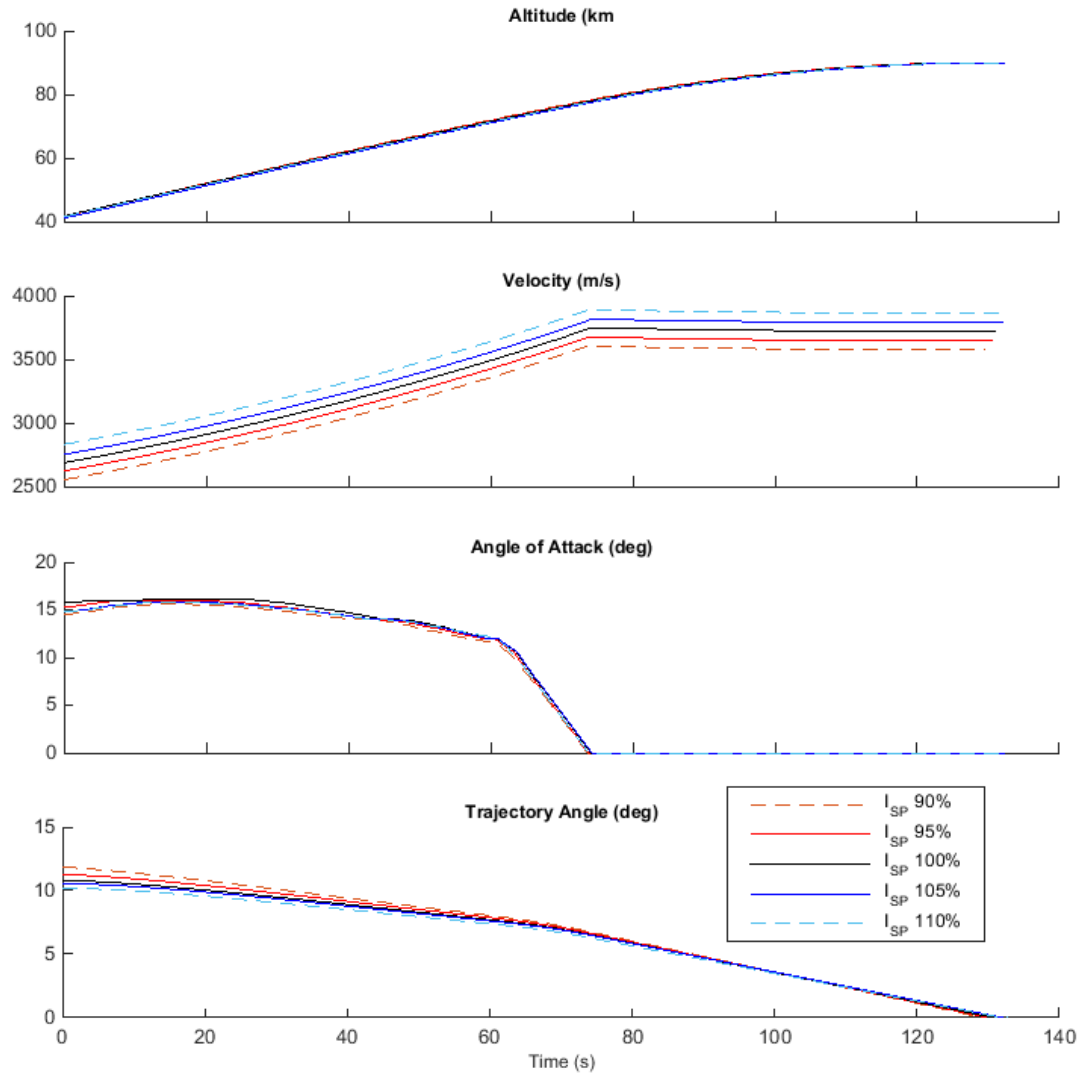


Figure D.4: Comparison of third stage rocket ascent trajectories with variation in the specific impulse of the SPARTAN.

D.1.3 Case 5: SPARTAN Drag Sensitivity Comparison

APPENDIX D. TRAJECTORY PLOT COMPARISONS

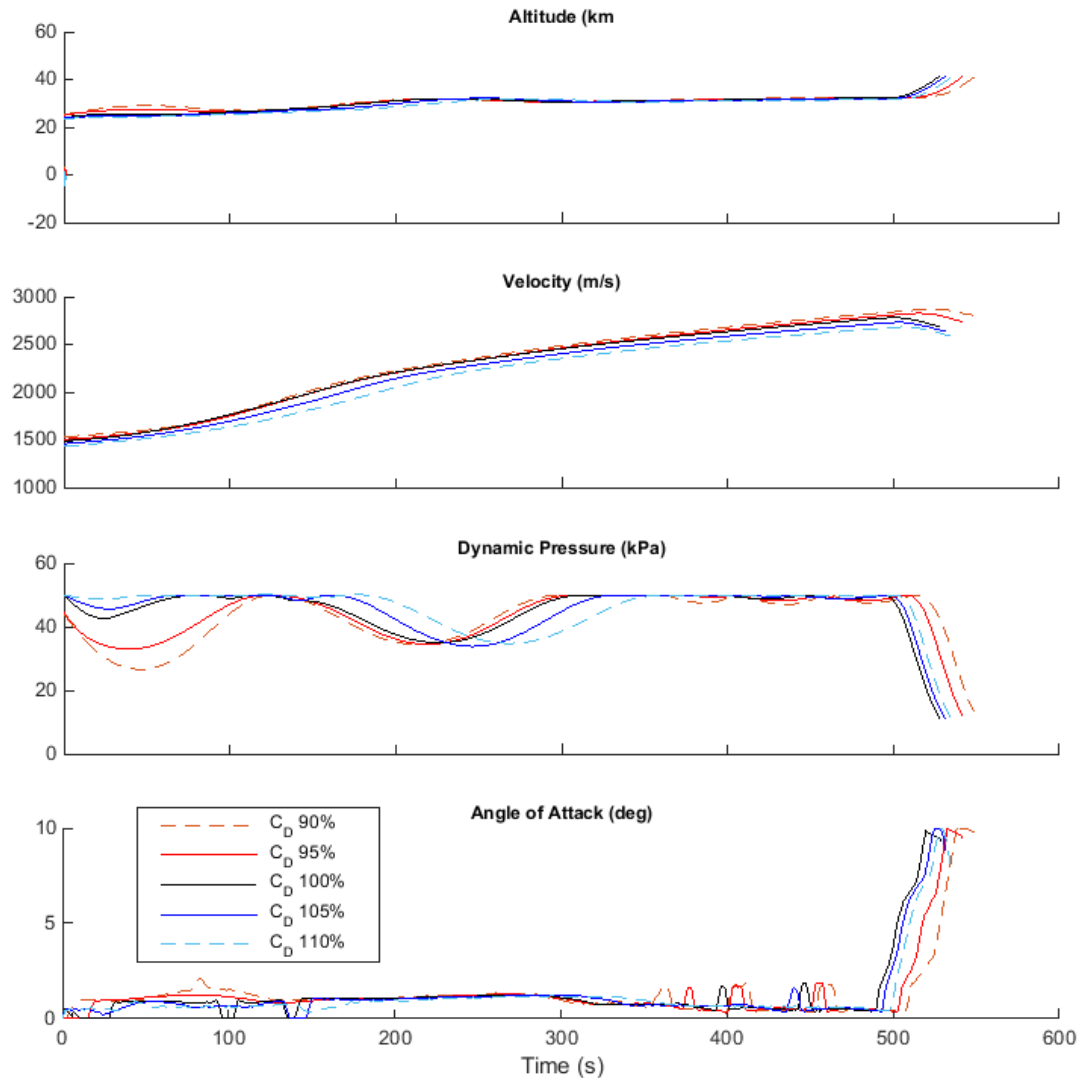


Figure D.5: Comparison of SPARTAN ascent trajectories with variation in the drag of the SPARTAN.

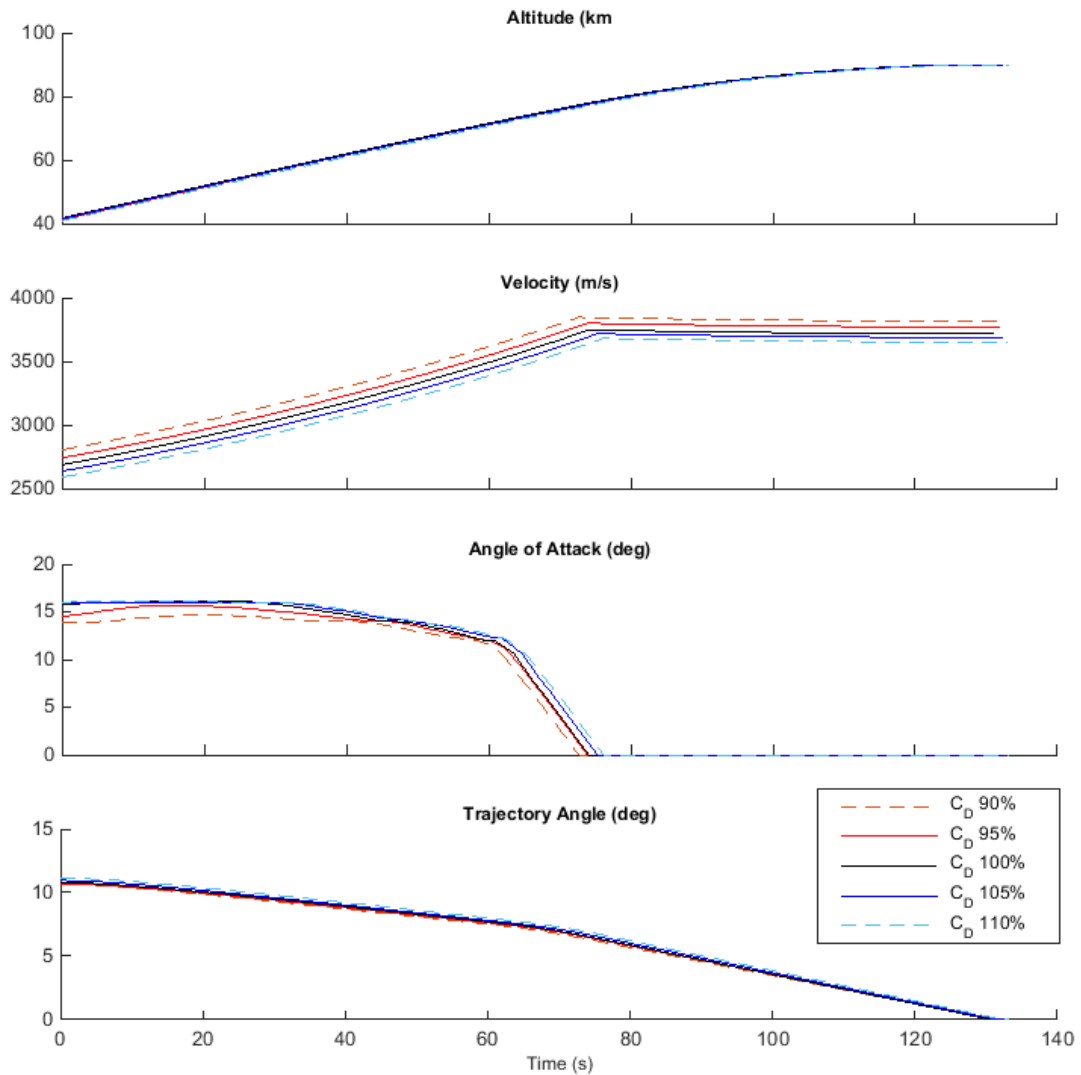


Figure D.6: Comparison of third stage rocket ascent trajectories with variation in the drag of the SPARTAN.

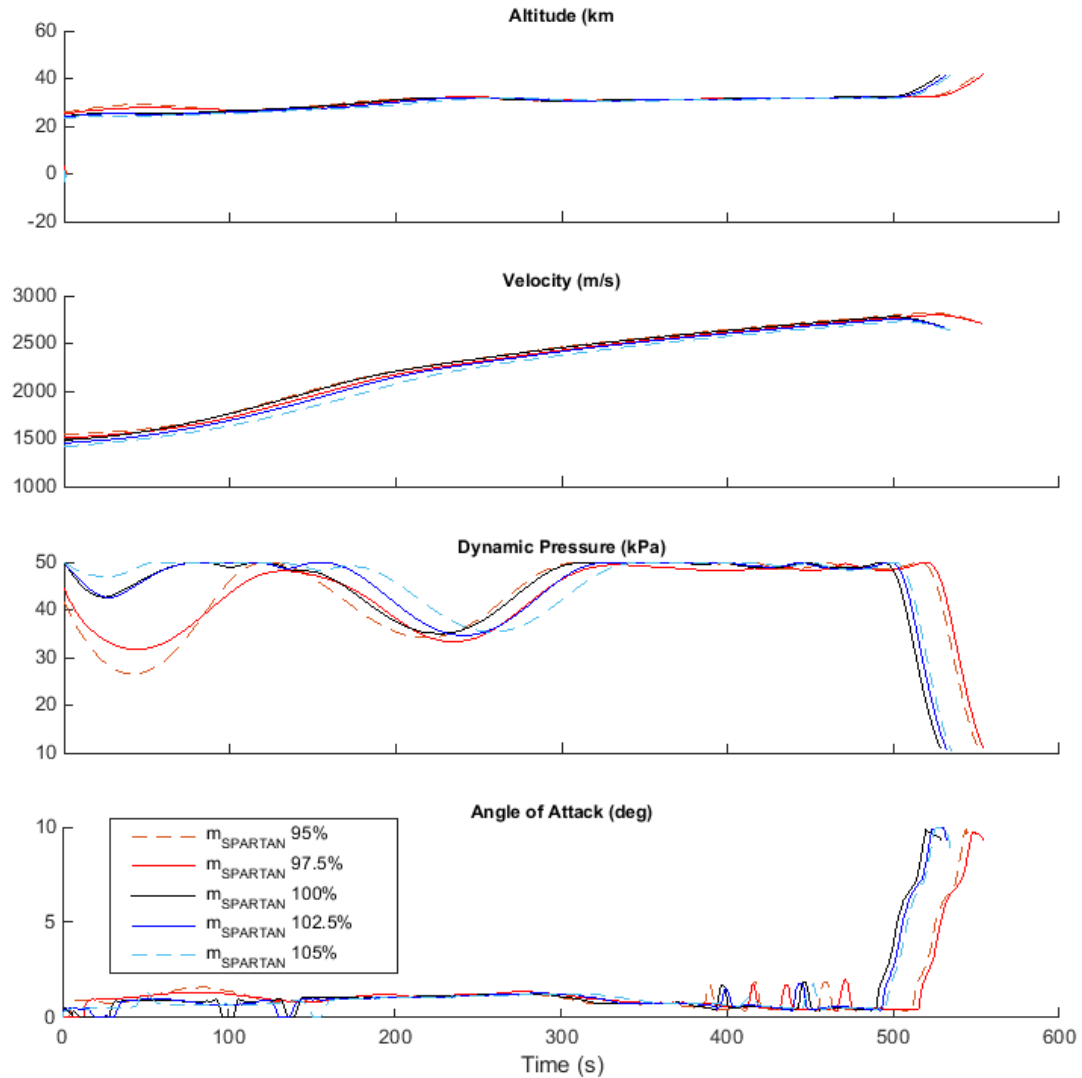
D.1.4 Case 6: SPARTAN Mass Sensitivity Comparison

Figure D.7: Comparison of SPARTAN ascent trajectories with variation in the mass of the SPARTAN.

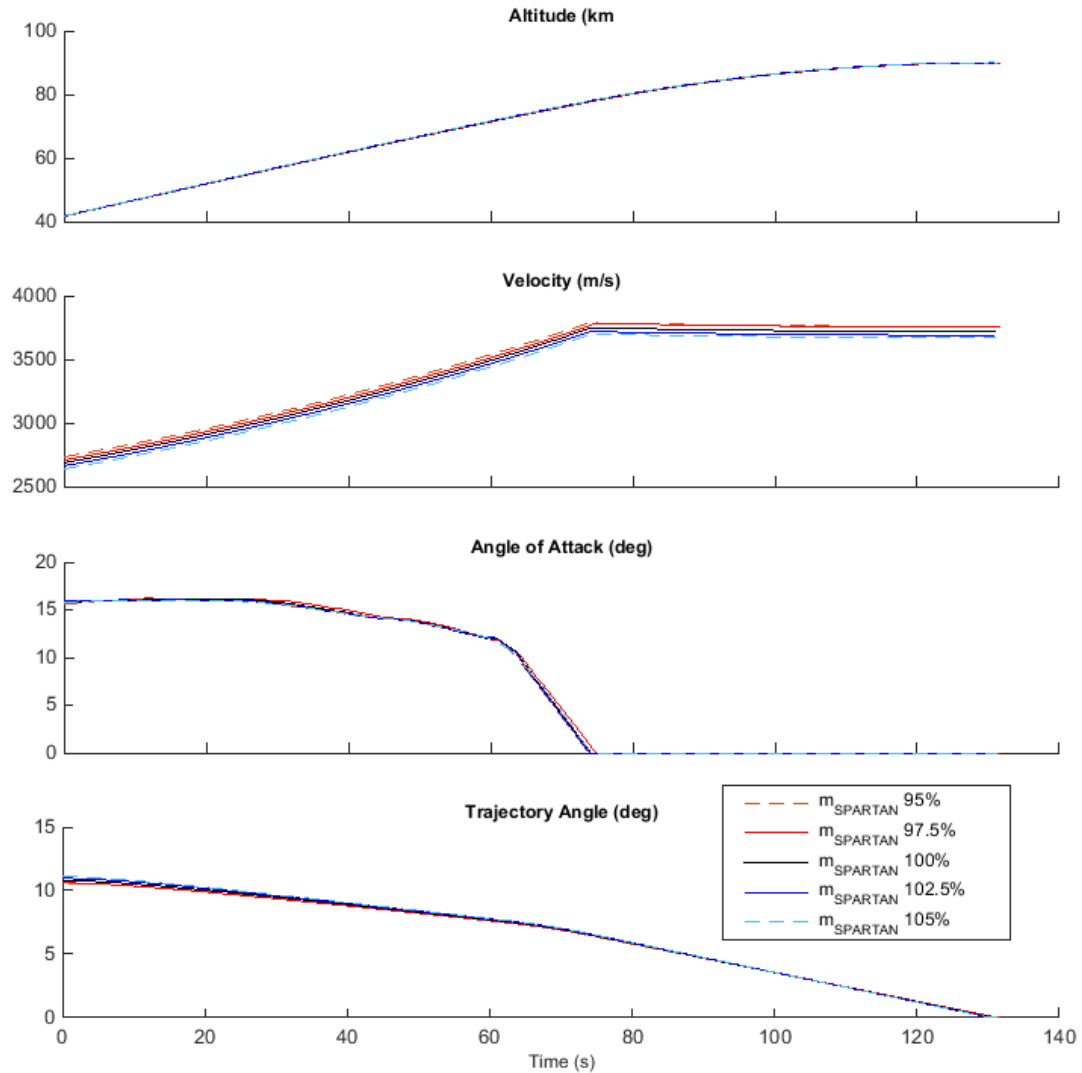


Figure D.8: Comparison of third stage rocket ascent trajectories with variation in the mass of the SPARTAN.

D.1.5 Case 7: SPARTAN Fuel Mass Sensitivity Comparison

APPENDIX D. TRAJECTORY PLOT COMPARISONS

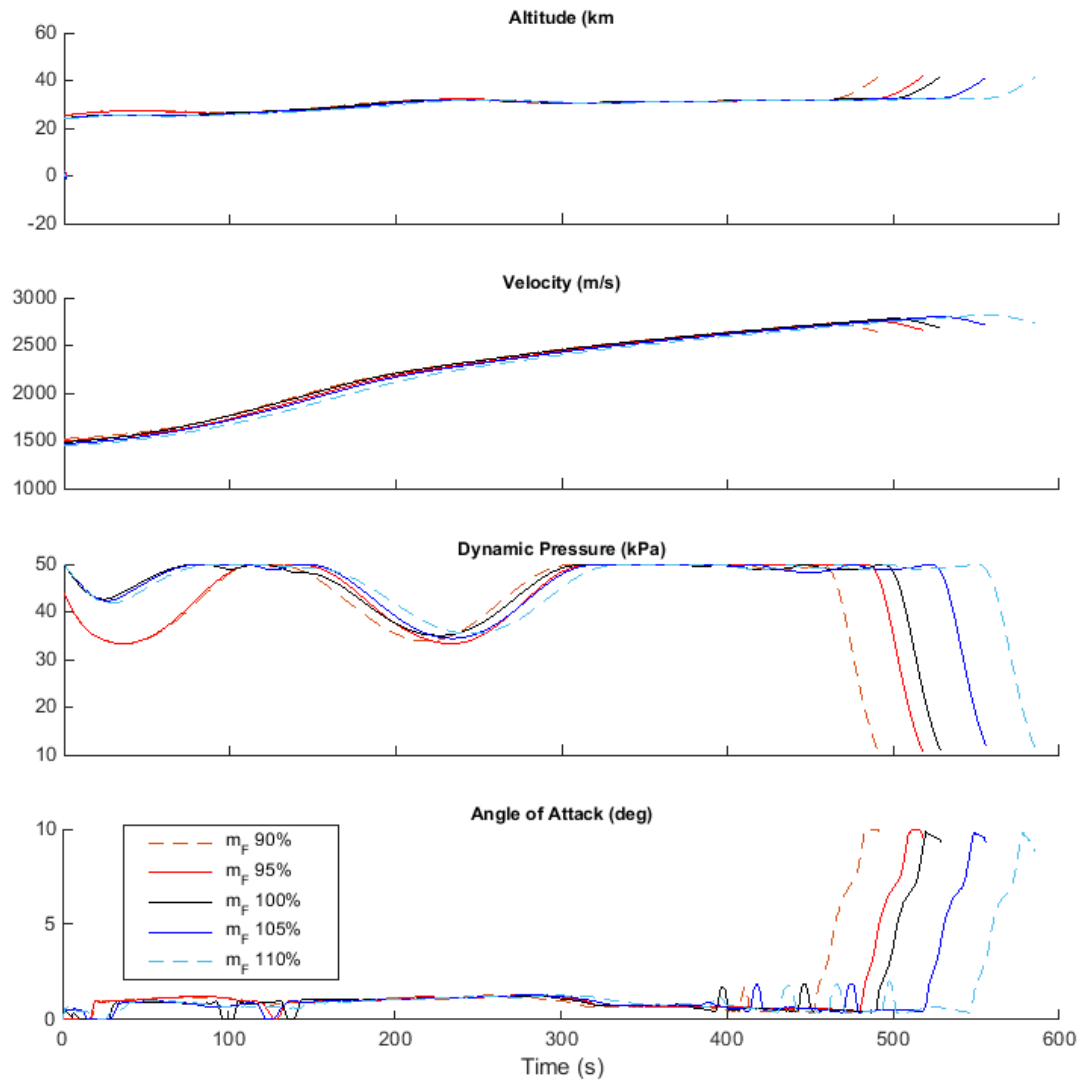


Figure D.9: Comparison of SPARTAN ascent trajectories with variation in the fuel mass of the SPARTAN.

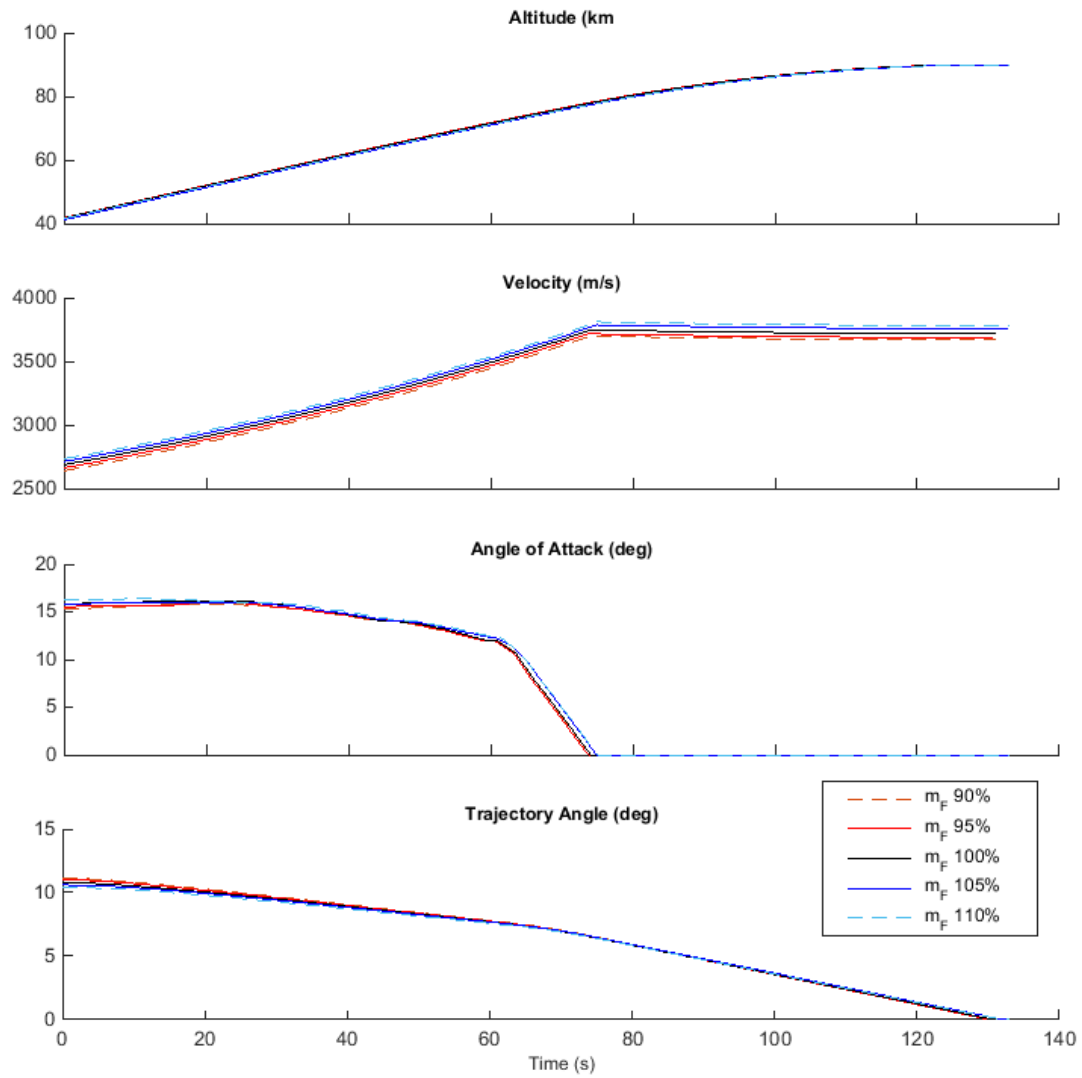


Figure D.10: Comparison of third stage rocket ascent trajectories with variation in the fuel mass of the SPARTAN.

D.1.6 Case 8: Third Stage Mass Sensitivity Comparison

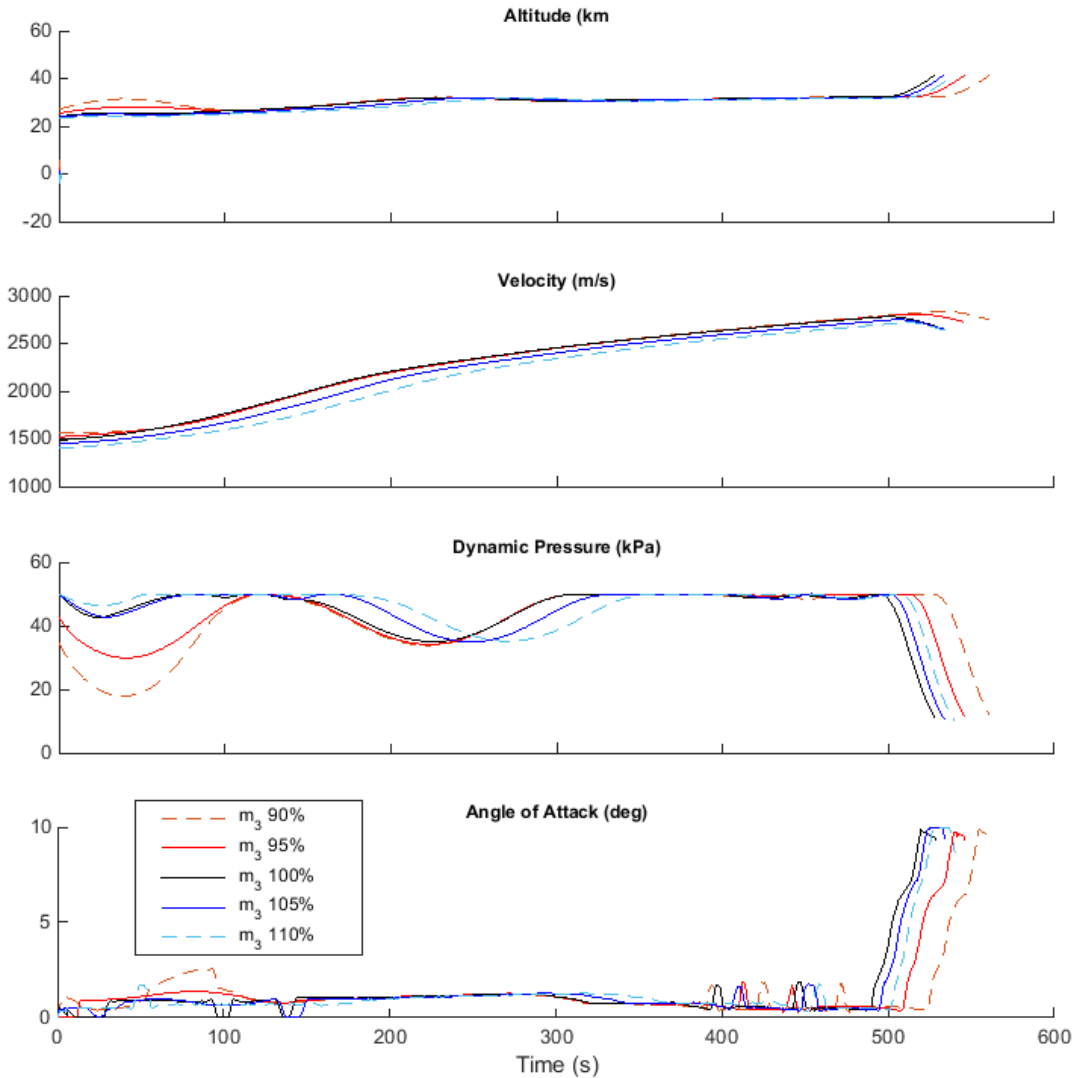


Figure D.11: Comparison of SPARTAN ascent trajectories with variation in the mass of the third stage.

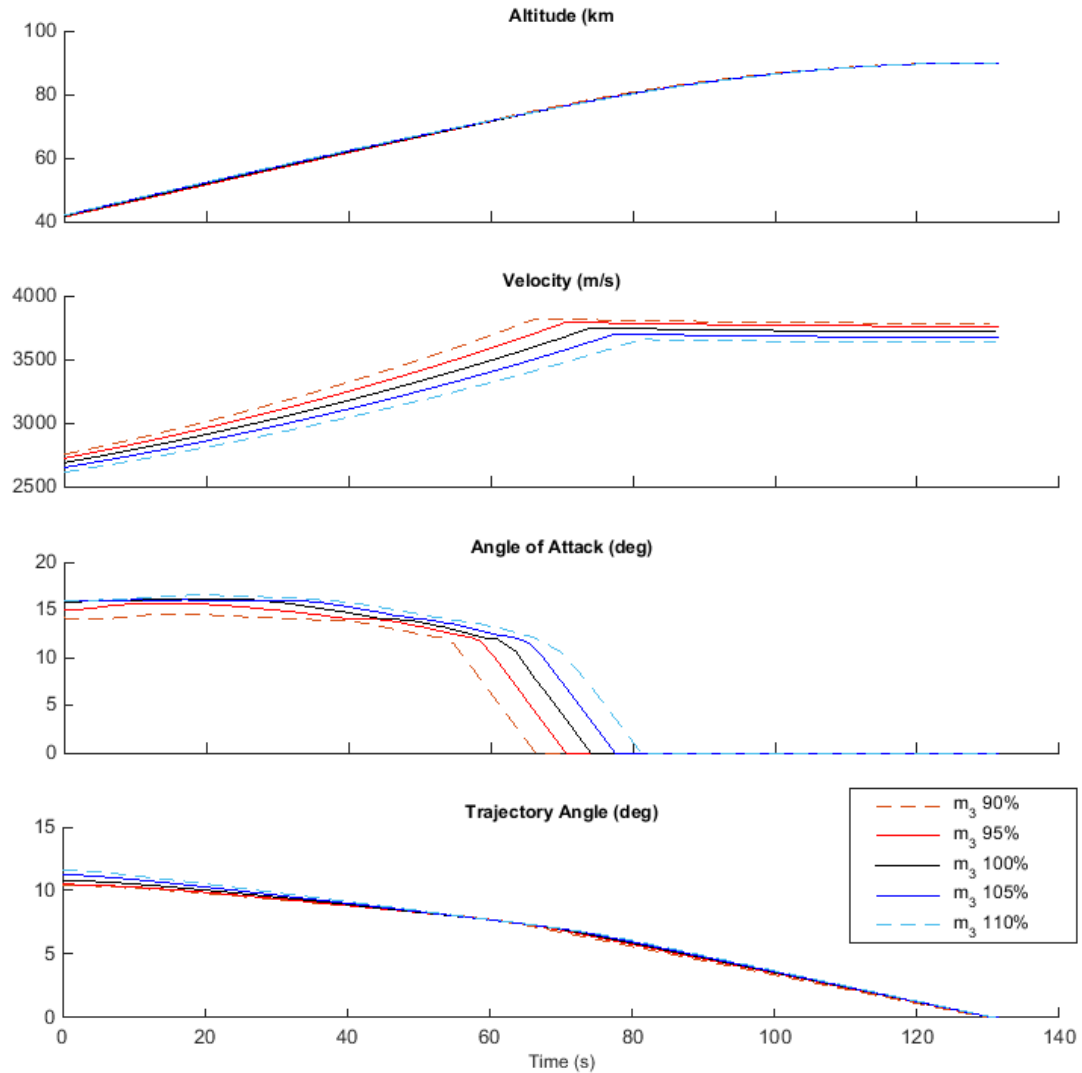


Figure D.12: Comparison of third stage rocket ascent trajectories with variation in the mass of the third stage.

D.1.7 Case 9: Third Stage Specific Impulse Sensitivity Comparison

APPENDIX D. TRAJECTORY PLOT COMPARISONS

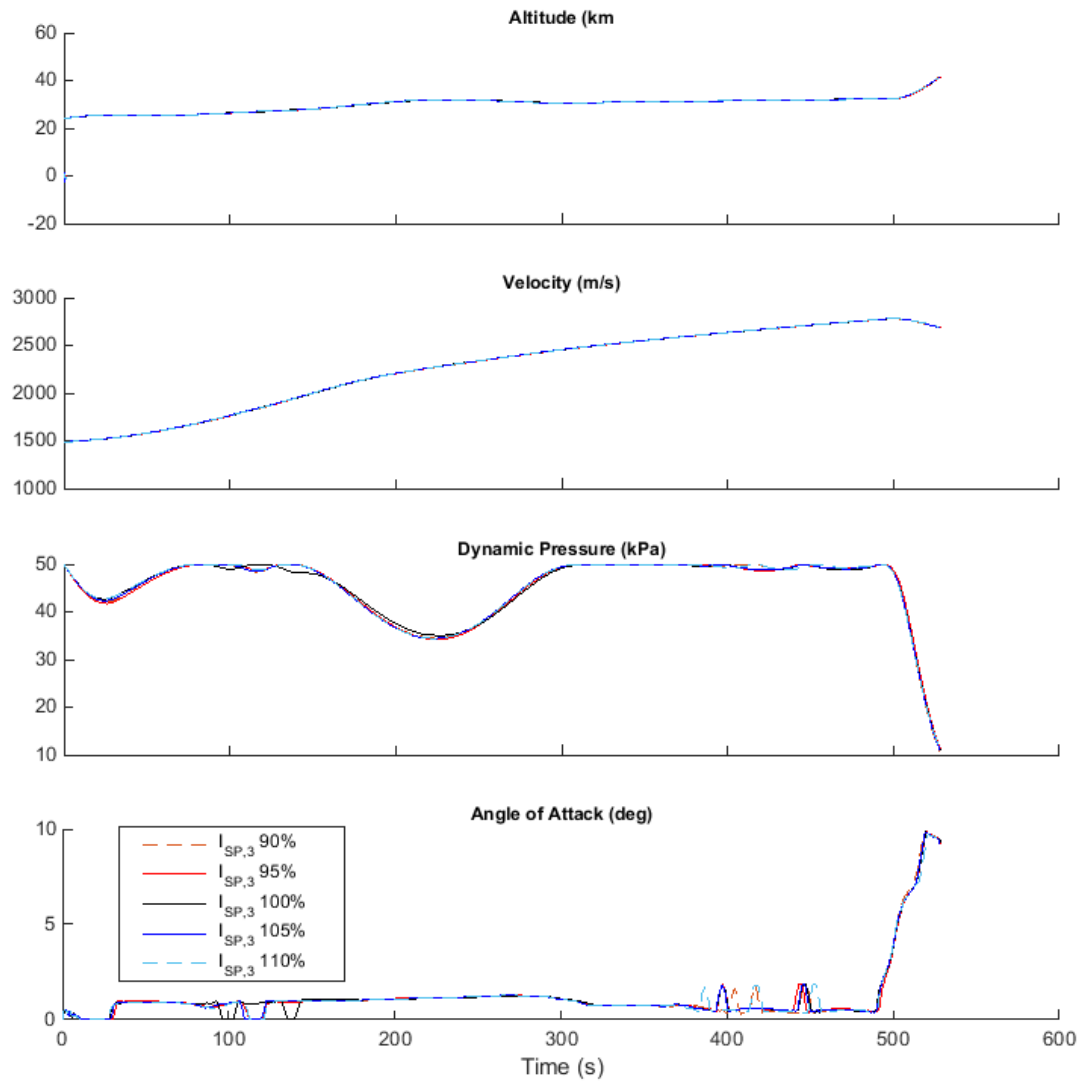


Figure D.13: Comparison of SPARTAN ascent trajectories with variation in the specific impulse of the third stage.

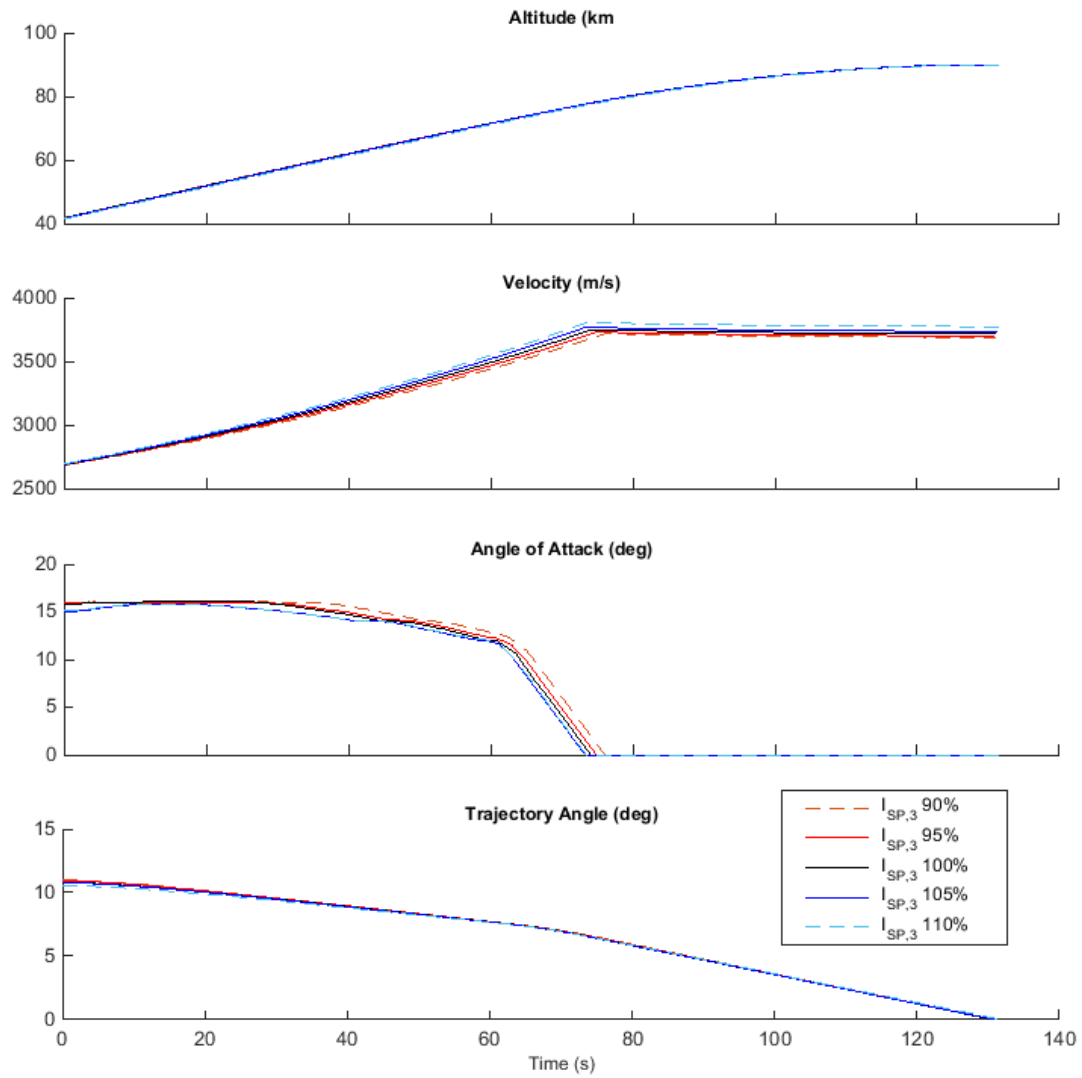


Figure D.14: Comparison of third stage rocket ascent trajectories with variation in the specific impulse of the third stage.

D.1.8 Case 10: Third Stage Drag Sensitivity Comparison

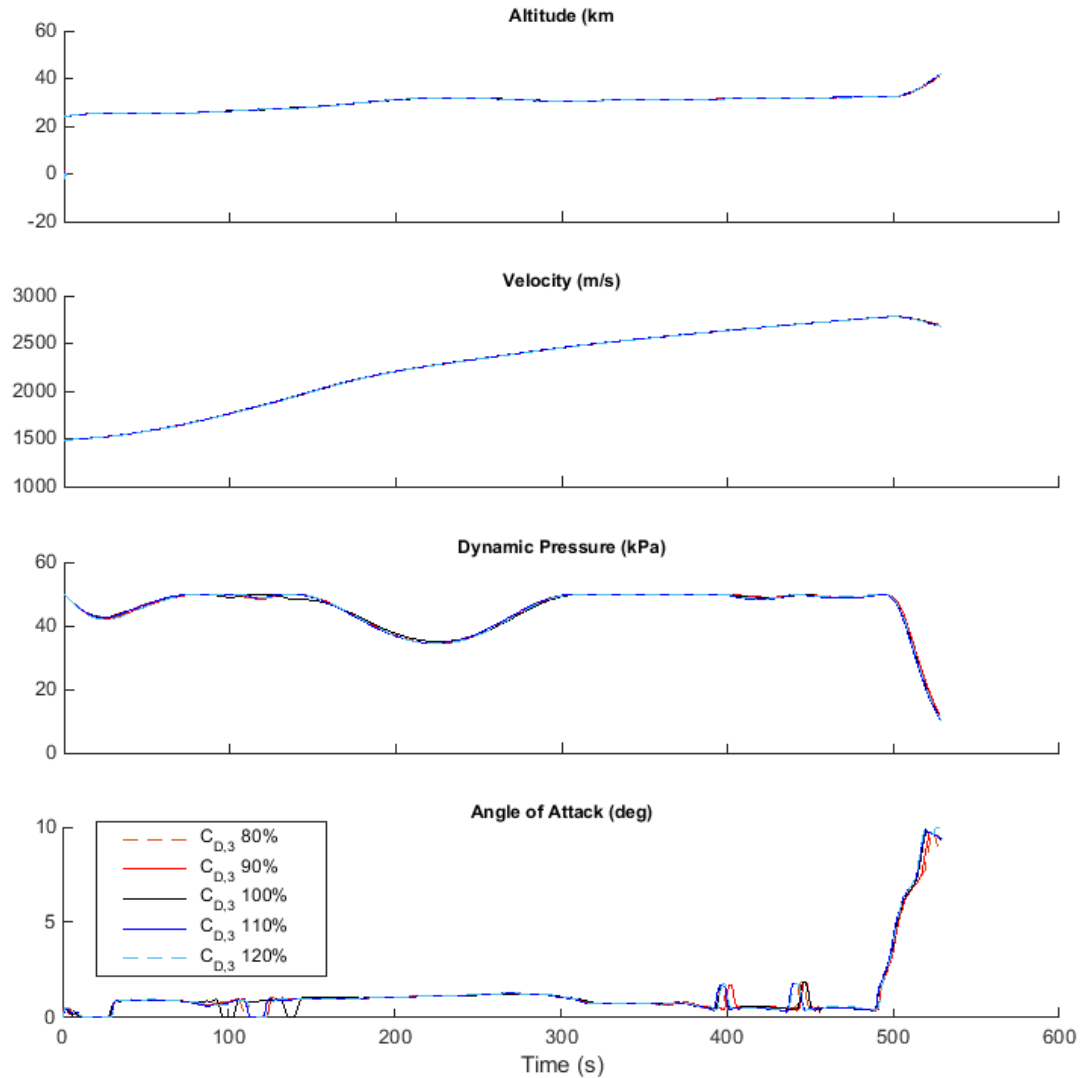


Figure D.15: Comparison of SPARTAN ascent trajectories with variation in the drag of the third stage.

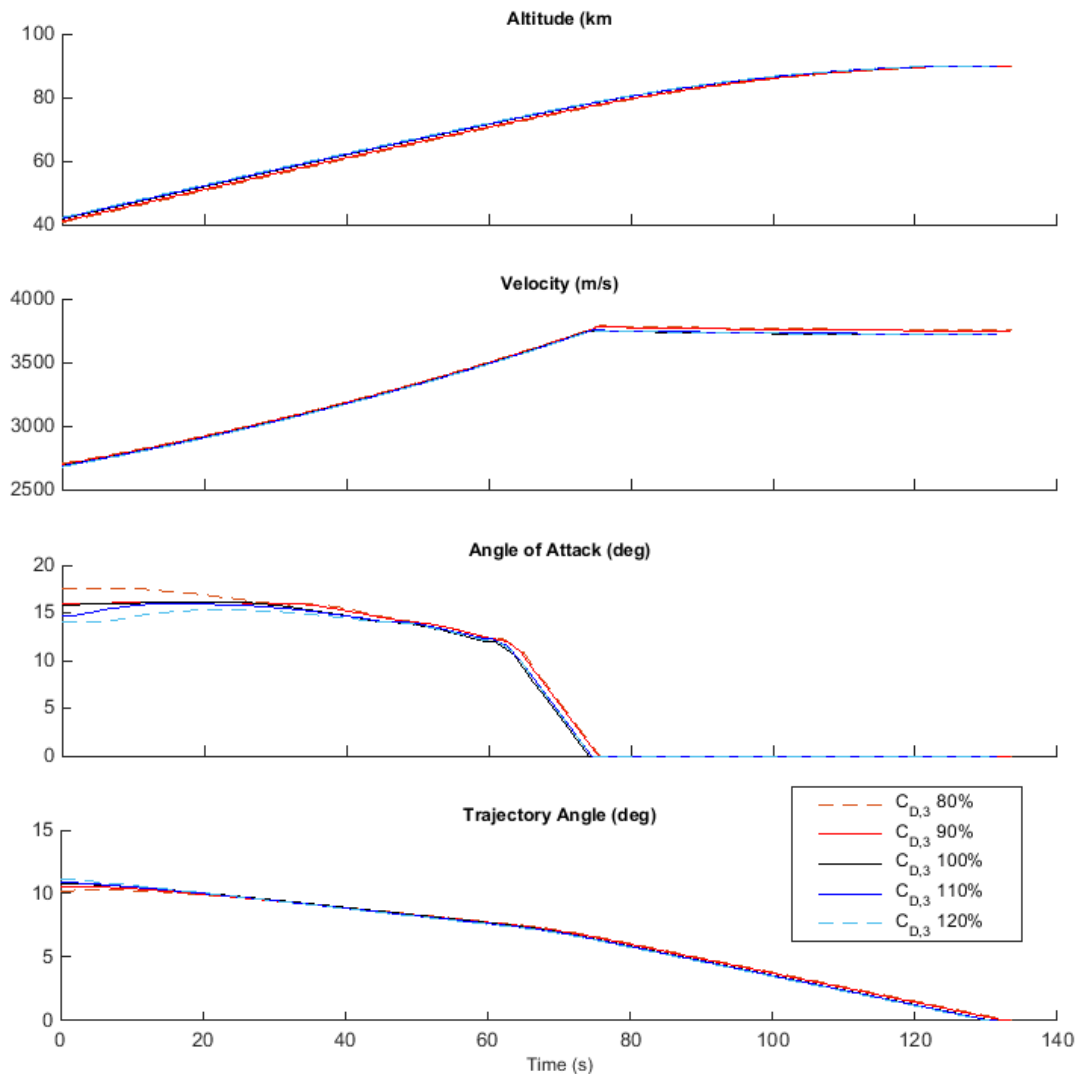


Figure D.16: Comparison of third stage rocket ascent trajectories with variation in the drag of the third stage.

D.2 Optimised Ascent Trajectory Comparisons With Fly-Back

D.2.1 Case 12: Dynamic Pressure Sensitivity Comparison

APPENDIX D. TRAJECTORY PLOT COMPARISONS

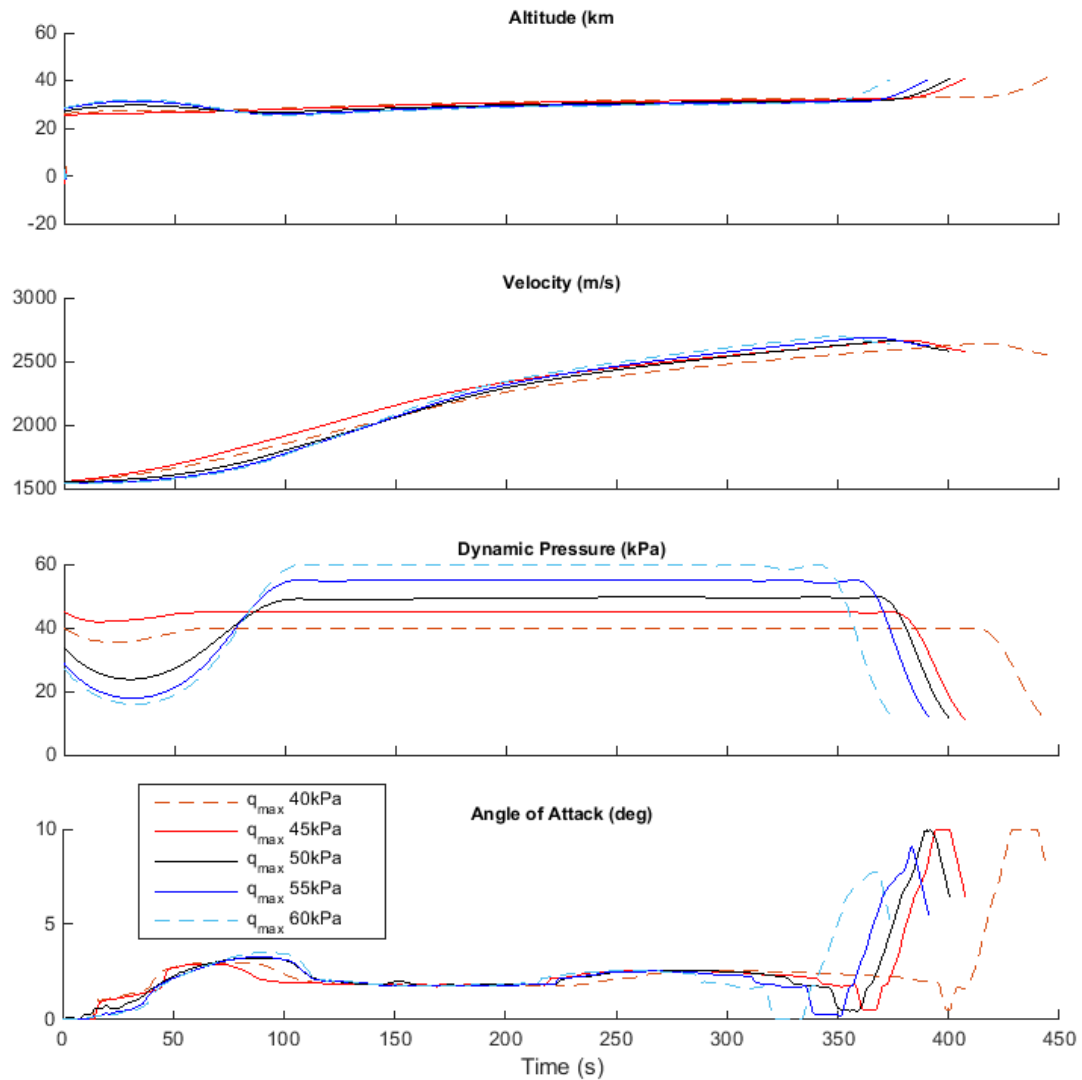


Figure D.17: Comparison of SPARTAN ascent trajectories with variation in the maximum dynamic pressure of the SPARTAN.

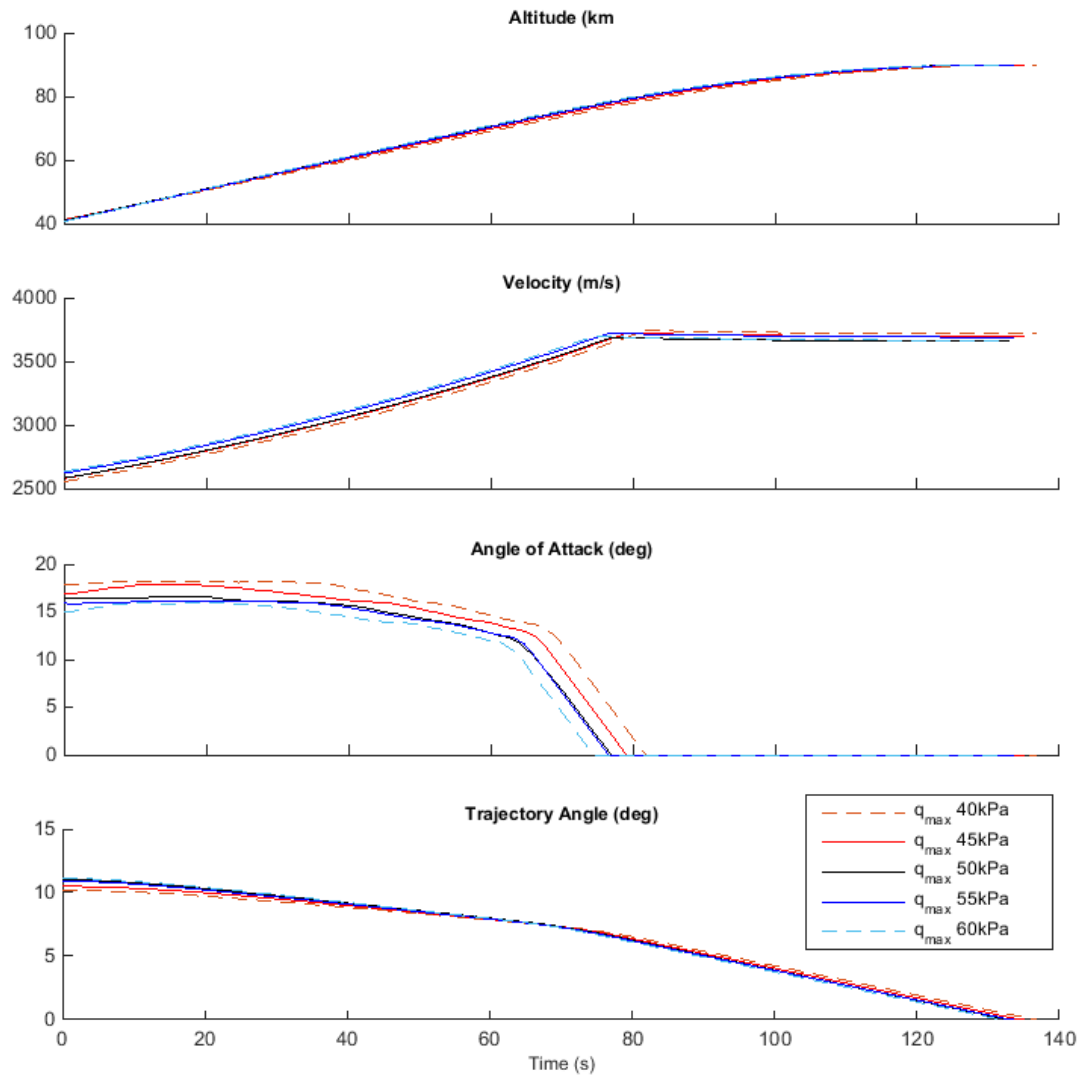


Figure D.18: Comparison of third stage rocket ascent trajectories with variation in the maximum dynamic pressure of the SPARTAN.

APPENDIX D. TRAJECTORY PLOT COMPARISONS

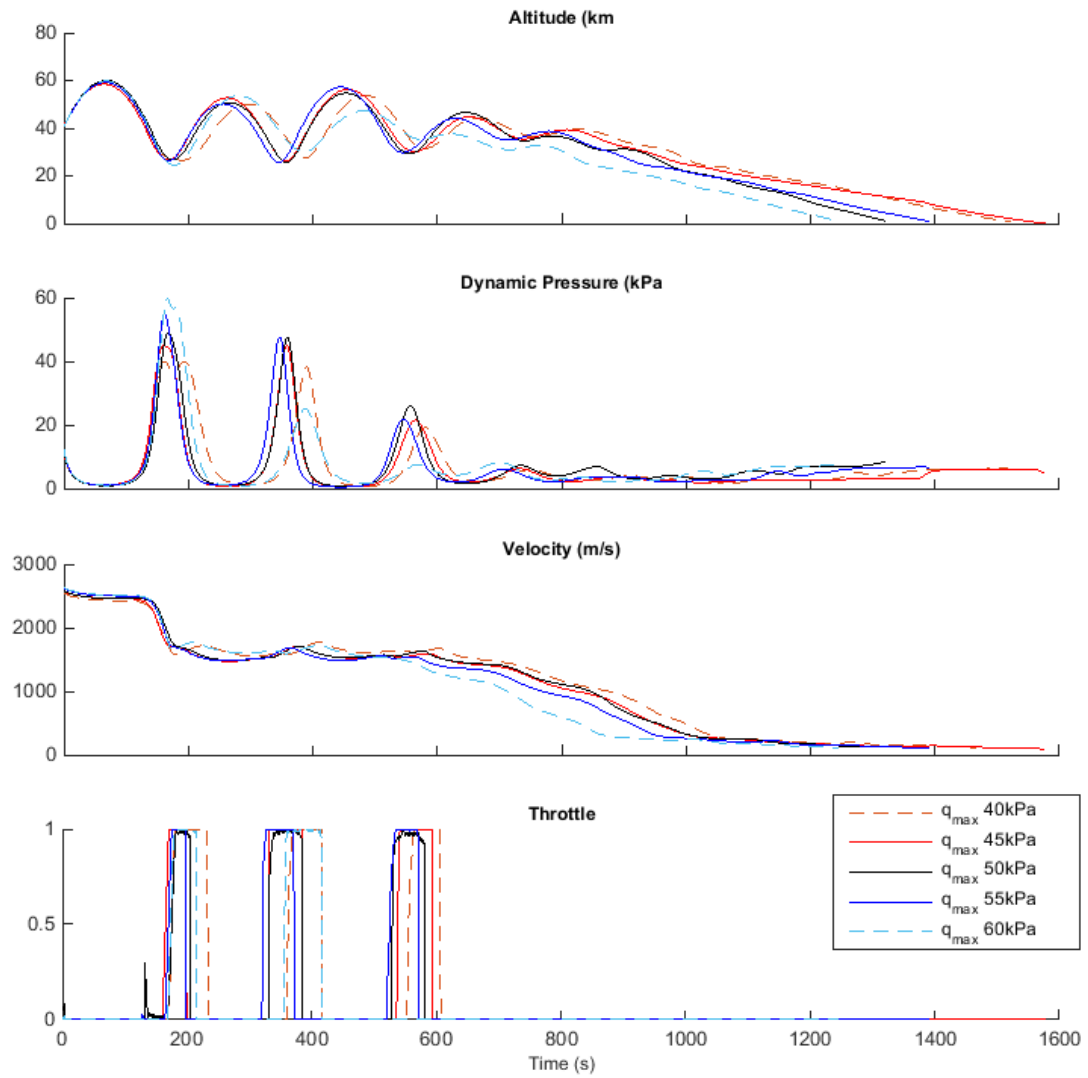


Figure D.19: Comparison of SPARTAN return trajectories with variation in the maximum dynamic pressure of the SPARTAN.

D.2.2 Case 13: SPARTAN Drag Sensitivity Comparison

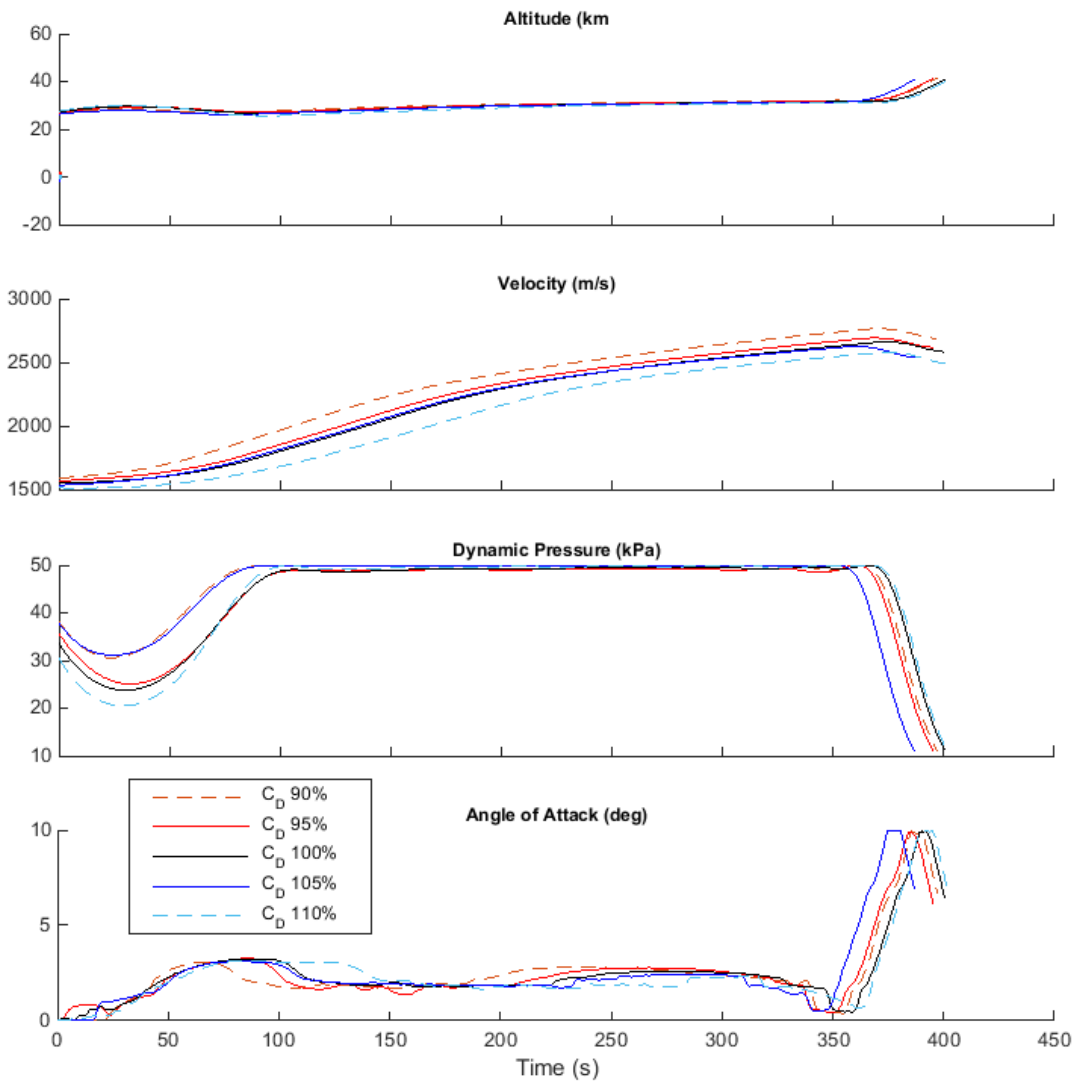


Figure D.20: Comparison of SPARTAN ascent trajectories with variation in the drag of the SPARTAN.

APPENDIX D. TRAJECTORY PLOT COMPARISONS

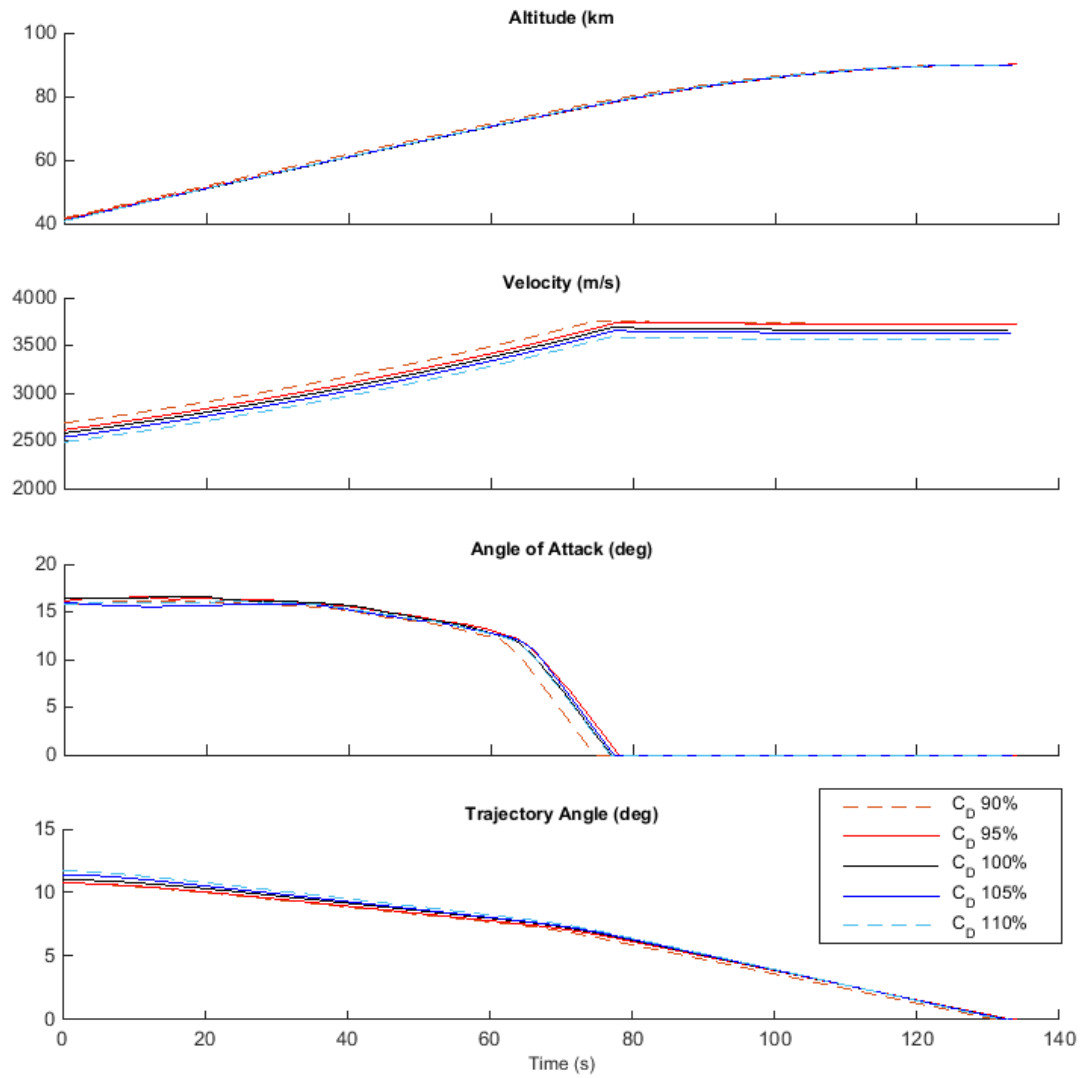


Figure D.21: Comparison of third stage rocket ascent trajectories with variation in the drag of the SPARTAN.

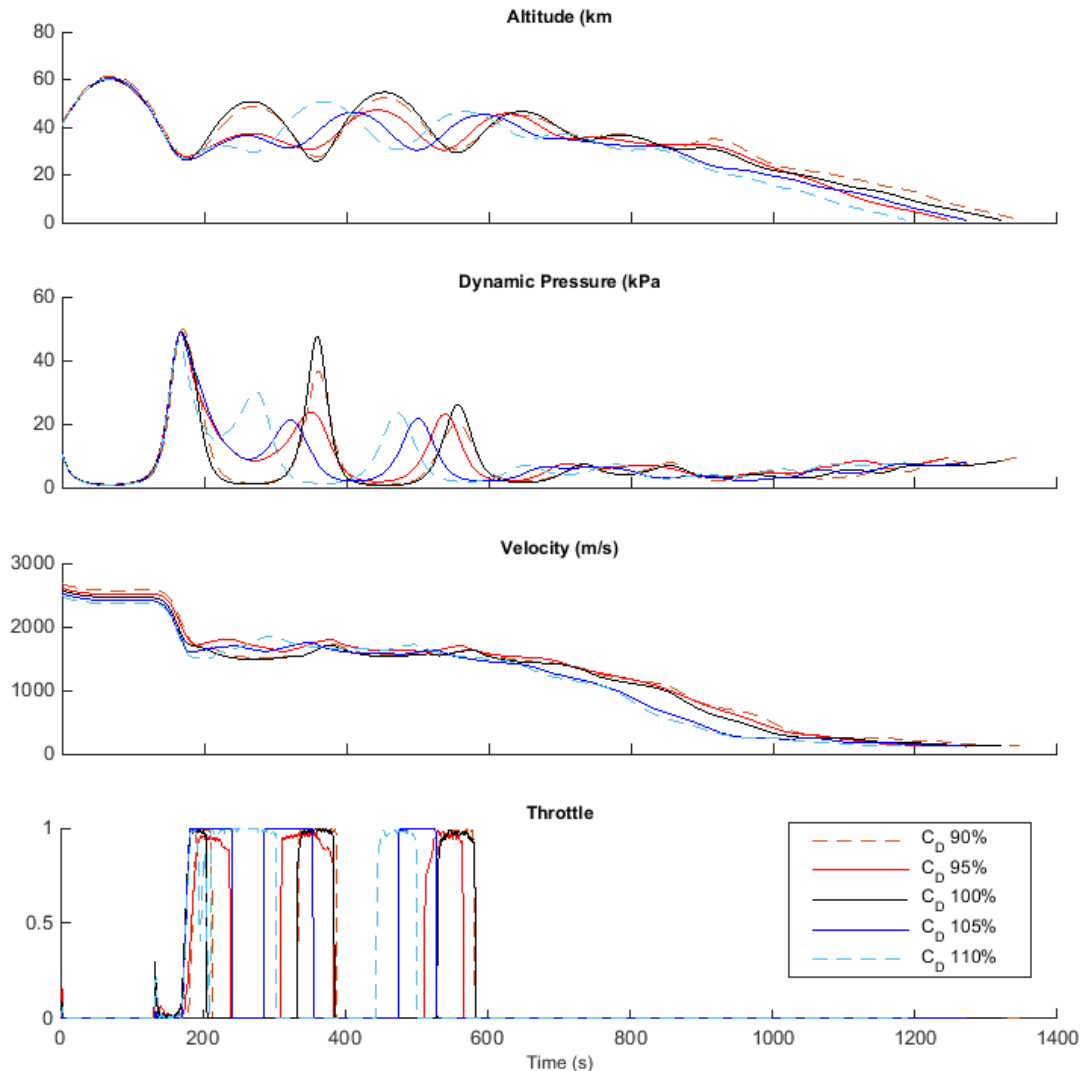


Figure D.22: Comparison of SPARTAN return trajectories with variation in the drag of the SPARTAN.

D.2.3 Case 14:SPARTAN Specific Impulse Sensitivity Comparison

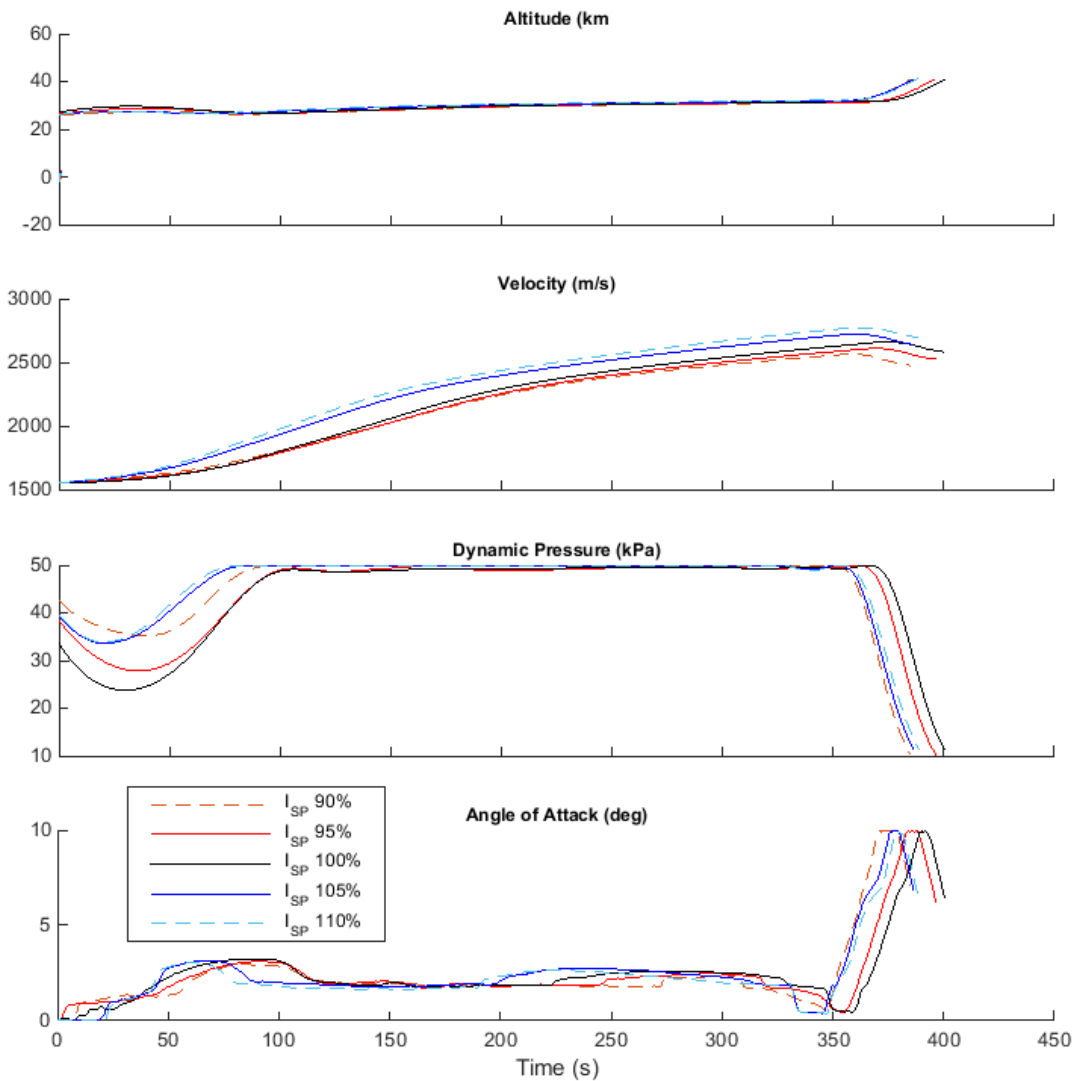


Figure D.23: Comparison of SPARTAN ascent trajectories with variation in the specific impulse of the SPARTAN.

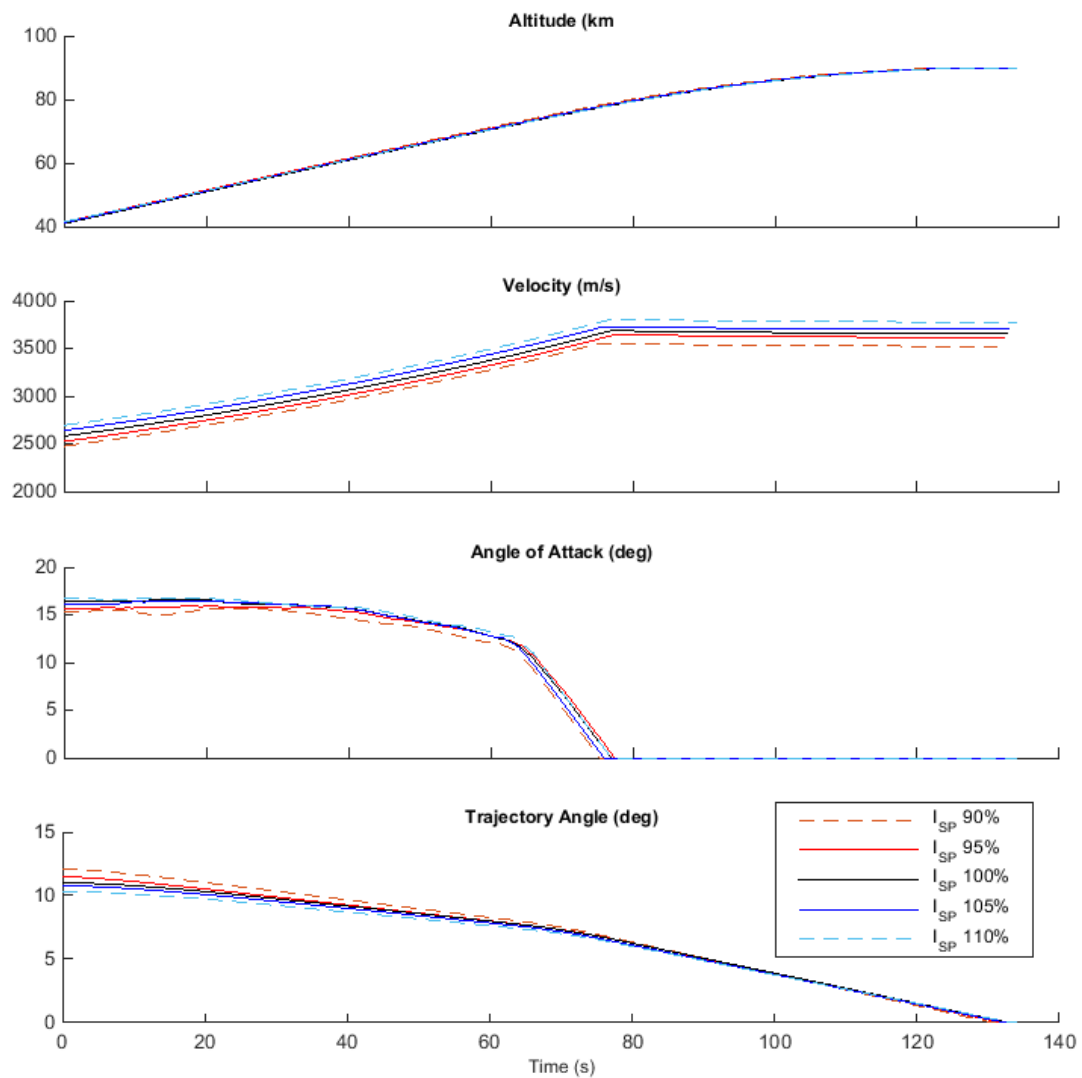


Figure D.24: Comparison of third stage rocket ascent trajectories with variation in the specific impulse of the SPARTAN.

APPENDIX D. TRAJECTORY PLOT COMPARISONS

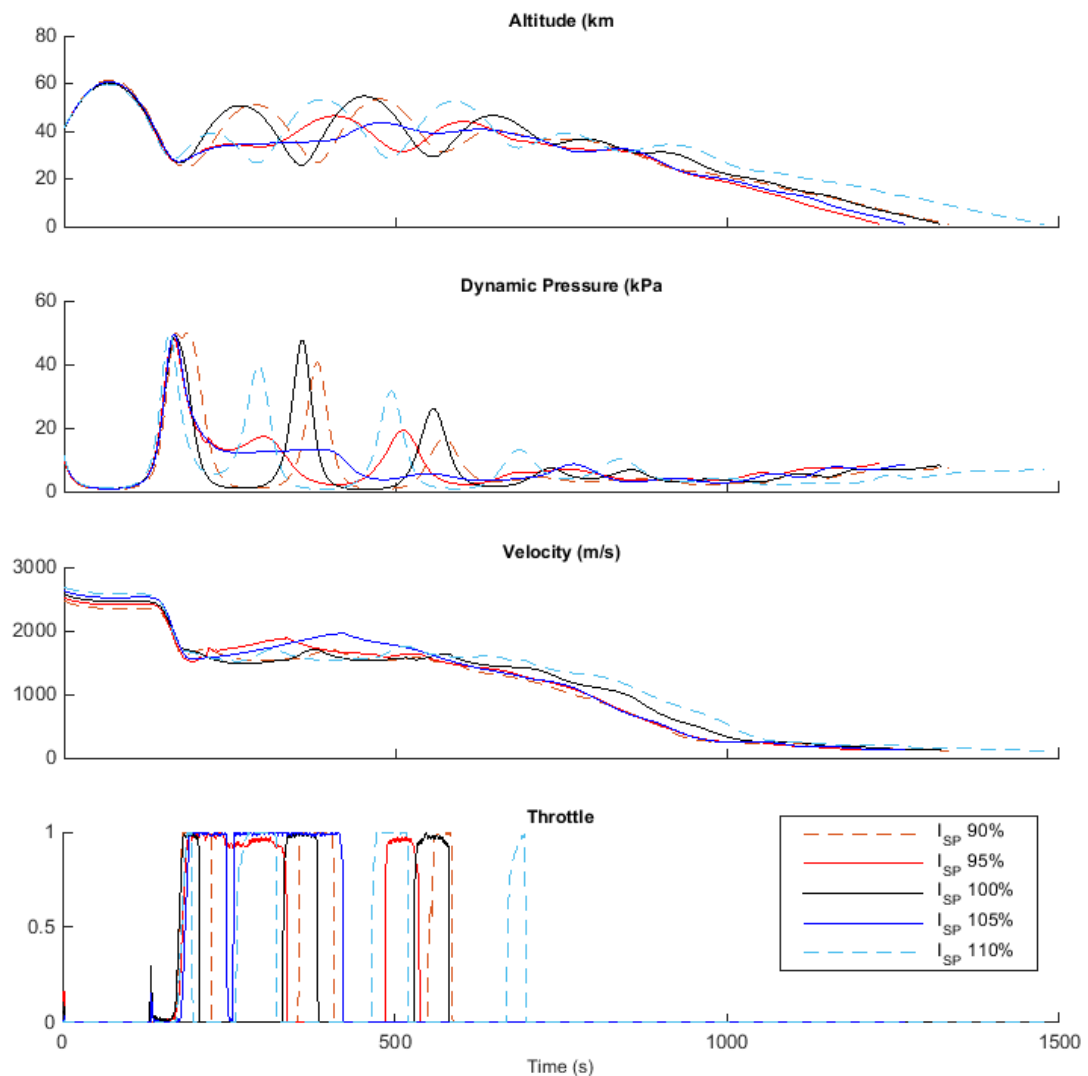


Figure D.25: Comparison of SPARTAN return trajectories with variation in the specific impulse of the SPARTAN.

D.2.4 Case 15: SPARTAN Mass Sensitivity Comparison

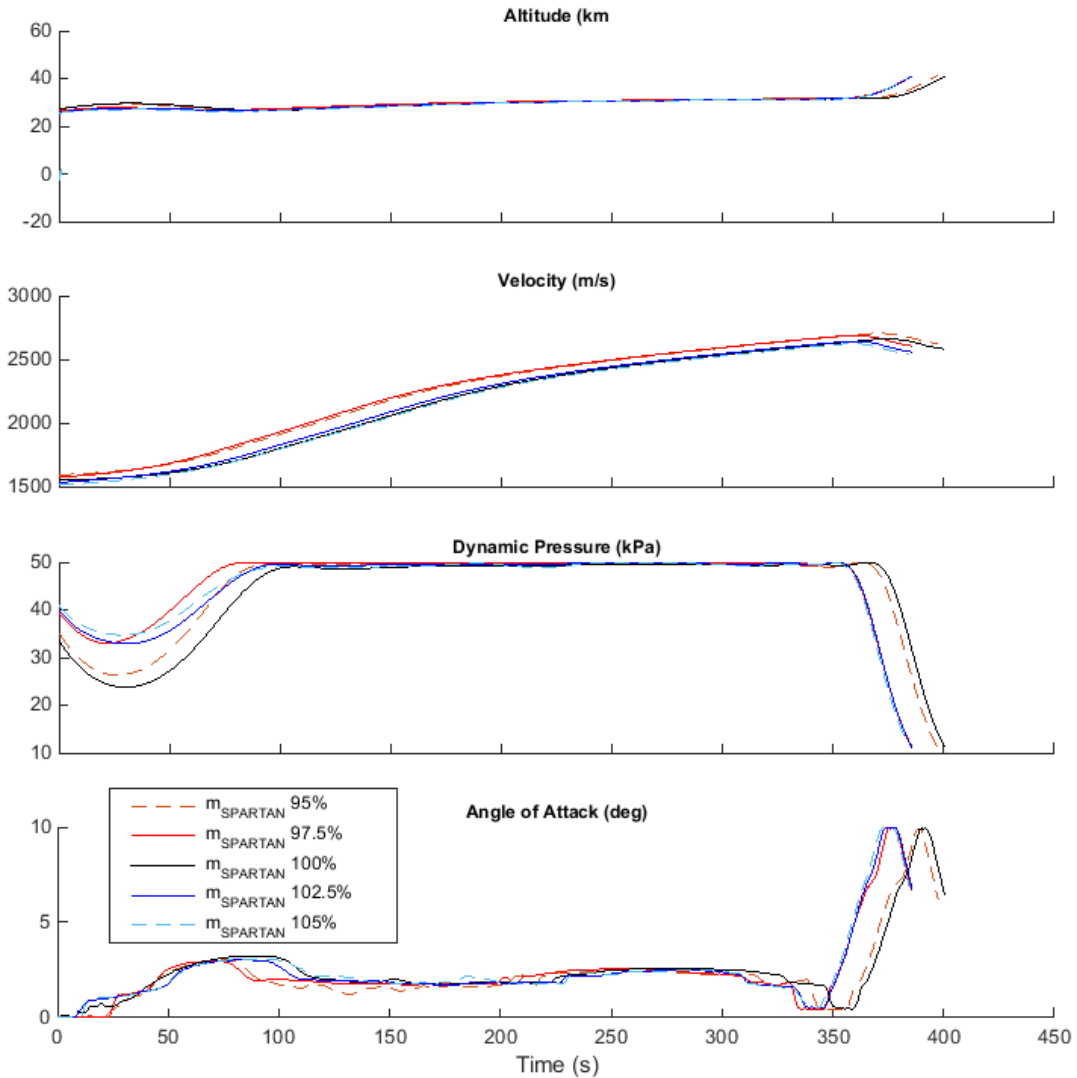


Figure D.26: Comparison of SPARTAN ascent trajectories with variation in the mass of the SPARTAN.

APPENDIX D. TRAJECTORY PLOT COMPARISONS

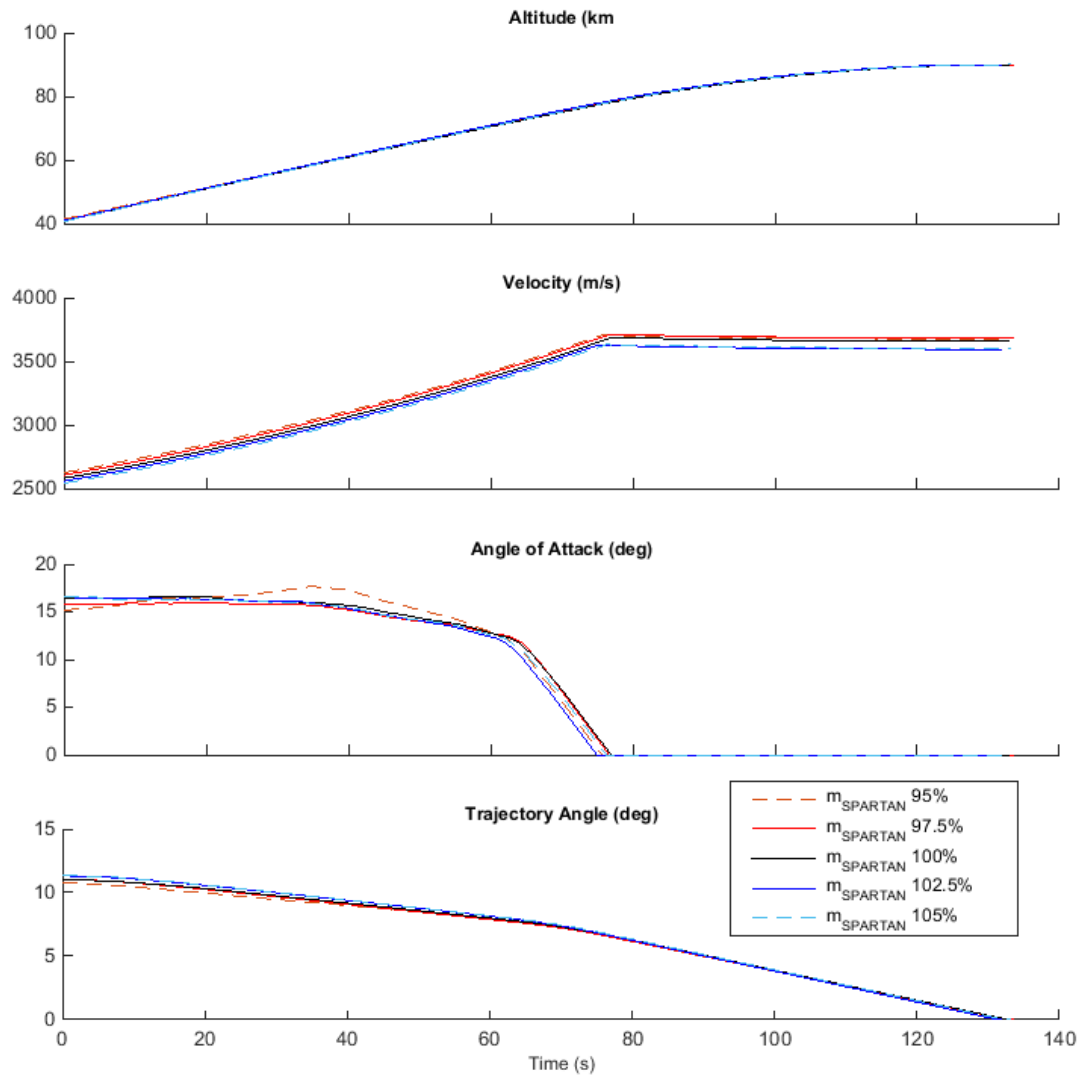


Figure D.27: Comparison of third stage rocket ascent trajectories with variation in the mass of the SPARTAN.

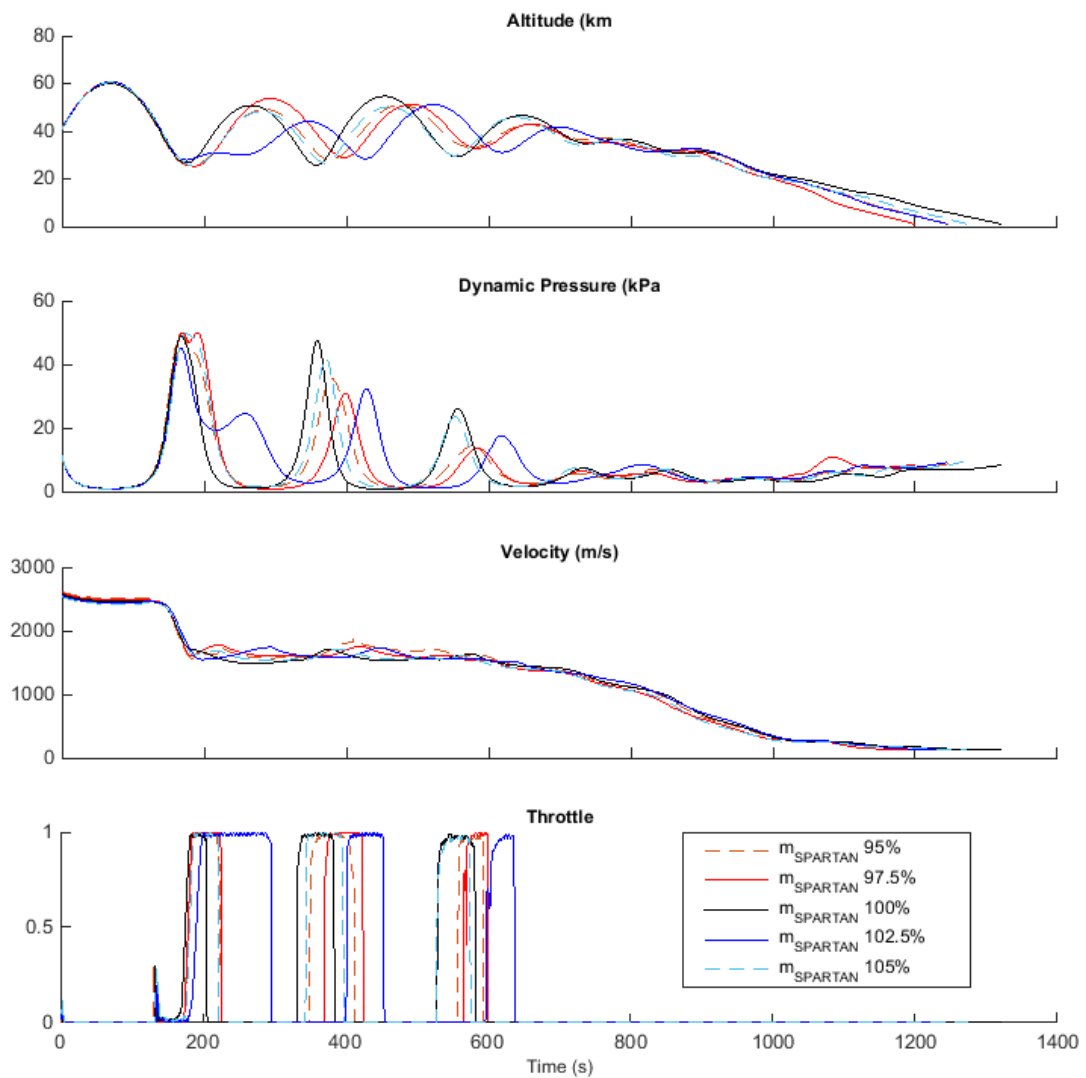


Figure D.28: Comparison of SPARTAN return trajectories with variation in the mass of the SPARTAN.

D.2.5 Case 16: SPARTAN Fuel Mass Sensitivity Comparison

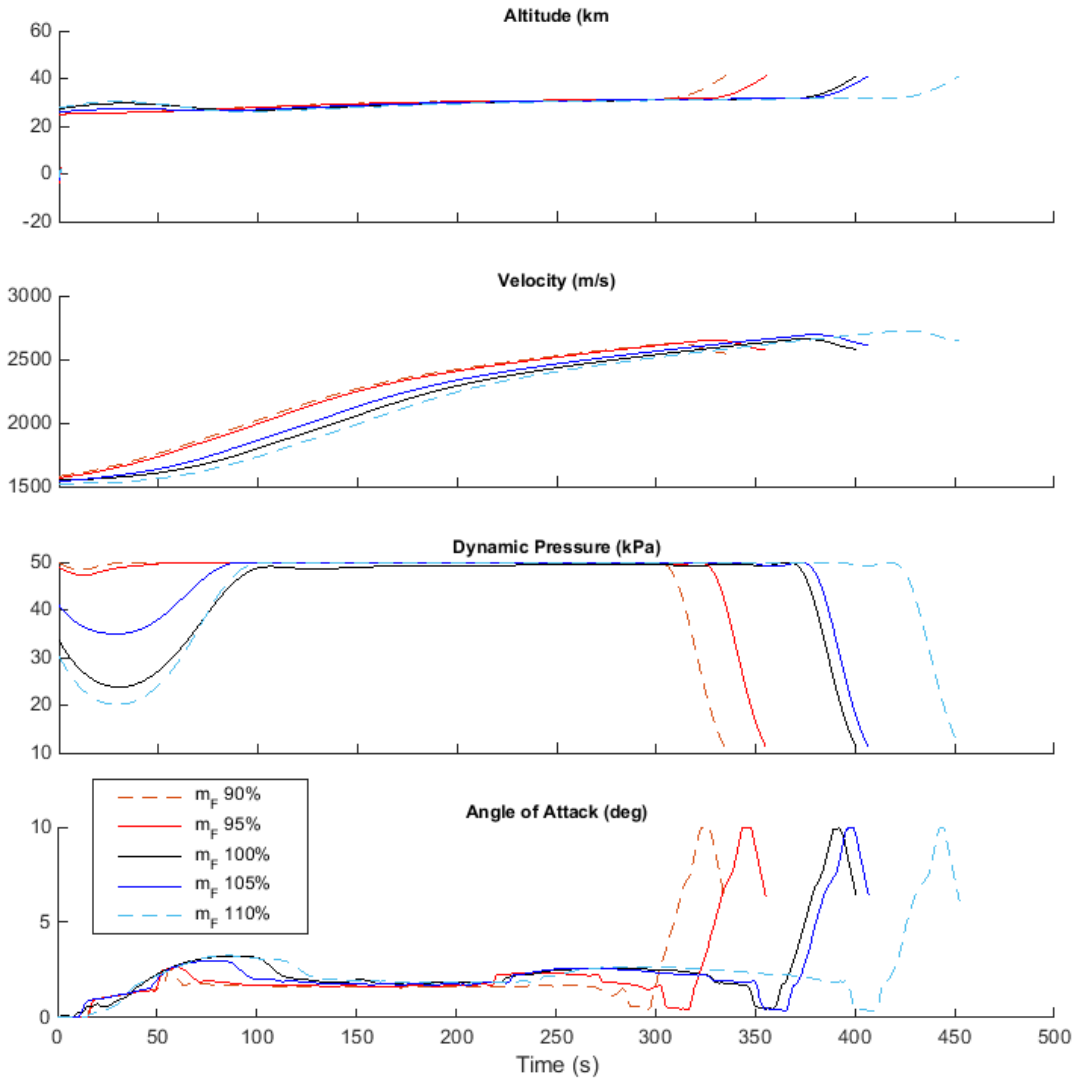


Figure D.29: Comparison of SPARTAN ascent trajectories with variation in the fuel mass of the SPARTAN.

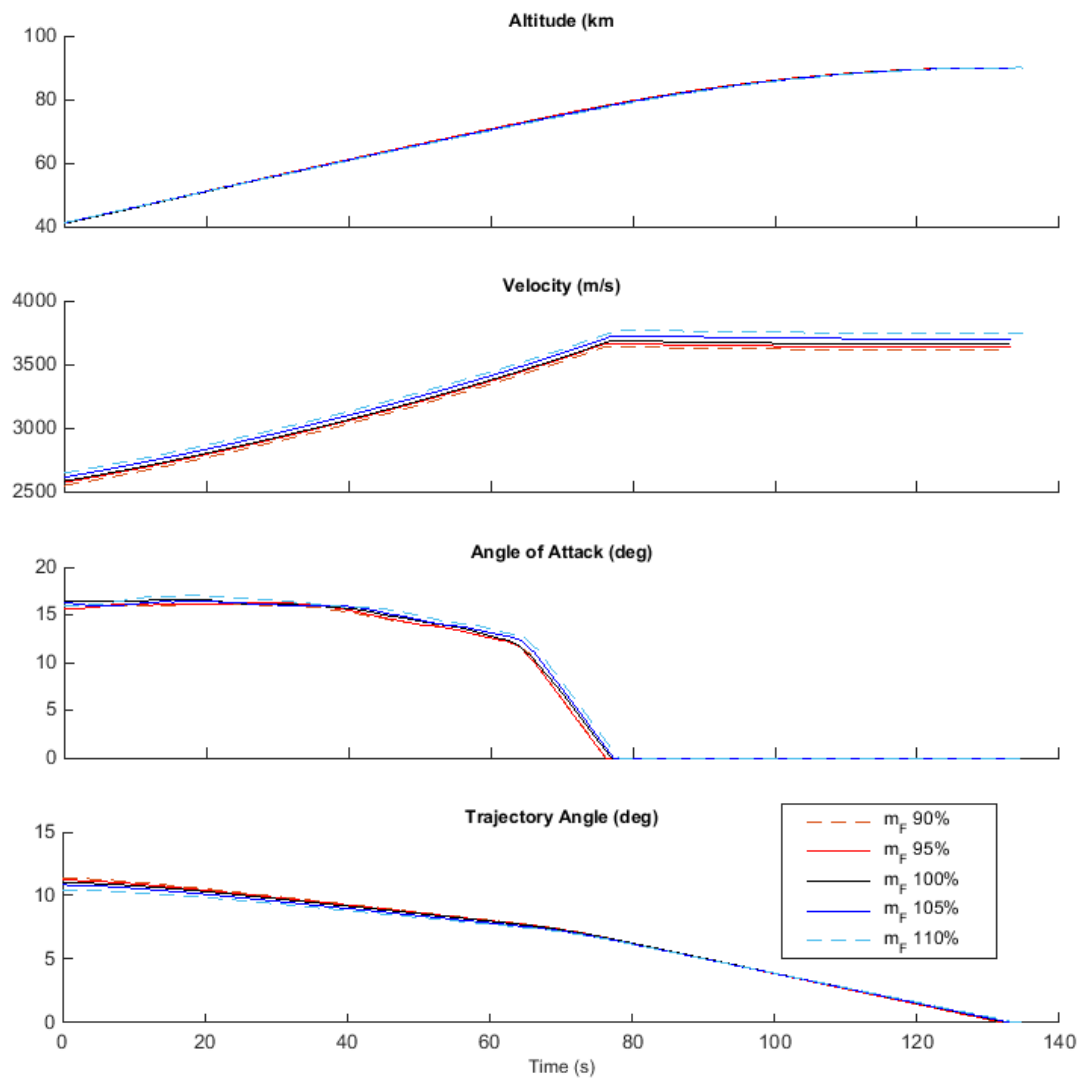


Figure D.30: Comparison of third stage rocket ascent trajectories with variation in the fuel mass of the SPARTAN.

APPENDIX D. TRAJECTORY PLOT COMPARISONS

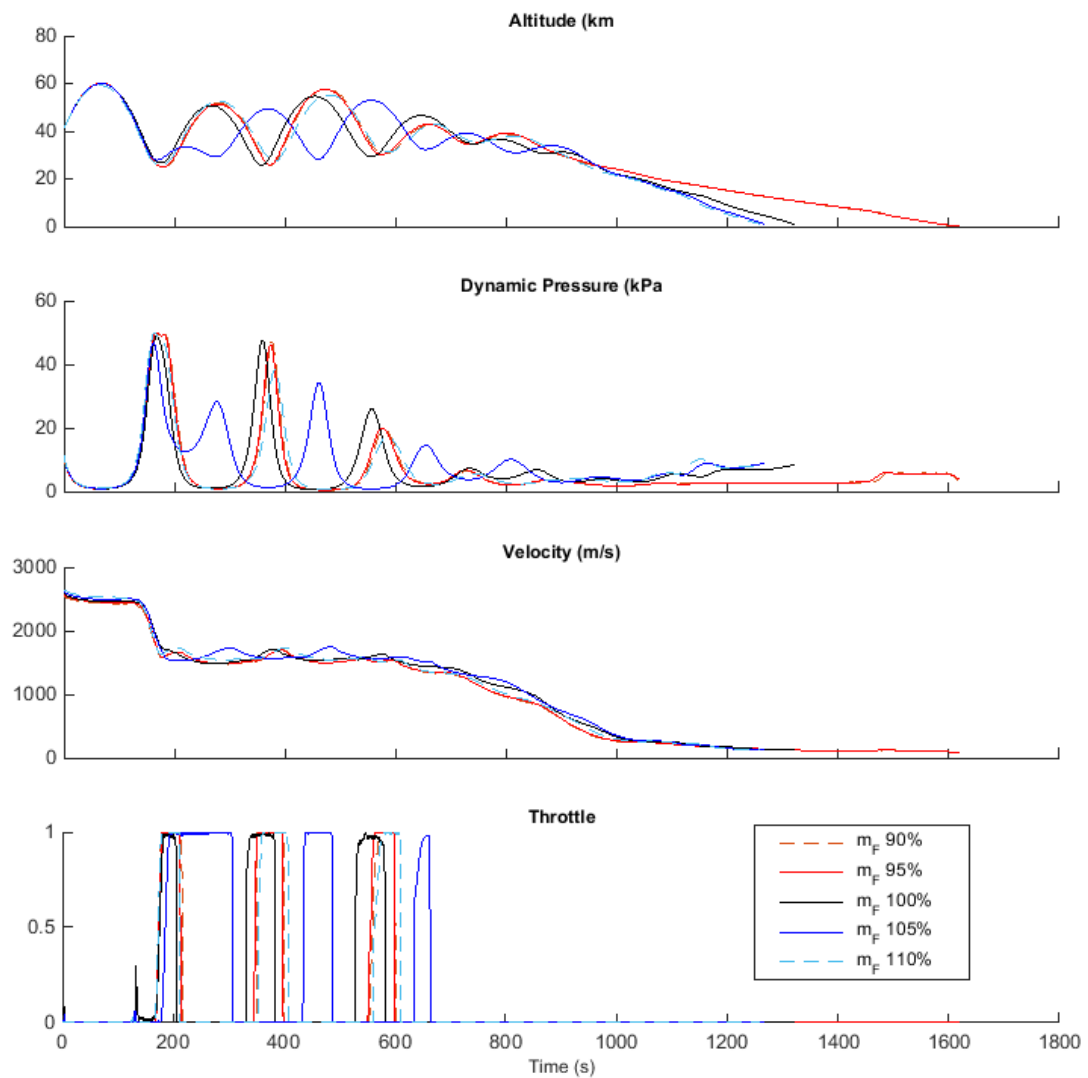


Figure D.31: Comparison of SPARTAN return trajectories with variation in the fuel mass of the SPARTAN.

D.2.6 Case 17: Third Stage Mass Sensitivity Comparison

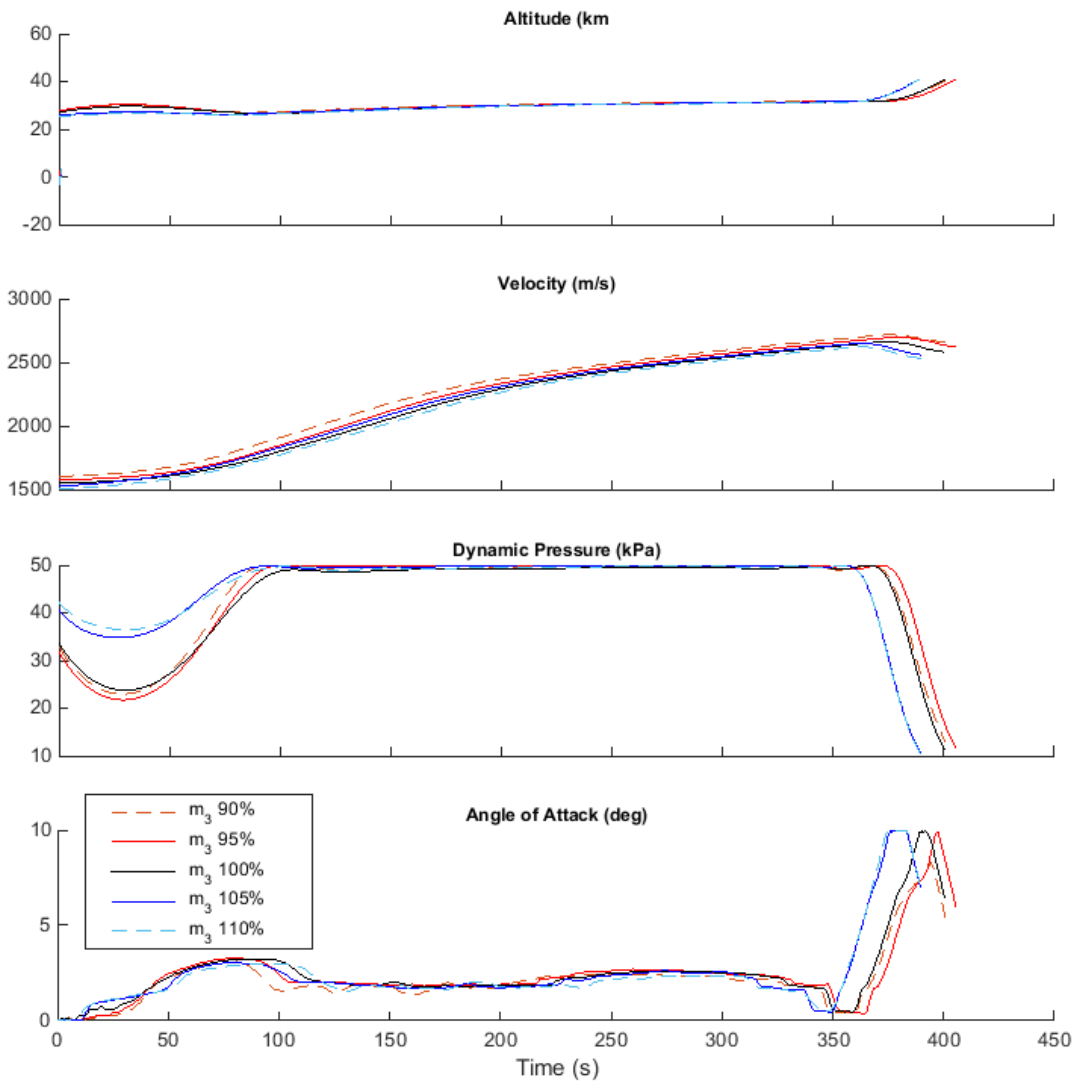


Figure D.32: Comparison of SPARTAN ascent trajectories with variation in the mass of the third stage.

APPENDIX D. TRAJECTORY PLOT COMPARISONS

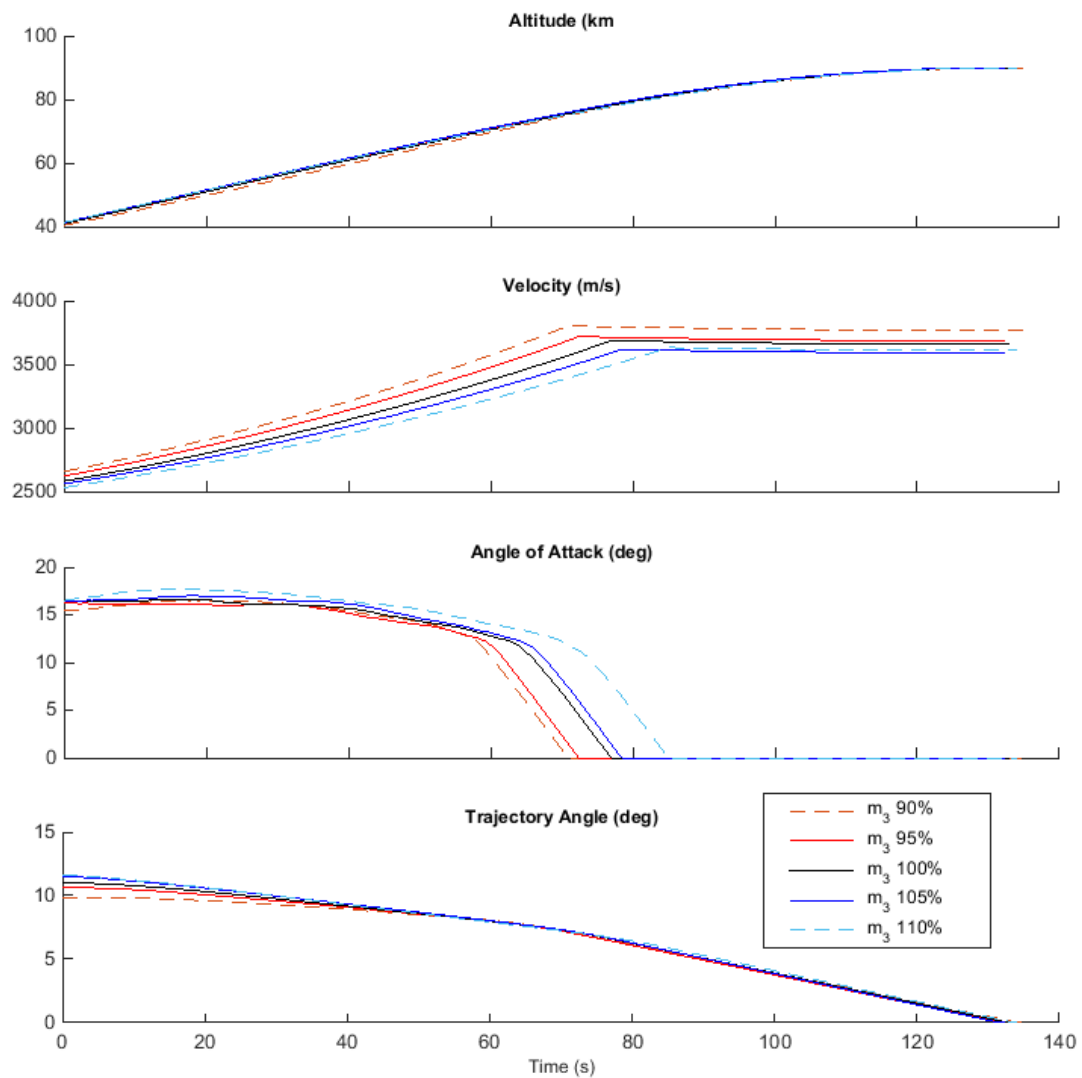


Figure D.33: Comparison of third stage rocket ascent trajectories with variation in the mass of the third stage.

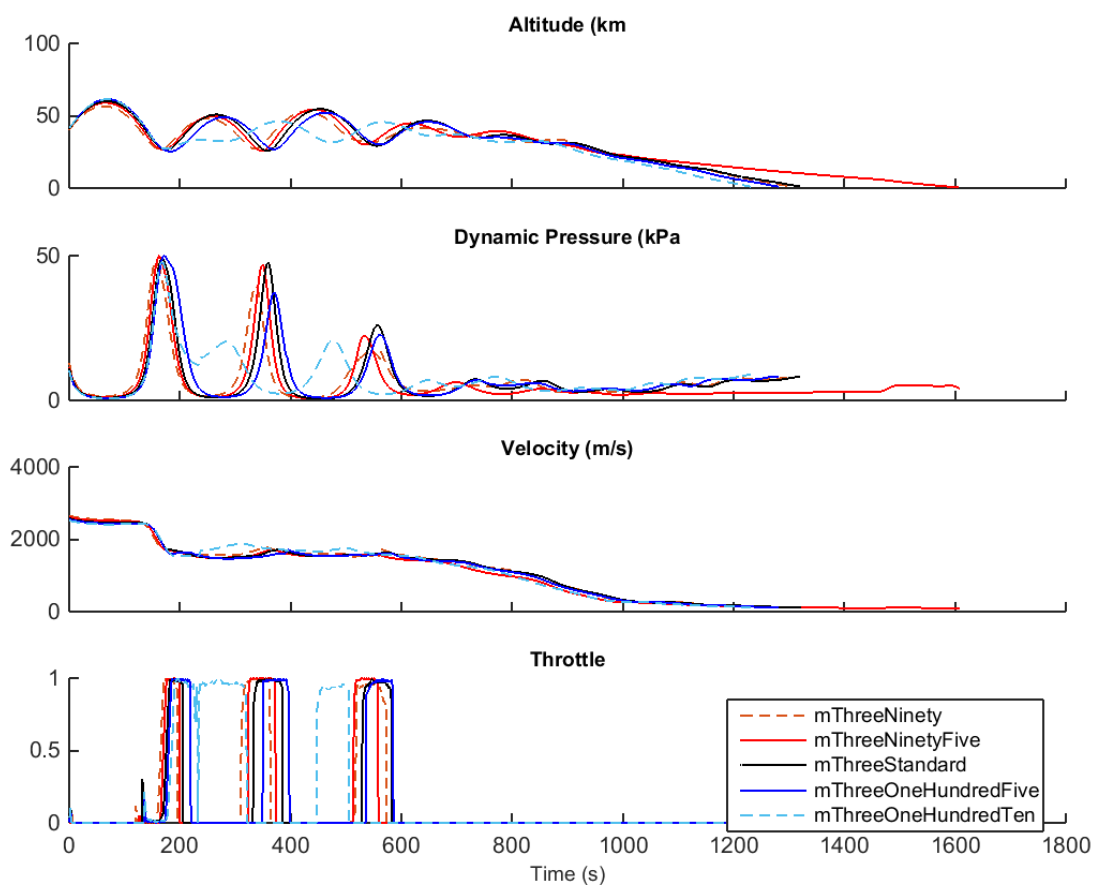


Figure D.34: Comparison of SPARTAN return trajectories with variation in the mass of the third stage.

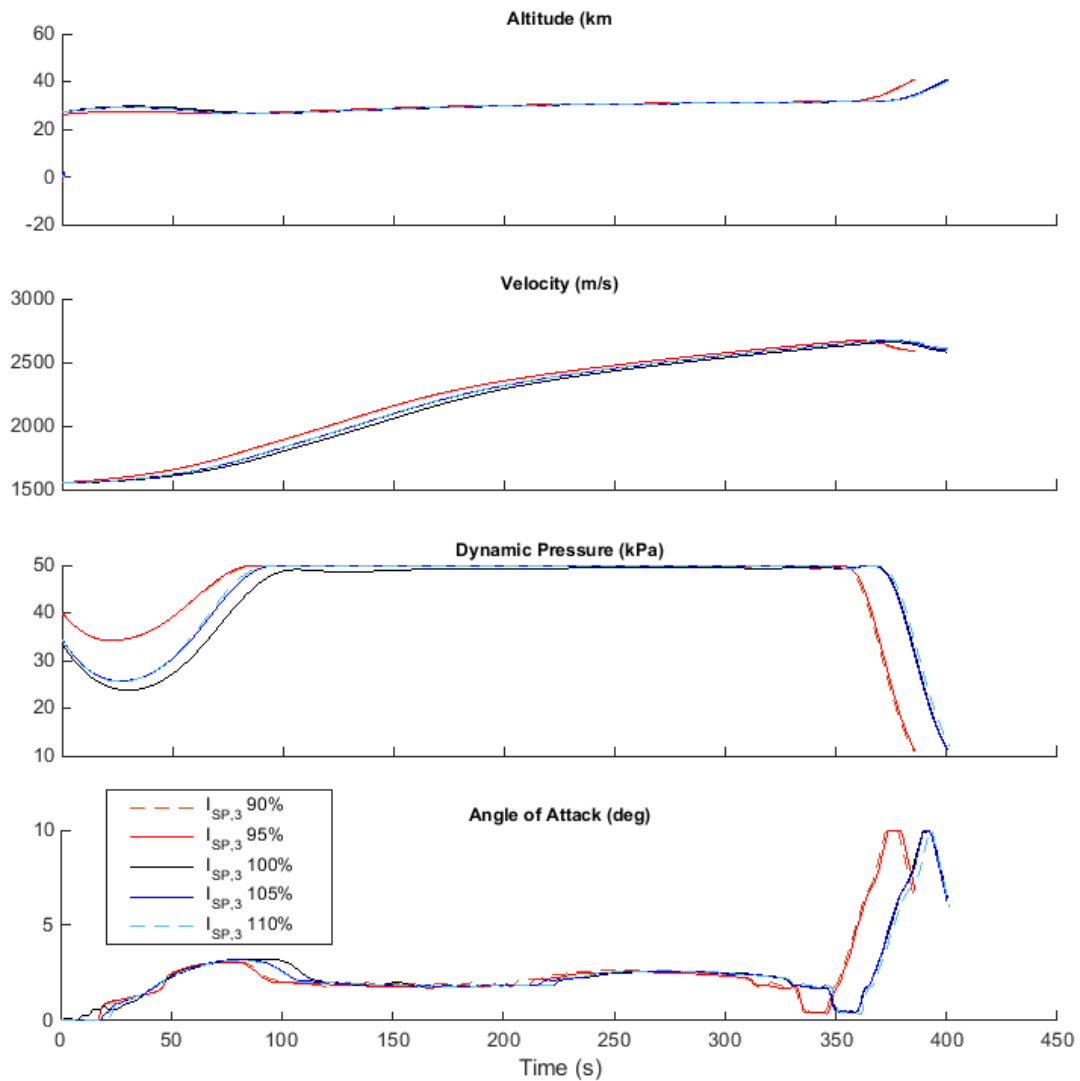
D.2.7 Case 18: Third Stage Specific Impulse Sensitivity Comparison

Figure D.35: Comparison of SPARTAN ascent trajectories with variation in the specific impulse of the third stage.

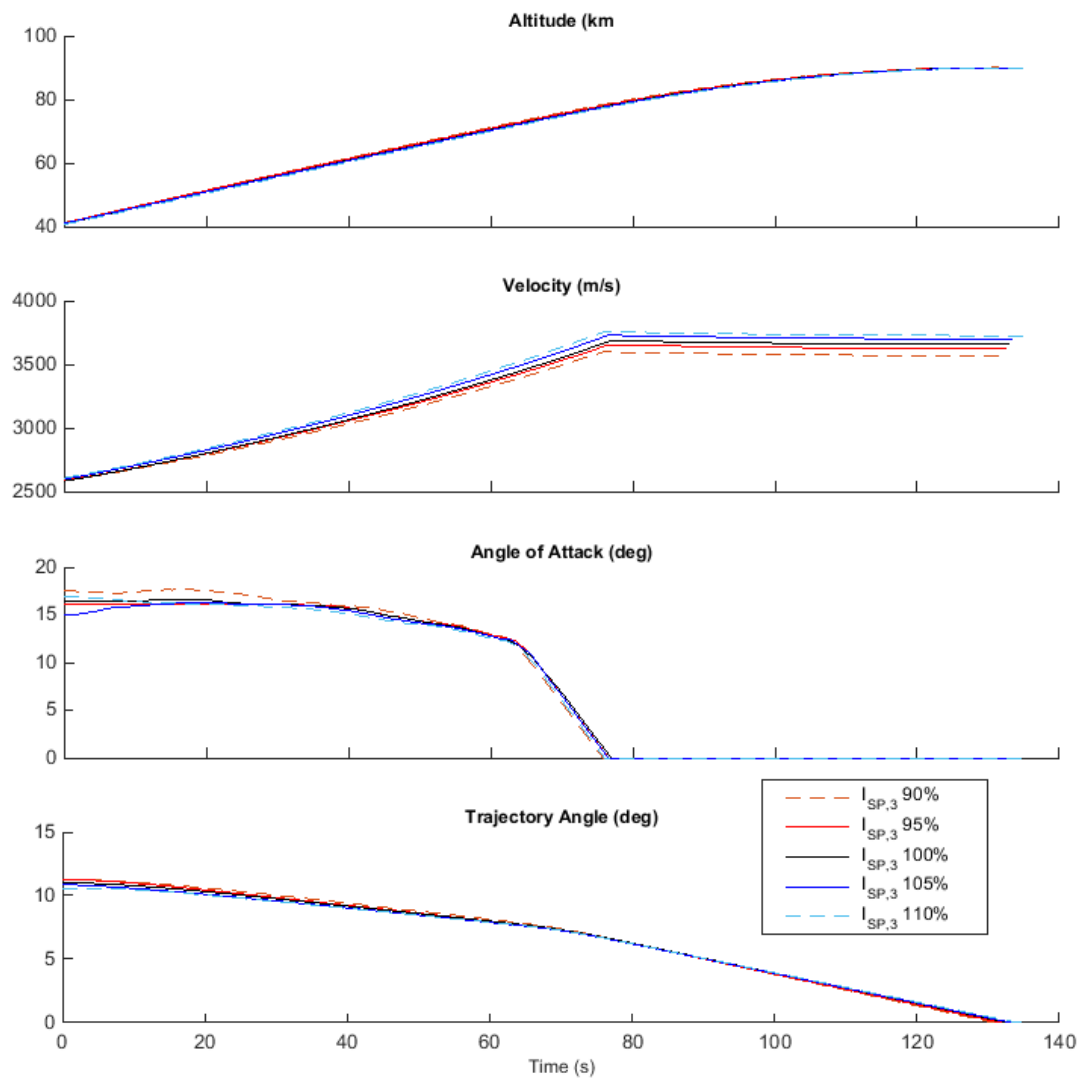


Figure D.36: Comparison of third stage rocket ascent trajectories with variation in the specific impulse of the third stage.

APPENDIX D. TRAJECTORY PLOT COMPARISONS

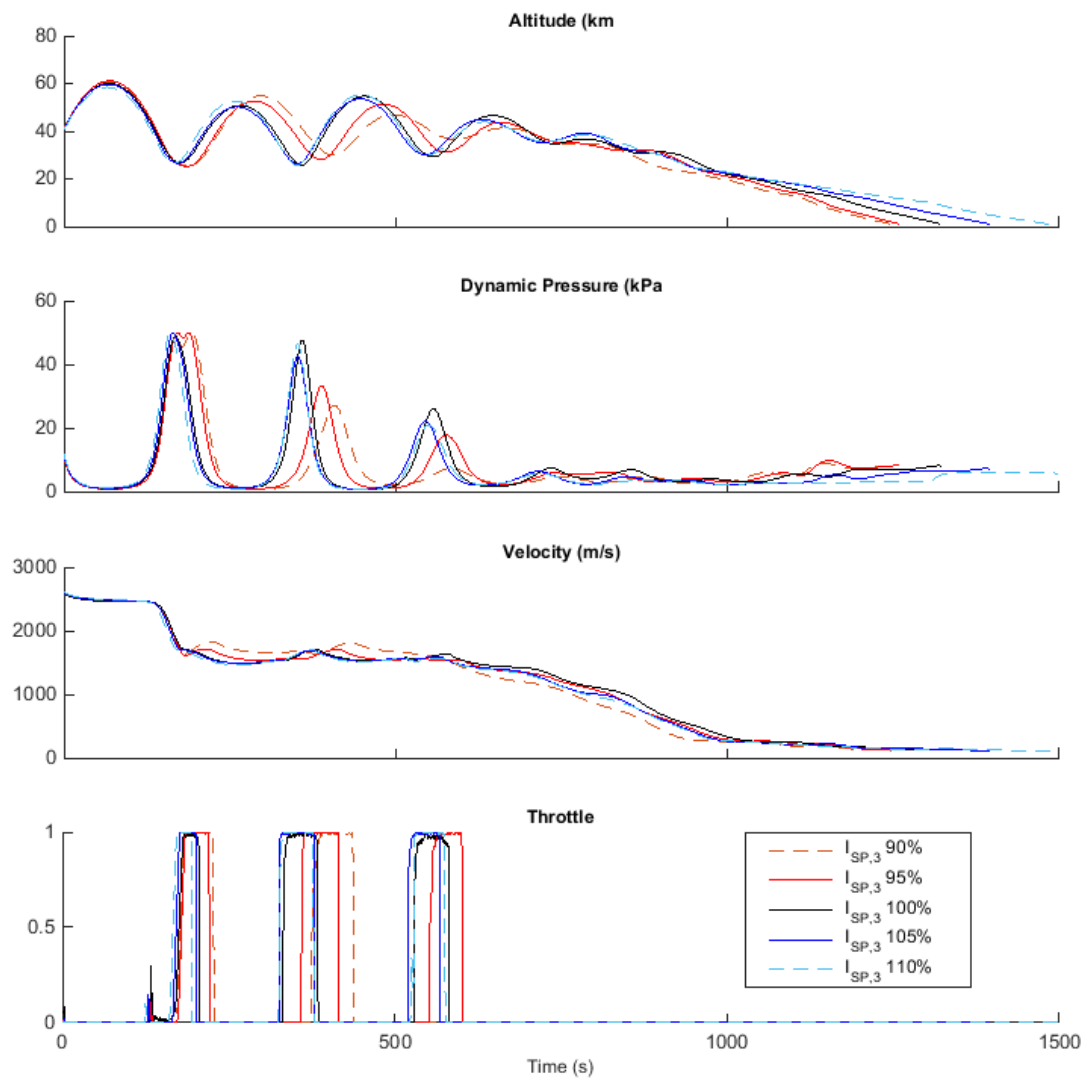


Figure D.37: Comparison of SPARTAN return trajectories with variation in the specific impulse of the third stage.

APPENDIX E

VISCOUS DRAG VARIATION

The viscous drag component of the SPARTAN’s aerodynamics is calculated using flat plate correlations, which require an estimation of the laminar to turbulent transition point on the body of the SPARTAN[122]. This transition point is difficult to estimate to a high degree of accuracy without prohibitively time consuming CFD, and can have a significant effect on the viscous drag of an aircraft[122]. The viscous drag component of the SPARTAN’s aerodynamics is varied, in order to assess the impact of the viscous drag model used. Optimal trajectories are calculated with the viscous drag set at levels of 20%, 50%, 107% and 115% of the baseline, which correspond to the possible viscous drag range due to transition point variation. Table E.1 details key trajectory parameters of the optimised trajectories, and Figures E.1, E.2 and E.3 show comparison plots of the optimised trajectories. This viscous drag comparison is intended as a reference to indicate the magnitude of variations in the viscous drag of the SPARTAN due to variations in modelling methods, and is not indicative of any physical design variations. The sensitivity of the launch system to the viscous drag of the SPARTAN is shown to be relatively low, indicating that the modelling process of the viscous drag is unlikely to have a large effect on the maximum payload-to-orbit achievable.

Trajectory Condition	vC _D :	20%	50%	100%	107%	115%	$\Delta/\Delta\%vC_D$
Payload to Orbit (kg)	212.9	196.0	170.2	166.5	166.2	-2.5	
Payload Variation (%)	25.09	15.12	0.00	-2.19	-2.36	-0.31	
Total η_{exergy} (%)	1.868	1.718	1.491	1.458	1.456	-0.00022	
1st Stage η_{exergy} (%)	8.501	8.550	8.597	8.584	8.624		-
Separation Alt, 1→2 (km)	24.84	25.95	27.14	26.89	27.61		-
Separation v, 1→2 (m/s)	1554	1552	1548	1549	1548		-
Separation γ, 1→2 (m/s)	2.1	3.7	5.6	5.1	6.4		-
2nd Stage η_{exergy} (%)	12.941	11.519	9.494	9.219	9.074	-0.154	
Separation Alt, 2→3 (km)	40.88	40.66	40.93	41.09	41.24		-
Separation v, 2→3 (m/s)	2863	2750	2581	2553	2549		-33.84
Separation γ, 2→3 (deg)	8.8	9.8	11.0	11.3	11.4		-0.1
Separation q, 2→3(kPa)	13.9	13.2	11.2	10.7	10.4		-0.17
2nd Stage L/D, 2→3	6.2	5.1	4.7	4.7	4.7		-0.07
2nd Stage Flight Time (s)	517.0	516.8	525.4	517.5	532.1		-
2nd Stage Return Fuel (kg)	212.2	239.9	268.0	283.7	245.3		-
3rd Stage η_{exergy} (%)	19.052	19.874	20.786	21.079	20.998		-
3rd Stage $t, q > 5\text{kpa}$ (s)	21.0	16.7	13.3	12.7	12.1		-0.24
3rd Stage max α (deg)	17.6	16.7	16.7	15.8	16.3		-
3rd Stage Fuel Mass (kg)	2801.8	2818.8	2844.5	2848.3	2848.6		-32.96

Table E.1: Summary of key trajectory parameters with SPARTAN viscous drag variation.

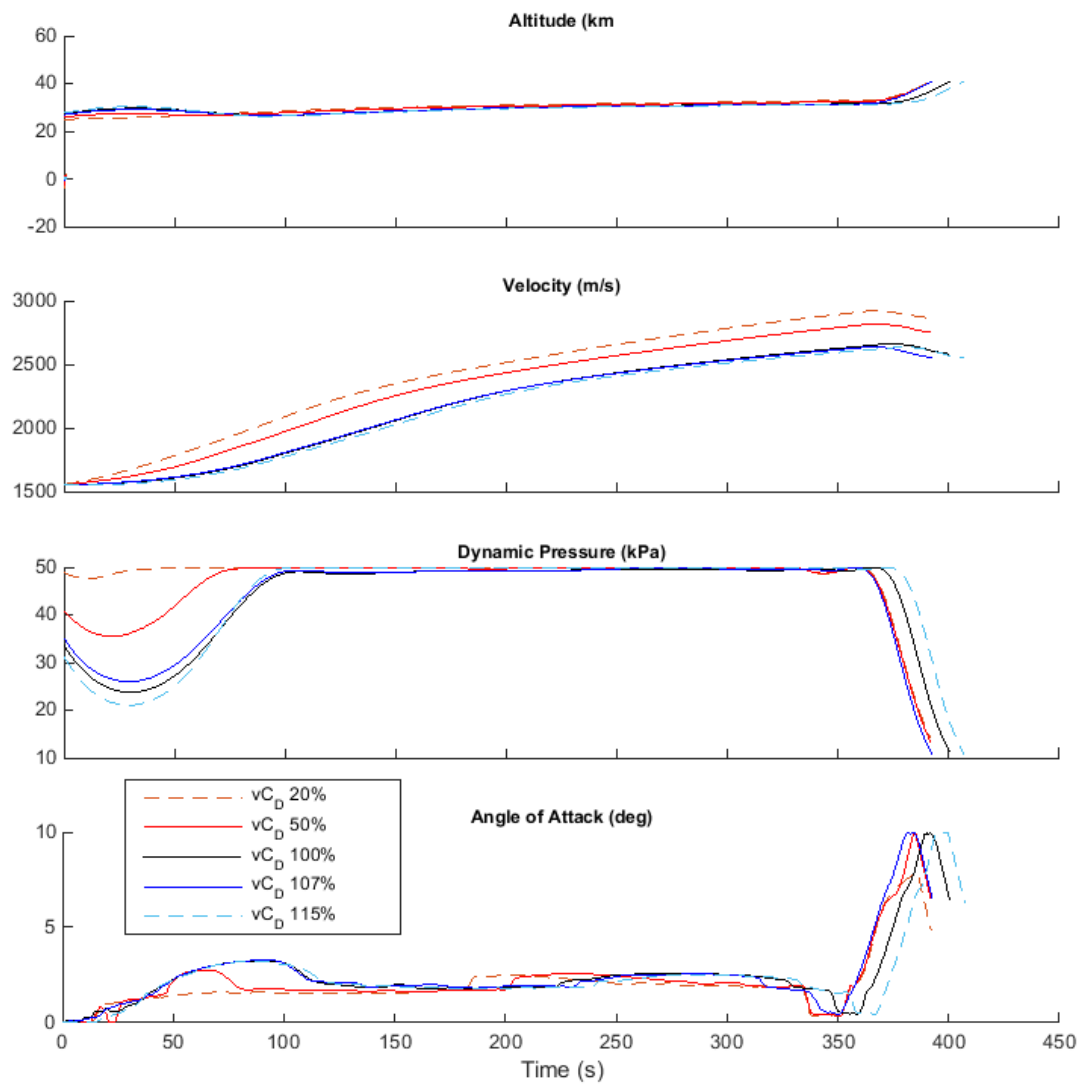


Figure E.1: Comparison of SPARTAN ascent trajectories with variation in the viscous drag of the SPARTAN.

APPENDIX E. VISCOUS DRAG VARIATION

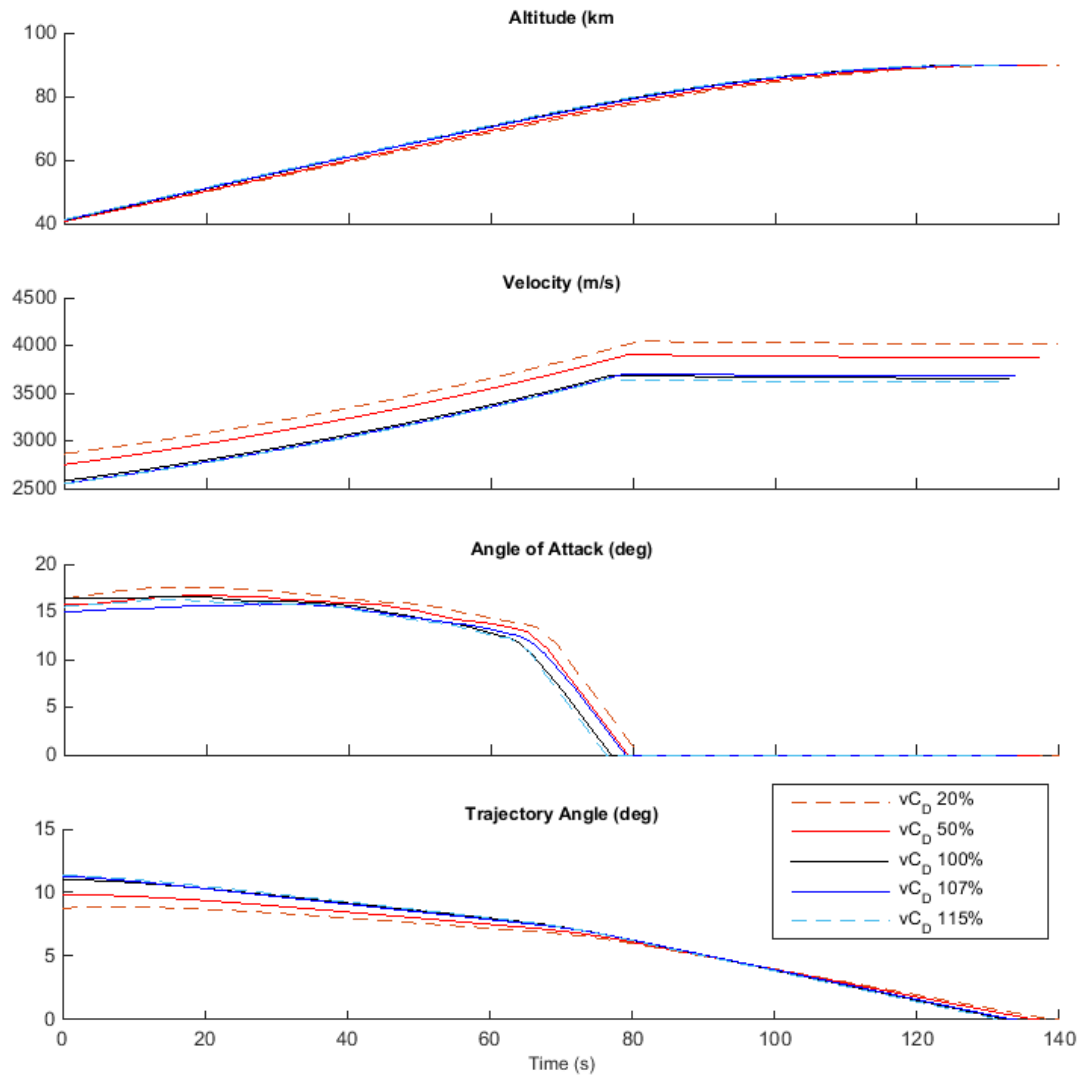


Figure E.2: Comparison of third stage ascent trajectories with variation in the viscous drag of the SPARTAN.

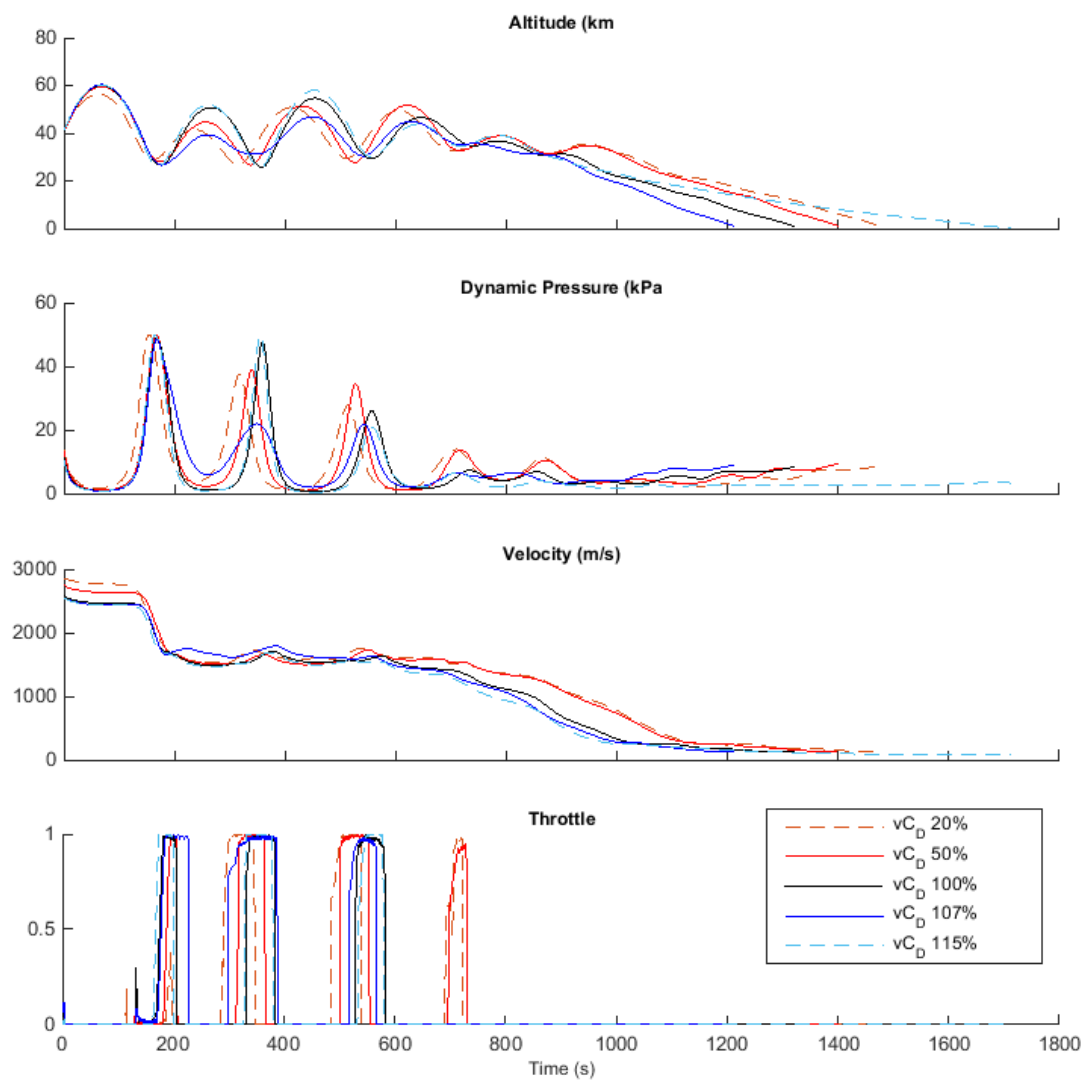


Figure E.3: Comparison of SPARTAN return trajectories with variation in the viscous drag of the SPARTAN.